

**Black holes begin to reveal  
their secrets** p. 116

**An mRNA vaccine to treat  
multiple sclerosis** p. 145

**Sleuthing out a killer  
of coho salmon** p. 185

# Science

\$15  
8 JANUARY 2021  
[sciencemag.org](http://sciencemag.org)

 AAAS

## SPINNING SPERM

Tubulin glycylation helps beating flagella  
promote sperm motility p. 144



## Pushing the Boundaries of Knowledge

As AAAS's first multidisciplinary, open access journal, *Science Advances* publishes research that reflects the selectivity of high impact, innovative research you expect from the *Science* family of journals, published in an open access format to serve a vast and growing global audience. Check out the latest findings or learn how to submit your research: [ScienceAdvances.org](https://www.scienceadvances.org)

Science  
Advances  
AAAS

---

**GOLD OPEN ACCESS, DIGITAL, AND FREE TO ALL READERS**

---



# CONTENTS

8 JANUARY 2021 • VOLUME 371  
ISSUE 6525

116

## NEWS

### IN BRIEF

**106** News at a glance

### IN DEPTH

#### **108** Viral evolution may herald new pandemic phase

Scientists worry about another 'very, very bad' wave, argue for stricter control measures  
*By K. Kupferschmidt*

#### **109** Dosing debates, transparency issues roil vaccine rollouts

U.K. decision to delay booster shots sparks concerns  
*By J. Cohen*

#### **110** Brexit deal secures U.K. access to research funds

Horizon Europe program will be open to U.K. researchers  
*By N. Wallace*

#### **111** Dismay greets end of U.S. effort to curb devastating forest pest

States, tribes oppose federal move to end quarantines and rely on tiny parasitic wasps to fight invasive beetle  
*By G. Popkin*  
PODCAST

#### **112** U.S. law sets stage for boost to artificial intelligence research

Congress authorizes ramp up in AI spending and backs planning for a national cloud computing resource  
*By J. Mervis*

#### **113** Decoy toxin harnessed to fight botulism

In animal studies, miniature antibodies work within nerves to reverse paralysis  
*By K. Servick*

SCIENCE TRANSLATIONAL MEDICINE RESEARCH ARTICLES 10.1126/SCITRANSLMED.AAZ4197 AND 10.1126/SCITRANSLMED.ABD7789

#### **114** Gene therapy beats premature-aging syndrome in mice

CRISPR-inspired base editor to be tried on progeria patients  
*By J. Kaiser*

#### **115** Will warming make animals darker—or lighter?

Long-standing belief that higher temperatures favor darker variants comes under fire  
*By S. Kean*

### FEATURES

#### **116** The hole truth

Now that black holes can be studied directly, scientists wonder whether they really are the strange beasts Albert Einstein's theory predicts  
*By A. Cho*

#### **118** Alternatives to black holes are scarce and strange *By A. Cho*

## INSIGHTS

### PERSPECTIVES

#### **120** SARS-CoV-2 spillover events

Spillover from mink to humans highlights SARS-CoV-2 transmission routes from animals  
*By P. Zhou and Z.-L. Shi*  
REPORT p. 172

#### **122** How mice feel each other's pain or fear

Distinct neuronal pathways mediate empathy with different affective states  
*By A. S. Klein and N. Gogolla*  
RESEARCH ARTICLE p. 153

#### **123** Between a hydrogen and a covalent bond

The bonds in aqueous FHF<sup>-</sup> are neither simple hydrogen nor covalent bonds  
*By M. Bonn and J. Hunger*  
RESEARCH ARTICLE p. 160

#### **125** Multikingdom diffusion barrier control

Plant microbiomes modulate selective nutrient uptake by regulating diffusion barriers  
*By W. Busch and J. Chory*  
RESEARCH ARTICLE p. 143

#### **126** COVID-19 testing: One size does not fit all

To control the pandemic, testing should be considered a public health tool  
*By M. J. Mina and K. G. Andersen*

### POLICY FORUM

#### **128** Coevolution of policy and science during the pandemic

Recent, high-quality science is being heard, but unevenly  
*By Y. Yin et al.*

### BOOKS ET AL.

#### **131** Play breeds better thinkers

Children need unstructured exploration and time to tackle problems that interest them  
*By K. Hirsh-Pasek*

**132 Probed, pierced, and revered**

Earth's mantle acts as a metaphor for the planet's unknowns, for its beauty, and for its fragility *By D. P. Dixon*

**LETTERS****133 Stay true to integrated pest management**

*By K. Wyckhuys et al.*

**133 Raising standards for global data-sharing**

*By E. S. Dove et al.*

**134 Response**

*By J. Bovenberg et al.*

**135 Technical Comment abstracts****RESEARCH****IN BRIEF**

**137** From *Science* and other journals

**REVIEW****140 Neurodevelopment**

Making sense of neural development by comparing wiring strategies for seeing and hearing

*A. A. Sitko and L. V. Goodrich*

REVIEW SUMMARY; FOR FULL TEXT:  
DOI.ORG/10.1126/SCIENCE.AAZ6317

**RESEARCH ARTICLES****141 Spliceosome**

Mechanism of spliceosome remodeling by the ATPase/helicase Prp2 and its coactivator Spp2 *R. Bai et al.*

RESEARCH ARTICLE SUMMARY; FOR FULL TEXT:  
DOI.ORG/10.1126/SCIENCE.ABE8863

**142 HIV**

Recapitulation of HIV-1 Env-antibody coevolution in macaques leading to neutralization breadth

*R. S. Roark et al.*

RESEARCH ARTICLE SUMMARY; FOR FULL TEXT:  
DOI.ORG/10.1126/SCIENCE.ABD2638

**143 Plant science**

Coordination between microbiota and root endodermis supports plant mineral nutrient homeostasis

*I. Salas-González et al.*

RESEARCH ARTICLE SUMMARY; FOR FULL TEXT:  
DOI.ORG/10.1126/SCIENCE.ABD0695  
PERSPECTIVE P. 125

**144 Cell biology**

Tubulin glycylation controls axonemal dynein activity, flagellar beat, and male fertility

*S. Gadadhar et al.*

RESEARCH ARTICLE SUMMARY; FOR FULL TEXT:  
DOI.ORG/10.1126/SCIENCE.ABD4914

**145 Multiple sclerosis**

A noninflammatory mRNA vaccine for treatment of experimental autoimmune encephalomyelitis

*C. Krienke et al.*

**153 Neuroscience**

Anterior cingulate inputs to nucleus accumbens control the social transfer of pain and analgesia

*M. L. Smith et al.*

PERSPECTIVE p. 122

**160 Chemical physics**

Crossover from hydrogen to chemical bonding

*B. Dereka et al.*

PERSPECTIVE P. 123

**REPORTS****164 Meteorites**

Carbonaceous chondrite meteorites experienced fluid flow within the past million years

*S. Turner et al.*

**168 Stellar astrophysics**

Lithium pollution of a white dwarf records the accretion of an extrasolar planetesimal

*B. C. Kaiser et al.*

**172 Coronavirus**

Transmission of SARS-CoV-2 on mink farms between humans and mink and back to humans

*B. B. Oude Munnink et al.*

PERSPECTIVE p. 120

**178 Ocean anoxia**

Microbial sulfate reduction and organic sulfur formation in sinking marine particles

*M. R. Raven et al.*

**181 Immunology**

Pre-T cell receptors topologically sample self-ligands during thymocyte  $\beta$ -selection

*X. Li et al.*

**185 Ecotoxicology**

A ubiquitous tire rubber-derived chemical induces acute mortality in coho salmon

*Z. Tian et al.*

**Structural virology**

**190** A broadly protective antibody that targets the flavivirus NS1 protein

*N. Modhiran et al.*

**194** Structural basis for antibody inhibition of flavivirus NS1-triggered endothelial dysfunction

*S. B. Biering et al.*

**DEPARTMENTS****105 Editorial**

Innovative partnerships

*By Sethuraman Panchanathan*

**206 Working Life**

Breaking through language barriers

*By Saman Razavi*

**ON THE COVER**

A mouse sperm lacking glycylation swims in circles. Glycylation is a posttranslational modification of tubulin that is predominately found in cilia and flagella, where it contributes to coordinating axonemal dynein motors that

power the flagellar beating. Lack of glycylation causes an abnormal flagellar beat and results in circular instead of straight sperm swimming. This in turn severely affects male fertility. See page 144.

*Illustration: C. Bickel/Science*



New Products ..... 201  
Science Careers ..... 202

SCIENCE (ISSN 0036-8075) is published weekly on Friday, except last week in December, by the American Association for the Advancement of Science, 1200 New York Avenue, NW, Washington, DC 20005. Periodicals mail postage (publication No. 484460) paid at Washington, DC, and additional mailing offices. Copyright © 2021 by the American Association for the Advancement of Science. The title SCIENCE is a registered trademark of the AAAS. Domestic individual membership, including subscription (12 months): \$165 (\$74 allocated to subscription). Domestic institutional subscription (51 issues): \$2148; Foreign postage extra: Air assist delivery: \$98. First class, airmail, student, and emeritus rates on request. Canadian rates with GST available upon request. GST #125488122. Publications Mail Agreement Number 1069624. Printed in the U.S.A.

**Change of address:** Allow 4 weeks, giving old and new addresses and 8-digit account number. **Postmaster:** Send change of address to AAAS, P.O. Box 96178, Washington, DC 20090-6178. **Single-copy sales:** \$15 each plus shipping and handling available from backissues.science.org; bulk rate on request. **Authorization to reproduce** material for internal or personal use under circumstances not falling within the fair use provisions of the Copyright Act can be obtained through the Copyright Clearance Center (CCC), www.copyright.com. The identification code for Science is 0036-8075. Science is indexed in the Reader's Guide to Periodical Literature and in several specialized indexes.



# Innovative partnerships

**W**hen I became director of the U.S. National Science Foundation (NSF) in June 2020, the world was in the midst of a pandemic that continues to reshape daily lives, work, education, and the research enterprise. As we enter 2021 with the promise of suppressing COVID-19, the world looks to the science and engineering community for solutions to speed global recovery. To generate the solutions needed from all sectors of science and engineering, the United States must create a vigorous culture of innovation nationwide, leverage public-private partnerships to tackle complex research questions, and align exploratory research with societal impacts.

As a U.S. government agency, NSF was created in 1950 to support research that benefits America's health, security, prosperity, and welfare while ensuring that its scientific infrastructure and workforce remain strong. The agency is fortunate to have had strong bipartisan support from Congress to fulfill this mission. As NSF plans for the future, it also draws inspiration from the past.

In the early 1980s, scientists across the country needed access to the most powerful computers that could advance discovery and innovation. NSF invested hundreds of millions of dollars to build supercomputers and provide remote access to them. What followed was a decade of rapid development, in partnership with research universities, telecommunications companies, and other federal agencies. The result—NSFNET—laid the foundation for the modern internet. Thirty-five years later, it is apparent how critical this and subsequent investments in computing and communications research have been in advancing global connectedness during the pandemic.

Examples like this offer lessons for creating a path forward. The United States must strengthen the synergies of curiosity-driven exploratory research and use-inspired translational research at speed and scale. NSF's goal today is to build on the intellectual energy captured by projects like NSFNET by driving collaborations across the scientific enterprise. Such partnerships allow public and private entities to align objectives and resources to more efficiently advance science and technology toward common goals. For example, last year NSF led the creation of seven new Artificial Intelligence Research Institutes. These institutes now serve as hubs for academia, indus-

try, and government to work together and enhance American competitiveness in this arena for decades to come.

Imagine the impact of creating engines of economic and talent development like this in every state, working on a range of crucial issues facing society, such as climate change, pandemic response, and diversity in science. NSF intends to build ecosystems across the country that bring together people from a range of socioeconomic backgrounds and abilities, to tackle such challenges. For example, NSF investments are intentionally bringing academic researchers together with civic leaders, local residents, and philanthropy in communities throughout the United States to understand the challenges they are facing—in accessibility and inclusivity, mobility and transportation, energy and water management, and resilience to

disasters, to name a few—to pilot sustainable, scalable research-based solutions. Likewise, in 2020, NSF launched the Historically Black Colleges and Universities (HBCUs) Science, Technology, Engineering, and Mathematics (STEM) Undergraduate Success Research Center. The Center studies successful broadening participation practices at 50 HBCUs to develop evidence-based interventions for transforming education. NSF is now forging collaborations between community colleges, minority-serving institutions, and companies to create experiential pathways for Americans to obtain the skills they need for jobs of the future. NSF will take this model to the next level—empowering regional innovation hubs across the country and with

international partners—to cultivate the dynamic collaborations between researchers that are necessary to tackle 21st-century science and engineering challenges.

America's role as global leader in science and engineering is at a tipping point. If the country is complacent, it will be surpassed by ambitious nations that are investing in their own workforces and infrastructure. There is an opportunity for the United States to continue to be innovative and impactful. It requires reaching into every corner of the country to create pathways to success for those who want to explore and learn, including thousands of young people who lack opportunities to realize their potential in STEM fields. It requires searching for every possible opportunity for partnership and collaboration—because the future depends on it now more than ever.

—Sethuraman Panchanathan



**Sethuraman Panchanathan**

is the director of the U.S. National Science Foundation, Alexandria, VA, USA. [spanchan@nsf.gov](mailto:spanchan@nsf.gov)

**“America's  
role as global  
leader in  
science and  
engineering  
is at a  
tipping point.”**

**“ We’ve [asked] the people with the least amount of resources ... to do the hardest part of the vaccination.”**

**Ashish Jha**, dean of public health at Brown University, in *The New York Times*, on why overburdened local health officials and hospitals are struggling to distribute COVID-19 vaccines.

## IN BRIEF

Edited by  
**Jeffrey Brainard**

New legislation will support wind projects like this one in Kansas.

### CLIMATE CHANGE

## United States takes steps to curb greenhouse gases

**T**he U.S. spending and coronavirus relief bills signed into law late last month included several provisions that made them, in effect, the most significant climate legislation passed in the country since 2009. Most importantly, the law requires companies to cut their production and use of hydrofluorocarbons, powerful greenhouse gases used in refrigeration, to 15% of 2012 levels by 2036. This brings the United States into de facto compliance with the 2016

Kigali agreement, signed by 197 nations but never ratified by the U.S. Senate. The law also extends tax credits for wind and solar power, and calls for spending \$35 billion on clean energy research, largely at the Department of Energy, over the next 5 years. (That number is aspirational; Congress will set actual budgets.) Those projects are to include the development of advanced nuclear power and technologies to store energy and capture carbon dioxide from the atmosphere.

## Japan's science council under fire

**GOVERNANCE** | The Science Council of Japan (SCJ) has found itself on the defensive in a dispute with government leaders about its independence. In October 2020, SCJ—Japan's national science academy—objected when Prime Minister Yoshihide Suga blocked the appointment of several scholars to the council's General Assembly, something never done before. Then on 9 December, Suga's Liberal Democratic

Party (LDP) proposed that SCJ—now a special governmental organization whose independence is protected by law—accept a less autonomous legal status and find both public and private funding. Party members also questioned the value of the council's scientific reports. In a response, SCJ defended its current legal status but promised to strengthen its advisory role and make other reforms. Supporters argue that changing its status could cripple its financial and political independence. LDP

instructed the council to further study the proposed change and report back by April.

## U.S. funders' oversight called lax

**FOREIGN INFLUENCE** | The five largest U.S. research agencies need to flesh out and clarify policies for grantees to disclose foreign ties and avoid conflicts of interest (COIs), according to a congressional watchdog. A report released last month by the Government Accountability Office (GAO)



documents that the National Institutes of Health has been by far the most aggressive in pursuing potential violators. It says that the departments of Defense and Energy lack agencywide definitions of financial COIs and that none of the agencies adequately addresses nonfinancial conflicts. The GAO findings could bolster a push in Congress for new measures to block the theft of federally funded research.

## EPA finalizes open data rule

**PUBLIC HEALTH** | In the waning days of Donald Trump's presidency, the U.S. Environmental Protection Agency (EPA) on 5 January unveiled its final rule restricting the scientific studies that can be used in writing regulations, in what it calls a move for transparency. The rule requires data underpinning key health studies used to set pollution limits—so-called dose-response studies—to be available for outside scrutiny. EPA's administrator could grant exceptions. Such limits have been championed by conservatives and business advocates, who complain that such studies cannot be double checked. The new rule's opponents "prefer the agency to make decisions in proverbial smoke-filled back rooms," says EPA Administrator Andrew Wheeler. But environmental groups and public health researchers say the measure will weaken the agency's ability to use the best science by making it harder to consider epidemiological studies that rely on confidential health information. The rule might not last long in its present form: President-elect Joe Biden's administration could rewrite it, or Congress might revoke it.

## Placebo recipients to get vaccine

**COVID-19** | Two makers of COVID-19 vaccines authorized for emergency use can offer the shots to people who had received a placebo in ongoing efficacy trials, the U.S. Food and Drug Administration (FDA) decided last week. Accepting a proposal by the manufacturer Pfizer, FDA said Pfizer and Moderna could provide vaccines to thousands of placebo recipients, but only when those people become eligible to receive the vaccines, which are in short supply. For now, this measure will allow trial volunteers to obtain the vaccines if they are members of groups, such as health care workers or residents of nursing homes, deemed at highest risk of developing COVID-19 or suffering severe illness from the infection. The gradual rollout of vaccines to placebo recipients means the studies can continue to accrue information about durability of protection

while not depriving participants who become eligible for vaccination.

## New director for MIT Media Lab

**LEADERSHIP** | Dava Newman, an aerospace engineer and former deputy NASA administrator, will lead the storied but troubled Media Lab at the Massachusetts Institute of Technology (MIT), the university announced last month. The lab's former director, Joi Ito, was forced to resign in September 2019, after *The New Yorker* revealed that he and others had masked the role of sex offender Jeffrey Epstein in funneling hundreds of thousands of dollars to the Media Lab. Newman, an MIT professor, will be the first woman to lead the lab when she takes over on 1 July. She said in a news release that making academia more diverse is "a highest priority," and she told *The Boston Globe* that the lab will work with donors "who hold our same values." Also last month, MIT reinstated Seth Lloyd, a mechanical engineering professor who took \$225,000

from Epstein for research. Lloyd had been on paid administrative leave. MIT will limit his pay for 5 years.

## India seeks broad journal deals

**PUBLISHING** | India's government said on 1 January that it wants to pay journal publishers a single price to allow access to paywalled content by readers anywhere in the country. The plan contrasts with the "transformative agreements" inked in recent years by institutional consortia in Europe; these enable the consortia's researchers to both read paywalled articles and publish their own articles open access, with no additional fees. But some European deals have carried higher prices than existing, subscription-based ones. To support open access, India's policy would require journal articles by authors it funds to be placed in institutional or central repositories. The proposals are included in a broader draft national plan for science and innovation that also aims to increase data sharing and improve gender equity.



### NUTRITION

## USDA rejects experts' advice on dietary sugar, alcohol

**T**he U.S. Department of Agriculture (USDA) last month issued new dietary guidelines that do not call for lower sugar and alcohol intake, contrary to what the agency's science advisers recommended. The guidelines, which the agency issues every 5 years, influence food manufacturers, school lunch menus, and ordinary Americans' eating and drinking habits. A panel of external experts last summer advised USDA that less than 6% of dietary calories should come from sugar added to food and beverages; instead, the new guidelines keep the previous recommendation of less than 10%. The advisers also recommended a daily limit of one alcoholic drink for men on days when they drink any alcohol, down from the current two. The agency said that "there was not a preponderance of evidence" in the experts' review supporting either change. The guidelines for women also remain unchanged, with at most one drink per day. Health advocates voiced disappointment.



Streets in downtown Glasgow were deserted on 5 January after the United Kingdom imposed a strict lockdown to curtail the spread of a new SARS-CoV-2 variant.

## COVID-19

# Viral evolution may herald new pandemic phase

Scientists worry about another ‘very, very bad’ wave, argue for stricter control measures

By **Kai Kupferschmidt**

**F**or COVID-19 researchers, the new year brings a strong sense of déjà vu. As in early 2020, the world is anxiously watching a virus spread in one country and trying to parse the risk for everyone else. This time it is not a completely new threat, but a rapidly spreading variant of SARS-CoV-2. In south-eastern England, where the B.1.1.7 variant first caught scientists’ attention last month, it has quickly replaced other variants, and it may be the harbinger of a new, particularly perilous phase of the pandemic.

“One concern is that B.1.1.7 will now become the dominant global variant with its higher transmission and it will drive another very, very bad wave,” says Jeremy Farrar, an infectious disease expert who heads the Wellcome Trust. Whereas the pandemic’s trajectory in 2020 was fairly predictable, “I think we’re going into an unpredictable phase now,” as a result the virus’ evolution, Farrar says.

The concern has led some countries to speed up vaccine authorizations or discuss dosing regimens that may protect

more people rapidly (see p. 109). But as the new variant surfaces in multiple countries, many scientists are calling for governments to strengthen existing control measures as well. U.K. Prime Minister Boris Johnson announced tough new restrictions on 4 January, including closing schools and asking people not to leave their homes unless strictly necessary. But other countries have hesitated. “I do feel like we are in another situation right now where a lot of Europe is kind of sitting and looking,” says virologist Emma Hodcroft of the University of Basel. “I really hope that this time we can recognize that this is our early alarm bell, and this is our chance to get ahead of this variant.”

In announcing the U.K. restrictions, Johnson said the new variant is between 50% and 70% more transmissible. But researchers have been careful to point out uncertainties. Cases have soared in the United Kingdom over the past month, but the rise occurred while different parts of the country had different levels of restrictions and amid changes in people’s behavior and regional infection rates in the run-up to Christmas—“a complex scenario” that

makes it hard to pinpoint the effect of the new variant, says evolutionary biologist Oliver Pybus of the University of Oxford.

Yet evidence has rapidly increased that B.1.1.7’s many mutations, including eight in the crucial spike protein, do enhance spread. “We’re relying on multiple streams of imperfect evidence, but pretty much all that evidence is pointing in the same direction now,” says Adam Kucharski, a modeler at the London School of Hygiene & Tropical Medicine. For instance, an analysis by Public Health England showed about 15% of the contacts of people infected with B.1.1.7 in England went on to test positive themselves, compared with 10% of contacts of those infected with other variants.

If other countries that have detected B.1.1.7 also see it surge, it will be “the strongest evidence we will have,” Pybus says. Data from Denmark, which leads the European Union in the sequencing of SARS-CoV-2, are not reassuring. Routine surveillance there has picked up the variant dozens of times; its frequency went from 0.2% of sequenced genomes in early December to 2.3% 3 weeks later. “We have had what looks like a poster child example



of exponential growth these last 4 weeks in Denmark,” says genomicist Mads Albertsen of Aalborg University.

The lack of evidence—so far—that the new variant makes people sicker is little consolation. Increased transmissibility of a virus is much more treacherous than increased pathogenicity because its effects grow exponentially, Kucharski says. “If you have something that kills 1% of people but a huge number of people get it, that’s going to result in more deaths than something that a small number of people get but it kills 2% of them.”

If the U.K. estimates of a 50% to 70% increase in the virus’ reproduction number, or  $R$ , hold true, “keeping the virus from spreading has become a lot harder,” says Viola Priesemann, a physicist at the Max Planck Institute for Dynamics and Self-Organization who has been modeling the pandemic and the effects of nonpharmaceutical interventions, such as physical distancing and school closures. “In Germany you would need two big additional measures to keep the reproduction number below 1,” Priesemann says.

Isolating patients and tracing, quarantining, and testing their contacts is one part of any attempt at doing so; those measures alone can reduce  $R$  from about 2 to about 1, Priesemann has shown for Germany. But that effect breaks down when case numbers reach a critical threshold and public health authorities are overwhelmed, which means tougher measures now can help contain spread of the new variant later. “It’s yet another reason to go for very low numbers,” says Priesemann, who co-authored a December 2020 letter to in *The Lancet* calling for Europe to adopt a joint strategy to bring down infections fast. Hodcroft agrees. “The case has never been stronger,” she says. “What’s the worst-case scenario here? We overshoot and we get cases so low that we can get rid of a lot of restrictions.”

Curtailling infections sharply has the added benefit of reducing the chances for the virus to evolve even further. Already other variants have emerged, notably one called 501Y.V2 in South Africa, that are just as worrying as B.1.1.7, Farrar adds. “It is essentially a numbers game: The more virus is circulating, the more chance mutants have to appear,” he says. In the long term, mutations could arise that threaten the efficacy of vaccines.

It’s dispiriting to feel like the world is back where it was in early 2020, says epidemiologist William Hanage of the Harvard T.H. Chan School of Public Health. “But we have to stop this virus. ... Fatalism is not a nonpharmaceutical intervention.” ■

## COVID-19

# Dosing debates, transparency issues roil vaccine rollouts

## U.K. decision to delay booster shots sparks concerns

By Jon Cohen

**L**ast-minute vaccine dosing changes that could gamble away proven COVID-19 protection and undermine public trust. Controversial approvals without any efficacy data. Vaccinemakers at odds with countries hosting their clinical trials. The COVID-19 vaccine landscape keeps changing almost daily, simultaneously raising hopes and triggering confusion and scientific debates. “It’s crazy,” says vaccine researcher John Moore of Weill Cornell Medicine. “Every morning, it’s just, ‘What’s going on?’”

Over the past few weeks, COVID-19 vaccines developed in the United Kingdom, China, and India moved toward widespread rollout, offering new weapons in the face of fast-spreading viral variants that threaten

to deepen the crisis (see p. 108). But many came with controversies, and U.K. regulators sparked a debate when they endorsed a sharp departure from the expected dosing schedule for a newly authorized vaccine from AstraZeneca and the University of Oxford and one from Pfizer and BioNTech.

The pandemic has driven most COVID-19 vaccinemakers to aim for a short 3 or 4 weeks between prime and booster shots, but the U.K. Medicines and Healthcare products Regulatory Agency (MHRA) said second shots can be given up to 12 weeks later.

Biostatistician Natalie Dean of the University of Florida thinks MHRA moved too quickly and without enough explanation of its dosing decision. “Clearly there were deliberations that the U.K. had about this, but we don’t have access to those discussions.”

MHRA didn’t cite the fast-spreading B.1.1.7 variant of SARS-CoV-2 in its dosing decision, announced last week when the agency authorized the AstraZeneca-Oxford vaccine. But some scientists say the strain’s threat, which led this week to a U.K.-wide lockdown, justifies delaying the booster to expand the population that can receive at least one dose of vaccine.

MHRA said an “exploratory analysis” of some participants in AstraZeneca-Oxford phase III trials in Brazil and the United Kingdom found an efficacy of 73% after a

single dose of the vaccine, which uses an adenovirus to deliver a gene that codes for the surface protein, spike, of SARS-CoV-2. This, oddly, was higher than the 62% efficacy after two full doses reported in *The Lancet*. Oxford’s Adrian Hill, who co-led the vaccine’s development, notes its efficacy trials started earlier than other groups, which may explain the discrepancy. “I’m afraid it’s possible that what’s happening is efficacy is declining over time,” Hill says. (The 62% figure has itself brought confusion, as the vaccine had a reported 90% efficacy when the first dose was halved.)

For all two-dose vaccines, intervals between a prime and booster are somewhat arbitrary, says pediatrician Paul Offit of the Children’s Hospital of Philadelphia, a member of an independent U.S. vaccine advisory committee. But some physicians and scientists worry that last-minute debates on dosing strategies will increase vaccine hesitancy. “Mixed messages and lack of evidence will inevitably lead to undermining the public trust in the vaccine and could negatively impact on uptake,” the Doctors’ Association UK wrote in a letter of concern to the U.K. health minister.

The British Society for Immunology issued a statement supporting MHRA’s “pragmatic” dosing schedule, but urged the government to launch a “robust” monitoring program to determine how the different intervals affect efficacy. Several scientists also called for more direct clinical trial comparisons of dosing intervals.

The United States seems unlikely to follow the U.K. example. “The MHRA has taken quite a significant risk,” says Moncef Slaoui, chief scientist for the U.S. government’s Operation Warp Speed program, which is now staging its own 30,000-person trial of the AstraZeneca-Oxford vaccine. “After the first dose, quite a lot of people actually are not primed,” he adds. The U.S. Food and Drug Administration (FDA) issued a statement that made similar scientific arguments, adding that the move could backfire if people who are not fully protected begin to increase their risk of exposure.

Nor do data on the two U.S. authorized vaccines, which both use messenger RNA encoding spike, clearly support a delayed booster. Made by Pfizer and BioNTech and

Science’s COVID-19 reporting is supported by the Pulitzer Center and the Heising-Simons Foundation.

Moderna, both have a reported efficacy of about 95% after two doses. But data Pfizer provided last month showed an efficacy of just 52.4% between the first and second dose of its vaccine, below FDA's threshold for emergency use given the result's statistical uncertainty.

Slaoui floated a different change to expand supply of the Moderna vaccine: cutting both doses in half. Moderna has data showing its vaccine stimulated a strong immune response in people between ages 18 and 55 at half the usual dose, he notes. But FDA doesn't like that idea, either. "There are some possible challenges with reliability and interpretation of the data that Slaoui based this on," says Peter Marks, who heads FDA's Center for Biologics Evaluation and Research. And in much of the United States, logistical problems, rather than sup-

comparable to that seen in trials elsewhere.

China's Sinovac and Sinopharm added to the confusion with their COVID-19 vaccines, which are based on whole, killed copies of SARS-CoV-2. A press release early last month from the United Arab Emirates said that a candidate from Sinopharm's China National Biotec Group was safe and had "86% efficacy against COVID-19 infection" in a UAE trial that involved 31,000 participants. But on 30 December, the state-owned company reported that the vaccine had 79.34% efficacy "against the disease."

Its statement contained no other important scientific information. Nevertheless, China gave the vaccine "conditional approval," instructing Sinopharm to complete the efficacy studies it has underway in UAE and several other countries. (The company did not reply to queries from *Science*.)



Doses of the AstraZeneca-Oxford COVID-19 vaccine, made at the Serum Institute of India, are stored in a cold room.

ply shortages, are currently the main limiting factor in the vaccination campaign.

In India, meanwhile, the Central Drugs Standard Control Organisation (CDSCO) created a furor on 3 January by granting "restricted emergency approval" for a vaccine containing killed, or "inactivated," SARS-CoV-2, based on early trials showing immune responses but not efficacy, as well as animal data. A phase III trial of the vaccine, produced by Bharat Biotech, hasn't even completed recruiting. Vineeta Bal of India's National Institute of Immunology calls the decision "unconscionable."

But CDSCO's director, V. G. Somani, said the approval was out of "abundant precaution," in case it was needed to protect the country against B.1.1.7. CDSCO also approved a local version of the AstraZeneca-Oxford vaccine, even though it hasn't fully analyzed data from a "bridging study" designed to show that the vaccine triggers an immune response in Indians

A similar muddle surrounds Sinovac's vaccine. On 23 December, investigators in Brazil announced that a trial with 13,000 participants had shown greater than 50% efficacy. But they said a contractual agreement with Sinovac prohibited them from revealing more information and the company wanted to compare results from other countries. One day later, researchers in Turkey revealed interim data, which were far more preliminary, from a Sinovac vaccine trial that suggested an efficacy of 91.25%.

Mauro Schechter, an infectious disease researcher at the Federal University of Rio de Janeiro, College City, says "the perception that Turkish investigators are at liberty to divulge their data but Brazilians are not" contributes to what he calls "an atmosphere of distrust" for Sinovac's vaccine, one of Brazil's only options now. And that's the last thing needed as the pandemic takes its deadly toll. ■

With reporting by Priyanka Pulla in India.

## EUROPE

# Brexit deal secures U.K. access to research funds

## Horizon Europe program will be open to U.K. researchers

By **Nicholas Wallace**

**T**he Brexit cliffhanger has ended with a favorable outcome for U.K. researchers. Just 1 week before a 1 January deadline, negotiators struck a long-term agreement on trade and cooperation that will ease the United Kingdom's exit from the European Union. The deal also includes a hoped-for provision for science. In exchange for a contribution to the EU budget, the United Kingdom will join the forthcoming Horizon Europe research program, which will spend €85 billion over the next 7 years.

"I am unbelievably relieved," says Vivienne Stern, director of advocacy group Universities UK International (UUKI). She says failure to reach agreement on Horizon Europe "would've been a tragedy" for U.K. researchers, and that the outcome is "a relief to the European and international research community."

Mike Galsworthy, co-founder of anti-Brexit campaign group Scientists for EU and a visiting researcher at the London School of Hygiene & Tropical Medicine, is also pleased about access to Horizon Europe. But he laments the loss of U.K. influence over the program and how the money is spent, because those decisions will only be made by EU countries.

U.K.-based researchers were among the largest beneficiaries of Horizon 2020, Horizon Europe's predecessor. They hoped that after Brexit, the country would pay for "associate" status, which allows researchers in non-EU countries such as Switzerland and Israel to apply for and receive EU funding. But there were fears that associate membership might be too costly.

Association fees are calculated on the basis of gross domestic product, but after Swiss and Israeli researchers won more from Horizon 2020 than their govern-



ments paid in, the European Union revised rules for Horizon Europe so that associate nations would pay more if they won ample funding.

The Brexit deal contains similar rules to ensure the United Kingdom won't underpay, but that is unlikely. UUKI previously put the 7-year cost of joining at more than €15 billion, more than double the €7 billion or so the country got from Horizon 2020. "The EU knew that they could ask for quite a lot from us because we have so grown into that program," Galsworthy says.

The United Kingdom will also pay to participate in nuclear research under the Euratom treaty, despite having withdrawn from the treaty itself. It will take part in ITER, an international fusion energy project, via an EU-run partnership that also includes Switzerland. And it will remain involved with the Copernicus Earth observation satellite program and the European Space Surveillance and Tracking system, which monitors threats from space debris.

However, the country will not get access to special military-only signals from the Galileo satellite navigation system—Europe's answer to GPS. The United Kingdom has contributed about €1.4 billion to Galileo's creation, more than 10% of its budget. Losing access to parts of Galileo is "a massive loss," given the U.K. investments, Galsworthy says.

One part of Horizon Europe will also be off-limits to U.K. researchers: the European Innovation Council Accelerator, a new equity fund that invests in tech startups (*Science*, 10 April 2020, p. 120). "There is obviously a nervousness in the EU about the U.K.'s innovation performance, and Horizon effectively helping the U.K. to compete as a near neighbor but competitor economy," Stern says.

After the United Kingdom announced its intention to leave the European Union in 2017, participation by U.K. researchers in Horizon projects fell sharply. Stern says she heard stories of U.K. researchers being asked to leave consortia for fear their presence might affect the success of Horizon 2020 bids. Now, Galsworthy says, "We need to try and gather back our position on Horizon Europe." But, he adds, some uncertainty remains, because the European Union could unilaterally "blow up" the entire deal if it believes the United Kingdom has reneged on any particular part of it.

The U.K.-EU deal took effect provisionally on 1 January. The U.K. Parliament has already ratified it, and both the European Council and European Parliament must give their approval by the end of February. ■

Nicholas Wallace is a journalist in Brussels.



Scientists hope this parasitic wasp from Asia can help stop the emerald ash borer's spread in North America.

## CONSERVATION SCIENCE

# Dismay greets end of U.S. effort to curb devastating forest pest

States, tribes oppose federal move to end quarantines and rely on tiny parasitic wasps to fight invasive beetle

By **Gabriel Popkin**

**L**ater this month, the U.S. Department of Agriculture (USDA) will formally admit defeat along one front of its battle against a devastating invasive insect. Starting 14 January, the agency will no longer regulate the movement of living ash trees or wood between states. This quarantine has, for more than 10 years, formed the cornerstone of the federal government's strategy for curbing the spread of the emerald ash borer, an iridescent green beetle that threatens to wipe out North America's ash trees, an ecological linchpin of many forests. Instead, USDA plans to ramp up an effort to control the borer by releasing tiny wasps that parasitize and kill the beetles.

The shift is controversial. Some scientists and environmental advocates agree that, after spending some \$350 million over the past 2 decades to fight the ash borer, the government should redirect scarce resources to more promising strategies. But others argue the surrender is premature, and some states are vowing to maintain local controls on ash tree and wood movement. "I worry that this decision hastens the rate at which [ash] trees are threatened," says Leigh Greenwood, a forest health specialist at the Nature Conservancy. "This is one layer of protection we're taking away."

The emerald ash borer first gained notoriety in 2002, when ash trees in the Detroit area started mysteriously dying. After researchers identified the insect, which was accidentally imported from Asia, Michigan and USDA's Animal and Plant Health Inspection Service (APHIS) imposed a quarantine that prohibited export of ash trees and wood from inside the infested zone. Biologists also began to set traps to monitor the spread of the beetle.

But stopping the borer's expansion has proved difficult; adults can fly up to 10 kilometers and often go undetected in new areas for years. The borer has attacked and killed tens of millions of trees in at least 35 states, mostly in the eastern and central United States; it has also infested southern Canada. USDA's quarantine zone has expanded along with the beetle. But in 2017, the International Union for Conservation of Nature declared the borer had caused six North American ash species to become endangered or critically endangered. And in 2018, APHIS proposed ending its quarantine. "The regulations haven't stopped it from spreading," Robyn Rose, who managed the agency's borer program, said that year.

USDA's proposal drew some 150 comments. Some scientists and groups supported the move, in part to free up scarce resources. But others argued that USDA's withdrawal could

hamper efforts to prevent the borer from spreading to several as-yet-uninfested western states and Mexico, which hold the only known populations of numerous ash species. Oregon officials, for example, fear losing Oregon ash, an important riverside tree. Other experts worry city budgets could be strained by the costs of removing thousands of dead ash trees if the beetle attacks urban forests. Several Native American tribes have argued the move would endanger ash trees on their lands, which are vital to cultural practices such as basketmaking.

Despite those concerns, USDA last month announced it would end the quarantine in favor of what it deems “more effective and less intrusive methods” to fight the borer. The agency will instead emphasize biological control, or introducing natural enemies of the borer. In particular, scientists have identified four species of parasitic wasps native to Asia that lay eggs in ash borer larvae or eggs.

So far, researchers have released the parasitoids on an experimental basis in 340 counties in 30 states. Three of the wasps have established self-sustaining populations. At some sites, researchers report the wasps have killed 20% to 85% of borer larvae feeding on ash saplings, and are helping young trees survive to reproductive age. “All the information seems to be pointing in the same direction—the parasitoids are having an impact,” says Herbert Bolton, who now manages the ash borer program at APHIS.

For biocontrol to protect ash trees in the long term, however, wasps would have to establish everywhere ash trees grow—a still-distant goal. And wasps appear less effective at protecting mature ash trees, perhaps because they can’t penetrate the thick bark to find borers. To keep older trees standing, APHIS is investigating strategies that include chemical pesticides, but such efforts would be practical only in select ash stands. USDA has also backed longer term efforts to breed borer-resistant ash trees that could be used to replant forests (*Science*, 13 November 2020, p. 756).

Minnesota won’t follow USDA’s lead, saying it will enforce its own internal quarantine. Other states plan to start to certify firewood—which can carry the borer—as pest-free, a task the federal government had been doing. Such piecemeal efforts won’t be enough, fears Reginald Defoe, resource manager for the Fond du Lac Band of Lake Superior Chippewa in northern Minnesota. After USDA released its proposal, he wrote that, without a uniform national policy, “the movement of [the borer] is anticipated to be much faster.” ■

Gabriel Popkin is a journalist in Mount Rainier, Maryland.



Researchers hope to use cloud computing and artificial intelligence to improve public transit.

#### RESEARCH POLICY

## U.S. law sets stage for boost to artificial intelligence research

Congress authorizes ramp up in AI spending and backs planning for a national cloud computing resource

By Jeffrey Mervis

**L**ow-income commuters who rely on public transit face many challenges—multiple transfers, long waits, and off-hour travel—that aren’t measured in the usual ridership surveys. Vanessa Frias-Martinez, a computer scientist at the University of Maryland, College Park, wants to ease their commute by harnessing two hot trends in computer science, cloud computing and artificial intelligence (AI), which Congress now hopes to scale up dramatically for U.S. scientists.

With support from the National Science Foundation, including an NSF-funded effort called CloudBank that subsidizes access to commercial cloud services, Frias-Martinez plans to track the movements of thousands of Baltimore residents while protecting their privacy. And by applying AI algorithms to the large data sets, she hopes to identify ways to eliminate transit bottlenecks and improve service. Frias-Martinez predicts CloudBank “will flatten the steep learning curve” for first-time cloud users like her.

Congress has now embraced a plan to ensure there are many more. The Na-

tional Artificial Intelligence Initiative Act (NAIIA) of 2020, which became law last week, aims to bolster AI activities at more than a dozen agencies. Its directives include a study of how to create a national research cloud that would build on CloudBank. It also calls for an expansion of a network of research institutes launched last summer, and the creation of a White House AI office and an advisory committee to monitor those efforts.

“It’s the closest thing to a national strategy on AI from the United States to be formally endorsed by Congress,” says Tony Samp, a former congressional staffer turned high-tech lobbyist for DLA Piper. He and others say the new law is meant to keep the country at the forefront of global AI research in the face of growing investments by other countries.

The NAIIA authorizes spending but doesn’t appropriate money. If funded, however, it would significantly ramp up federal AI investments. It authorizes \$4.8 billion for NSF over the next 5 years, with another \$1.15 billion for the Department of Energy (DOE) and \$390 million for National Institute of Standards and Technology (NIST).

PHOTO: NIC ANTAYA FOR THE BOSTON GLOBE/GETTY IMAGES



NSF, which funds the vast majority of federally supported AI academic research, estimates it spent \$510 million on AI in 2020, so the NAIIA would roughly double that effort.

The military is also upping its AI game. The NAIIA is appended to the National Defense Authorization Act, a 4500-page bill providing annual policy guidance to the Department of Defense that survived a presidential veto. This year's version of the must-pass bill raises the stature of the Pentagon's Joint Artificial Intelligence Center formed in 2018 and gives it new authority to use AI to improve combat readiness and fight wars.

The NAIIA both codifies what some federal agencies are already doing and gives them an extensive to-do list. For example, it endorses NSF's network of seven AI research institutes, launched last summer with help from the U.S. Department of Agriculture and in partnership with industry, and backs similar centers at DOE and the Department of Commerce—which includes NIST and the National Oceanic and Atmospheric Administration. The NSF institutes, each funded at roughly \$20 million over 5 years, will support research in applying AI to a variety of topics including weather forecasting, sustainable agriculture, drug discovery, and cosmology.

NSF is already soliciting proposals for a second round of multidisciplinary institutes, and many AI advocates would like to see its growth continue. A white paper for President-elect Joe Biden, for example, calls for an initial investment of \$1 billion, and a 2019 community road map envisions each institute supporting 100 faculty members, 200 AI engineers, and 500 students.

Their popularity has revived a recurring debate about how to grow such an initiative without hurting the core NSF research programs that support individual investigators. "We're very proud of the institutes, which have gotten a lot of attention, and we think they can be wonderfully transformational," says Margaret Martonosi, head of NSF's Computing and Information Science and Engineering (CISE) directorate. But Martonosi also notes that CISE spends even more on its core programs—and still rejects more good proposals than it funds.

Cloud computing could also boost AI, because it enables researchers to compile and analyze the huge data sets required to train AI algorithms. It, too, gets a big shoutout in the new law, which directs the NSF director and the president's science adviser to assemble a 12-member task force to study the feasibility of a National Research Resource (NRR). Such a national cloud would scale up what CloudBank is

now doing and give researchers the tools to analyze large public data sets containing, say, anonymized government health records or satellite data.

"At present, only a handful of companies can afford the substantial computational resources required to develop and train the machine learning models underlying today's AI," says Stanford University's John Etchemendy. "What's more, the large data troves required to train these algorithms are for the most part controlled by either industry or government. Academic researchers struggle to gain access to both." Etchemendy, a former longtime provost, and computer scientist Fei-Fei Li direct Stanford's Institute for Human-Centered Artificial Intelligence and co-authored a proposal for an NRR that legislators used as a template in the NAIIA.

Columbia University computer scientist Jeannette Wing, whose resume includes leading NSF's computing directorate and running Microsoft's research shop, would like to see "all universities use the cloud routinely for all research and all educational activities." Scientists who continue to rely on their own institutional computing resources, expertise, and support staff, she believes, will find it increasingly difficult to keep pace with competitors who can address cutting-edge research questions via the cloud.

Creating such a ubiquitous network, which she calls an academic cloud, won't be easy. "Current commercial cloud providers have interfaces and services that are not nontechie friendly and price points that are out of line for academics," she explains. But she thinks those problems can be solved.

How a national cloud would be structured or managed poses another challenge. Some have suggested linking it to DOE's network of national labs, or to the supercomputing centers that DOE and NSF support. Etchemendy hopes the government will decide to contract with commercial cloud services such as Amazon Web Services, Google Cloud, Microsoft Azure, and IBM Cloud rather than starting from scratch.

"The commercial cloud providers are doing the innovation, and they invest massive amounts of money to keep it up-to-date," he says. "It would be a huge mistake to build a facility like a supercomputer center because it would be obsolete within a few years."

Even if the spending levels authorized by the new law are aspirational, AI advocates say the act demonstrates the remarkable support that the field now enjoys. "There was a real sense of urgency on this issue," Samp says. "I also think [the NAIIA] provides a foundation for years to come." ■

## BIOMEDICINE

# Decoy toxin harnessed to fight botulism

In animal studies, miniature antibodies work within nerves to reverse paralysis

By Kelly Servick

**A** new strategy to fight the world's most potent poison has passed its first tests in animals. Two research teams have developed neutered forms of botulinum toxin that chase their deadly counterpart into nerves and disarm it. The treatment, if it works in people, would be the first to reverse the paralyzing effects of the toxin inside cells and might spare patients long periods on a ventilator. "In a life-threatening situation, this will be very, very helpful," says Brenda Anne Wilson, a toxin microbiologist at the University of Illinois, Urbana-Champaign.

Made by bacteria that can grow in improperly preserved food and in infected wounds, the toxin penetrates motor nerves and hacks apart proteins critical for nerve signaling. "It's not killing the neurons, but it silences them," says Konstantin Ichtchenko, a biochemist at the New York University School of Medicine. In tiny quantities, botulinum toxin can control muscle spasms and relax wrinkles. But a larger dose can paralyze breathing.

Botulism is rare, with fewer than 200 U.S. cases logged per year, but the toxin is also a terrifying potential bioweapon. The current treatment, a cocktail of antibodies, can inactivate the toxin in blood, but can't enter nerves. By the time symptoms emerge, some toxin is out of reach.

Now, Ichtchenko's team and another led by Min Dong, a neuroscientist and microbiologist at Boston Children's Hospital, have hitched neutralizing antibodies to a modified form of the toxin itself, which is adept at slipping into nerve cells. "We basically just created a Trojan horse," Ichtchenko says.

Harnessing neurotoxins for drug delivery isn't new, but using them to send in antibodies is "very intuitive and very elegant," says Saak Ovsepian, a neurobiologist at the Czech Republic's National Institute of Mental Health, whose team published

a similar approach in 2011 using botulinum toxin to ferry gene-carrying viruses into neurons.

To devise its Trojan horse, Ichchenko's group made three genetic tweaks to a natural form of botulinum toxin that prevent it from slicing up cellular proteins. Dong notes, however, that the disarmed toxin can still cause muscle paralysis at high doses. So his study, headed by microbiologist Shin-Ichiro Miyashita, now at the Tokyo University of Agriculture, combined components of a disease-causing form with a related botulinum toxin that doesn't naturally invade or disable human nerves. The resulting drug caused no toxicity in mice even at doses where a modified version of a common botulinum toxin was deadly.

Both teams linked their engineered toxin to a tiny antibody, derived from alpacas, that can inactivate the toxin. Compared with full-size antibodies, nanobodies can be more readily engineered to reach specific targets in cells and better keep their structure once inside, says Anne Messer, a molecular biologist at the Neural Stem Cell Institute.

Dong's group injected mice with a lethal dose of botulinum toxin and administered its treatment 9 hours later—when paralysis had already set in. The 10 mice given the highest treatment dose were mobile within 6 hours, whereas untreated mice struggled to breathe and had to be euthanized, the team reports this week in *Science Translational Medicine*. In another set of experiments, the group linked the modified toxin to two different nanobodies and successfully disarmed two common varieties of botulinum toxin at once. In the same issue of the journal, Ichchenko's team describes successful tests in mice, guinea pigs, and macaque monkeys. All six monkeys given the treatment were alive 10 days after getting the toxin; none of seven untreated monkeys lived past 3.5 days.

James Marks, a molecular biologist at the University of California, San Francisco, notes that in contrast to lab animals that are given a single relatively small botulinum dose, human victims often have a large "reservoir" of toxin in their gut that enters the bloodstream over days or weeks. So even if this approach works, patients will likely also need the approved antitoxin treatment to remove toxin from the blood.

Both teams plan to refine their products and seek approval from the U.S. Food and Drug Administration, which can authorize drugs based on animal studies when human efficacy tests aren't ethical. Experimental drugs face "a long, hard road" from animal results to an approved product, Marks says. "But this is where it starts." ■

## BIOMEDICINE

# Gene therapy beats premature-aging syndrome in mice

## CRISPR-inspired base editor to be tried on progeria patients

By Jocelyn Kaiser

**O**ne mouse is hunched over, graying, and barely moves at 7 months old. Others, at 11 months, have sleek black coats and run around. The videos and other results from a new study have inspired hope for treating children born with progeria, a rare, fatal, genetic disease that causes symptoms much like early aging. In mice with a progeria-causing mutation, a cousin of the celebrated genome editor known as CRISPR corrected the DNA mistake, preventing the heart damage typical of the disease, a research team reports this week in *Nature*. Treated mice lived about 500 days, more than twice as long as untreated animals.

Although the developers of the progeria therapy aim to improve it, they are also taking steps toward testing the current version in affected children, and some other scientists endorse a rush. The mouse results are "beyond anyone's wildest expectations," says Fyodor Urnov, a gene-editing researcher at the University of California, Berkeley. "The new data are an imperative to treat a child with progeria ... and do so in the next 3 years."

About 400 people in the world are estimated to have Hutchinson-Gilford progeria syndrome, which results from a single-base change in the gene for a protein called lamin A that helps support the membrane forming the nucleus in cells. The resulting abnormal protein, called progerin, disrupts the nuclear membrane and is toxic to cells in many tissues. Toddlers soon become bald and have stunted growth, body fat loss, stiff joints, wrinkled skin, osteoporosis, and atherosclerosis. People with progeria die on average around age 14 from a heart attack or stroke.

Researchers have previously used CRISPR to disrupt activity of the mutated gene for lamin A in progeria mice. But their health improved only modestly, and disabling a person's good copy of the gene could cause harm. So David Liu of Harvard University and the Broad Institute turned to base editing, a DNA-changing method originally inspired by CRISPR and developed in his lab.

Unlike CRISPR, which makes double-strand cuts in DNA, the base editor used in the progeria study nicks just one strand and swaps out a single base. Base editors have treated several single-tissue disorders in mice, and Liu wanted to try one on an "infamous and devastating" disease that involves multiple organs or tissues.

Liu's group teamed up with Vanderbilt University cardiologist Jonathan Brown and Francis Collins, director of the National Institutes of Health, whose group was one of two that identified the progeria mutation in 2003. The team first tested the base-editing approach in cultured cells from two progeria patients, finding that it corrected the mutation while making few unwanted changes elsewhere in the genome. They then packaged DNA encoding the base editor into adeno-associated viruses (AAVs) and injected these into young mice with the progeria mutation.

When the mice were examined 6 months later, between 20% and 60% of their bone, skeletal muscle, liver, heart, and aorta carried the DNA fix. Progerin levels fell and lamin A levels rose in several tissues. Even though the mice were already 2 weeks old when treated, or about age 5 in human years, their aortas months later bore virtually no signs of the fibrous tissue growth or loss of smooth muscle cells seen in mice and children with progeria.

Some of the rodents developed liver tumors, a problem seen before in mice receiving high-dose AAV gene therapy. No people have been shown to have developed liver tumors as a result of such treatments. Still, lowering the AAV dose to improve safety "is a goal," Liu says. He and Collins are evaluating more efficient base editors to that end.

Study co-author Leslie Gordon, a Brown University physician whose son died from progeria and who co-founded the Progeria Research Foundation, doesn't want to wait for "the next iteration" before developing plans and raising money to test the treatment in children. Her foundation is talking to companies, including Beam Therapeutics, which Liu co-founded, in hopes of launching a clinical trial. "We will find a way to get this done for these kids," Gordon says. ■

**"We will find a way to get this done for these kids."**

**Leslie Gordon,**  
Brown University





Tawny owls in Finland are increasingly russet (right) instead of pale gray, which provides better camouflage against snow.

## EVOLUTION

# Will warming make animals darker—or lighter?

Long-standing belief that higher temperatures favor darker variants comes under fire

By Sam Kean

A 19th century claim has fueled a 21st century debate about how a warming climate might reshape animals. Beginning in the early 1800s, biologists identified multiple “rules” describing the ecological and evolutionary impacts of temperature. One rule held that animals have bigger appendages (ears, beaks) in hot climates, to help dissipate body heat. Another said that, within any group of animals, the biggest generally reside closer to the poles—think of polar bears towering over midlatitude brown bears—because larger bodies help retain heat.

And Gloger’s rule, named after German biologist Constantin Gloger, declared that animals in warmer regions usually have darker exteriors, whereas those in cooler regions are lighter. Among mammals, darker skin and hair was thought to protect against damaging ultraviolet light, which is more plentiful in Sun-soaked equatorial areas. Among birds, the specific melanin pigments in darker feathers seem to resist bacterial infestation, an advantage in the Petri dish of the tropics.

Last year, Li Tian of the China University of Geosciences and Michael Benton of the University of Bristol revived interest in these largely forgotten rules when the two paleontologists used them to predict how climate

change might remake animal bodies. Among other things, they relied on Gloger’s rule to propose that, as Earth warms, most animals would get darker. Simple enough.

But a series of essays in *Current Biology*, including two last month, showed that other biologists consider the matter far from settled. “I was a bit taken aback,” says Kaspar Delhey, an ornithologist who lives in Australia and works remotely for the Max Planck Institute for Ornithology in Germany. “I thought, ‘There’s more work to do.’” Delhey has led a campaign over the past few years to replace Gloger’s rule with something more accurate. “It has been surrounded by confusion since forever,” he says, partly because the 1833 book where Gloger laid out his data “was very dense and awfully written.”

Last month, Delhey and three colleagues published a response to Tian and Benton in *Current Biology*. Their main beef is that Gloger’s rule conflates temperature and humidity. Humidity leads to lush plant life, which offers shadows to hide from predators. Animals therefore tend to be darker in wet places to camouflage themselves. Many warm places are steamy, but cool, wet forests tend to have the darkest birds, Delhey says.

Delhey argues that if you control for humidity, Gloger’s rule gets flipped on its head—warming leads to lighter animals. That’s especially true for cold-blooded critters, he

says. Insects and reptiles rely on external heat sources, and in cold places, their dark exteriors help soak up sunlight. In warmer climates, that constraint is relaxed, and they end up lighter. Delhey calls this the “thermal melanism hypothesis.”

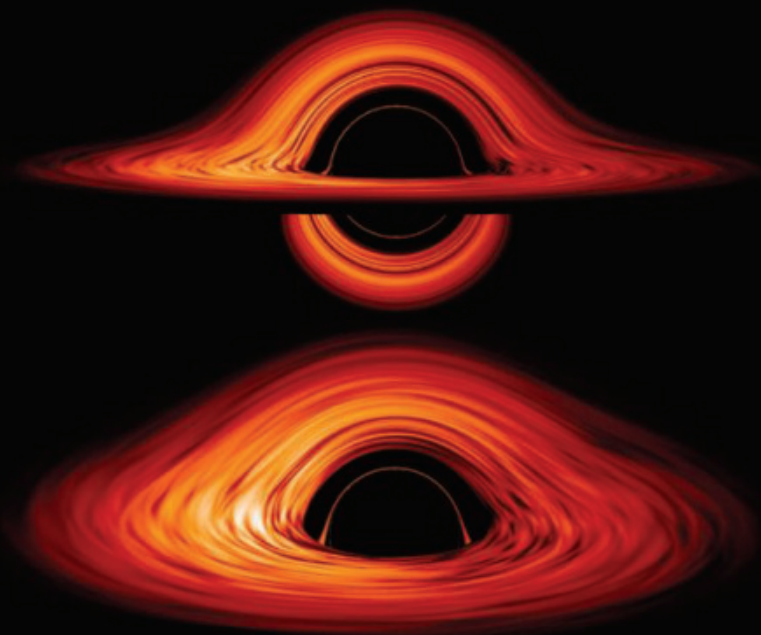
Tian and Benton say they welcome the clarifications. Still, in a reply to the Delhey group, they cite cases where their prediction of darker animals in warmer climates holds true. Tawny owls in Finland are either russet or pale gray, with the gray providing camouflage against snow. But as snow cover has decreased in Finland, russet owls grew from about 12% of the population in the early 1960s to 40% in 2010.

But they acknowledge that predictions of climate-driven color effects get especially tricky when temperature and humidity both change. Climate models predict the Amazon will get hotter and drier, which all parties agree will lighten animal color. But the boreal forests of Siberia could get hotter and wetter, in which case the temperature and humidity predictions conflict. Unlike in physics or chemistry, Benton says, biological laws “are not absolute. It’s not like gravity.”

And even when general trends hold, it’s still difficult to predict how individual species will change. Lauren Buckley, a biologist at the University of Washington, Seattle, has studied butterfly color in high-altitude regions. Butterflies soak up heat by basking in sunshine, but only one small patch on the underside of the wings actually absorbs the heat. “If you didn’t know that,” she points out, “you could quantify all sorts of exotic colorations on the top of the wing, and it wouldn’t actually matter.” In sum, “We need to think about the full picture of how organisms are interacting with their environments.”

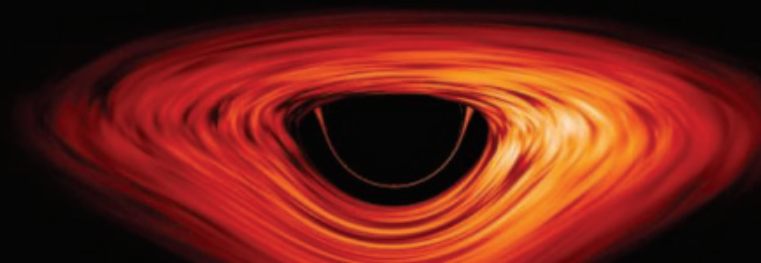
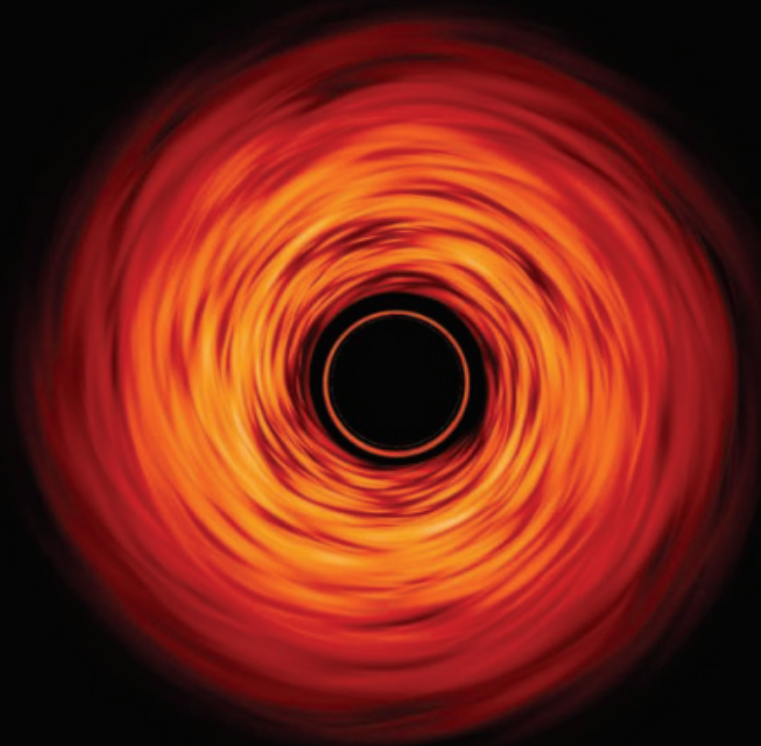
Changes in coloration will also likely depend on the animal’s temperature-regulation system—with cold-blooded creatures growing generally lighter and birds and mammals showing a wider range of outcomes. To improve predictions, Buckley suggests using museum specimens to broaden time frames, although their colors can fade over time. For his part, Tian plans to run experiments with warmed tanks of beetles and mollusks, actively trying to induce color changes.

Alas, scientists may soon have more data on this topic as the planet’s temperatures push higher. And if global warming gets truly dire, even the most time-tested ecogeographic rules may prove meaningless as habitats disappear and species vanish. However intriguing the science, Delhey acknowledges, “It does make one sad.” ■



# THE HOLE TRUTH

Now that black holes can be studied directly, scientists wonder whether they really are the strange beasts Albert Einstein's theory predicts *By Adrian Cho*





**W**hile working on his doctorate in theoretical physics in the early 1970s, Saul Teukolsky solved a problem that seemed purely hypothetical. Imagine a black hole, the ghostly knot of gravity that forms when, say, a massive star burns out and collapses to an infinitesimal point. Suppose you perturb it, as you might strike a bell. How does the black hole respond?

Teukolsky, then a graduate student at the California Institute of Technology (Caltech), attacked the problem with pencil, paper, and Albert Einstein's theory of gravity, general relativity. Like a bell, the black hole would oscillate at one main frequency and multiple overtones, he found. The oscillations would quickly fade as the black hole radiated gravitational waves—ripples in the fabric of space itself. It was a sweet problem, says Teukolsky, now at Cornell University. And it was completely abstract—until 5 years ago.

In February 2016, experimenters with the Laser Interferometer Gravitational-Wave Observatory (LIGO), a pair of huge instruments in Louisiana and Washington, reported the first observation of fleeting gravitational ripples, which had emanated from two black holes, each about 30 times as massive as the Sun, spiraling into each other 1.3 billion light-years away. LIGO even sensed the “ring down”: the shudder of the bigger black hole produced by the merger. Teukolsky's old thesis was suddenly cutting-edge physics.

“The thought that anything I did would ever have implications for anything measurable in my lifetime was so far-fetched that the last 5 years have seemed like living in a dream world,” Teukolsky says. “I have to pinch myself, it doesn't feel real.”

Fantastical though it may seem, scientists can now study black holes as real objects. Gravitational wave detectors have spotted four dozen black hole mergers since LIGO's breakthrough detection. In April 2019, an international collaboration called the Event Horizon Telescope (EHT) produced the first image of a black hole. By training radio telescopes around the globe on the supermassive black hole in the heart of the nearby galaxy Messier 87 (M87), EHT imaged a fiery ring of hot gas surrounding the black hole's inky “shadow.” Meanwhile, astronomers are tracking stars that zip close to the black hole in the center of our own Galaxy, following paths that may hold clues to the nature of the black hole itself.

In a simulation, seen from various angles, a black hole's intense gravity warps the image of the disk of hot, glowing gas surrounding it.

The observations are already challenging astrophysicists' assumptions about how black holes form and influence their surroundings. The smaller black holes detected by LIGO and, now, the European gravitational wave detector Virgo in Italy have proved heavier and more varied than expected, straining astrophysicists' understanding of the massive stars from which they presumably form. And the environment around the supermassive black hole in our Galaxy appears surprisingly fertile, teeming with young stars not expected to form in such a maelstrom. But some scientists feel the pull of a more fundamental question: Are they really seeing the black holes predicted by Einstein's theory?

**“Even though it's very unlikely, it would be so amazingly important if we found that there was any deviation” from general relativity.**

Sean Carroll,  
California Institute of Technology

Some theorists say the answer is most likely a ho-hum yes. “I don't think we're going to learn anything more about general relativity or the theory of black holes from any of this,” says Robert Wald, a gravitational theorist at the University of Chicago. Others aren't so sure. “Are black holes strictly the same as you would expect with general relativity or are they different?” asks Clifford Will, a gravitational theorist at the University of Florida. “That's going to be a major thrust of future observations.” Any anomalies would require a rethink of Einstein's theory, which physicists suspect is not the final word on gravity, as it doesn't jibe with the other cornerstone of modern physics, quantum mechanics.

Using multiple techniques, researchers are already gaining different, complementary views of these strange objects, says Andrea Ghez, an astrophysicist at the University of California, Los Angeles, who shared the 2020 Nobel Prize in Physics for inferring the existence of the supermassive black hole in the heart of our Galaxy. “We're still a long way from putting a complete picture together,” she says, “but we're certainly getting more of the puzzle pieces in place.”

**CONSISTING OF PURE** gravitational energy, a black hole is a ball of contradictions. It contains no matter, but, like a bowling ball, possesses mass and can spin. It has no sur-

face, but has a size. It behaves like an imposing, weighty object, but is really just a peculiar region of space.

Or so says general relativity, which Einstein published in 1915. Two centuries earlier, Isaac Newton had posited that gravity is a force that somehow reaches through space to attract massive objects to one another. Einstein went deeper and argued that gravity arises because massive things such as stars and planets warp space and time—more accurately, spacetime—causing the trajectories of freely falling objects to curve into, say, the parabolic arc of a thrown ball.

Early predictions of general relativity differed only slightly from those of Newton's theory. Whereas Newton predicted that a planet should orbit its star in an ellipse, general relativity predicts that the orientation of the ellipse should advance slightly, or precess, with each orbit. In the first triumph of the theory, Einstein showed it accounted for the previously unexplained precession of the orbit of the planet Mercury. Only years later did physicists realize the theory also implied something far more radical.

In 1939, theorist J. Robert Oppenheimer and colleagues calculated that when a sufficiently massive star burned out, no known force could stop its core from collapsing to an infinitesimal point, leaving behind its gravitational field as a permanent pit in spacetime. Within a certain distance of the point, gravity would be so strong that not even light could escape. Anything closer would be cut off from the rest of the universe, David Finkelstein, a theorist at Caltech, argued in 1958. This “event horizon” isn't a physical surface. An astronaut falling past it would notice nothing special. Nevertheless, reasoned Finkelstein, who died just days before LIGO's announcement in 2016, the horizon would act like a one-way membrane, letting things fall in, but preventing anything from getting out.

According to general relativity, these objects—eventually named black holes by famed theorist John Archibald Wheeler—should also exhibit a shocking sameness. In 1963, Roy Kerr, a mathematician from New Zealand, worked out how a spinning black hole of a given mass would warp and twist spacetime. Others soon proved that, in general relativity, mass and spin are the only characteristics a black hole can have, implying that Kerr's mathematical formula, known as the Kerr metric, describes every black hole there is. Wheeler dubbed the result the no-hair theorem to emphasize that two black holes of the same mass and spin are as indistinguishable as bald pates. Wheeler himself was bald, Teukolsky notes, “so maybe it was bald pride.”

Some physicists suspected black holes

# Alternatives to black holes are scarce and strange

**A**t one time, many physicists resisted the notion of a black hole, a ghostly, self-sustaining gravitational field so intense that not even light can escape. Now, theorists have few alternatives to these creepy holes in the universe.

Any alternative to a black hole must be some dark, dense material orb that's slightly bigger than a black hole of the same mass. (Were the thing smaller, its own gravity would create a black hole around it.) Observers might detect the orb's surface by spotting matter crashing onto it and heating up. Or they might deduce the greater size of the object as it swirls around a companion and tears into it before merging.

One hypothetical possibility is a gravastar: a thin material shell filled with dark energy, the mysterious space-stretching stuff that appears to be accelerating the expansion of the universe. A gravastar would have a solid surface rather than an event horizon, the point of no return that is the defining feature of a black hole. It satisfies the mathematical requirements of Albert Einstein's

theory of gravity, general relativity, says Carlos Palenzuela Luque, a gravitational theorist at the University of the Balearic Islands. However, nobody knows how a gravastar could ever form, he says.

Easier to produce might be a boson star, which would consist of exotic, massive Higgs bosons or nearly massless hypothetical particles called axions. Higgs bosons or axions could crowd into a single quantum wave, yielding a density approaching that of a black hole. However, Palenzuela Luque notes, boson stars would likely have masses in a narrow range, whereas a black hole can have any mass. Observed masses vary by factors of billions.

Black hole alternatives "is an area that's maybe undertheorized," says Sean Carroll, a theorist at the California Institute of Technology. But that would surely change if observations showed the current description of black holes isn't quite right. "When we have something to guide our search, we will be able to say something new," Palenzuela Luque says. "Right now, everything is so speculative." —A.C.

might not exist outside theorists' imaginations, says Sean Carroll, a theorist at Caltech. Skeptics argued that black holes might be an artifact of general relativity's subtle math, or that they might only form under unrealistic conditions, such as the collapse of a perfectly spherical star. However, in the late 1960s, Roger Penrose, a theorist at the University of Oxford, dispelled such doubts with rigorous math, for which he shared the 2020 Nobel Prize in Physics. "Penrose exactly proved that, no, no, even if you have a lumpy thing, as long as the density became high enough, it was going to collapse to a black hole," Carroll says.

Soon enough, astronomers began to see signs of actual black holes. They spotted tiny x-ray sources, such as Cygnus X-1, each in orbit around a star. Astrophysicists deduced that the x-rays came from gas flowing from the star and heating up as it fell onto the mysterious object. The temperature of the gas and the details of the orbit implied the x-ray source was too massive and too small to be anything but a black hole. Similar reasoning suggested quasars, distant galaxies spewing radiation, are powered by supermassive black holes in their centers.

But no one could be sure those black holes actually are what theorists had pictured, notes Feryal Özel, an astrophysicist at the University of Arizona (UA). For example, "Very little that we have done so far establishes the presence of an event horizon," she says. "That is an open question."

Now, with multiple ways to peer at black holes, scientists can start to test their understanding and look for surprises that could revolutionize physics. "Even though it's very unlikely, it would be so amazingly

important if we found that there was any deviation" from the predictions of general relativity, Carroll says. "It's a very high-risk, high-reward question."

**SCIENTISTS HOPE TO ANSWER** three specific questions: Do the observed black holes really have event horizons? Are they as featureless as the no-hair theorem says? And do they distort spacetime exactly as the Kerr metric predicts?

Perhaps the simplest tool for answering them is one that Ghez developed. Since 1995, she and colleagues have used the 10-meter Keck telescope in Hawaii to track stars around a radio source known as Sagittarius A\* (Sgr A\*) in the center of our Galaxy. In 1998, the stars' high speeds revealed they orbit an object 4 million times as massive as the Sun. Because Sgr A\* packs so much mass into such a small volume, general relativity predicts it must be a supermassive black hole. Reinhard Genzel, an astrophysicist at the Max Planck Institute for Extraterrestrial Physics, independently tracked the stars to reach the same conclusion and shared the Nobel Prize with Ghez.

Much of the information comes from a single star, dubbed SO2 by Ghez, which whips around Sgr A\* once every 16 years. Just as the orbit of Mercury around the Sun precesses, so, too, should the orbit of SO2. Ghez and colleagues are now trying to tease out that precession from the extremely complicated data. "We're right on the cusp," she says. "We have a signal, but we're still trying to convince ourselves that it's real." (In April 2020, Genzel and colleagues claimed to have seen the precession.)

If they get a little lucky, Ghez and com-

pany hope to look for other anomalies that would probe the nature of the supermassive black hole. Close to the black hole, its spin should modify the precession of a star's orbit in a way that's predictable from Kerr's mathematical description. "If there were stars even closer than the ones they've seen—maybe 10 times closer—then you could test whether the Kerr metric is exactly correct," Will says.

The star tracking will likely never probe very close to the event horizon of Sgr A\*, which could fit within the orbit of Mercury. But EHT, which combines data from 11 radio telescopes or arrays around the world to form, essentially, one big telescope, has offered a closer look at a different supermassive black hole, the 6.5-billion-solar-mass beast in M87.

The famous image the team released 2 years ago, which resembles a fiery circus hoop, is more complicated than it looks. The bright ring emanates from hot gas, but the dark center is not the black hole itself. Rather it is a "shadow" cast by the black hole as its gravity distorts or "lenses" the light from the gas in front of it. The edge of shadow marks not the event horizon, but rather a distance about 50% farther out where spacetime is distorted just enough so that passing light circles the black hole, neither escaping nor falling into the maw.

Even so, the image holds clues about the object at its center. The spectrum of the glowing ring could reveal, for example, whether the object has a physical surface rather than an event horizon. Matter crashing onto a surface would shine even brighter than stuff sliding into a black hole, Özel explains. (So far researchers have



seen no spectral distortion.) The shadow's shape can also test the classical picture of a black hole. A spinning black hole's event horizon should bulge at the equator. However, other effects in general relativity should counteract that effect on the shadow. "Because of a very funky cancellation of squishing in different directions, the shadow still looks circular," Özel says. "That's why the shape of the shadow becomes a direct test of the no-hair theorem."

Some researchers doubt EHT can image the black hole with enough precision for such tests. Samuel Gralla, a theorist at UA, questions whether EHT is even seeing a black hole shadow or merely viewing the disk of gas swirling around the black hole from the top down, in which case the dark spot is simply the eye of that astrophysical hurricane. But Özel says that even with limited resolution, EHT can contribute significantly to testing general relativity in the conceptual terra incognita around a black hole.

Gravitational waves, in contrast, convey information straight from the black holes themselves. Churned out when black holes spiral together at half the speed of light, these ripples in space-time pass unimpeded through ordinary matter. LIGO and Virgo have now detected mergers of black holes with masses ranging from three to 86 solar masses.

The mergers can probe the black holes in several ways, says Frank Ohme, a gravitational theorist and LIGO member at the Max Planck Institute for Gravitational Physics. Assuming the objects are classical black holes, researchers can calculate from general relativity how the chirp-like gravitational wave signal from a merger should speed up, climax in a spike, and then ring down. If the massive partners are actually larger material objects, then as they draw close they should distort each other, altering the peak of the signal. So far, researchers see no alterations, Ohme says.

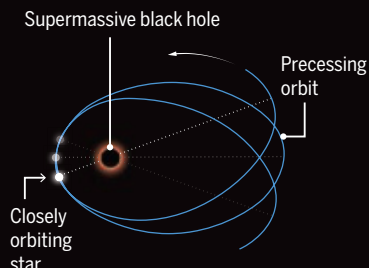
The merger produces a perturbed black hole just like the one in Teukolsky's old thesis, offering another test of general relativity. The final black hole undulates briefly but powerfully, at one main frequency and

## How to probe a black hole

Albert Einstein's theory of gravity, general relativity, predicts that the collapse of enough mass can leave a self-sustaining gravitational field so strong that, inside a distance called the event horizon, nothing can escape, not even light. But are black holes exactly the inscrutable things general relativity predicts? Observers may now have the tools to find out.

### 1. Trace the stars

Tracking the orbits of stars around the black hole in our Galaxy's center can reveal whether the black hole warps space and time exactly as general relativity predicts.



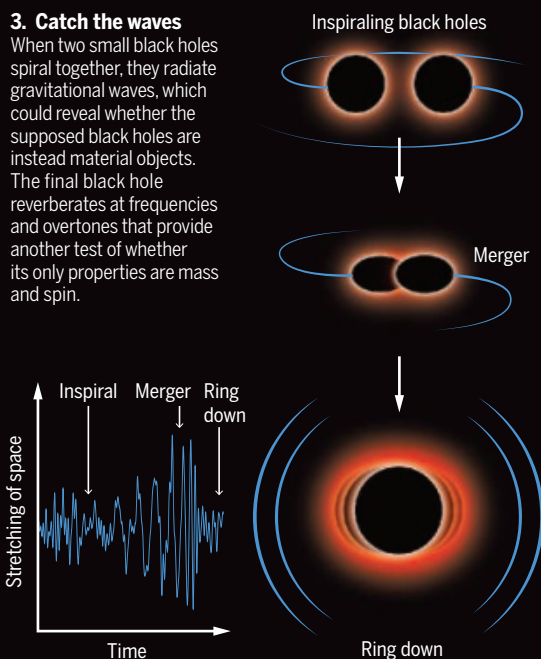
### 2. Take a picture

An image of a supermassive black hole holds clues to whether, as general relativity predicts, it has an event horizon rather than a surface, and mass and spin are its sole properties.



### 3. Catch the waves

When two small black holes spiral together, they radiate gravitational waves, which could reveal whether the supposed black holes are instead material objects. The final black hole reverberates at frequencies and overtones that provide another test of whether its only properties are mass and spin.



multiple shorter lived overtones. According to the no-hair theorem, those frequencies and lifetimes only depend on the final black hole's mass and spin. "If you analyze each mode individually, they all have to point to the same black hole mass and spin or something's wrong," Ohme says.

In September 2019, Teukolsky and col-

leagues teased out the main vibration and a single overtone from a particularly loud merger. If experimenters can improve the sensitivity of their detectors, Ohme says, they might be able to spot two or three overtones—enough to start to test the no-hair theorem.

**FUTURE INSTRUMENTS MAY** make such tests much easier. The 30-meter optical telescopes being built in Chile and Hawaii should scrutinize the neighborhood of Sgr A\* with a resolution roughly 80 times better than current instruments, Ghez says, possibly spying closer stars. Similarly, EHT researchers are adding more radio dishes to their network, which should enable them to image the black hole in M87 more precisely. They're also trying to image Sgr A\*.

Meanwhile, gravitational wave researchers are already planning the next generation of more sensitive detectors, including the Laser Interferometer Space Antenna (LISA), made up of three satellites flying in formation millions of kilometers apart. To be launched in the 2030s, LISA would be so sensitive that it could spot an ordinary stellar-mass black hole spiraling into a much bigger supermassive black hole in a distant galaxy, says Nicolas Yunes, a theoretical physicist at the University of Illinois, Urbana-Champaign.

The smaller black hole would serve as a precise probe of the spacetime around the bigger black hole, revealing whether it warps and twists exactly as the Kerr metric dictates. An affirmative result would cement the case that black holes are what general relativity predicts, Yunes says. "But you have to wait for LISA."

In the meantime, the sudden observability of black holes has changed the lives of gravitational physicists. Once the domain of thought experiments and elegant but abstract calculations like

Teukolsky's, general relativity and black holes are suddenly the hottest things in fundamental physics, with experts in general relativity feeding vital input to billion-dollar experiments. "I felt this transition very literally myself," Ohme says. "It was really a small niche community, and with the detection of gravitational waves that all changed." ■

# INSIGHTS



## PERSPECTIVES

### CORONAVIRUS

## SARS-CoV-2 spillover events

Spillover from mink to humans highlights SARS-CoV-2 transmission routes from animals

By **Peng Zhou<sup>1</sup>** and **Zheng-Li Shi<sup>1,2</sup>**

**S**evere acute respiratory syndrome (SARS), Middle East respiratory syndrome (MERS), and COVID-19 all broke out in recent decades and are caused by different strains of coronavirus (CoV). These viruses are considered to originate from bats and to have been transmitted to humans through inter-

mediate hosts. SARS-CoV was identified in palm civets in wildlife markets and MERS-CoV in dromedary camels (1), but the direct source of the COVID-19 causative agent, SARS-CoV-2, is still undetermined. On page 172 of this issue, Oude Munnink *et al.* (2) report an in-depth investigation of SARS-CoV-2 infections in animals and humans working or living in 16 mink farms in the Netherlands. SARS-CoV-2 infections were

detected in 66 out of 97 (68%) of the owners, workers, and their close contacts. Some people were infected with viral strains with an animal sequence signature, providing evidence of SARS-CoV-2 spillover back and forth between animals and humans within mink farms.

Besides mink, multiple species of wild or domestic animals may also carry SARS-CoV-2 or its related viruses. Experimental infections and binding-affinity assays between the SARS-CoV-2 spike (a surface protein that mediates cell entry) and its receptor, angiotensin-converting enzyme II (ACE2), demonstrate that SARS-CoV-2 has a wide host range (3). After the SARS-CoV-2 outbreak, several groups reported SARS-related CoVs in horseshoe bats in China and in pangolins smuggled from South

PHOTO: MADIS CLAUS RASMUSSEN/RITZAU SCANPIX/AFP VIA GETTY IMAGES



A mutated strain of severe acute respiratory syndrome coronavirus 2 (SARS-CoV-2) has been found in mink farms, such as this one in Naestved, Denmark, causing a mass cull in November 2020.

Asian countries, but according to genome sequence comparison, none are directly the progenitor virus of SARS-CoV-2 (4). Domestic cats and dogs, as well as tigers in zoos, have also been found to be naturally infected by SARS-CoV-2 from humans, but there is no evidence that they can infect humans, and so they are unlikely to be the source hosts of SARS-CoV-2 (4, 5).

To date, SARS-CoV-2 infections in mink farms have been reported in eight countries (the Netherlands, Denmark, Spain, France, Sweden, Italy, the United States, and Greece), according to the World Organisation for Animal Health (6). In addition to animal-to-human transmission in farms, cold food supplier chains are raising substantial concern. In various cities in China, several small-scale COVID-19 outbreaks caused by virus-contaminated uncooked seafood or pork from overseas countries have been documented. It was found that viral genome signatures in these outbreaks were different from the viral strains present in China (7, 8). There is evidence that SARS-CoV-2 can survive up to 3 weeks in meat and on the surface of cold food packages without losing infectivity (7, 8). Thus, meat from SARS-CoV-2-infected animals or food packaging contaminated by SARS-CoV-2 could be a source of human infection (see the figure).

This raises concerns about public health and agriculture in the prevention and control of SARS-CoV-2. Most SARS-CoV-2-infected animals do not display an obvious clinical syndrome, and infections would be unrecognized without routine diagnosis. The massive mink culling of infected farms is an efficient way to prevent further transmission of the virus. However, it cannot be applied to all domestic animals (if other species are found to be SARS-CoV-2 hosts). Thus, out of caution, extensive and strict quarantine measures should be implemented in all domestic farms with high-density animal populations. Because the virus is able to jump between some animals (such as mink) and humans, similar strategies should be

applied to people in key occupations involving animal-human interfaces, such as animal farmers, zookeepers, or people who work in slaughterhouses. Notably, there is limited evidence of animal-to-human transmission of SARS-CoV-2 except for mink. Research on whether other domestic animals carry SARS-CoV-2, whether they can transmit it to humans, and factors related to spillover should be conducted.

The RNA genome of SARS-CoV-2 seems relatively stable during transmission within human populations, although accumulated

more adaptive pressure in the early stage of the epidemic (palm civet to human) than in later stages (human to human) (10).

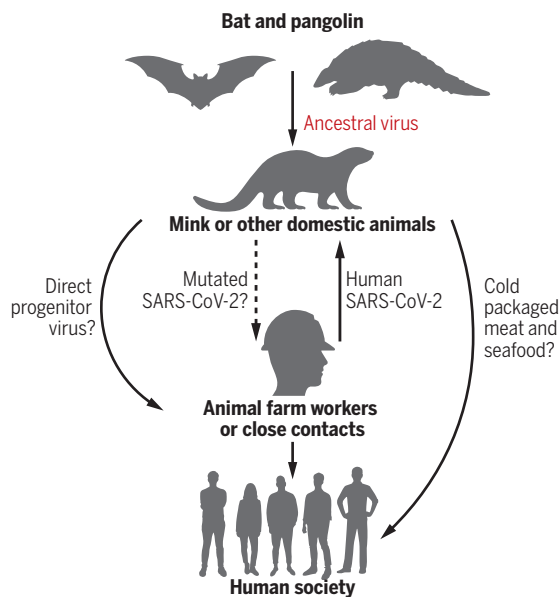
Mutations that occur in SARS-CoV-2 in animals may increase its pathogenesis or transmissibility in humans. Five clusters of SARS-CoV-2 strains were found in mink, each characterized by a specific mink-related variant. In Denmark, the cluster 5 strain of mink SARS-CoV-2 was less immunogenic to COVID-19 patient serum than was human SARS-CoV-2 because of mutations of the spike proteins in the mink strains (11). This cluster 5 strain has infected at least 12 people, and the clinical presentation, severity, and transmission among those infected are similar to those of other circulating human SARS-CoV-2 strains (12). Currently, there is no evidence that any mutation from mink strains of SARS-CoV-2 escapes neutralization by antibodies designed to target the prevalent human strains. However, considering the possible risk of spillover of SARS-CoV-2 between humans and some animals, it is imperative to closely monitor mutations in the viral genome from infected animals and humans, particularly the genome regions affecting diagnostic tests, antiviral drugs, and vaccine development.

It is anticipated that vaccines will allow control of COVID-19. Vaccines have been developed against the current prevalent viral strains and could face challenges if there is continued spillover from animals. The viral genome mutations likely produced during interspecies transmission between animals and humans raise concerns about whether the current vaccines can protect against emerging strains in the future. The extensive sequencing of viral genomes from animals and humans and worldwide data sharing will be central to efforts to monitor the key mutations that could affect vaccine efficacy. Laboratory-based studies should test whether the observed mutations affect key features of the virus, including pathogenesis, immunogenicity, and cross-neutralization. Moreover, preparedness of vaccines based on newly detected variants should be considered in advance. In the long term, vaccination of animals should also be considered to avoid economic losses in agriculture.

There has been debate about whether bats or pangolins, which carry coronaviruses with genomes that are ~90 to 96% similar to human SARS-CoV-2, were the animal source of the first human outbreak (4). Evolutionary analyses of viral genomes

## Possible SARS-CoV-2 transmission chains

Severe acute respiratory syndrome coronavirus 2 (SARS-CoV-2) spillover likely occurred from bat and/or pangolin (ancestral virus) through unidentified intermediate host animals (direct progenitor virus). Human SARS-CoV-2 strains infect susceptible domestic animals (such as mink) and likely adapt to these species through mutation. The virus can be transmitted from mink back to farm workers and close contacts. SARS-CoV-2 can also be transmitted to humans through contact with contaminated uncooked meat or food packaging.



mutations have been detected. It is generally accepted that coronaviruses tend to exhibit rapid evolution when jumping to a different species. To keep the replication error rate low, coronaviruses encode several RNA-processing and proofreading enzymes that are thought to increase the fidelity of viral replication. However, viruses tend to have reduced fidelity in favor of adaptation to a new host species (9), although the mechanisms underlying this phenomenon are unclear. The coronaviral spike protein is prone to have more mutations because it is the first virus-host interaction protein and thus faces the strongest selection pressure. This molecular evolution can be observed in SARS-CoV genomes, which were under

<sup>1</sup>CAS Key Laboratory of Special Pathogens, Wuhan Institute of Virology, Chinese Academy of Sciences, Wuhan 430071, China. <sup>2</sup>Shanghai Public Health Clinical Center, Fudan University, Shanghai, China. Email: zlsli@wh.iov.cn

from bats and pangolins indicate that further adaptations, either in animal hosts or in humans, occurred before the virus caused the COVID-19 pandemic (13). Therefore, an animal species that has a high population density to allow natural selection and a competent ACE2 protein for SARS-CoV-2—mink, for example—would be a possible host of the direct progenitor of SARS-CoV-2.

Another debate concerns the source of SARS-CoV-2 that caused the COVID-19 outbreak at the end of 2019. The current data question the animal origin of SARS-CoV-2 in the seafood market where the early cases were identified in Wuhan, China. Given the finding of SARS-CoV-2 on the surface of imported food packages, contact with contaminated uncooked food could be an important source of SARS-CoV-2 transmission (8). Recently, SARS-CoV-2 antibodies were found in human serum samples taken outside of China before the COVID-19 outbreak was detected (14, 15), which suggests that SARS-CoV-2 existed for some time before the first cases were described in Wuhan. Retrospective investigations of pre-outbreak samples from mink or other susceptible animals, as well as humans, should be conducted to identify the hosts of the direct progenitor virus and to determine when the virus spilled over into humans. ■

#### REFERENCES AND NOTES

1. J. Cui, F. Li, Z. L. Shi, *Nat. Rev. Microbiol.* **17**, 181 (2019).
2. B. B. Oude Munnink *et al.*, *Science* **371**, 172 (2020).
3. L. Wu *et al.*, *Cell Discov.* **6**, 68 (2020).
4. B. Hu, H. Guo, P. Zhou, Z. L. Shi, *Nat. Rev. Microbiol.* **10**, 1038/41579-020-00459-7 (2020).
5. D. McAloose *et al.*, *mBio* **11**, e02220-20 (2020).
6. World Organisation for Animal Health, COVID-19 Portal: Events in Animals (2020); [www.oie.int/en/scientific-expertise/specific-information-and-recommendations/questions-and-answers-on-2019-novel-coronavirus/events-in-animals/](http://www.oie.int/en/scientific-expertise/specific-information-and-recommendations/questions-and-answers-on-2019-novel-coronavirus/events-in-animals/).
7. P. Liu *et al.*, *Biosaf. Health* **10**, 1016/j.bshealth.2020.11.003 (2020).
8. J. Han, X. Zhang, S. He, P. Jia, *Environ. Chem. Lett.* **10**, 1007/s10311-020-01101-x (2020).
9. R. L. Graham, R. S. Baric, *J. Virol.* **84**, 3134 (2010).
10. Chinese SARS Molecular Epidemiology Consortium, *Science* **303**, 1666 (2004).
11. European Centre for Disease Prevention and Control, "Rapid Risk Assessment: Detection of New SARS-CoV-2 Variants Related to Mink" (2020); [www.ecdc.europa.eu/sites/default/files/documents/RRA-SARS-CoV-2-in-mink-12-nov-2020.pdf](http://www.ecdc.europa.eu/sites/default/files/documents/RRA-SARS-CoV-2-in-mink-12-nov-2020.pdf).
12. R. Lassauiniere *et al.*, "SARS-CoV-2 spike mutations arising in Danish mink and their spread to humans" (2020); [https://files.ssi.dk/Mink-cluster-5-short-report\\_AFO2](https://files.ssi.dk/Mink-cluster-5-short-report_AFO2).
13. K. G. Andersen, A. Rambaut, W. I. Lipkin, E. C. Holmes, R. F. Garry, *Nat. Med.* **26**, 450 (2020).
14. G. Apolone *et al.*, *Tumori J.* **10**, 1177/0300891620974755 (2020).
15. S. V. Basavaraju *et al.*, *Clin. Infect. Dis.* **ciab1785** (2020).

#### ACKNOWLEDGMENTS

Supported by China National Science Foundation for Excellent Scholars award 81822028 (P.Z.) and Strategic Priority Research Program of the Chinese Academy of Sciences awards XDB29010101 (Z.-L.S.) and XDB29010204 (P.Z.).

10.1126/science.abf6097

## NEUROSCIENCE

# How mice feel each other's pain or fear

Distinct neuronal pathways mediate empathy with different affective states

By Alexandra S. Klein<sup>1,2</sup> and Nadine Gogolla<sup>1</sup>

Empathic behaviors play crucial roles in human society by regulating social interactions, promoting cooperation toward a common goal, and providing the basis for moral decision-making (1, 2). Understanding the neural basis of empathy is crucial to understanding not only the human mind but also the neural mechanisms that give rise to social behaviors and the principles of our societies. Functional imaging studies in humans have identified essential brain regions that are engaged when people empathize with the affective experiences of others. However, human neuroimaging studies provide only limited spatial resolution and are solely correlative in nature. It has thus remained unclear how empathy with distinct affective experiences is set apart within the brain. On page 153 of this issue, Smith *et al.* (3) investigated the social transfer of pain, pain relief, or fear in mice to address how the sharing of diverse affective states is differentiated within the brain.

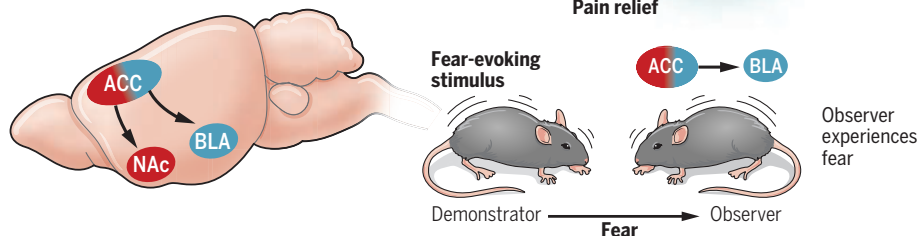
Although long thought of as an exclusively human ability, a basic requirement for

empathy is "the ability to share the affective state of others" (4, 5). It was proposed that empathy can be viewed as a multilevel process, in which the simplest form—namely, adopting another's affective state (emotion contagion)—lies at the core of all empathic behaviors. More complex levels of empathy, including prosocial behaviors and learning from the state of the other, evolved later and build on this core of affect sharing (4, 5). According to this definition, there is ample evidence that many animal species exhibit primitive forms of empathy, suggesting that the building blocks of human empathy are deeply rooted in evolution.

To date, numerous studies have demonstrated that rodents also express empathic behaviors, including emotion contagion, but also observational affective learning, or prosocial behaviors such as consolation or helping behaviors (6–8). Furthermore, homologous brain regions have consistently been described to underlie empathy in humans and animals. One of the most consistently found brain regions in humans and rodents, the anterior cingulate cortex (ACC), has been shown to be involved when

## Empathy circuits in mice

Smith *et al.* induced three different affective states in demonstrator mice and investigated the neuronal pathways required in the observer mice to share the diverse affective states of the other. Although the pathway from the anterior cingulate cortex (ACC) to the nucleus accumbens (NAc) was essential for the transfer of both pain and pain relief, a neuronal pathway from the ACC to the basolateral amygdala (BLA) mediated the social transfer of fear.





empathizing with different sensory and affective states, including pain, disgust, or fear (9–14). However, whether the ACC contributes to discrimination of the transfer of different affective states that elicit distinct empathic behaviors is an important unanswered issue.

Smith *et al.* demonstrate that the social transfer of pain or fear are mediated by two separate projections from the ACC to distinct subcortical targets in mice (see the figure). Social transfer of pain refers to the phenomenon that a brief exposure to a conspecific (an animal of the same species) who is experiencing pain will lead to a transfer of the same emotion state to the observer. As a result, the observer, who has not experienced any pain itself, is more sensitive to painful stimuli and experiences pain more easily, a phenomenon called hyperalgesia. Similarly, observing a conspecific being in fear will transfer and induce fear reactions in the observer. Using these primitive forms of empathy-like behaviors in mice, Smith *et al.* demonstrate that social transfer of pain relied on a neural pathway from the ACC to the nucleus accumbens (NAc) in the observer mouse. However, this pathway was not required for the social transfer of fear, which involved a separate pathway from the ACC to the basolateral amygdala (BLA). Notably, the authors also found that a positive affective state, the relief from pain, could be socially transmitted. Observer mice who were in pain themselves exhibited lessened pain responses when they had a chance to observe other mice that had undergone pain-relief treatment with morphine. A deeper understanding of how and why analgesia can be transmitted socially may well have important future implications for pain management in humans.

The authors report that the same neuronal pathway from the ACC to the NAc is involved in both the socially mediated positive and negative modulation of subjective pain. How does this single neuronal pathway drive socially transferred analgesia and hyperalgesia at the same time? Perhaps different cell types are targeted in the NAc, which affect distinct downstream brain regions. Understanding this will be an important matter for future studies. Disentangling the circuits for social transmission more generally for positive versus negative affective states may improve our understanding of social and emotion disorders in humans.

The findings of Smith *et al.* also raise the question of whether the ACC-to-BLA fear

projection might be involved not only in the social transfer of fear but also in the “relief from fear.” It has already been shown that mice are able to reduce their fear behavior in the presence of a nonfearful partner (6, 15). However, the neuronal basis of this social buffering of fear remains elusive. The ACC-to-BLA projection may be a promising candidate for this phenomenon.

One of the most accepted theories for the neuronal mechanisms of empathy is the “perception-action model” (PAM) (4, 5). According to this view, attending to another’s affective state is assumed to activate the observer’s own neuronal representation and associated feelings of the same state. Smith *et al.* could show that a socially shared emotion causes a generalized pain state in the observer. Both hyperalgesia and analgesia modulated different forms of pain sensitivity and affected the entire body of the observer mouse, suggesting that the observer mouse may truly experience a generalized change of internal state. Indeed, studies in monkeys and rodents have demonstrated the existence of “mirror neurons” in the ACC. These are single nerve cells that are activated both when an individual observes a sensory experience or motor action, or experiences or performs the same condition itself. Pain-sensitive mirror neurons have recently been reported in the ACC of rats (12). It will be important to investigate whether it is the activity in mirror neurons or other neuronal mechanisms that account for the social modulation of pain. ■

#### REFERENCES AND NOTES

1. J. Decety, J. M. Cowell, *AJOB Neurosci.* **6**, 3 (2015).
2. C. Chen, R. M. Martínez, Y. Cheng, *Front. Psychol.* **9**, 2584 (2018).
3. M. L. Smith, N. Asada, R. C. Malenka, *Science* **371**, 153 (2021).
4. F. B. M. de Waal, S. D. Preston, *Nat. Rev. Neurosci.* **18**, 498 (2017).
5. F. B. M. de Waal, *Annu. Rev. Psychol.* **59**, 279 (2008).
6. K. Z. Meyza *et al.*, *Neurosci. Biobehav. Rev.* **76** (part B), 216 (2017).
7. I. Ben-Ami Bartal, J. Decety, P. Mason, *Science* **334**, 1427 (2011).
8. J. P. Burkett *et al.*, *Science* **351**, 375 (2016).
9. B. Wicker *et al.*, *Neuron* **40**, 655 (2003).
10. C. Corradi-Dell’Acqua, A. Tüsche, P. Vuilleumier, T. Singer, *Nat. Commun.* **7**, 10904 (2016).
11. B. C. Bernhard, T. Singer, *Annu. Rev. Neurosci.* **35**, 1 (2012).
12. M. Carrillo *et al.*, *Curr. Biol.* **29**, 1301 (2019).
13. S. A. Allsop *et al.*, *Cell* **173**, 1329 (2018).
14. A. Kim, S. Keum, H. S. Shin, *Genes Brain Behav.* **18**, e12521 (2019).
15. Y. F. Guzmán *et al.*, *Behav. Brain Res.* **201**, 173 (2009).

#### ACKNOWLEDGMENTS

We thank the Gogolla laboratory for their support and enthusiasm, the Max Planck Society, the European Research Council (ERC) under the European Union’s Horizon 2020 research and innovation program (ERC-2017-STG grant 758448 to N.G.), and the L’Agence Nationale de la Recherche–Deutsche Forschungsgemeinschaft (ANR-DFG) project “SAFENET” (ANR-17 CE37-0021) for financial support.

<sup>1</sup>Circuits for Emotion Research Group, Max Planck Institute of Neurobiology, Martinsried, Germany. <sup>2</sup>International Max Planck Research School for Molecular Life Sciences, Munich, Germany. Email: ngogolla@neuro.mpg.de

#### CHEMICAL PHYSICS

## Between a hydrogen and a covalent bond

The bonds in aqueous FHF<sup>−</sup> are neither simple hydrogen nor covalent bonds

By Mischa Bonn and Johannes Hunger

The concept of a molecule as a unit of bound atoms can be traced to Robert Boyle’s 1661 treatise “The Sceptical Chymist” (1). Chemists often depict the strong covalent bonds in molecules formed through electronic interactions of atoms by sticks or springs. By contrast, much weaker attractive forces between molecules in liquids and solids, such as van der Waals forces, are typically unspecific and nondirectional and cannot be represented by sticks or springs. An exception is the hydrogen bond (H-bond) (2), which can create relatively strong directional interactions between molecules when the atoms that carry opposite partial charges attract each other. Discrimination between very strong H-bonds and covalent bonds can become somewhat arbitrary. On page 160 of this issue, Dereka *et al.* (3) study what happens if the strength of an intramolecular hydrogen bond becomes comparable to the strength of the intermolecular covalent bonds, blurring the concept of what a “molecule” is.

This study touches on the foundations of chemistry, in that our understanding of chemical bonding as sticks or springs is not without contention. Indeed, it is not evident how to precisely define such “chemical bonds” (4), and as recently as 2013, an international conference was called to explore new ways to define, describe, and make sense of chemical bonding (5). Such efforts are not purely academic exercises. During chemical conversion, covalent bonds often have to convert to weaker H-bonds (6), and proton transport in water relies on the continuous interconversion of covalent and H-bonds.

Dereka *et al.* captured the intermediate case in a liquid for a negatively charged fluoride-hydrogen-fluoride (FHF<sup>−</sup>) com-

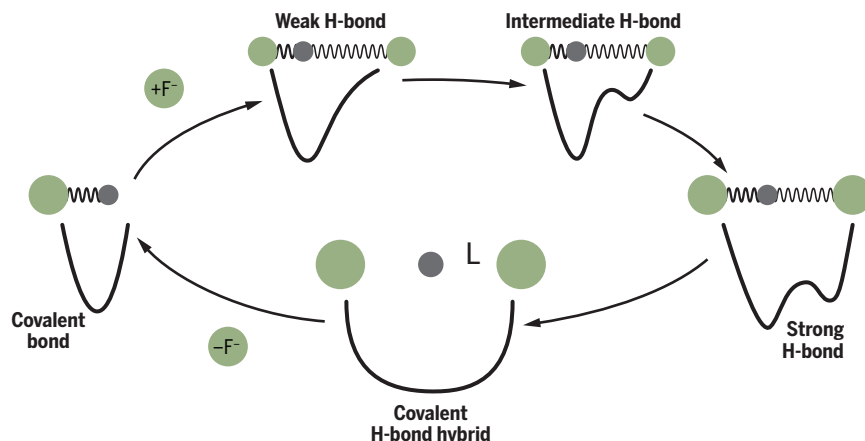
Max Planck Institute for Polymer Research, Ackermannweg 10, 55128 Mainz, Germany. Email: bonn@mpip-mainz.mpg.de

## When bonding gets blurry

Covalent bonds to hydrogen atoms in molecules can weaken in the presence of hydrogen bond acceptors. The study by Dereka *et al.* of  $\text{FHF}^-$  can provide insight into such bonds in other contexts, such as the Zundel cation of water.

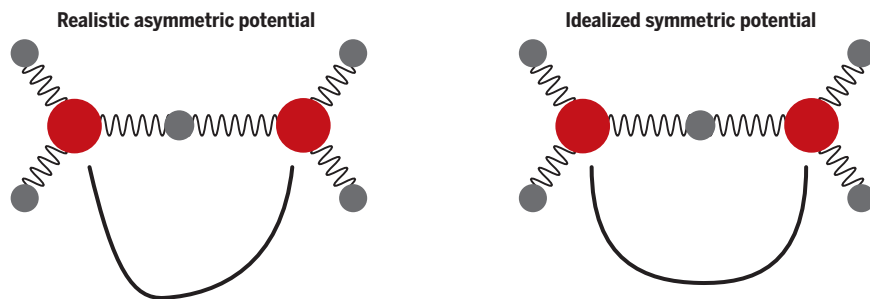
### From covalent to hydrogen bonds and back

The bottom left potential shows a conventional, covalent chemical bond of HF. In solution, the interaction of the proton with a  $\text{F}^-$  anion creates structures with increasingly strong hydrogen bonds (H-bonds) (moving clockwise), weakening the covalent bond. For the bottom symmetrical potential, the distinction between hydrogen and covalent bonds vanishes.



### An almost ideal case

The Zundel ion, a proton sandwiched between two water molecules, is an example of a hybrid between covalent and hydrogen bonding but is extremely short-lived in liquid water. The  $\text{F-H-F}^-$  anion provides a long-lived proxy to study this structure.



plex in water, where the hydrogen atom is precisely equally shared between two fluorine atoms. This state is stable, despite water molecules frequently colliding with the complex. These types of bonds can be characterized by different potential energy surfaces upon displacing the hydrogen's nucleus out of its equilibrium position (see the figure, top) (7).

The potential for the proton of a covalent bond  $\text{F-H}$  is relatively harmonic and symmetric with respect to the potential minimum position. When H-bonds are formed upon interaction with a fluoride anion, the hydrogen atom interacts weakly with the H-bond acceptor, which slightly weakens the strong covalent bond with the partner fluorine within its molecule and induces asymmetry. For increasingly strong H-bonds, the covalent bond further weakens, and the hydrogen becomes increasingly

delocalized between its covalent partner atom and the H-bond accepting group.

Using advanced spectroscopic tools to study the H-atom moving in this potential, that is, the molecular vibrations, Dereka *et al.* showed that the  $\text{FHF}^-$  anion exists as a symmetric molecular entity in water for a sufficient time to study it. The distance between the  $\text{F}^-$  anions in solution is so short that the proton resides in a fully symmetric potential with no barrier for the transfer between the two  $\text{F}^-$  ions. Thus, the proton is precisely centered and equally shared between the two  $\text{F}^-$  anions. An extensive computational study revealed that the bonds are neither simply covalent nor a simple H-bond. The authors captured the very transition between covalent and H-bonding and could show that the pure interaction of the partial charge of the atoms is insufficient to quantitatively describe bonding.

The existence of a hybrid covalent-hydrogen bonded state not only challenges our current understanding of what a chemical bond exactly is but also offers the opportunity to better understand chemical reactions, where “intermediate reaction states” are often invoked but rarely studied directly. The obtained charge distribution upon bonding could, for example, be directly used to improve our current models to describe bond breaking and formation classically, notably in reactive force fields (8). The findings also have direct implications for proton transfer reactions in catalysis or proton transfer in water (9). The  $\text{FHF}^-$  anion can be viewed as a proxy of the idealized, positively charged Zundel cation (10–12) in water, where two water molecules share one excess proton ( $\text{H}^+$ ) (see the figure, bottom). Unlike the Zundel cation, the molecular simplicity of  $\text{FHF}^-$  allows for an unambiguous correlation of the bonding properties and spectroscopic signatures.

The study of Dereka *et al.* holds substantial promise for obtaining a deeper understanding of strong bonding with its unprecedented snapshot of such a bonding intermediate. Future work will undoubtedly focus on the dynamics of the interconversion in different systems (13). Many exciting questions remain open, including what role the environment (for example, the fluctuating solvent) plays in such interconversion, what molecular motions trigger these interconversions, and how these systems can be steered in a desired direction. Forthcoming answers to these questions should be relevant for proton transport in biology and technologies such as fuel-cell membranes. ■

### REFERENCES AND NOTES

1. R. Boyle, *The Sceptical Chymist* (Dover, London, 1661).
2. P. A. Kollman, L. C. Allen, *Chem. Rev.* **72**, 283 (1972).
3. B. Dereka *et al.*, *Science* **371**, 160 (2021).
4. P. Ball, *Nature* **469**, 26 (2011).
5. J. M. Ugalde, P. Bultinck, F. M. Bickelhaupt, A. N. Alexandrova, *J. Phys. Chem. A* **120**, 9353 (2016).
6. R. Srinivasan, J. S. Feenstra, S. T. Park, S. Xu, A. H. Zewail, *J. Am. Chem. Soc.* **126**, 2266 (2004).
7. G. S. Denisov, J. Mavri, L. Sobczyk, in *Hydrogen Bonding—New Insights* (Springer Netherlands, 2006), pp. 377–416.
8. C. Chen, C. Arnsten, G. A. Voth, *J. Chem. Phys.* **147**, 161719 (2017).
9. D. Marx, M. E. Tuckerman, J. Hutter, M. Parrinello, *Nature* **397**, 601 (1999).
10. M. Thämer, L. De Marco, K. Ramasesha, A. Mandal, A. Tokmakoff, *Science* **350**, 78 (2015).
11. F. Dahms, B. P. Fingerhut, E. T. J. Nibbering, E. Pines, T. Elsaesser, *Science* **357**, 491 (2017).
12. J. A. Fournier, W. B. Carpenter, N. H. C. Lewis, A. Tokmakoff, *Nat. Chem.* **10**, 932 (2018).
13. F. Dahms *et al.*, *Angew. Chem.* **128**, 10758 (2016).

### ACKNOWLEDGMENTS

We are grateful for support from the MaxWater Initiative of the Max Planck Society.

10.1126/science.abf3543



# Multikingdom diffusion barrier control

Plant microbiomes modulate selective nutrient uptake by regulating diffusion barriers

By Wolfgang Busch<sup>1</sup> and Joanne Chory<sup>1,2</sup>

**D**espite their differences in evolutionary history, both plants and animals have evolved specialized barrier systems to control their interaction with the external world. Such barriers are crucial for selective nutrient uptake. In the animal gut, epithelial cells that are firmly connected by tight junctions play a key role. In plants, nutrient uptake occurs in the root, where a cell layer called the endodermis plays a similar role to the gut epithelium. The diffusion barriers around the endodermis separate the inside of the plant from the outside and allow the endodermal cells to determine which nutrients are taken up. As in the animal gut, the root microbiome is influential for nutrient uptake. On page 143 of this issue, Salas-González *et al.* (1) reveal an interplay of the developing endodermis and microbes that is tightly related to a plant's ability to take up nutrients efficiently.

Land plants acquire their nutrients and water from the soil through their root system. To allow for selective nutrient uptake, barriers have evolved that inhibit passive diffusion through the cell walls. The key diffusion barriers for nutrient uptake are formed around the endodermis and consist of impregnating layers of hydrophobic polymers. One of these layers, the Casparian strip, is made of lignin, which is a cross-linked polymer deposited in the cell walls of the endodermis. It gives rise to a ring that encompasses the endodermal cell layer and seals the cell wall space (2). The other diffusion barrier is the lipophilic polyester polymer suberin, which is deposited at the inner surface of the cell walls and effectively covers the entire surface of the endodermal cells (3). Together, these layers seal the outside of the root from the inside, thereby forcing any nutrient to pass by cellular uptake and subjecting them to homeostatic mechanisms, thus enabling the plant to have control over the nutrients it takes up. Thus, the endoder-

mis has a function similar to that of the gut epithelium in animals, but the barrier function is conferred by lignin and suberin layers as opposed to tight junctions in the gut epithelia.

The diffusion barriers at the endodermis can be modulated by nutrient concentrations (4). For instance, there is increased deposition of suberin in response to high-salt conditions. Conversely, nutrient-deficient conditions for several minerals, such as iron or zinc, lead to reduced suberin deposition. This is reminiscent of nutrient-dependent modulation of the permeability of endothelial barrier function in the animal gut. For instance, glutamine increases intestinal barrier function, (5) whereas dietary fats can decrease barrier function (6).

Now, the discovery of Salas-González *et*

advantages. *Arabidopsis* is a self-fertilizing species, thereby giving rise to multiple isogenic progeny that can be used to systematically study the causes and mechanisms of the interplay of host genotypes, nutrition, and microbial effects on diffusion barriers and their consequences on organismal health. Moreover, a large array of mutants is available, including mutants that are defective in the formation of the diffusion barriers or that are involved in plant-microbe interactions or nutrient sensing and homeostasis. Use of such mutants could reveal whether specific microbe-derived molecules or metabolites, or combinations of molecular signals and nutrient concentrations, trigger the impact on barrier formation.

The work by Salas-González *et al.* has revealed an important facet of the complex interplay of selective nutrient uptake, nutrients, and microbes. In addition to the fundamental principles that such studies in this area can provide, there are agricultural

prospects, too. Plant nutrition is highly relevant to our need to feed a growing global population by developing crops with high nutritional value. The latter is a particular challenge, because nutrient deficiencies still affect a notable fraction of the global human population (e.g., iron deficiency) and carbon fertilization by the increasing carbon dioxide concentrations in the atmosphere is projected to lead to a reduction of key nutrients in food crops (8). Tailoring root microbiomes to fine-tune nutrient uptake for maximizing yield and plant nutritional quality might provide an opportunity to address these issues in a way that is faster to roll out and that might require less effort than engineering crop genetics. ■

**“...the dynamic relations of barriers in plant and animal systems seem to share a number of fundamental properties.”**

*al.* adds another layer of regulation of the diffusion barriers in plant roots and illuminates the pathways underpinning this regulation. They show that particular bacterial strains within the root microbiome have the capacity to change the composition and function of the endodermal diffusion barriers through the repression of the abscisic acid hormone signaling pathway, which is a main player in the response of plants to environmental stresses. This modulation can improve plant health in stressful conditions. Again, this finding is reminiscent of mechanisms in animal guts, even though the molecular mechanisms underpinning it are mostly unknown. In animal guts, microbes have been shown to regulate the barrier function of the epithelium, which is accompanied by stress-protective effects (7). Therefore, the dynamic relations of barriers in plant and animal systems seem to share a number of fundamental properties.

Studying host-nutrient-microbiome interactions using experimental perturbations requires a large number of experiments, because the matrix of experimental conditions grows large very quickly. The *Arabidopsis* system used by Salas-González *et al.* offers a number of specific

## REFERENCES AND NOTES

1. I. Salas-González *et al.*, *Science* **371**, eabd0695 (2021).
2. S. Naseer *et al.*, *Proc. Natl. Acad. Sci. U.S.A.* **109**, 10101 (2012).
3. J. Zeier, A. Goll, M. Yokoyama, I. Karahara, L. Schreiber, *Plant Cell Environ.* **22**, 271 (1999).
4. M. Barberon *et al.*, *Cell* **164**, 447 (2016).
5. B. Wang *et al.*, *Amino Acids* **47**, 2143 (2015).
6. M. W. Rohr, C. A. Narasimulu, T. A. Rudeski-Rohr, S. Parthasarathy, *Adv. Nutr.* **11**, 77 (2020).
7. P. A. Bron, P. van Baarlen, M. Kleerebezem, *Nat. Rev. Microbiol.* **10**, 66 (2011).
8. R. H. Beach *et al.*, *Lancet Planet. Health* **3**, e307 (2019).

<sup>1</sup>Plant Biology Laboratory, Salk Institute for Biological Studies, 10010 North Torrey Pines Road, La Jolla, CA 92037, USA. <sup>2</sup>Howard Hughes Medical Institute, Salk Institute for Biological Studies, 10010 North Torrey Pines Road, La Jolla, CA 92037, USA. Email: wbusch@salk.edu; chory@salk.edu

## VIEWPOINT: COVID-19

# COVID-19 testing: One size does not fit all

To control the pandemic, testing should be considered a public health tool

By **Michael J. Mina**<sup>1,2,3,4</sup> and  
**Kristian G. Andersen**<sup>5,6</sup>

**T**ests for detecting severe acute respiratory syndrome coronavirus 2 (SARS-CoV-2) were developed within days of the release of the virus genome (1). Multiple countries have been successful at controlling SARS-CoV-2 transmission by investing in large-scale testing capacity (2). Most testing has focused on quantitative polymerase chain reaction (qPCR) assays, which are capable of detecting minute amounts of viral RNA. Although powerful, these molecular tools cannot be scaled to meet demands for more extensive public health testing. To combat COVID-19, the “one-size-fits-all” approach that has dominated and confused decision-making with regard to testing and the evaluation of tests is unsuitable: Diagnostics, screening, and surveillance serve different purposes, demand distinct strategies, and require separate approval mechanisms. By supporting the innovation, approval, manufacturing, and distribution of simpler and cheaper screening and surveillance tools, it will be possible to more effectively limit the spread of COVID-19 and respond to future pandemics.

Many types of tests are available for COVID-19 for clinical and public health use (see the figure). Testing can be performed in a central laboratory, at the point of care (POC), or in the community at the workplace, school, or home. COVID-19 testing begins with specimen collection. For medical use, a nasopharyngeal swab collected by a health care professional has been used for detection of virus infections. Demands on testing throughput for COVID-19, however, have driven new collection approaches, including saliva and less invasive nasal swabs. COVID-19 tests include molecular tests such as qPCR, isothermal amplification, and CRISPR, as well as antigen tests that detect SARS-CoV-2 proteins directly. Although rapid

antigen tests have lower analytical sensitivity (i.e., require greater amounts of virus material to turn positive) than qPCR-based tests, their ability to detect infectious individuals with culturable virus is as high as for qPCR (3). Specificity (i.e., correctly identifying those not infected with SARS-CoV-2) of antigen tests achieves comparable results to molecular tests (4).

Diagnostic testing for COVID-19 focuses on accurately identifying patients who are infected with SARS-CoV-2 to establish the presence or absence of disease and is performed on symptomatic patients or asymptomatic individuals who are at high risk of infection. This type of testing requires assays that are highly sensitive, so as to not miss COVID-19 patients (false negatives), and specific, so as to not wrongly diagnose SARS-CoV-2-negative individuals as having COVID-19 (false positives). These tests are typically performed by centralized high-complexity laboratories with specialized equipment using qPCR assays, with results that can be reported within 12 to 48 hours. Major bottlenecks in testing, however, have led to turnaround times exceeding 5 to 10 days in some regions, making such tests useless to prevent transmission.

POC diagnostic testing at medical facilities can be qPCR assays, isothermal amplification, or antigen-based (4). These POC tests often require instruments that run a limited number of tests and can return results in under an hour. The need for an instrument limits the number of tests that can be performed and where they can be used. However, newer antigen tests are becoming available that do not require instruments or skilled operators, potentially allowing for much more distributed POC testing.

Surveillance testing of populations can be used both as a tool for understanding historical exposures and as a measure of ongoing community transmission. For the former, serological testing of individuals for the presence of SARS-CoV-2-specific antibodies is used to identify those previously infected. For the latter, surveillance testing can be an effective way to monitor real-time SARS-CoV-2 spread in communities. One promising method is wastewater surveillance, which has been used to assess community transmission of poliovirus (5) and has shown potential for COVID-19 (6). qPCR testing of wastewater is used to detect SARS-CoV-2, and frequency dynamics of viral genetic ma-

terial indicate COVID-19 infections in a community. Surveillance can also be performed from swab or saliva samples taken directly from individuals, and, in populations with low COVID-19 prevalence, pooling can be used to increase capacity and lower cost.

For surveillance testing, the goal is not identification of every case but rather the collection of data from representative samples that accurately measure prevalence and serve to inform public health policy and resource allocation. Because the focus is on extrapolations to the population and not the individual, tests with known deviations from 100% sensitivity and specificity are still appropriate when the variance can be statistically corrected (7). To be most effective, results should include reported qPCR cycle thresholds, which is an estimate of viral load (7), to model epidemic trajectory and allow for real-time evaluation of mitigation programs (8), including once vaccination programs have begun.

Screening testing of asymptomatic individuals to detect people who are likely infectious has been critically underused yet is one of the most promising tools to combat the COVID-19 pandemic (9). Infection with SARS-CoV-2 does not lead to symptoms in ~20 to 40% of cases, and symptomatic disease is preceded by a presymptomatic incubation period (10). However, asymptomatic and presymptomatic cases are key contributors to virus spread, complicating our ability to break transmission chains (10).

Entry screening to detect infectious individuals before accessing facilities (e.g., nursing homes, restaurants, and airports), along with symptom screening and temperature checks, can be beneficial, particularly in high-risk facilities such as skilled nursing facilities. When used strategically, entry-screening measures can be effective at suppressing transmission. Entry screening requires testing that provides rapid results—ideally within 15 min—to be most effective. The required sensitivity and specificity of entry-screening tests are, like all tests, context dependent. Entry-screening tests for a nursing home, for example, must be highly sensitive because the consequences of bringing SARS-CoV-2 into a nursing home can be devastating. Such tests must also be highly specific because the consequences of grouping a false-positive person with COVID-19-positive individuals could be deadly. Conversely,

<sup>1</sup>Center for Communicable Disease Dynamics, Departments of Epidemiology and Immunology and Infectious Diseases, Harvard T.H. Chan School of Public Health, Boston, MA, USA.

<sup>2</sup>Department of Pathology, Clinical Microbiology, Brigham and Women's Hospital, Harvard Medical School, Boston, MA, USA. <sup>3</sup>Ragon Institute of MGH, MIT, and Harvard, Cambridge, MA, USA. <sup>4</sup>Broad Institute of MIT and Harvard, Cambridge, MA, USA. <sup>5</sup>Department of Immunology and Microbiology, The Scripps Research Institute, La Jolla, CA, USA. <sup>6</sup>Scripps Research Translational Institute, La Jolla, CA, USA.

Email: mmina@hsph.harvard.edu; andersen@scripps.edu



because children have substantially reduced mortality from COVID-19, entry screening into schools might require greater compromise that balances resources and sensitivity to test as many individuals as possible with a need to minimize disruptive false positives. Key to use of tests for entrance screening is that a negative test alone should not be considered sufficient to enter—that should be based on satisfying other requirements, including masks and physical distancing. Conversely, a positive test should be sufficient to bar entry in most settings.

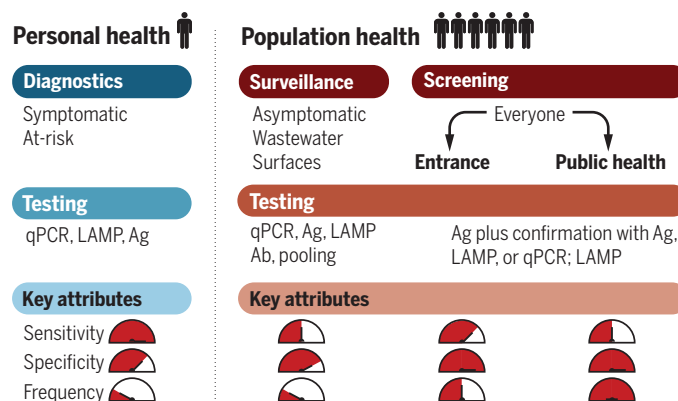
Public health screening is potentially the most powerful form of COVID-19 testing, aimed at outbreak suppression through maximizing detection of infectious individuals. This type of screening entails frequent serial testing of large fractions of the population, through self-administered at-home rapid tests, or in the community at high-contact settings, such as schools and workplaces (9). Public health screening can achieve herd effects by stopping onward spread through detection of asymptomatic or pre-symptomatic cases (fig. S1).

Notably, not every transmission chain needs to be severed to achieve herd effects. Mathematical models that incorporate relevant variation in viral loads and test accuracy suggest that with frequent testing of a large fraction of a population, a sufficient number of cases could be detected to create herd effects (11). For example, Slovakia undertook public health screening to address COVID-19 (12): During a 2-week period, ~80% of the population was screened using rapid antigen tests. With 50,000 cases identified, combined with other public health measures, it reduced incidence by 82% within 2 weeks (12). An important feature of large-scale public health screening is that centrally controlled reporting and contact tracing programs are not essential to induce herd effects as they are for surveillance testing. In a robust public health screening program, sufficient numbers of people are routinely testing themselves, such that contact tracing is subsumed by the screening program (11).

Similar to home pregnancy tests, screening tests should be easy to obtain and administer, fast, and cheap. Like diagnostic tests, these tests must produce very low false-positive rates. If a screening test does not achieve high-enough specificity (e.g., >99.9%), screening programs can be paired with secondary confirmatory testing. Unlike diagnostic tests,

## COVID-19 testing strategies

Testing for SARS-CoV-2 can be for personal or population health. Collection can be from symptomatic or asymptomatic individuals, as well as from wastewater and swabs of surfaces. The tests may be performed in central laboratories, at the POC, or using rapid tests. Attributes of tests differ according to application.



Ab, antibody; Ag, antigen; LAMP, loop-mediated isothermal amplification; POC, point of care; qPCR, quantitative polymerase chain reaction; SARS-CoV-2, severe acute respiratory syndrome coronavirus 2.

however, the sensitivity of screening tests should not be determined based on their ability to diagnose patients but rather by their ability to accurately identify people who are most at risk of transmitting SARS-CoV-2. Such individuals tend to have higher viral loads (13), which makes the virus easier to detect (14). A focus on identifying infectious people means that frequency and abundance of tests should be prioritized above achieving high analytical sensitivity (11). Indeed, loss in sensitivity of individual tests, within reason, can be compensated for by frequency of testing and wider dissemination of tests (9). In addition, public health messaging should ensure appropriate expectations of screening, particularly around sensitivity and specificity so that false negatives and false positives do not erode public trust.

Tests for public health screening require rapid, decentralized solutions that can be scaled for frequent screening of large numbers of asymptomatic individuals. Lateral-flow antigen tests and upcoming paper-based synthetic biology and CRISPR-based assays fit these needs and could be scaled to tens of millions of daily tests (9). These tests are simple and cheap, can be self-administered, and do not require machines to run and return results. The Abbott BinaxNOW rapid antigen test, which recently received an Emergency Use Authorization (EUA) in the United States as a diagnostic device, also comes with a smartphone app, allowing self-reporting of COVID-19 status that could be used instead of centralized reporting by public health agencies. Critically, despite being shown to be highly effective at detecting infectious individuals (14), very few of these tests are currently approved for screening of asymp-

tomatic individuals, substantially limiting their utility. If such tests were made available direct to consumer (priced to allow equitable access) or produced and provided free of charge by governments, individuals could obtain their COVID-19 status at their own choosing and without complex medical decisions.

Testing is a central pillar of clinical and public health response to global health emergencies, including the COVID-19 pandemic. Nearly all testing modalities have a role, and the one-size-fits-all approach to testing by many Western countries has failed. Many lower- and middle-income countries—including Senegal, Vietnam, and Ghana—have fared far better in their COVID-19 response, often using strong testing programs.

The focus on diagnostic tests and the use of preexisting authorization pathways focused on qPCR-based clinical diagnostics not only slows the development and deployment of new surveillance and screening tests but also confuses the picture of what metrics effective public health tools should achieve. Testing to diagnose a patient with COVID-19 is fundamentally different from testing a person to prevent onward transmission. Regulatory pathways should be modified to incorporate these differences so that public health and screening tests are appropriately evaluated. It is necessary to be innovative and produce, distribute, and continuously improve the tests that exist to save lives and gain control of the COVID-19 pandemic.

## REFERENCES AND NOTES

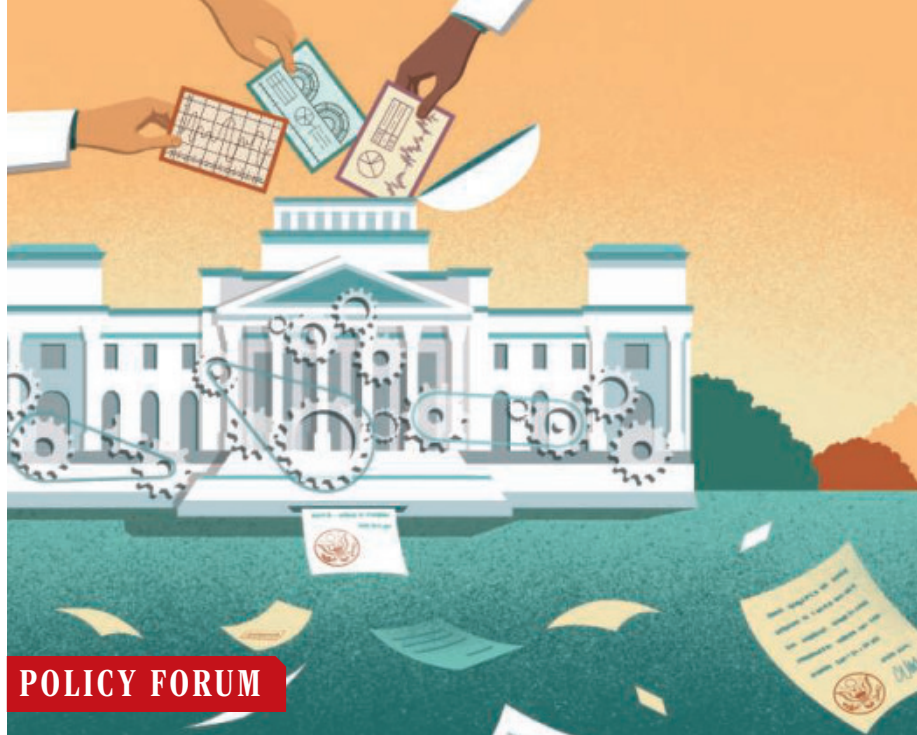
1. V. M. Corman et al., *Euro. Surveill.* **25**, 2000045 (2020).
2. M. G. Baker et al., *N. Engl. J. Med.* **383**, e56 (2020).
3. A. Pekosz et al., *medRxiv* 10.1101/2020.10.02.20205708 (2020).
4. R. Weissleder et al., *Sci. Transl. Med.* **12**, abc1931 (2020).
5. H. Asghar et al., *J. Infect. Dis.* **210**, S294 (2014).
6. A. Nemudryi et al., *Cell Rep. Med.* **1**, 100098 (2020).
7. R. Kahn et al., *medRxiv* 10.1101/2020.05.02.20088765 (2020).
8. J. A. Hay et al., *medRxiv* 10.1101/2020.10.08.20204222 (2020).
9. M. J. Mina et al., *N. Engl. J. Med.* **383**, e120 (2020).
10. X. He et al., *Nat. Med.* **26**, 672 (2020).
11. D. B. Larremore et al., *Sci. Adv.* 10.1126/sciadv.abd5393 (2020).
12. M. Pavelka et al., "The effectiveness of population-wide, rapid antigen test based screening in reducing SARS-CoV-2 infection prevalence in Slovakia," CMMID Repository, 11 November 2020; <https://bit.ly/36BkvV5>.
13. E. A. Meyerowitz et al., *Ann. Intern. Med.* 10.7326/M20-5008 (2020).
14. V. M. Corman et al., *medRxiv* 10.1101/2020.11.12.20230292 (2020).

## SUPPLEMENTARY MATERIALS

[science.sciencemag.org/content/371/6525/126/suppl/DC1](https://science.sciencemag.org/content/371/6525/126/suppl/DC1)

Published online 21 December 2020

10.1126/science.abe9187



## POLICY FORUM

### SCIENCE FOR POLICY: COVID-19

# Coevolution of policy and science during the pandemic

Recent, high-quality science is being heard, but unevenly

By **Yian Yin**<sup>1,2,3</sup>, **Jian Gao**<sup>1,2,4</sup>,  
**Benjamin F. Jones**<sup>1,2,4,5,6</sup>, **Dashun Wang**<sup>1,2,3,4</sup>

**D**isconnects between science and policy, in which important scientific insights may be missed by policy-makers and bad scientific advice may infect decision-making, are a long-standing concern (1–7). Yet, our systematic understanding of the use of science in policy remains limited (1, 4–6), partly because of the difficulty in reliably tracing the coevolution of policy and science at a large, global scale (3). Today, the world faces a common emergency in the COVID-19 pandemic, which presents a dynamic, uncertain, yet extraordinarily consequential policy environment across the globe. We combined two large-scale databases that capture policy and science and their interactions, allowing us to examine the coevolution of policy and science

during the pandemic. Our analysis suggests that many policy documents in the COVID-19 pandemic substantially access recent, peer-reviewed, and high-impact science. And policy documents that cite science are especially highly cited within the policy domain. At the same time, there is a heterogeneity in the use of science across policy-making institutions. The tendency for policy documents to cite science appears mostly concentrated within inter-governmental organizations (IGOs), such as the World Health Organization (WHO), and much less so in national governments, which consume science largely indirectly through the IGOs. This close coevolution between policy and science offers a useful indication that a key link is operating, but it has not been a sufficient condition for effectiveness in containing the pandemic.

The rapid production of new science during COVID-19 raises key questions about its use in policy during the pandemic. There is long-standing skepticism over connections between science and policy, which are often thought to be highly disconnected spheres. For example, the “two communities” theory in knowledge utilization (7) highlights a substantial gap between scientists and policy-makers, disconnecting research from the policy process. Related viewpoints sug-

gest that policy-makers may not be able to distinguish relatively robust scientific ideas from less established ones (2). Particularly in the pandemic setting, there is substantial concern that policy may take up non-vetted and potentially incorrect scientific results. For example, preprint servers have played an outsized role in disseminating COVID-19-related research (8). Although open science greatly facilitates the sharing of data and research (8) and allows the wider community to check and interrogate the results and claims, publicly releasing science before it passes peer review may undermine the rigor of scientific evidence accessible to the public (9). In the age of misinformation, this may create enduring harms if the evidence presented turns out to be less robust. Such concerns are further heightened by examples of widely reported and then retracted results regarding COVID-19 (10).

To explore COVID-19 science and policy, we harnessed a large-scale database, Overton, which records policy documents sourced globally from government agencies, think tanks, and IGOs. For each policy document, we then matched scientific references to our second dataset, Dimensions, a large-scale publication and citation database, offering a distinct opportunity to examine the role of science in the global policy response to COVID-19. Further details on all data collection, integration, and analyses (including examples of policy documents and the scientific papers they reference, systematic comparisons with alternative data sources, and external validations on the overall coverage of our datasets) are provided in the supplementary materials (SM).

## POLICY, SYNCHRONY, SHIFTS

Our Overton dataset captures 37,725 policy documents published by government agencies and think tanks from 114 countries and 55 IGOs, from 2 January to 26 May 2020. Policy documents are defined by Overton as “research, briefs, reviews, or reports written with the goal of influencing or changing policy,” and scientific and policy references are demarcated within each document. The data includes all major economies and large population centers, with a notable exception of mainland China. Together, our data cover 66.3% of the world population, 79.3% of total gross domestic product, and 95.6% of confirmed deaths worldwide due to COVID-19 (as of 30 May 2020). Within this corpus, we identified COVID-19-related policy documents through keyword filtering (7730 documents in total), which allowed us to compare COVID-19 policy documents with all other policy documents published in 2020 (see SM for data description and validation).

<sup>1</sup>Center for Science of Science and Innovation, Northwestern University, Evanston, IL, USA. <sup>2</sup>Northwestern Institute on Complex Systems, Northwestern University, Evanston, IL, USA. <sup>3</sup>McCormick School of Engineering, Northwestern University, Evanston, IL, USA. <sup>4</sup>Kellogg School of Management, Northwestern University, Evanston, IL, USA. <sup>5</sup>National Bureau of Economic Research, Cambridge, MA, USA. <sup>6</sup>Brookings Institution, Washington, DC, USA.  
Email: bjones@kellogg.northwestern.edu; dashun.wang@northwestern.edu

As a first look at the policy data and its practical relevance, we examined how the evolution of COVID-19 policy documents corresponds to facts on the ground. The policy documents mirror the case dynamics (see the first figure), showing a synchrony between the share of COVID-19 policy documents among all policy documents and the number of total confirmed cases (see SM for fit statistics).

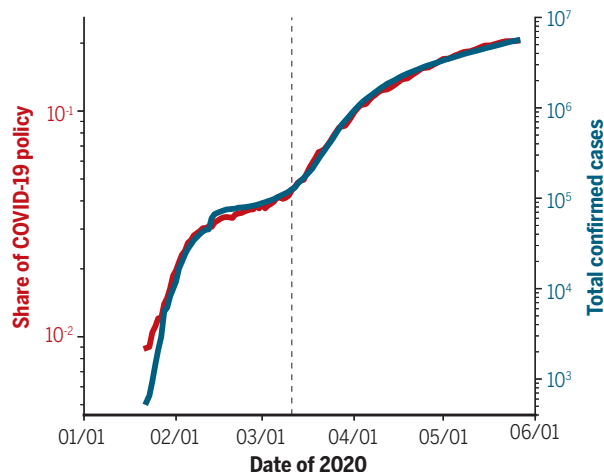
We further examined the content of the COVID-19 policy documents, breaking them down by field (see the first figure) and topic (fig. S7). Both analyses show substantial shifts in policy attention related to the pandemic. In the early stage of the outbreak (January and February 2020), about 90% of COVID-19 policy documents belong to the health and science category, showing a clear, initial focus on medical and public health issues. The policy priorities show a visible shift, however, since WHO declared COVID-19 a pandemic on 11 March 2020, with a rise in attention to issues around the economy and society, suggesting a growing policy balance between health and socioeconomic implications of the pandemic. These shifts are observed in COVID-19 policy documents only; we repeated the analyses for other policy documents published in the same period, finding that the distributions of fields and topics remained relatively stable during this period (see SM).

## POLICY FRONTIER ROOTED IN SCIENCE

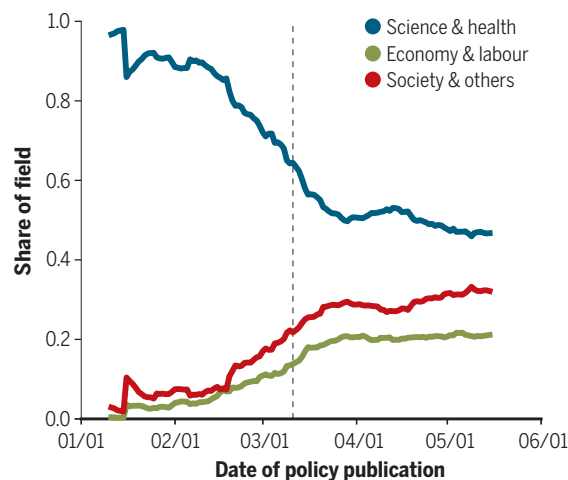
Much like the global policy frontier, the scientific understanding of COVID-19 also evolved rapidly, as exemplified by the strong response from the global research enterprise. According to Dimensions data, more than 40,000 papers on coronavirus research were published from 1 January through 30 May 2020. Our findings reveal close connections between the evolving COVID-19 policy frontier and the evolving scientific frontier.

The fraction of COVID-19 policy documents that cite at least one scientific paper fluctuates in early 2020 but then features a steady increase with time, especially after WHO's pandemic declaration (fig. S12A). Also, COVID-19 policies are disproportionately centered on the latest scientific frontier (see the second figure). Out of all scientific references drawn on by COVID-19

## The evolution of policy during the pandemic



The share of COVID-19 policy documents among all policy documents published up to a given day (red line) versus the global confirmed case count (blue line), as traced by the Johns Hopkins COVID-19 tracking map (15).



The share of three broad subject categories within the COVID-19 policy documents (21-day moving average).

policy documents, 19.9% of the scientific papers were published in 2020. This rate of using the newest science is highly unusual, more than 10 times greater than seen for other policy documents. Predictably, the latest science cited is primarily related to COVID-19 (88.4%).

The close connection between science and policy is also reflected in the fields of science that COVID-19 policy documents cite (see SM), showing a clear shift from drawing primarily on the biomedical literature to citing economics, society, and other fields of study, which is consistent with overall shifts in policy focus (see the first figure). Together, these results suggest that despite the extremely recent development in COVID-19-related research, new scientific work has rapidly found its way into policy documents, prompting us to

next examine the quality of scientific evidence that informs policy.

We examined the quality of science that appears in policy documents along two dimensions. First, we separated COVID-19-related papers into two groups on the basis of whether or not they are referenced by COVID-19 policy documents, and we measured each paper's scientific impact within the science community, approximated by the number of citations the paper received from other scientific papers. We found a large difference between the two groups (see the second figure): Papers referenced in policy documents garner on average 40 times more citations than those not referenced in policy documents (average citations, 67.72 versus 1.67). Overall, this result shows that the coronavirus research used by policy-makers aligns with what scientists heavily engage with themselves.

Further, we broke down the policy coverage of COVID-19 research according to publication venues (see the second figure). We found that different venues differ widely in publication volume, with preprint servers such as medRxiv, bioRxiv, and SSRN publishing an order of magnitude more COVID-19-related papers than did peer-reviewed journals. Yet despite the volume of preprints, their impact in policy is rather limited because these preprint servers show consistently fewer policy citations than average. By contrast, COVID-19 policy documents disproportionately reference peer-reviewed insights, drawing especially heavily on top medical

journals, both general (such as *Lancet*) and specialized (such as *Clinical Infectious Diseases*). Although peer review does not necessarily guarantee high-quality science (9), amid growing concerns over the quality and abundance of coronavirus research posted on preprint servers, these results nevertheless show that during this crisis, peer-reviewed journals continue to remain a crucial institution in supplying scientific evidence for policy-making.

Overall, the COVID-19 policy frontier appears to be deeply grounded in extremely recent, peer-reviewed scientific insights, and science directly drawn on by this policy frontier appears to be especially impactful within the research community itself. Moreover, policy documents that are grounded in the scientific frontier also tend to garner substantially more ci-



tations within the global policy network. Specifically, separating COVID-19 policy documents by whether they cite science or not, we found that COVID-19 policy documents that cite at least one scientific paper are associated with more than twice the number of citations from other policy documents (see fig. S12B). To test whether this difference in use can be explained by other covariates, we further used a regression model (see SM) to control for the policy document's source, date, number of scientific references, and self-citations, arriving at the same conclusions.

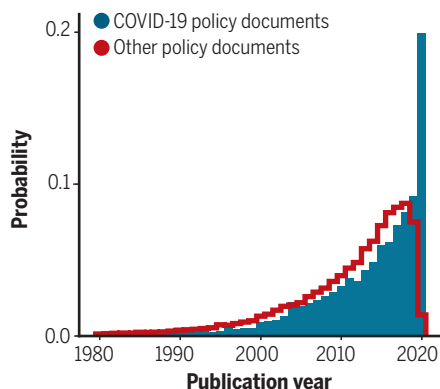
Together, these results show that despite the rapidly evolving nature of the pandemic, the policy and scientific frontier of COVID-19 are closely interlinked, with documents and articles that are directly along the policy-science interface (policy documents that cite science and the cited science itself) being more impactful within their own domains. But what policy institutions contribute most strongly to the policy-science interface? Our final analysis examines the policy institutions that cite science, comparing national governments, think tanks, and intergovernmental organizations. We found that although government agencies produced the most COVID-19 policy documents among the three types of institutions (fig. S13), they are the least likely to cite science (fig S14).

By contrast, policy documents that are grounded in science are disproportionately produced by IGOs, especially by WHO (fig. S14). These differences in the use of science persist when we compare the indirect use of science (citing other policy documents that cite science), showing that IGOs again draw disproportionately more on the policy-science interface (fig. S14, inset). Many have argued that nations work best together through international institutions, especially in a crisis such as COVID-19 (11). These results suggest a key role of WHO and other IGOs in the global policy response to COVID-19, acting as central conduits that link policy to science.

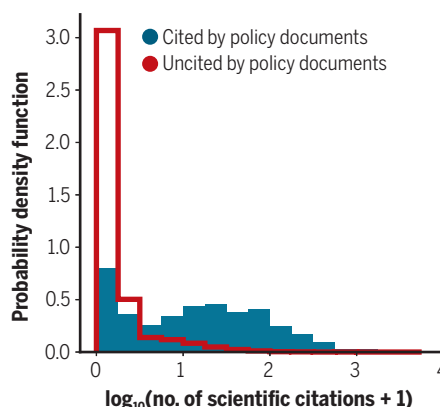
## SCIENCE IS BEING HEARD

Taken together, our results show that policy documents in the COVID-19 pandemic substantially access recent, peer-reviewed, and high-impact science. At the same time, our reference-based measures are but a proxy for the uses of science in policy (1), and policies may cite science for different reasons (6). Policy-relevant science may be interpreted differently depending on one's specific interests (4) and may even be distorted during the dissemination process (5). Further, although our data captures among the largest collection of policy documents,

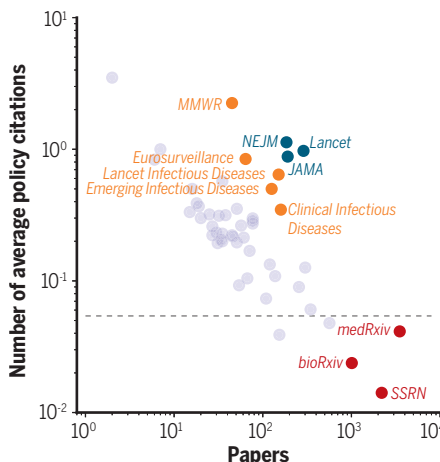
## Science use in policy documents



Distribution of publication years of scientific papers (published from 1980 to 2020) cited by policy documents. The unusual spike in citing papers published in 2020 indicates that COVID-19 policy documents draw heavily on recent scientific evidence.



COVID-19 scientific papers that are cited by policy documents have greater citation impact within science.



For different journals and preprint servers, we measured the number of COVID-19 related papers (x axis) and the average number of citations from COVID-19 policy documents to these papers (y axis) in 2020. Shown here are the top 50 publication outlets based on the total number of citations from COVID-19 policy documents. The black dashed line indicates the average number of citations measured on all COVID-19 papers. MMWR, Morbidity and Mortality Weekly Report; NEJM, The New England Journal of Medicine; JAMA, The Journal of the American Medical Association

there could be potential biases in data sample and coverage that future research may help to further elucidate. Also, our data capture science-policy interactions up to 26 May 2020, and the observed patterns may continue to evolve as the pandemic unfolds worldwide. Nevertheless, our results suggest that COVID-19 policy documents appear neither isolated from scientific advances nor reliant on dubious science. These findings appear encouraging for the scientific community as scientists, journals, and funders work expeditiously to advance and validate new research, with the hope that their work might affect the course of the pandemic.

Ultimately, although scientific advances provide a global public good, and IGOs can help coordinate global action, national policy approaches and death rates have varied greatly (12). Although some countries have been quite successful in containing the outbreak (13), some have been actively antagonistic to IGOs and scientific advice (11, 14). In the current picture, science is breaking through, and scientific results are being heard, but they are not being heard everywhere. ■

## REFERENCES AND NOTES

1. National Research Council, *Using Science as Evidence in Public Policy* (National Academies Press, 2012).
2. C. P. Snow, *Science and Government* (Oxford Univ. Press, 1961).
3. R. Haunschild, L. Bornmann, *Scientometrics* **110**, 1209 (2017).
4. S. S. Jasanoff, *Soc. Stud. Sci.* **17**, 195 (1987).
5. S. Hilgartner, *Soc. Stud. Sci.* **20**, 519 (1990).
6. C. H. Weiss, *Pub. Admin. Rev.* **39**, 426 (1979).
7. N. Caplan, *Am. Behav. Sci.* **22**, 459 (1979).
8. M. Zastrow, *Nature* **581**, 109 (2020).
9. A. J. London, J. Kimmelman, *Science* **368**, 476 (2020).
10. A. H. J. Kim et al., *Ann. Intern. Med.* **172**, 819 (2020).
11. H. H. Thorp, *Science* **368**, 341 (2020).
12. T. Hale, A. Petherick, T. Phillips, S. Webster, "Variation in government responses to COVID-19," Blavatnik School of Government working paper BSG-WP-2020/2032 (2020).
13. S. Hsiang et al., *Nature* **584**, 262 (2020).
14. J. Tollefson, *Nature* **586**, 190 (2020).
15. E. Dong, H. Du, L. Gardner, *Lancet Infect. Dis.* **20**, 533 (2020).

## ACKNOWLEDGMENTS

We thank E. Adie and all members of the Center for Science of Science and Innovation (CSSI) at Northwestern University for their helpful discussions. This work uses data sourced from Overton.io and Dimensions.ai and is supported by the Air Force Office of Scientific Research under awards FA9550-17-1-0089 and FA9550-19-1-0354, National Science Foundation grant SBE 1829344, and the Alfred P. Sloan Foundation G-2019-12485. The authors declare no competing interests. Deidentified data necessary to reproduce all plots and statistical analyses are available at [http://kellogg-cssi.github.io/covid\\_policy\\_science](http://kellogg-cssi.github.io/covid_policy_science) and at Figshare (10.6084/m9.figshare.13326611). Y. Y. and J. G. contributed equally to this work.

## SUPPLEMENTARY MATERIALS

[science.sciencemag.org/content/371/6525/128/suppl/DC1](https://science.sciencemag.org/content/371/6525/128/suppl/DC1)

10.1126/science.abe3084



BOOKS *et al.*

## PSYCHOLOGY

# Play breeds better thinkers

Children need unstructured exploration and time to tackle problems that interest them

By **Kathy Hirsh-Pasek**

In a digital, global world where information is projected to double every 12 hours (1), the memorization of facts will become less of a commodity than the ability to think, find patterns, and generate new ideas from old parts (2, 3). Thus, a cradle-to-career approach to educating children must be mindful of how children learn to learn, not just what they learn (4). Combining insight, scientific acumen, and exquisite narrative, *The Intellectual Lives of Children* allows readers to peer into the minds of infants, toddlers, and preschoolers as they explore and learn in everyday moments, emphasizing what constitutes real learning.

Children are bursting with playful curiosity. By age 3, they ask questions about everything they see—Why does a tree have leaves? Why does the Sun come up each day?—and by age 5, they pose even deeper questions, about God and morals. These questions not only provide fodder for knowledge, they help children discover the causal relationships among things—all with adult mentors by their side.

Children also need time to explore. One child might collect dead things like worms and slugs, and another, assorted leaves of different shapes and colors. These collections, Engel argues, become treasured resources for the discovery of patterns, and they invite even more inquisitiveness. Indeed, the adults who guide this exploration by asking questions themselves reinforce curiosity and innovation. Hidden in these playful encounters are rich opportunities for learning.



**The Intellectual Lives of Children**  
Susan Engel  
Harvard University Press,  
2021. 240 pp.

Yet explorations take time—the time to meander and discover, the unscheduled time to be bored. As Engel writes, “when children are allowed to dive into a topic thoroughly, they...connect isolated facts in order to generate new ideas.” They learn grit and they learn to have agency over their own learning. As such, the real mental work for children takes place in plain sight as they play—when a child builds a platform of chairs and pillows to retrieve cookies from an out-of-reach cookie jar and when she uses kitchen utensils to fish for the toy that is lodged under the couch.

As adults, we often overlook the fact that learning is happening during periods of unstructured play, or we dismiss these intervals as unproductive. Hurried parents often lack the ability to carve out that time,

Learning is not linear and intellectual exploration takes time, argues Engel.

fearing that their children might be late for their next scheduled activity.

“Watch and listen for twenty minutes in almost any school in the United States and it becomes clear that the educational system does not concern itself with children’s intellectual lives,” admonishes Engel in the opening pages of the book. Instead, she hopes to reenvision schools as “idea factories” built on inspiring curiosity and problem solving: “Imagine assessing students’ progress under some new headings: poses interesting questions, speculates,...articulates important problems and spends time solving them.”

In one lovely example, Engel describes a teacher who challenged her students to construct a record-breaking straw chain that would eventually measure 3.8 miles. “Winning the record would be fun, but the enduring benefit would be coming to grips with vast quantities,” explains the teacher, whose goal was to help the children to better understand the sheer depth of the Mariana Trench.

The puzzles and problems that captivate children and the ways they set about solving them are reminiscent of how philosophers Karl Popper and Thomas Kuhn conceptualized the thinking of scientists (5, 6). Both children and scientists bring the tools in their respective arsenals to bear on things that matter to them. Their learning is not linear and is certainly not funneled through flashcards (7).

In the past few decades, developmental science has made great strides in understanding the mental richness of infants, toddlers, and preschoolers. Engel’s book helps parents and educators see what scientists have learned, offering tips for how to make the learning even more apparent. For example, she encourages parents to see children as active thinkers and suggests that by asking open-ended questions and letting them explore, children will be better prepared to thrive in a complex and ever-changing world. ■

## REFERENCES AND NOTES

1. S. Sorkin, “Thriving in a world of ‘knowledge half-life,’” *Enterprising Insights*, 5 April 2019.
2. R. M. Golinkoff, K. Hirsh-Pasek, *Becoming Brilliant* (APA Press, 2016).
3. D. H. Pink, *A Whole New Mind* (Penguin, 2006).
4. K. Hirsh-Pasek, H. S. Hadani, E. Blinkoff, R. M. Golinkoff, “A new path to education reform: Playful learning promotes 21st-century skills in schools and beyond,” *The Brookings Institution: Big Ideas Policy Report*, 28 October 2020.
5. K. Popper, *The Logic of Scientific Discovery* (Hutchinson, 1959).
6. T. S. Kuhn, *The Structure of Scientific Revolutions* (Univ. of Chicago Press, 1962).
7. A. Gopnik, A. N. Meltzoff, P. K. Kuhl, *The Scientist in the Crib* (William Morrow, 1999).

10.1126/science.abf3679

The reviewer is at the Department of Psychology, Temple University, Philadelphia, PA 19122, USA, and the Brookings Institution, Washington, DC 20036, USA. Email: khirshpa@temple.edu



## GEOGRAPHY

# Probed, pierced, and revered

Earth's mantle acts as a metaphor for the planet's unknowns, for its beauty, and for its fragility

By **Deborah P. Dixon**

In her new book, *The Mantle of the Earth*, geographer Veronica della Dora explains how Earth's mantle has provided a capacious metaphor for the terrain that sustains human life and the manner in which it is imagined and investigated. This is a metaphor that thrives on the lifting of veils and the piercing of interiors, as well as the “warp and weft” of a web of life and the weaving together of social and physical phenomena into narratives that convey the rich texture of this environment.

In its ambitious scope and humanistic approach, the book is an excellent example of the erudite scholarship that traces the emergence and mutability of an earthly imagination manifest in changing cartographic practices over time. These practices animate the wedding of Zeus with Chthonia, the formless Earth, and the placement of a woven mantle across the subterranean depths, transforming Chthonia into Gê, or Gaia, the visible, life-sustaining Mother Earth. They also underlie the nodes and links of Berners-Lee's World Wide Web, which “nets” people and things together, and the digital layers of geocoded content that make up platforms such as Google Earth. The ways in which these innovative technologies compose and map content and the ways in which people engage with that content make clear their place in a history of Western environmental thinking about Earth's mantle.

The book is at its best when it sets up movements and counter-movements in how Earth's mantle is imagined and investigated. There is, for example, a brilliant exposé of how, in Renaissance Europe, the dissection of the mantle by mapmakers echoed the contemporaneous slicing open and pinning back of the tissues of the human body in anatomical science. As della Dora writes, “Cartographers dissected the earth in continents and regions, and, thanks to Ptolemy's projec-

tions, they flattened it on atlas tables. Likewise, anatomists cut up the human body in pieces on the surface of the dissection table and flattened them on the tables of the anatomical atlas.” This anatomical approach to Earth was well in evidence in G. K. Gilbert's explanation of geomorphology four centuries later, when he wrote of erosion as “a dissection which lays bare the very anatomy of the rocks” (1).

As della Dora makes clear, however, clinical interrogations of Earth's mantle were counterpointed by a Romantic, poetic appreciation of the communion between



Like mist, Earth's mantle acts as a veil, concealing what lies beneath.

mind and nature, self and cosmos, that expressed the enchanting truth of what it meant simply to “be” amid the shimmering mantle. “Lying on the grass in direct contact with the primordial earthly matter while gazing at the heavenly vault,” she writes, “the Romantic hero links the low to the high, the beautiful to the sublime.”

The book tracks the cut and thrust of scientific investigation forward into the 20th century, framing the International Geophysical Year of 1957–58—which della Dora calls a “scientific Olympics of sorts”—

**The Mantle of the Earth: Genealogies of a Geographical Metaphor**  
Veronica della Dora  
University of Chicago Press,  
2020. 416 pp.



as a pivotal one for mantle explorations. Rocket and space programs, ocean drilling projects, and seismic soundings beneath Antarctica's ice sheets were propelled by “[d]reams of control over and large-scale modifications of the ancient earth's mantle” as well as “the dream of piercing beyond it into the unknown—of lifting Isis's veil.” Such efforts, however, contrasted with a growing environmental consciousness in the West, precipitated by nuclear fallout and accumulating toxins, that focused public attention on the fragility of Earth's “green mantle.”

The book refers to “the Western eye” and historically and culturally specific ways of seeing the world. At times, however, there is scope for critically unpacking claims of a universal human way of knowing—such as when della Dora references anthropologist Edmund Leach's speculation that a division into two sexes and a sense of mind-body separation prompt binary-driven mythologies (2). Beyond parochializing such claims, an interrogation of how the mantle as metaphor “unveils a plurality of worlds” could have been furthered by noting how seeing and knowing have historically been framed, including by liberal humanism itself.

As an account of ideas and artifacts, the book provides a sweeping backdrop to current-day scientific technologies and practices. The conceptual underpinnings to this process, however, tend to be folded away from view. ■

## REFERENCES AND NOTES

1. G. K. Gilbert, “Report on the Geology of the Henry Mountains,” Department of the Interior, U.S. Geographical and Geological Survey of the Rocky Mountain Region, Washington, D.C., 5 March 1877.
2. E. Leach, *Genesis as Myth and Other Essays* (Jonathan Cape, 1969).

The reviewer is at the School of Geographical and Earth Sciences, University of Glasgow, Glasgow G12 8QQ, UK. Email: [deborah.dixon@glasgow.ac.uk](mailto:deborah.dixon@glasgow.ac.uk)

10.1126/science.abf0570



## LETTERS

Edited by Jennifer Sills

## Stay true to integrated pest management

On 2 October 2020, the United Nations Food and Agriculture Organization (FAO) and CropLife International signed a letter of intent to establish a strategic partnership (1). Moving forward, CropLife International's aspirations should be closely scrutinized. Checks and balances are essential to ensure that private interests do not take precedence over the common good.

For decades, both the FAO and CropLife International have advocated the uptake of integrated pest management—an approach that strategically integrates different crop protection methods to safeguard crop yields, secure farmer livelihoods, and preserve natural capital (2). However, their respective interpretations of the system's core constituents, underlying principles, and ultimate goals differ substantially. The FAO emphasizes how preventing pests through good agronomy, biological diversity, and ecological processes can lower the amount of pesticide required, whereas CropLife International focuses on the responsible use of agrochemicals, with far less desirable results.

The FAO's interpretation of integrated

pest management has led to successes worldwide. Its Farmer Field Schools have transferred ecological concepts and non-chemical technologies to millions of small farmers, resulting in pesticide reductions of 92% in Bangladesh rice, 78% in India cotton, and 61% in Vietnamese tea (3). These FAO programs have attained pesticide cuts of 50 to 80% on millions of farms without yield loss (4), thus lifting farmers' profits, curbing energy use, and bolstering rural economies (5). Unfortunately, when some programs were dismantled in the mid-1990s, achievements were rapidly undone (6); Indonesia's pesticide use has since risen substantially.

Meanwhile, CropLife International's approach—i.e., pesticide-centered control—continues to proliferate across the globe (7, 8). For example, insecticide-coated seeds are zealously backed by chemical enterprises (9), even though their on-farm use violates integrated pest management principles, triggers resistance development, exacerbates pollution, and degrades the resilience of farmland ecosystems (10). By thus deviating from established decision-making criteria and tolerating technology integration that occurs by chance instead of by design, this approach leads to ineffective pest control and negative social-ecological outcomes (11). Agro-ecology, digital tools, and innovative farming schemes can all remediate chemical

Indonesia's use of pesticide has increased since programs to implement alternatives were dismantled.

dependencies, but agro-industry meddling constitutes a prominent hurdle (12).

Ultimately, globe-spanning alliances that include agro-industry should only be built to scale up environmentally compatible practices and to pursue agri-food system transformations that are protective of human and environmental health. In the spirit of integrated pest management, as correctly interpreted and implemented by the FAO, biodiversity and ecological safeguards should constitute plant health programs' first line of defense, whereas pesticide use needs to be consciously downgraded to a measure of last resort.

Kris Wyckhuys<sup>1,2,3\*</sup>, Francisco Sanchez-Bayo<sup>4</sup>, Alexandre Aebi<sup>5</sup>, Maarten Bijleveld van Lexmond<sup>6</sup>, Jean-Marc Bonmatin<sup>7</sup>, Dave Goulson<sup>8</sup>, Edward Mitchell<sup>5,9</sup>

<sup>1</sup>Institute of Plant Protection, China Academy of Agricultural Sciences, Beijing, China. <sup>2</sup>University of Queensland, Brisbane, QLD, Australia. <sup>3</sup>Chrysalis Consulting, Hanoi, Vietnam. <sup>4</sup>University of Sydney, Sydney, NSW, Australia. <sup>5</sup>University of Neuchâtel, Neuchâtel, Switzerland. <sup>6</sup>International Union for Conservation of Nature Task Force on Systemic Pesticides, Neuchâtel, Switzerland.

<sup>7</sup>Centre de Biophysique Moléculaire, Centre National de la Recherche Scientifique, Orléans, France. <sup>8</sup>University of Sussex, Brighton, UK. <sup>9</sup>Botanical Garden of Neuchâtel, Neuchâtel, Switzerland.

\*Corresponding author.

Email: kagwyckhuys@gmail.com

## REFERENCES AND NOTES

1. "Letter of intent between the Food and Agriculture Organization of the United Nations and CropLife International" (2020); [www.fao.org/fileadmin/user\\_upload/newsroom/docs/CropLife.pdf](http://www.fao.org/fileadmin/user_upload/newsroom/docs/CropLife.pdf).
2. S. E. Naranjo, *J. Agric. Food Chem.* **59**, 11 (2011).
3. H. van den Berg, J. Jiggins, *World Dev.* **35**, 4 (2007).
4. D. G. Bottrell, K. G. Schoenly, *J. Asia Pac. Entomol.* **15**, 1 (2012).
5. H. Waddington *et al.*, *Campbell Systemat. Rev.* **10**, 1 (2014).
6. C. Thorburn, *Agroecol. Sustain. Food Syst.* **38**, 3 (2014).
7. E. S. Bernhardt *et al.*, *Front. Ecol. Environ.* **15**, 2 (2017).
8. P. J. Landrigan *et al.*, *Lancet* **391**, 10119 (2018).
9. C. Hitaj *et al.*, *BioScience* **70**, 5 (2020).
10. G. Labrie *et al.*, *PLOS ONE* **15**, 2 (2020).
11. L. P. Pedigo, M. E. Rice, *Entomology and Pest Management* (Waveland Press, 2014).
12. D. Goulson, *One Earth* **2**, 4 (2020).

10.1126/science.abf8072

## Raising standards for global data-sharing

In their Policy Forum "How to fix the GDPR's frustration of global biomedical research" (2 October 2020, p. 40), J. Bovenberg *et al.* argue that the biomedical research community has struggled to share data outside the European Union as a result of the EU's General Data Protection Regulation (GDPR), which strictly limits the international transfer of personal data. However, they do not acknowledge the law's



flexibility, and their solutions fail to recognize the importance of multilateral efforts to raise standards for global data-sharing.

Bovenberg *et al.* express concern about the thwarting of “critical data flows” in biomedical research. However, the limited number of critical commentaries (1, 2) and registered complaints (3) indicate that hindered data exchange may not be a substantial global problem. Moreover, the authors concede that during the COVID-19 pandemic, data transfers remain ongoing because transfers “necessary for important reasons of public interest” are already provided in the law [(4), Article 49(1)(d)]. The European Data Protection Board (EDPB) has cautioned that transfers according to this derogation shall not become the rule in practice (5), but this conditional support for international COVID-19 data sharing shows that the law already provides suitable flexibility. This flexibility also shows the EDPB’s recognition of the pressing social need that biomedical research represents for the global research community during the COVID-19 pandemic, while also seeking to ensure that this remains the exception and not the beginning of a normalized practice.

Bovenberg *et al.* contend that pseudonymized data should not be considered personal data in the hands of an entity that does not possess the key needed for re-identification. This proposal runs against well-established guidance in EU member states such as Ireland (6) and Germany (7), and it does not take into account the cases in which identifiers remain attached to transferred biomedical data or in which data could be identified without a key.

Bovenberg *et al.* also neglect to state that the GDPR has special principles and safeguards for particularly sensitive re-identifiable data, not just for the protection of privacy but also for the security and integrity of health research data—aims that align with all high-quality scientific research. Respecting these standards (both technical and organizational) is fundamental to ensuring better data security and accuracy in the transferring of huge datasets of sensitive health data that are essential to global collaboration [(4), Articles 5 and 9, Recitals 53 and 54, and (8)]. Thus, these rules should not be subject to exemptions, which would result from not classifying pseudonymized data as personal data.

The purpose of the GDPR’s strict rules is to ensure that when personal data are transferred to non-EU countries, the level of protection ensured in the European Union is not undermined. The EU’s Court of Justice decisions (9, 10) make it clear that ensuring an adequate level of protection in non-EU countries, especially independent

oversight and judicial remedies—which the Court found lacking in the United States—is a matter of fundamental rights. This discrepancy is an opportunity for non-EU countries, including the United States, to raise their data protection standards to the level of the European Union’s, not for the European Union to decrease its own standards in a regulatory race to the bottom. We encourage research organizations and country delegations to work with the European Commission, national data protection authorities, and the EDPB to craft interoperable rules on data sharing applicable for biomedical research in ways that do not undermine fundamental rights owed to data subjects.

Edward S. Dove<sup>1\*</sup>, Jiahong Chen<sup>2</sup>, Nóra Ni Loideain<sup>3</sup>

<sup>1</sup>School of Law, University of Edinburgh, Edinburgh, UK. <sup>2</sup>Horizon Digital Economy Research, University of Nottingham, Nottingham, UK. <sup>3</sup>Institute of Advanced Legal Studies, School of Advanced Study, University of London, London, UK.

\*Corresponding author.

Email: edward.dove@ed.ac.uk

#### REFERENCES AND NOTES

1. R. Eiss, *Nature* **584**, 498 (2020).
2. R. Becker *et al.*, *J. Med. Internet Res.* **22**, e19799 (2020).
3. A. Jelinek, EDPB response letter to Mark W. Libby, Chargé d’Affaires, United States Mission to the European Union (2020); [https://edpb.europa.eu/sites/edpb/files/files/file1/edpb\\_letter\\_out2020-0029\\_usmission\\_covid19.pdf](https://edpb.europa.eu/sites/edpb/files/files/file1/edpb_letter_out2020-0029_usmission_covid19.pdf).
4. GDPR (2016); <https://gdpr-info.eu/>.
5. EDPB, “Guidelines 03/2020 on the processing of data concerning health for the purpose of scientific research in the context of the COVID-19 outbreak” (2020).
6. Data Protection Commission, “Guidance on Anonymisation and Pseudonymisation” (2019); [www.dataprotection.ie/sites/default/files/uploads/2019-06/190614%20Anonymisation%20and%20Pseudonymisation.pdf](http://www.dataprotection.ie/sites/default/files/uploads/2019-06/190614%20Anonymisation%20and%20Pseudonymisation.pdf).
7. German Federal Ministry of the Interior, Building and Community, “Draft for a Code of Conduct on the use of GDPR compliant pseudonymisation” (2019); [www.gdd.de/downloads/aktuelles/whitepaper/Data\\_Protection\\_Focus\\_Group-Draft\\_CoC\\_Pseudonymisation\\_V1.0.pdf](http://www.gdd.de/downloads/aktuelles/whitepaper/Data_Protection_Focus_Group-Draft_CoC_Pseudonymisation_V1.0.pdf).
8. D. Anderson *et al.*, *Int. Data Privacy L.* **10**, 180 (2020).
9. Case C-362/14 Maximilian Schrems v. Data Protection Commissioner (Court of Justice of the EU, 2015).
10. Case C-311/18 Data Protection Commissioner v. Facebook Ireland Limited and Maximilian Schrems (Court of Justice of the EU, 2020).

10.1126/science.abf4286

## Response

Dove *et al.* suggest that despite the lack of viable mechanisms for transferring research data from Europe to other countries, in practice such transfers take place anyway. However, the fact that some transfers continue to occur in circumstances of regulatory ambiguity is not a solution; rather, these exceptions exacerbate the legal, regulatory, ethical, and operational challenges. Issues of cross-border research data transfer in the wake of the latest Court of Justice decision abound, and the General Data Protection Regulation (GDPR) has stalled at least 40 U.S. National Institutes of Health clinical and observational studies on risk

factors and exposures for cancer (1).

Dove *et al.* point to the European Data Protection Board (EDPB) guidance on COVID-19 as evidence that GDPR contains sufficient flexibilities, but this guidance specifies that the ability to make such cross-border transfers should be temporary (2). COVID-19 research, like much other research, requires longitudinal study of data over many years. A “temporary measure” does not suffice in the long term.

In dismissing our proposal that pseudonymized data need not always be considered personal data, Dove *et al.* assert that such an approach is unrealistic given the guidance in certain EU Member States. However, those rules concern anonymization generally and do not focus on the more protected and secure research context. The European Court of Justice in the Breyer case and several commentators in the research community have proposed that a contextual approach to pseudonymization could permit pseudonymized data to be treated as anonymized when adequate safeguards are in place (3–6).

Dove *et al.*’s assertion that some identifiers remain attached to transferred biomedical data mistakenly ignores that all identifiers will be removed, as discussed in our Policy Forum. Any subsequent attempt to reidentify deidentified data would either require unauthorized access, breach of law and contract, or both. This risk cannot be completely prevented, but it exists both outside and within the EU. What matters is that the EDPB contends that both pseudonymization and encryption with the keys retained solely under the control of the data exporter could provide effective supplementary measures (7).

Dove *et al.* suggest that our proposals will lead to a “regulatory race to the bottom,” but they do not recognize that the U.S. and EU laws are each imperfect in their implementation. The EU Court of Justice expressed concern about particular elements of the U.S. national security regime (notably lack of redress to a judicial authority), but the types of pseudonymized data transferred in the course of scientific research are unlikely to be of interest to the U.S. intelligence community (8). Dove *et al.* hope that the United States and other countries will “raise their data protection standards to the level of the European Union’s,” but they overlook the fact that the GDPR itself does not protect subjects from use of their data for national surveillance intelligence (9, 10). In addition, they neglect to acknowledge that the EU Fundamental Rights Agency has documented the limited individual redress to a judicial authority existing in EU Member States under their

national surveillance laws. Notably, only “in four Member States [out of 27], an expert body’s decision or preliminary assessment can be appealed before a judge” (10). Thus, 23 Member States’ legislation present gaps to data protection that are similar to those in the United States.

We believe that the European Union should resolve this double standard before insisting on the higher standard for non-EU countries. In the meantime, our solutions offer a balanced approach to the trade-offs between privacy, global science, and public health.

Jasper Bovenberg<sup>1\*</sup>, David Peloquin<sup>2</sup>, Barbara Bierer<sup>3</sup>, Mark Barnes<sup>2,4</sup>, Bartha Maria Knoppers<sup>5</sup>

<sup>1</sup>Legal Pathways Life Sciences Law, Haarlem, Netherlands. <sup>2</sup>Ropes & Gray LLP, Boston, MA 02199–3600, USA. <sup>3</sup>Multi-Regional Clinical Trials Center of Harvard University and Brigham and Women’s Hospital, Cambridge, MA 02115, USA. <sup>4</sup>Yale Law School, New Haven, CT 06511, USA. <sup>5</sup>Centre of Genomics and Policy, Faculty of Medicine, McGill University, Montreal, QC, Canada. \*Corresponding author. Email: legalpathways@legalpathways.eu

#### REFERENCES AND NOTES

1. R. Eiss, *Nature* **584**, 498 (2020).
2. European Data Protection Board, “Guidelines 03/2020 on the processing of data concerning health for the

purpose of scientific research in the context of the COVID-19 outbreak” (2020).

3. Case C-582/14 *Patrick Breyer v. Bundesrepublik Deutschland* (2016), ECR I-769.
4. PHG Foundation, “The GDPR and genomic data,” (2020); [www.phgfoundation.org/documents/gdpr-and-genomic-data-report.pdf](http://www.phgfoundation.org/documents/gdpr-and-genomic-data-report.pdf).
5. M. Mourby et al., *Comput. Law Secur. Rev.* **34**, 222 (2018).
6. E.-B. van Veen, *Eur. J. Canc.* **104**, 70 (2018).
7. European Data Protection Board, “Recommendations 01/2020 on measures that supplement transfer tools to ensure compliance with the EU level of protection of personal data” (2020).
8. U.S. Department of Commerce, “Information on U.S. privacy safeguards relevant to SCCs and other EU legal bases for EU-U.S. data transfers after *SCHREMS II*” (white paper) (2020).
9. GDPR (2016), Recital 16, Article 2(2)(d) and Article 23(1)(a); <https://gdpr-info.eu/>.
10. EU Agency for Fundamental Rights, “Surveillance by intelligence services: Fundamental rights safeguards and remedies in the EU—Volume II: Field perspectives and legal update” (2017).

10.1126/science.abf5425

#### TECHNICAL COMMENT ABSTRACTS

Comment on “Global distribution of earthworm diversity”

S. W. James, C. Csuzdi, C.-H. Chang, N. M. Aspe, J. J. Jiménez, A. Feijoo, M. Blouin, P. Lavelle Phillips et al. (Reports, 25 October 2019,

p. 480) incorrectly conclude that tropical earthworm communities are less diverse and abundant than temperate communities. This result is an artifact generated by some low-quality datasets, lower sampling intensity in the tropics, different patterns in richness-area relationships, the occurrence of invasive species in managed soils, and a focus on local rather than regional richness.

Full text: [dx.doi.org/10.1126/science.abf4629](https://doi.org/10.1126/science.abf4629)

Response to Comment on “Global distribution of earthworm diversity”

Helen R. P. Phillips, Maria J. I. Briones, George G. Brown, Thibaud Decaens, Erin Cameron, Nico Eisenhauer

James et al. claim that there are areas of concern in our work. We believe that they have misunderstood the methods behind our paper and that differences in scale have been overlooked. Once those misunderstandings have been resolved, their remaining criticisms are either not sustained or agree with our statements. To advance the field, we recommend additional sampling using comparable methodologies in underrepresented areas.

Full text: [dx.doi.org/10.1126/science.abf4744](https://doi.org/10.1126/science.abf4744)



International  
Human Frontier  
Science Program  
Organization

## CALL FOR LETTERS OF INTENT FOR RESEARCH GRANTS:

AWARD YEAR 2022

Initiation deadline: 18 March 2021  
Submission deadline: 30 March 2021

The Human Frontier Science Program (HFSP) supports innovative basic research that applies novel and interdisciplinary approaches to understand fundamental biological problems and includes scientific exchanges across national and disciplinary boundaries.

HFSP research projects extend the frontiers of knowledge. Successful applications will entail risk and aim to develop novel lines of research for each participating partner that must be different from their ongoing research. The participation of scientists from disciplines outside the traditional life sciences such as chemistry, computer science, engineering, mathematics, nanoscience or physics is considered a key requisite in HFSP grant applications.

To stimulate novel, daring ideas and innovative approaches, preliminary results are not required in HFSP research grant applications. Special emphasis is placed on encouraging scientists early in their careers to participate in the Program Grants. Applicants are expected to develop new lines of research through the collaboration.

Awards are for 3 years and made to international (preferably intercontinental) teams of 2 – 4 members who have not collaborated before. **Research Grants – Program** are for independent scientists at all stages of their careers. **Research Grants – Early Career** (formerly Young Investigator Grants) are for teams of researchers who are all within 5 years of establishing an independent laboratory and within 10 years of obtaining their PhDs. The amount is dependent upon team size, up to \$465,000 per year for a team of four. The principal applicant must be located in one of the HFSP member countries; co-applicants may be located in any country.

Applicants are advised to use the quiz on the HFSP website to check their eligibility and to read the guidelines carefully ([www.hfsp.org](http://www.hfsp.org)). Starting end of January 2021 principal applicants can initiate an application via the HFSP Extranet until March 18, 2021. Submission deadline for the letter of intent is March 30, 2021.

Specific enquiries: [grant@hfsp.org](mailto:grant@hfsp.org).





# 2021

AAAS MARTIN AND  
ROSE WACHTEL  
CANCER RESEARCH

# AWARD

Recognize the work of an early career scientist who has performed outstanding work in the field of cancer research. Award nominees must have received their Ph.D. or M.D. within the last 10 years. The winner will deliver a public lecture on his or her research, receive a cash award of **\$25,000**, and publish a Focus article in *Science Translational Medicine*.

For more information visit  
[www.aaas.org/aboutaaas/awards/wachtel](http://www.aaas.org/aboutaaas/awards/wachtel)  
or e-mail [wachtelprize@aaas.org](mailto:wachtelprize@aaas.org).  
Deadline for submission: **February 1, 2021.**



Science Translational Medicine

# RESEARCH

## IN SCIENCE JOURNALS

Edited by Michael Funk

### METEORITES

#### Recent fluid flow in ancient meteorites

**C**arbonaceous chondritic meteorites are thought to be fragments broken off parent bodies that orbit in the outer Solar System, largely unaltered since their formation. These meteorites contain evidence of reactions with liquid water that was thought to have been lost or completely frozen billions of years ago. Turner *et al.* examined uranium and thorium isotopes in several carbonaceous chondrites, finding nonequilibrium distributions that imply that uranium ions were transported by fluid flow. Because this signature disappears after several half-lives of the radioactive isotopes, the meteorites must have been exposed to liquid within the past million years. The authors suggest that ice may have melted during the impacts that ejected the meteorites from their parent bodies. —KTS *Science*, this issue p. 164



Carbonaceous chondrites, such as the well-studied Murchison meteorite, retain signs of the presence of liquid water within the past million years.

PHOTO: SBS ECLECTIC IMAGES/ALAMY STOCK PHOTO

### ECOTOXICOLOGY

#### Tire tread particles turn streams toxic

For coho salmon in the U.S. Pacific Northwest, returning to spawn in urban and suburban streams can be deadly. Regular acute mortality events are tied, in particular, to stormwater runoff, but the identity of the causative toxicant(s) has not been known. Starting from leachate from new and aged tire tread wear particles, Tian *et al.* followed toxic fractions through chromatography steps, eventually isolating a single molecule that could induce acute toxicity at threshold concentrations of ~1 microgram per liter. The compound, called 6PPD-quinone, is an oxidation product of an additive intended to prevent damage to tire rubber from ozone. Measurements from road runoff and immediate receiving waters show concentrations of 6PPD-quinone high enough to account for the acute toxicity events. —MAF

*Science*, this issue p. 185

### STRUCTURAL VIROLOGY

#### Two antibodies against flaviviruses

Flaviviruses are a group of RNA viruses that include the human pathogens dengue virus, Zika virus, and West Nile virus. The envelope protein (E) on the virus surface has been the target of vaccine development, but problems have arisen with antibodies against E, leading to enhanced infection. Now, Modhiran *et al.* and Biering *et al.* describe two different antibodies that bind to the flavivirus NS1 protein and prevent it from disrupting epithelial cells, which is associated with severe disease. Both antibodies cross-react with multiple flavivirus NS1 proteins. The antibodies reduce viremia and increase survival in mouse models of flavivirus disease. Both papers include structures of NS1 bound to an antibody, which give insight into the protective mechanism. —VV

*Science*, this issue p. 190, p. 194



**CANCER****To respond or not to respond**

Patients with cancer are frequently treated with chemotherapy, but it does not always work and it is difficult to predict who will respond to the treatment. In addition to the direct effects of chemotherapy, antitumor immune responses can also play an important role. By examining the immune responses in patients with muscle-invasive bladder cancer, Vollmer *et al.* identified a key role for the CXCR3 chemokine system of ligands and receptors. The activity of this system before initiation of treatment was associated with subsequent response to chemotherapy in multiple independent cohorts of patients, suggesting a potential rational approach to the selection of therapies. —YN and MN

*Sci. Transl. Med.* **13**, eabb3735 (2021).

**MULTIPLE SCLEROSIS****Precision therapy for immune tolerance**

Autoimmune diseases, such as multiple sclerosis (MS), result from a breach of immunological self-tolerance and tissue damage by autoreactive T lymphocytes. Current treatments can cause systemic immune suppression and side effects such as increased risk of infections. Krienke *et al.* designed a messenger RNA vaccine strategy that lacks adjuvant activity and delivers MS autoantigens into lymphoid dendritic cells. This approach expands a distinct type of antigen-specific effector regulatory T cell that suppresses autoreactivity against targeted autoantigens and promotes bystander suppression of autoreactive T cells against other myelin-specific autoantigens. In mouse models of MS, the vaccine delayed the onset and reduced the severity of established disease without showing overt symptoms of general immune suppression. —PNK

*Science*, this issue p. 145

**CHEMICAL PHYSICS****The nature of short hydrogen bonds**

Hydrogen bonding (H-bonding) unquestionably plays an important role in chemical and biological systems and is responsible for some of their unusual properties. Strong, short H-bonds constitute a separate class that, owing to their elusive characterization, has remained a point of contention over the past several decades. Using femtosecond two-dimensional infrared spectroscopy in conjunction with quantum chemical calculations, Dereka *et al.* demonstrate a powerful way to investigate the nature of short H-bonding (see the Perspective by Bonn and Hunger). Their quantitative characterization of multiple coupled motions in the model system of bifluoride anion  $[F-H-F]^-$  in aqueous solution reveals several distinctive features of a crossover from conventional to short, strong H-bonding. —YS

*Science*, this issue p. 160  
see also p. 123

**OCEAN ANOXIA****Where they can't breathe**

Climate warming is causing the expansion of marine oxygen-deficient zones, which are regions in which dissolved oxygen concentrations are so low that many marine animals cannot survive. This phenomenon also might affect the global cycles of carbon, sulfur, nitrogen, and trace metals in the oceans. Raven *et al.* show how ocean anoxia affects microbial sulfur processing in sinking marine particles. They observed cryptic microbial sulfate reduction, which forms organic sulfur that is resistant to acid hydrolysis, a process that could enhance carbon preservation in sediments underlying oxygen-deficient water columns. This may help explain some of the more extreme episodes of organic carbon preservation associated with marine anoxia in Earth's history. —HJS

*Science*, this issue p. 178

**IN OTHER JOURNALS**

Edited by Caroline Ash  
and Jesse Smith

Copepods use pheromone trails and hydrodynamic signals to track down females under turbulent conditions.

**SYNTHETIC BIOLOGY****A microfactory in yeast peroxisomes**

Considerable synthetic biology efforts are focused on engineering yeast to produce valuable metabolites. Production in the cytosol can be challenging because of toxicity or crosstalk with cellular pathways. Dusséaux *et al.* harnessed the yeast peroxisome to produce geranyl diphosphate (GPP), a precursor to monoterpenoids, and cannabinoids. Targeting the entire pathway for GPP synthesis, along with an enzyme that converts GPP to the monoterpene limonene, to the peroxisome gives a 125-fold improvement in yield of limonene compared with production in the cytoplasm. Additional monoterpenes can be synthesized with the same platform using the appropriate monoterpene synthase. Peroxisomal production also facilitates downstream processing involving oxidation by cytochrome P450 enzymes. Peroxisome microfactories could be used

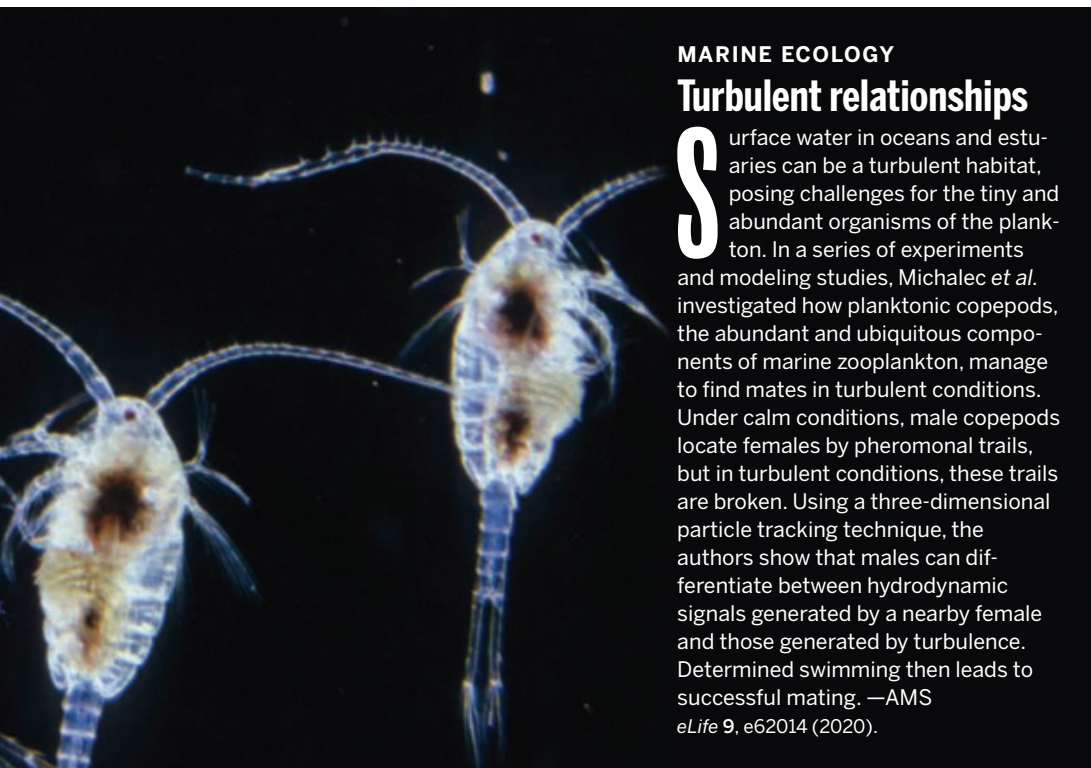
for the modular assembly and optimization of other complex pathways. —VV

*Proc. Natl. Acad. Sci. U.S.A.* **117**,  
31789 (2020).

**SCIENTIFIC WORKFORCE****Keep calm and measure the gap**

Academic conferences are fertile ground for data collection on gender inequities, owing to their importance in career development, networking, and increasing visibility. Corona-Sobrinho *et al.* developed a tool based on performance indicators that allows for real-time monitoring and evaluation of gender roles and inequalities at academic conferences. In developing the tool, three relevant perspectives (participation, organizational structure, and attitudes) were identified, along with a specific list of performance indicators for each, allowing for both individual and combined analysis. Results are shown as a traffic light visualization, with red meaning bad and green meaning good, making





## MARINE ECOLOGY

### Turbulent relationships

**S**urface water in oceans and estuaries can be a turbulent habitat, posing challenges for the tiny and abundant organisms of the plankton. In a series of experiments and modeling studies, Michalec *et al.* investigated how planktonic copepods, the abundant and ubiquitous components of marine zooplankton, manage to find mates in turbulent conditions. Under calm conditions, male copepods locate females by pheromonal trails, but in turbulent conditions, these trails are broken. Using a three-dimensional particle tracking technique, the authors show that males can differentiate between hydrodynamic signals generated by a nearby female and those generated by turbulence. Determined swimming then leads to successful mating. —AMS

*eLife* 9, e62014 (2020).

it easy to see which areas are, or are not, performing well. Recommendations are provided to ensure that one's academic conference stays in the green. —MMc

*PLOS ONE* 15, e0243549 (2020).

## SYMBIOSIS

### Tiny tomato suppressor

Acarid arthropods are common and economically important pests of crop plants. The tomato russet mite *Aculops lycopersici* is only 175 micrometers long but can potentially suppress the host plant's natural resistance. It has a highly streamlined genome of 32.5 megabases, more closely resembling that of a protist than a metazoan. Greenhalgh *et al.* discovered that this mite leaves no room in its genome for hangers-on. It contains few transposons, has slimmed intergenic spaces to almost none, has almost done away with chemosensory apparatus and detox pathways, and has even reduced its number of legs from eight to four in the interests of economy. However, it has retained the capacity to

suppress the tomato's jasmonic acid signaling pathway, which blocks the ability of the tomato host plant to produce defensive metabolites and proteins. However, the selective forces resulting in this genome diminution remain a puzzle—perhaps one is the poor nutritional value of tomato plants. —CA

*eLife* 9, e56689 (2020).



Tomato russet mites disable the immune responses of tomato plants.

## WOUND REPAIR

### Sensing and repairing epidermal injury

The skin protects underlying tissues and organs from potentially damaging microbes and other agents. Epithelial integrity must be reestablished after a skin injury that results in a surface break. For this to happen, cells use altered signaling and mechanical cues to trigger the repair process. Kennard and Theriot examined the mechanism of repair after injury to the zebrafish tailfin. By imaging the actin cytoskeleton, they noted different initial wound responses in zebrafish larvae in different environmental conditions. Cells are sensitive to external sodium chloride at the wound site, suggesting that a change in electrical potential is involved. Applying electric fields triggers actin polarization and basal cell migration, even in absence of wounding. Understanding how skin responds to osmotic and electrical changes may lead to methods for tissue repair. —BAP

*eLife* 9, e62386 (2020).

## MATERIALS SCIENCE

### Tuning boron-carbon-nitride films

Thin films formed from boron, carbon, and nitrogen (BCN films) can exhibit a wide range of optical and electronic properties if they can be made as phase-pure materials. Giusto *et al.* report on a simple solution-based route to hydrogenated BCN films. Gels formed with different melamine and boric acid ratios (1:1 and 2:1) were deposited on substrates and then heated in dry nitrogen to produce homogeneous, optically transparent films with optical bandgaps of 2.9 and 3.4 electron volts, respectively. The material derived from the 2:1 gel exhibited  $sp^2$  bonding and avoided segregation into graphene and hexagonal boron nitride. Addition of small amounts of benzoguanamine to the gels allowed for additional compositional and bandgap tuning. —PDS

*J. Am. Chem. Soc.* 142, 20883 (2020).

## ATMOSPHERIC CHEMISTRY

### HONO formation in the troposphere

Nitrous acid (HONO) is an important tropospheric intermediate. Current atmospheric models, which assume its formation in the heterogeneous reaction of nitrogen dioxide ( $NO_2$ ) and water, fail to correctly predict the high concentrations of HONO that are detected in the troposphere. Using sub-nanosecond first-principles molecular dynamics simulations, Martins-Costa *et al.* show that HONO forms from  $NO_2$  preferentially in bulk water with very low probability of its desorption from the surface of liquid water. The present results call into question the catalytic role of the air-water interface and suggest that further studies that take into account various tropospheric chemical species adsorbed on the aqueous droplets are required to elucidate the mechanism of this important atmospheric chemistry. —YS

*J. Am. Chem. Soc.* 142, 20937 (2020).

## REVIEW SUMMARY

## NEURODEVELOPMENT

## Making sense of neural development by comparing wiring strategies for seeing and hearing

A. A. Sitko and L. V. Goodrich\*

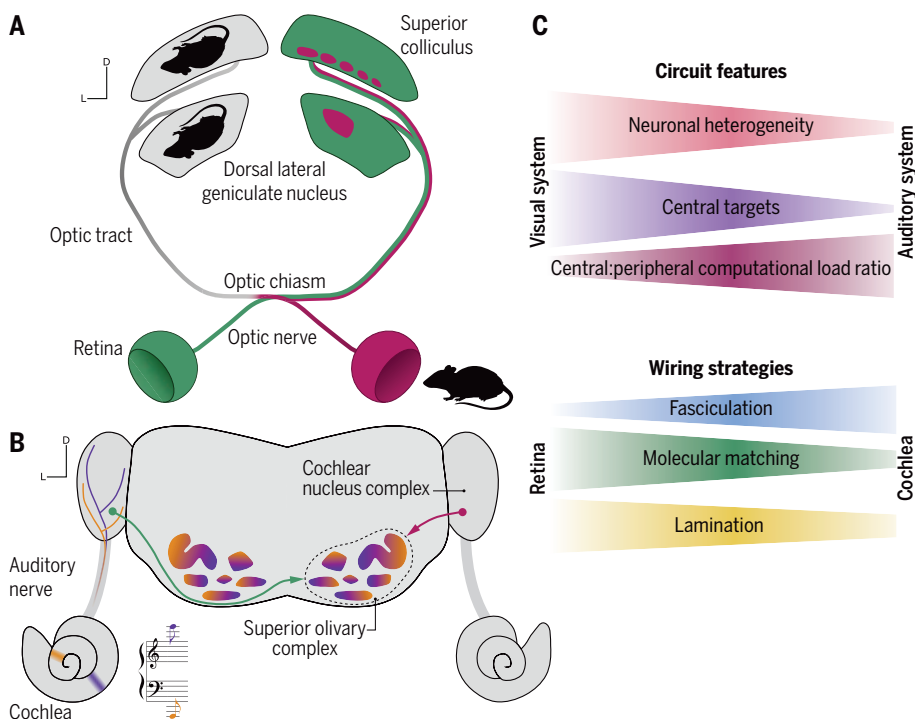
**BACKGROUND:** Since its infancy just over a century ago, the developmental neurobiology field has identified many unifying principles of neural circuit formation. We have come to appreciate the ways in which, for instance, transcriptional regulation of cell fate, molecular mechanisms of axon guidance and synapse formation, and activity-dependent refinement wire a variety of circuits across species. Certain systems, such as the vertebrate spinal cord or visual system, were historically popular choices for research because of their accessibility. Today, the field is poised to build on this foundation by studying how common mechanisms operate flexibly to assemble diverse circuits throughout the nervous system. By studying the fine details of how individual circuits acquire their characteristic features, we can learn more about the versatility and complexity of circuit assem-

bly mechanisms and begin to unravel the rules that govern how and when certain strategies are used. To illustrate the value of such an approach, we present some examples of basic developmental events that unfold similarly and differently in the functionally specialized circuits for seeing and hearing, with a focus on the local circuitry and primary afferent projections of the vertebrate retina and cochlea.

**ADVANCES:** Comparing and contrasting the development of retinal and cochlear circuitry in the context of each system's functional demands reveals a common theme: Similar developmental events and strategies are evident in both circuits, but each system's unique circuit features arise from relative differences in their reliance on those common mechanisms. For instance, neuronal heterogeneity and wiring

complexity in the sense organ, as well as the number of central targets, are all relatively greater in the visual system than in the auditory system of vertebrates. As such, the retina relies heavily on neuronal identity-driven adhesion codes to assemble local synaptic connections among a large number of different neuronal subtypes. In turn, fasciculation plays a more prominent role in maintaining spatial relationships among cochlear afferents, whose identity is shaped by synaptic activity. The relative simplicity of wiring in the cochlea versus the retina parallels the computational handling in the two circuits: Both systems perform a combination of local and central computations to encode sensory stimuli, but more extensive parsing occurs locally in the retina than in the cochlea. Instead, auditory afferents project to the auditory brainstem and then arborize locally in their target to initiate a series of parallel computations. Within the different cellular contexts of these developing circuits, even the same molecules can mediate distinct functions. For example, canonical Eph/ephrin gradients guide retinotopic mapping, whereas in the cochlea, the same molecules mediate fasciculation and segregation of peripheral inputs. Therefore, the formation of topographic maps in the visual and auditory systems, although superficially similar, appears to rely on overlapping yet distinct mechanisms.

**OUTLOOK:** Although there is broad agreement about the basic development events that form a functional circuit, we remain unable to explain the wiring of any circuit completely. Looking forward, we need to define the full range of developmental strategies and identify points of flexibility that adapt each mechanism to specific wiring challenges. With the availability of sophisticated methods to visualize and manipulate developing circuits, today's researchers are no longer limited to experimentally accessible systems and can characterize phenotypes with ever greater resolution and depth, from the position of an individual synapse to the effects of a single manipulation on the whole genome. By taking a deep dive into the contributions of supposedly well-understood developmental processes in circuits with fundamentally different architectures, we can reveal novel roles for familiar mechanisms and molecules, thereby expanding our knowledge of how dynamic and versatile strategies are harnessed to create the diverse circuits needed for complex behavior. ■



**A balancing act: Wiring visual and auditory circuits.** (A and B) Afferent projections from the retina (A) and cochlea (B) initiate circuits for seeing and hearing. In both systems, sensory stimuli are encoded topographically. However, information from the two sides of the head (green and magenta) converges at different levels. D, dorsal; L, lateral. (C) Wiring features specialized to meet the specific functional demands of sight and hearing arise by common cellular and molecular strategies operating in different ways and to different extents.

The list of author affiliations is available in the full article online. Department of Neurobiology, Harvard Medical School, Boston, MA, USA.

\*Corresponding author. Email: [lisa\\_goodrich@hms.harvard.edu](mailto:lisa_goodrich@hms.harvard.edu)  
Cite this article as A. A. Sitko and L. V. Goodrich, *Science* 371, eaaz6317 (2021). DOI: [10.1126/science.aaz6317](https://doi.org/10.1126/science.aaz6317)

**S** READ THE FULL ARTICLE AT  
<https://doi.org/10.1126/science.aaz6317>



## RESEARCH ARTICLE SUMMARY

## SPLICEOSOME

## Mechanism of spliceosome remodeling by the ATPase/helicase Prp2 and its coactivator Spp2

Rui Bai\*, Ruixue Wan\*†, Chuangye Yan\*, Qi Jia, Jianlin Lei, Yigong Shi†

**INTRODUCTION:** Splicing of precursor messenger RNA (pre-mRNA) is carried out by the spliceosome. During each splicing cycle, the spliceosome undergoes assembly, activation, catalysis, and disassembly. The assembled spliceosome exists in eight major functional states. Spliceosome remodeling between neighboring states is driven by conserved adenosine triphosphatase (ATPase)/helicases. Together with its coactivator Spp2, the ATPase/helicase Prp2 harnesses the energy of adenosine 5'-triphosphate (ATP) binding and hydrolysis to translocate 3'-to-5' on the single-stranded pre-mRNA, thus remodeling the activated spliceosome (known as the B<sup>act</sup> complex) into the catalytically activated spliceosome (the B\* complex). The B\* complex catalyzes the branching reaction.

Since 2015, cryo-electron microscopy (cryo-EM) structures of all major states of the assembled spliceosome have been determined at near-atomic resolutions, generating crucial information on the active site and overall organization of the spliceosome. How spliceosome remodeling occurs, however, remains poorly

understood because none of the ATPase/helicases in the presence of the spliceosome has been visualized in atomic details owing to limited resolution. In particular, it remains largely unknown how Prp2 remodels the B<sup>act</sup> complex and why Prp2 requires its coactivator Spp2.

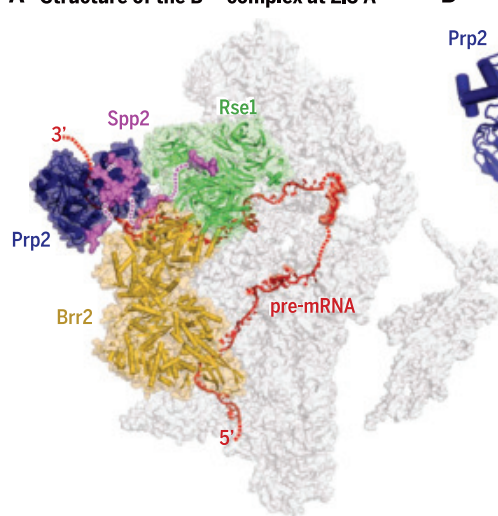
**RATIONALE:** To address these questions, we need to examine the detailed structural features of Prp2 and Spp2 in the B<sup>act</sup> complex and compare these features with those of Prp2 and Spp2 in isolation. Atomic resolution is required, which may need improvement in sample preparation. Structure-guided biochemical analyses may be needed to corroborate the conclusions.

**RESULTS:** We used galactose-inducible expression of an ATPase-defective Prp2 mutant to stall remodeling of the endogenous B<sup>act</sup> complex. This strategy resulted in marked enrichment of the B<sup>act</sup> complex in the final cryo-EM sample. We determined the cryo-EM structure of the *S. cerevisiae* B<sup>act</sup> complex at 2.5 Å—the highest resolution achieved for an intact spliceosome

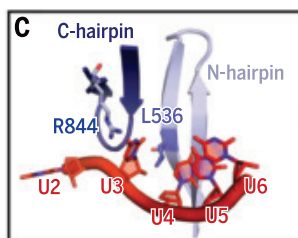
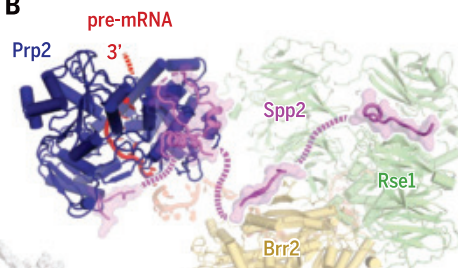
to date—which allows atomic identification of 12 new proteins, including Prp2 and Spp2 (see the figure). Prp2 weakly associates with the spliceosome and fails to function in the absence of Spp2. Spp2 uses its C-terminal sequences to stably associate with Prp2 and its N-terminal sequences to anchor on the spliceosome, thus tethering Prp2 to the B<sup>act</sup> complex and allowing Prp2 to function. In the spliceosome, pre-mRNA is loaded into a featured channel between the N and C halves of Prp2, where Leu<sup>536</sup> from the N half and Arg<sup>844</sup> from the C half serve as barbed wires to prevent backward sliding of pre-mRNA toward its 5' end. Conserved residues in the channel make hydrogen bonds mainly to the backbone phosphates, but not the nucleobases, of the pre-mRNA, explaining its sequence-independent recognition by Prp2.

We then determined the cryo-EM structures of Prp2 in three related functional states: free Prp2, Spp2-bound Prp2, and Spp2-bound ADP-loaded Prp2. These structures, together with that of Prp2 in the B<sup>act</sup> complex and other published information, yield a working mechanism for Prp2. Relative movement between the RecA1 and RecA2 domains of Prp2, driven by ATP binding and hydrolysis, results in pre-mRNA translocation. In step 1, ATP binding to RecA1 is predicted to trigger the movement of RecA2 toward RecA1, allowing Leu<sup>536</sup> to push the nucleobase of pre-mRNA to translocate by one nucleotide toward its 3' end. Because of the translocation, Arg<sup>844</sup> loses its association with the departing nucleobase and associates with the newly arrived upstream nucleobase. In step 2, ATP hydrolysis leads to the relaxation of RecA2 back to its original position, allowing Leu<sup>536</sup> to shift its interactions to an upstream nucleobase. The movement of RecA2 is safeguarded by Arg<sup>844</sup>, which may prevent backward sliding of pre-mRNA. Last, ADP is released, and Prp2 is reset for the next cycle. In our model, Leu<sup>536</sup> and Arg<sup>844</sup> serve as two hands to alternately bind and push pre-mRNA toward its 3' end.

**CONCLUSION:** As a coactivator, Spp2 stably associates with Prp2 and tethers it to B<sup>act</sup>, enabling Prp2 function. ATP binding and hydrolysis trigger interdomain movement in Prp2, which allows Leu<sup>536</sup> and Arg<sup>844</sup> to alternately bind and push pre-mRNA unidirectionally toward its 3' end. ■

A Structure of the B<sup>act</sup> complex at 2.5 Å

## B



**Mechanism of action for the ATPase/helicase Prp2 in the activated spliceosome.** (A) Structure of the B<sup>act</sup> complex. (B) Spp2 uses its N-terminal sequences to anchor on the spliceosome and its C-terminal sequences to associate with Prp2, tethering Prp2 to the spliceosome and enabling its function. (C) Leu<sup>536</sup> (L536) and Arg<sup>844</sup> (R844) of Prp2 prevent backward sliding of pre-mRNA by only allowing 5'-to-3' movement of the RNA bases.

The list of author affiliations is available in the full article online.

\*These authors contributed equally to this work.

†Corresponding author. Email: wanruixue@westlake.edu.cn (R.W.); syg@westlake.edu.cn (S.Y.)

Cite this article as R. Bai et al., *Science* 371, eabe8863 (2021). DOI: 10.1126/science.abe8863

**READ THE FULL ARTICLE AT**  
<https://doi.org/10.1126/science.abe8863>

## RESEARCH ARTICLE SUMMARY

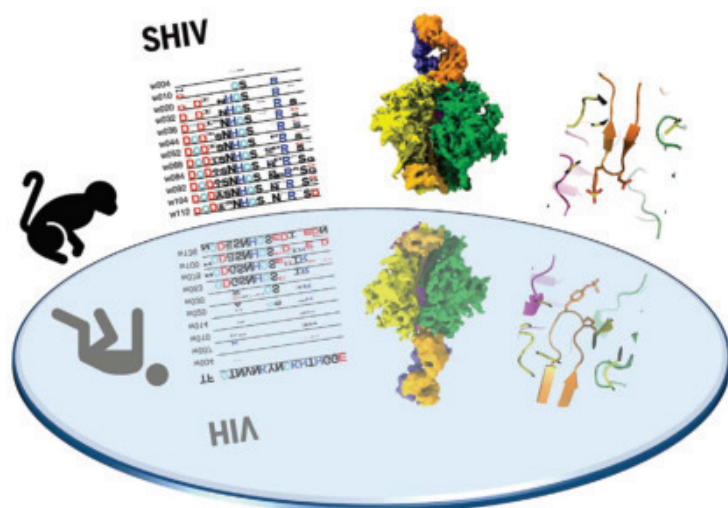
## HIV

## Recapitulation of HIV-1 Env-antibody coevolution in macaques leading to neutralization breadth

Ryan S. Roark\*, Hui Li\*, Wilton B. Williams\*, Hema Chug\*, Rosemarie D. Mason\*, Jason Gorman\*, Shuyi Wang, Fang-Hua Lee, Juliette Rando, Mattia Bonsignori, Kwan-Ki Hwang, Kevin O. Saunders, Kevin Wiehe, M. Anthony Moody, Peter T. Hraber, Kshitij Wagh, Elena E. Giorgi, Ronnie M. Russell, Frederic Bibollet-Ruche, Weimin Liu, Jesse Connell, Andrew G. Smith, Julia DeVoto, Alexander I. Murphy, Jessica Smith, Wenge Ding, Chengyan Zhao, Neha Chohan, Maho Okumura, Christina Rosario, Yu Ding, Emily Lindemuth, Anya M. Bauer, Katharine J. Bar, David Ambrozak, Cara W. Chao, Gwo-Yu Chuang, Hui Geng, Bob C. Lin, Mark K. Louder, Richard Nguyen, Baoshan Zhang, Mark G. Lewis, Donald D. Raymond, Nicole A. Doria-Rose, Chaim A. Schramm, Daniel C. Douek, Mario Roederer, Thomas B. Kepler, Garnett Kelsoe, John R. Mascola, Peter D. Kwong, Bette T. Korber, Stephen C. Harrison, Barton F. Haynes, Beatrice H. Hahn, George M. Shaw†

**INTRODUCTION:** It is widely believed that the development of an effective neutralizing antibody-based HIV-1 vaccine will require consistent activation of multiple germline precursor B cells that express immunoglobulin receptors specific for one or more of the canonical broadly neutralizing antibody (bNAb) epitope clusters, followed by efficient antigen-driven selection for antibody affinity maturation. How to accomplish this feat by immunization has proven to be a daunting scientific challenge. One roadblock to rational HIV-1 vaccine design is the lack of a suitable outbred primate model in which bNAbs can be commonly induced, thereby enabling the molecular, biological, and immunological mechanisms responsible for such responses to be studied in a reproducible and iterative fashion.

**RATIONALE:** Given that most HIV-1 bNAbs identified to date have come from humans chronically infected by HIV-1, we hypothesized that one means to elicit such antibodies in primates might be by infecting rhesus macaques (RMs) with simian-human immunodeficiency virus (SHIV) strains that bear primary HIV-1 envelope proteins (Envs), including those that induced bNAbs in humans. SHIV-infected RMs could then be used to assess the potential of particular HIV-1 Envs to elicit bNAbs and to characterize the coevolutionary pathways of bNAb lineages and the cognate Env intermediates that elicited them, thus serving as a molecular guide for rational vaccine design. Recent innovations in SHIV design make this experimental strategy testable.





## RESEARCH ARTICLE SUMMARY

## PLANT SCIENCE

# Coordination between microbiota and root endodermis supports plant mineral nutrient homeostasis

Isai Salas-González\*, Guilhem Reyt\*, Paulina Flis\*, Valéria Custódio, David Gopaulchan, Niokhor Bakhoun, Tristan P. Dew, Kiran Suresh, Rochus Benni Franke, Jeffery L. Dangl, David E. Salt, Gabriel Castrillo†

**INTRODUCTION:** All living organisms have evolved homeostatic mechanisms to control their mineral nutrient and trace element content (ionomes). In plant roots and animal guts, these mechanisms involve specialized cell layers that function as a diffusion barrier to water, solutes, and immunoactive ligands. To perform this role, it is essential that the cells forming these layers are tightly sealed together. Additionally, these cells must perform their homeostatic function while interacting with the local microbiota. In animals, resident microbes influence the function of intestinal diffusion barriers and, in some cases, miscoordination of this interplay can cause dysbiosis.

In plants, two types of extracellular root diffusion barriers have been characterized at the endodermis: Casparian strips, which seal cells together, and suberin deposits, which influence transport across the cell plasma membrane. Whether and how these root diffusion barriers

coordinate with the microbiota inhabiting the root is unknown. Such coordination could influence plant performance, agronomic yields, and the nutritional quality of crops.

**RATIONALE:** We explored and characterized the interplay between the regulatory networks controlling the performance of the root diffusion barrier and the functionally complex and metabolically dynamic microbiota inhabiting the root. To address this, we explored the presumptive reciprocal nature of this interaction using two complementary approaches.

First, we profiled the microbiome of a collection of plants with a range of specific alterations to the root diffusion barrier to determine whether the regulatory network controlling the synthesis and deposition of the barrier components also controls the structure of the root microbiome. Second, we deployed a collection of bacterial strains iso-

lated from the shoots and roots of plants grown in natural soils to establish the influence of the microbiome over root barrier function. Last, we coupled both approaches to identify the molecular links between the root diffusion barrier and their associated microbiota.

**RESULTS:** We analyzed a nonredundant and diverse collection of 19 root diffusion barrier mutants and overexpression lines to reveal the influence of the root diffusion barrier regulatory network on the assembly of the plant microbiota. We screened 416 individual bacterial strains for their ability to modify the function of the Casparian strip and suberin deposits in the endodermis and uncovered a new role for the plant microbiota in influencing root diffusion barrier functions with an impact on plant mineral nutrient homeostasis. We designed and deployed a bacterial synthetic community combined with ionomics and transcriptomics to discover the molecular mechanisms underlying the coordination between root diffusion barriers and the plant microbiota.

Our research has three main findings: (i) The regulatory network controlling the endodermal root diffusion barriers also influences the composition of the plant microbiota; (ii) individual members of the plant microbiome, bacterial synthetic communities, or natural microbial communities control the development of endodermal diffusion barriers, especially suberin deposition, with consequences for the plant's ionome and abiotic stress tolerance; and (iii) the capacity of the plant microbiome to influence root diffusion barrier function is mediated by its suppression of signaling dependent on the phytohormone abscisic acid.

**CONCLUSION:** Our findings that the plant microbiome influences root diffusion barrier function generalizes the role of the microbiome in controlling cellular diffusion barriers across kingdoms. In addition, we defined the molecular basis of how diffusion barriers in multicellular organisms incorporate microbial function to regulate mineral nutrient balance. This discovery has potential applications in plant and human nutrition and food quality and safety. Microbial-based strategies to control suberization of plant roots presents new opportunities to design more resilient crops, new biofortification strategies, and carbon-sequestration approaches. ■

The list of author affiliations is available in the full article online.  
\*These authors contributed equally to this work.

†Corresponding author. Email: gabriel.castrillo@nottingham.ac.uk

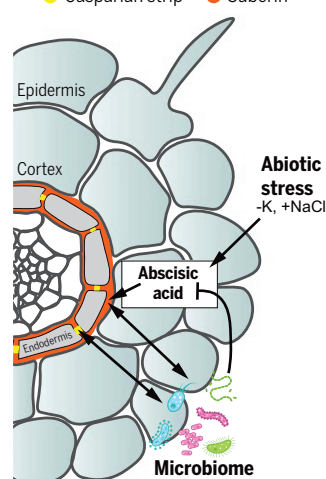
Cite this article as: I. Salas-González et al., *Science* 371, eabd0695 (2021). DOI: 10.1126/science.abd0695

**READ THE FULL ARTICLE AT**  
<https://doi.org/10.1126/science.abd0695>

## A Arabidopsis root cross section

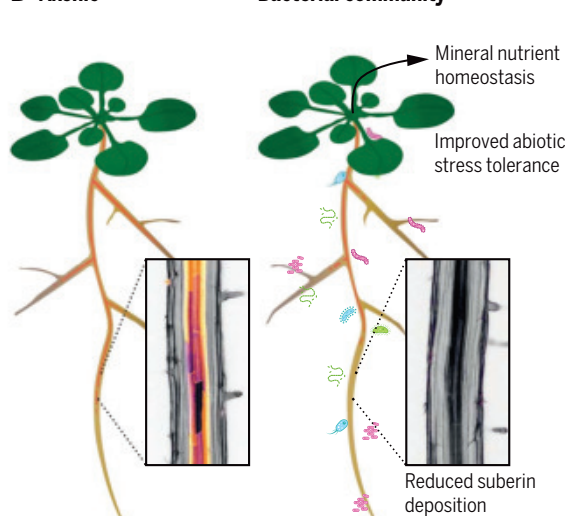
Endodermal barriers:

● Casparian strip ● Suberin



## B Axenic

## Bacterial community



**The microbiota influences root diffusion barriers.** (A) Model showing the interplay between the microbiota and root diffusion barriers. Microbes influence Casparian strip synthesis and co-opt plant-based abscisic acid signaling to control endodermal suberization. (B) Schematic representation of suberin accumulation in plants grown under axenic conditions or with the root microbiota. Root-inhabiting microbes reduce endodermal suberization optimizing mineral nutrient homeostasis and abiotic stress responses in the plant.

## RESEARCH ARTICLE SUMMARY

## CELL BIOLOGY

## Tubulin glycylation controls axonemal dynein activity, flagellar beat, and male fertility

Sudarshan Gadadhar\*, Gonzalo Alvarez Viar†, Jan Niklas Hansen†, An Gong†, Aleksandr Kostarev, Côme Ialy-Radio, Sophie Leboucher, Marjorie Whitfield, Ahmed Ziyat, Aminata Touré, Luis Alvarez\*†, Gaia Pigino\*†, Carsten Janke\*

**INTRODUCTION:** Microtubules are key components of the eukaryotic cytoskeleton. Although they are involved in a wide variety of functions, microtubules are structurally highly similar across most cell types and organisms. It was suggested that a “tubulin code,” formed by combinations of tubulin posttranslational modifications, adapts individual microtubules to specific functions within living cells. However, clear-cut functional and mechanistic data verifying this concept are still scarce. Glycylation

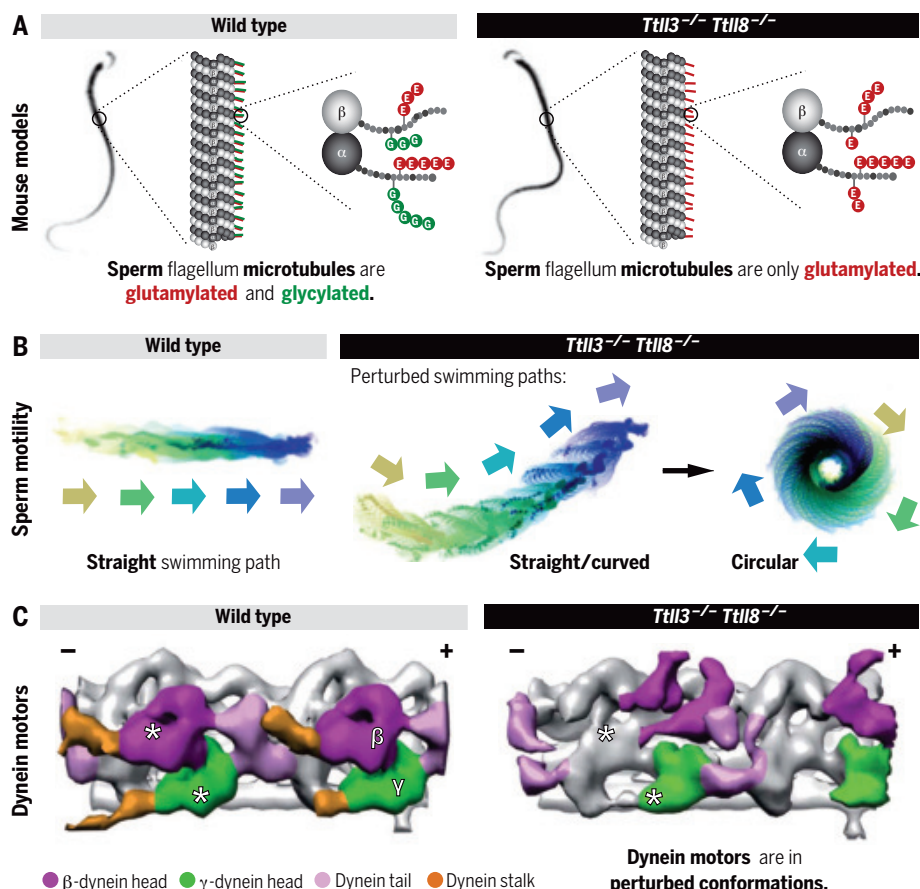
is among the least explored posttranslational modifications of tubulin and has, so far, exclusively been found on microtubules of cilia and flagella from a variety of species. Previous work has suggested that glycylation might be essential for cilia and flagella, but mechanistic insight remains lacking.

**RATIONALE:** Two enzymes from the tubulin-tyrosine ligase-like (TTL) family, TTL3 and TTL8, are essential to initiate glycylation

of tubulin in mammals. To entirely abolish glycylation at the organism level and to determine its physiological function, we generated a double-knockout mouse lacking both glycylation enzymes (*Ttl3*<sup>-/-</sup>*Ttl8*<sup>-/-</sup>). Inactivation of these two enzymes led to a lack of glycylation in all analyzed cilia and flagella. This allowed us to investigate the role of glycylation in the function of these organelles.

**RESULTS:** Despite the absence of glycylation in *Ttl3*<sup>-/-</sup>*Ttl8*<sup>-/-</sup> mice, no gross defects were observed at the organism and tissue levels. Motile ependymal cilia in brain ventricles as well as motile cilia in the respiratory tract were present and appeared normal. Sperm flagella were also assembled normally, and sperm were able to swim. However, in vitro fertility assays showed that male *Ttl3*<sup>-/-</sup>*Ttl8*<sup>-/-</sup> mice were subfertile. Computer-assisted sperm analyses revealed motility defects of *Ttl3*<sup>-/-</sup>*Ttl8*<sup>-/-</sup> sperm. Further analyses showed that lack of glycylation leads to perturbed flagellar beat patterns, causing *Ttl3*<sup>-/-</sup>*Ttl8*<sup>-/-</sup> sperm to swim predominantly along circular paths. This is highly unusual for mammalian sperm and interferes with their ability to reach the oocyte for fertilization. To determine the molecular mechanisms underlying this aberrant flagellar beat, we used cryo-electron tomography. The three-dimensional structure of the 96-nm repeat of the *Ttl3*<sup>-/-</sup>*Ttl8*<sup>-/-</sup> sperm axoneme showed no aberrations in its overall assembly. By contrast, the structure of both outer and inner dynein arms (ODAs and IDAs) was perturbed in *Ttl3*<sup>-/-</sup>*Ttl8*<sup>-/-</sup> flagella. Classification analysis showed that the incidence and distribution of pre-powerstroke and post-powerstroke conformations of ODAs and IDAs were altered in *Ttl3*<sup>-/-</sup>*Ttl8*<sup>-/-</sup> sperm. These ultrastructural findings indicate that glycylation is required to efficiently control the dynein powerstroke cycle, which is essential for the generation of a physiological flagellar beat.

**CONCLUSION:** Our work shows that tubulin glycylation regulates the beat of mammalian flagella by modulating axonemal dynein motor activity. Lack of glycylation leads to perturbed sperm motility and male subfertility in mice. Considering that human sperm are more susceptible than mouse sperm to deficiencies in sperm motility, our findings imply that a perturbation of tubulin glycylation could underlie some forms of male infertility in humans. ■



**Tubulin glycylation controls sperm motility.** (A) Microtubules in sperm flagella are rich in tubulin posttranslational modifications. Mice deficient for the glycylation enzymes TTL3 and TTL8 lack glycylation. (B) Mammalian sperm swim in linear paths. In the absence of glycylation, abnormal, mostly circular swimming patterns are observed, which impede progressive swimming. (C) Absence of glycylation leads to perturbed distribution of axonemal dynein conformations in *Ttl3*<sup>-/-</sup>*Ttl8*<sup>-/-</sup> flagella, which impedes normal flagellar beating.

The list of author affiliations is available in the full article online.

\*Corresponding author. Email: carsten.janke@curie.fr (C.J.); sudarshan.gadadhar@curie.fr (S.G.); pigino@mpi-cbg.de (G.P.); luis.alvarez@caesar.de (L.A.)

†These authors contributed equally to this work.

Cite this article as S. Gadadhar et al., *Science* 371, eabd4914 (2021). DOI: 10.1126/science.abd4914

**S** **READ THE FULL ARTICLE AT**  
<https://doi.org/10.1126/science.abd4914>



## RESEARCH ARTICLES

## MULTIPLE SCLEROSIS

## A noninflammatory mRNA vaccine for treatment of experimental autoimmune encephalomyelitis

Christina Krienke<sup>1,2</sup>, Laura Kolb<sup>1\*</sup>, Elif Diken<sup>1\*</sup>, Michael Streuber<sup>1</sup>, Sarah Kirchhoff<sup>1</sup>, Thomas Bukur<sup>1</sup>, Özlem Akilli-Öztürk<sup>1</sup>, Lena M. Kranz<sup>3</sup>, Hendrik Berger<sup>3</sup>, Jutta Petschenka<sup>1,4</sup>, Mustafa Diken<sup>1,3</sup>, Sebastian Kreiter<sup>1,3</sup>, Nir Yogeve<sup>5,6</sup>, Ari Waisman<sup>2,5</sup>, Katalin Karikó<sup>3</sup>, Özlem Türeci<sup>3,7</sup>, Ugur Sahin<sup>1,2,3†</sup>

The ability to control autoreactive T cells without inducing systemic immune suppression is the major goal for treatment of autoimmune diseases. The key challenge is the safe and efficient delivery of pharmaceutically well-defined antigens in a noninflammatory context. Here, we show that systemic delivery of nanoparticle-formulated 1-methylpseudouridine-modified messenger RNA (m1Ψ mRNA) coding for disease-related autoantigens results in antigen presentation on splenic CD11c<sup>+</sup> antigen-presenting cells in the absence of costimulatory signals. In several mouse models of multiple sclerosis, the disease is suppressed by treatment with such m1Ψ mRNA. The treatment effect is associated with a reduction of effector T cells and the development of regulatory T cell (T<sub>reg</sub> cell) populations. Notably, these T<sub>reg</sub> cells execute strong bystander immunosuppression and thus improve disease induced by cognate and noncognate autoantigens.

**A**ntigen-specific tolerization for the treatment of autoimmune diseases may selectively blunt autoimmunity without compromising normal immune function. In the past decades, various approaches have been studied, including delivery of autoimmune antigens using DNA, synthetic peptides, recombinant proteins, coated nanoparticles, or immunomodulatory cellular therapies [reviewed in (1)]. However, clinical translation remained elusive, with largely negative or inconclusive outcomes in human studies, and only a few approaches are in early clinical testing. One impediment is the polyclonal complexity of autoimmune diseases driven by distinctive, diverse autoreactive immune cell repertoires of patients. The interindividual variability requires either personalized treatment tailored for the autoantigenic immune profiles of the patients or therapies that mediate bystander tolerance to suppress both cognate and noncognate autoimmune lymphocytes without broad immune suppression (2).

The physiological induction and maintenance of peripheral tolerance is based on the presentation of self-antigens by lymphoid antigen-presenting cells (APCs) with low-level surface expression of costimulatory molecules, such as CD86. We sought to develop a therapeutic approach that would emulate natural mechanisms of immune tolerance. We recently introduced a liposomal formulation for systemic delivery of mRNA-encoded vaccine antigens (mRNA-LPX) into lymphoid tissue-resident CD11c<sup>+</sup> APCs (3). mRNA vaccination induces strong type 1 T helper (T<sub>H</sub>1) cell responses driven by high levels of interferon-α (IFN-α), released from APCs upon Toll-like receptor (TLR) signaling (3). Replacement of uridine (U) by incorporation of 1-methylpseudouridine (m1Ψ) during in vitro transcription and subsequent removal of double-stranded mRNA contaminants is known to abrogate TLR7-triggering activity and to reduce inflammatory properties of single-stranded mRNA (4–6). We hypothesized that the use of such nucleoside-modified, purified mRNA (m1Ψ mRNA) for in vivo delivery of autoimmune disease target antigens into CD11c<sup>+</sup> APCs in a noninflammatory context would enable systemic tolerogenic antigen presentation in lymphoid tissues.

#### Noninflammatory delivery of antigen-encoding m1Ψ mRNA into the spleen expands antigen-specific CD4<sup>+</sup> regulatory T cells

To test this hypothesis, we engineered nanoparticle-formulated mRNA-LPX (herein referred to as mRNA) consisting of nonimmunogenic (m1Ψ) or immunogenic (U) mRNA complexed with liposomes that lack inherent adjuvant activity. In a first experiment, mRNA coding for the reporter gene firefly luciferase

(LUC) or saline as control was administered intravenously into albino C57BL/6 mice, and the translation and expression of the LUC protein was assessed.

In line with previous reports, administration of U mRNA led to strong activation of CD11c<sup>+</sup> APCs and lymphocytes, and secretion of high levels of IFN-α (Fig. 1, A to C, and fig. S1, A and B). By contrast, we did not observe secretion of IFN-α or other inflammatory cytokines or significant activation of CD11c<sup>+</sup> APCs, CD8<sup>+</sup> and CD4<sup>+</sup> T cells, or natural killer (NK) and B cells in m1Ψ mRNA-treated mice (Fig. 1, A to C, and fig. S1, A and B). Notably, translation of LUC was profoundly higher and prolonged in m1Ψ mRNA-treated animals (Fig. 1, D and E). These findings suggest that m1Ψ mRNA is suitable for noninflammatory delivery of proteins into splenic CD11c<sup>+</sup> APCs.

To study the effects of m1Ψ mRNA in an autoimmune disease, we chose experimental autoimmune encephalomyelitis (EAE), a clinically relevant mouse model of multiple sclerosis (MS), in which we previously demonstrated tolerance induction by selectively expressing MOG<sub>35–55</sub>, the epitope of myelin oligodendrocyte glycoprotein, in dendritic cells (DCs) (7). We assessed the effect of antigen-encoding m1Ψ mRNA treatment on T cell expansion. Naïve Thy1.2<sup>+</sup> C57BL/6 mice were immunized with MOG<sub>35–55</sub> m1Ψ or U mRNA, and the expansion of both endogenous T cells and adoptively transferred MOG<sub>35–55</sub>-T cell receptor transgenic Thy1.1<sup>+</sup> CD4<sup>+</sup> T cells from 2D2 mice (8) was assessed. Both MOG<sub>35–55</sub>-encoding mRNAs induced proliferation of adoptively transferred CD4<sup>+</sup> 2D2 T cell, with MOG<sub>35–55</sub> m1Ψ mRNA being superior (Fig. 1F). Similarly, endogenous MOG<sub>35–55</sub>-specific CD4<sup>+</sup> T cells in naïve mice were expanded by both MOG<sub>35–55</sub>-encoding mRNAs (Fig. 1G). However, the functional properties of the T cells induced with either of these mRNAs differed profoundly. MOG<sub>35–55</sub> m1Ψ mRNA treatment was capable of expanding or inducing de novo Foxp3<sup>+</sup> regulatory T cells (T<sub>reg</sub> cells) in both wild-type C57BL/6 and 2D2-Foxp3-eGFP transgenic mice (Fig. 1H and fig. S2A), whereas overall frequencies of CD4<sup>+</sup> Foxp3<sup>+</sup> T cells did not change (Fig. 1H). CD4<sup>+</sup> T cells from vaccinated 2D2 animals inhibited the in vitro proliferation of antigen-specific naïve CD4<sup>+</sup> T cells in a dose-dependent manner. By contrast, CD4<sup>+</sup> T cells of MOG<sub>35–55</sub> U mRNA or control-treated mice showed little to no suppressive activity (fig. S2B).

We studied the cytokine response profiles upon in vitro antigen restimulation and the phenotypes of expanded T cells in repetitive-vaccinated C57BL/6 mice in more detail. Whereas MOG<sub>35–55</sub> U mRNA-expanded T cells exhibited a functional T<sub>H</sub>1 effector profile with secretion of IFN-γ, tumor necrosis factor-α (TNFα), interleukin-6 (IL-6), granulocyte-macrophage colony-stimulating factor, and

<sup>1</sup>TRON – Translational Oncology at the University Medical Center of the Johannes Gutenberg University gGmbH, Freiligrathstr. 12, Mainz 55131, Germany. <sup>2</sup>Research Center for Immunotherapy (FZI), University Medical Center at the Johannes Gutenberg University, Langenbeckstr. 1, Mainz 55131, Germany. <sup>3</sup>Biopharmaceutical New Technologies (BioNTech) Corporation, An der Goldgrube 12, Mainz 55131, Germany. <sup>4</sup>Cancer Immunology and Immune Modulation, Boehringer Ingelheim Pharma GmbH & Co. KG, Birkendorfer Str. 65, 88397 Biberach an der Riss, Germany. <sup>5</sup>Institute for Molecular Medicine, University Medical Center of the Johannes Gutenberg University, Mainz 55131, Germany. <sup>6</sup>Clinic and Polyclinic for Dermatology and Venereology, University Hospital Cologne, Kerpenerstr. 62, Cologne 50937, Germany. <sup>7</sup>CI3 – Cluster for Individualized Immunointervention e.V., Hölderlinstraße 8, 55131 Mainz, Germany.

\*These authors contributed equally to this work.

†Corresponding author. Email: sahin@uni-mainz.de

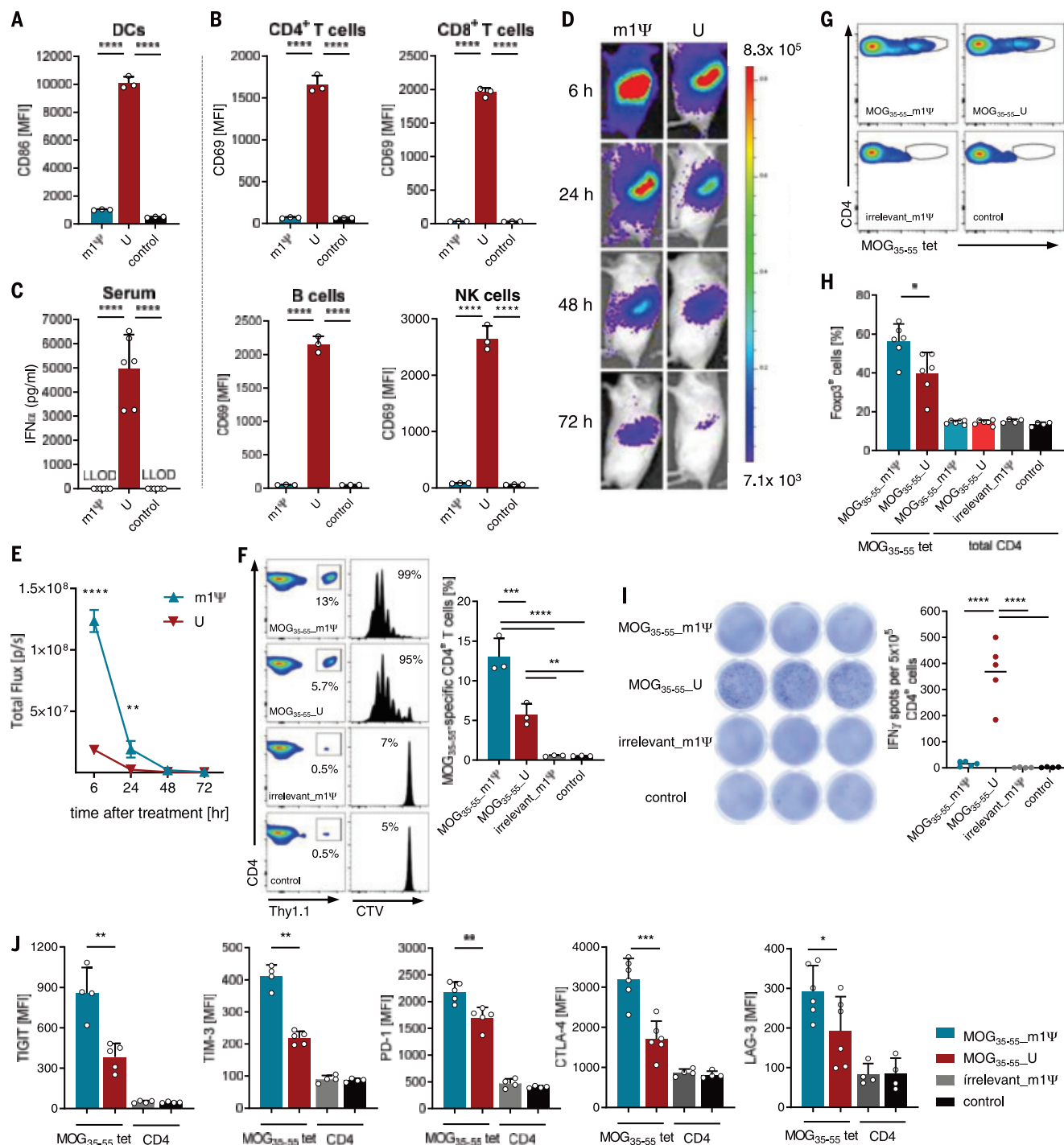


**Fig. 1. Antigen-encoding m1Ψ mRNA potentially expands antigen-specific CD4<sup>+</sup> T<sub>reg</sub> cells by noninflammatory delivery into the spleen.** (A and B) Activation of splenic immune cells 24 hours after ( $n = 3$ ) and (C) IFN- $\alpha$  serum levels 6 hours after intravenous injection of LPX-formulated mRNAs and saline (control) in C57BL/6 mice ( $n = 6$ ). (D and E) Bioluminescence imaging of albino C57BL/6 mice ( $n = 5$ ) after intravenous injection of m1Ψ or U LUC mRNA. Representative mice are shown. (F) Frequency and proliferation profiles of MOG<sub>35-55</sub>-specific CD4<sup>+</sup> T cells isolated from Thy1.1<sup>+</sup> 2D2 mice, cell trace violet (CTV)-labeled, and transferred into naïve Thy1.2<sup>+</sup> C57BL/6 recipient mice. Twenty-four hours after adoptive cell transfer, C57BL/6 mice were treated with mRNAs or saline (control). Mice were sacrificed on day 4, and spleens were analyzed for proliferating CD4<sup>+</sup> Thy1.1<sup>+</sup> cells ( $n = 3$ ). (G) Expansion of

endogenous MOG<sub>35-55</sub>-specific CD4<sup>+</sup> T cells and (H) frequency of splenic Foxp3<sup>+</sup> T<sub>reg</sub> cells ( $n = 6$ ) in C57BL/6 mice after treatment (days 0, 3, 7, and 10) with mRNA or saline (control) analyzed by MOG<sub>35-55</sub>-tetramer (tet) staining 3 days after last dosing ( $n = 4$  to 6). (I) CD4<sup>+</sup> T cells of mice from (G) tested for IFN- $\gamma$  secretion by enzyme-linked immune absorbent spot (ELISpot) upon restimulation with MOG<sub>35-55</sub> peptide ( $n = 4$  to 5). (J) Phenotype of tet<sup>+</sup> CD4<sup>+</sup> T cells of mice from (G). Data were compared by using one-way analysis of variance (ANOVA) and post hoc Tukey's test in (A) to (C), (F), and (I) or by unpaired two-tailed Student's  $t$  test in (H) and (J). Mean fluorescence intensity (MFI) of bulk CD4 T cells of control groups from (H) and (J) are depicted to show baseline expression levels. Error bars indicate mean  $\pm$  SD. \* $P \leq 0.05$ ; \*\* $P \leq 0.01$ ; \*\*\* $P \leq 0.001$ ; \*\*\*\* $P \leq 0.0001$ . LLOD, lower limit of detection.



IL-2 (Fig. 1I and fig. S3), splenic CD4<sup>+</sup> T cells from MOG<sub>35-55</sub> m1Ψ mRNA-treated mice did not secrete these proinflammatory cytokines, even when exposed to very high antigen concentrations. The only measurable factors were low levels of anti-inflammatory and T<sub>H</sub>2 type-associated cytokines such as IL-10, IL-5, and IL-13 (fig. S3). The T cell exhaustion markers TIGIT, TIM-3, PD-1, CTLA-4, and LAG-3 were strongly up-regulated on MOG<sub>35-55</sub> m1Ψ mRNA-expanded tetramer<sup>+</sup> T cells (Fig. 1J).

### Exposure to m1Ψ mRNA does not impair the capability to mount immune responses

CD11c<sup>+</sup> APCs of mice first exposed to m1Ψ mRNA and thereafter injected with U mRNA did not show any impairment in their ability to respond to this TLR-agonistic stimulus with up-regulation of costimulatory molecules and IFN-α secretion (Fig. 2, A and B). To investigate whether the induction and expansion of MOG<sub>35-55</sub>-specific CD4<sup>+</sup> T<sub>reg</sub> cells affects de novo priming of antigen-specific immune responses, we exploited two broadly used model systems. First, C57BL/6 mice underwent prime-boost (days 6 and 13) vaccination with U mRNA encoding the ovalbumin (OVA) epitope SIINFEKL and were concurrently exposed to MOG<sub>35-55</sub>-encoding m1Ψ mRNA (days 0, 3, 7, and 10). SIINFEKL-specific CD8<sup>+</sup> T cells were expanded above 40% of total blood CD8<sup>+</sup> T cells (Fig. 2C) and displayed properties of effector T (T<sub>eff</sub>) cells such as cognate IFN-γ secretion and highly potent and antigen-specific killing (Fig. 2, D and E), which suggested uncompromised T cell priming and expansion. In a second experiment, mice were immunized intramuscularly with a self-amplifying RNA (saRNA) vaccine encoding influenza hemagglutinin (HA) (day 6) concurrent to repeated treatment with MOG<sub>35-55</sub> m1Ψ mRNA or controls. Again, the capability of mice to mount a protective immune response and develop neutralizing antibodies was unimpaired (Fig. 2, F and G). Overall, both studies demonstrate that MOG<sub>35-55</sub> m1Ψ mRNA-induced antigen-specific CD4<sup>+</sup> T<sub>reg</sub> cells do not suppress functional immune responses against nonmyelin antigens.

### Treatment with antigen-encoding m1Ψ mRNA ameliorates EAE in mice

Next, we studied the tolerogenic potential of MOG<sub>35-55</sub> m1Ψ mRNA in C57BL/6 mice with MOG<sub>35-55</sub>-induced EAE. Treatment with MOG<sub>35-55</sub> m1Ψ mRNA was capable of blocking all clinical signs of EAE in mice (Fig. 3A), whereas control animals showed the typical course of the disease with rapid monophasic progression. In mice started on MOG<sub>35-55</sub> m1Ψ mRNA treatment when a paralysis of the tail or beginning of the hindlimbs were noted (disease score of 1 to 2 of EAE), further disease progression could be prevented, and motor

functions were restored (Fig. 3B and fig. S4A). This included occasional cases of reversion of paralysis, which was most likely attributable to an anti-inflammatory effect rather than tissue repair.

Various effects were observed in mice treated with antigen-encoding m1Ψ mRNA compared with control animals. In the brain and spinal cord, the total amount of infiltrating CD4<sup>+</sup> T cells, MOG<sub>35-55</sub>-specific CD4<sup>+</sup> T cells and subsets of CD4<sup>+</sup> T cells secreting IFN-γ and IL-17A were considerably lower (Fig. 3, C, D, and F, and figs. S4B and S5). Demyelination of the spinal cord was also considerably reduced (Fig. 3E). In the spleen of MOG<sub>35-55</sub> m1Ψ mRNA-treated animals, we observed an increase of lymphocytes (fig. S5), including MOG<sub>35-55</sub>-specific CD4<sup>+</sup> T cells with low CD62L, CCR6, and CCR7 expression, and up-regulation of CD69 (fig. S6). CCR6, CCR7, and CD62L are critical for access of T cells to the central nervous system (CNS) (9–12), and the transmembrane C-type lectin CD69 is known to promote lymphocyte retention in the spleen (13).

Next, we analyzed the autoantigen-specific CD4<sup>+</sup> T cells in those mice in which the manifestation of EAE was prevented by treatment with MOG<sub>35-55</sub> m1Ψ mRNA on days 7 and 10. MOG<sub>35-55</sub>-specific splenic CD4<sup>+</sup> T cells from treated animals showed down-regulation of the activation marker CD44 and strong expression of coinhibitory molecules (Fig. 3G). At the peak of disease (day 16 after disease induction), CD5, ICOS, LAG-3, PD-1, CTLA-4, TIGIT, and TIM-3 were up-regulated in tetramer<sup>+</sup> splenic CD4<sup>+</sup> T cells. Furthermore, we detected a highly activated T<sub>reg</sub> cell population (Fig. 3, H and I) and lower numbers of T<sub>H</sub>1 and T<sub>H</sub>17 MOG<sub>35-55</sub>-specific CD4<sup>+</sup> T cells (Fig. 3H). Similar findings in mice with symptomatic EAE (disease score of 1 to 2 at start of treatment) further confirmed the potent disease-suppressive activity of antigen-encoding m1Ψ mRNA (fig. S4).

We extended our study of the preventive and therapeutic effect of m1Ψ mRNA to other EAE mouse models. The SJL model is based on autoreactivity against the PLP<sub>139-151</sub> epitope and is characterized by recurring EAE symptoms resulting in a relapsing-remitting disease, similar to the clinical presentation of MS in patients. Treatment of SJL mice with PLP<sub>139-151</sub> m1Ψ mRNA twice a week starting from day 7 after EAE induction resulted in almost full disease control (fig. S7A). Even when the mice were treated after the first disease peak (starting on day 14 after disease induction), progression of the disease was halted (fig. S7B).

### Treatment with m1Ψ mRNA leads to therapeutically effective bystander tolerance

In another experimental setup, we addressed a key challenge in human MS, namely that antigen spread leads to a complex antimyelin autoreactivity pattern and the specificity of

autoreactive T cell clones in individual patients, and thus, the potential targets for direct antigen-specific tolerization is unknown. A clinically viable approach would be to use bystander tolerance by inducing T<sub>reg</sub> cells, which, once activated by their cognate antigen, would suppress T cells against other antigens in the inflamed tissue.

We evaluated bystander activity in two experimental settings. F1 C57BL/6 x SJL mice with PLP<sub>139-151</sub> peptide-induced EAE were vaccinated with m1Ψ mRNA encoding either PLP<sub>139-151</sub> (the disease-causing autoantigen), MOG<sub>35-55</sub> (unrelated autoantigen, against which m1Ψ mRNA is capable of inducing potent effector T<sub>reg</sub> cells), or irrelevant m1Ψ mRNA (Fig. 4A and fig. S7C). MOG<sub>35-55</sub> m1Ψ mRNA treatment showed a dose-dependent therapeutic effect on EAE, similar to the curative effect mediated by vaccination with PLP<sub>139-151</sub> m1Ψ mRNA, indicating a strong T<sub>reg</sub> cell-mediated bystander suppression, also given the fact that antigen spread has been described for this particular EAE model (14). Antigen-specific T<sub>reg</sub> cells were notably expanded and highly activated, constituting >80% of de novo expanded MOG<sub>35-55</sub>-specific CD4<sup>+</sup> splenic T cells (Fig. 4, B and C). T<sub>eff</sub> cell infiltration into the brain and spinal cord in m1Ψ mRNA-treated mice was reduced (Fig. 4, D to F), and no signs of demyelination in the spinal cord were detected (Fig. 4G).

We also investigated a complex EAE model driven by multiple pathogenic autoreactive T cell clones against MOG<sub>35-55</sub>, PLP<sub>139-151</sub>, PLP<sub>178-191</sub>, MBP<sub>84-104</sub>, and MOBP<sub>15-36</sub>, which could be successfully treated with the mixture of m1Ψ mRNAs coding for the corresponding four disease-inducing autoantigenic epitopes. m1Ψ mRNA encoding MOG<sub>35-55</sub> were therapeutically almost as effective as those encoding the cocktail of all four disease targets. This suggests that even polyclonal autoimmune disease driven by a broad autoreactive T cell repertoire can be sufficiently controlled by m1Ψ mRNA targeting a strong bystander tolerance-mediating T cell epitope (fig. S7D).

One potential risk associated with antigen-specific tolerization is the induction of autoantibodies against respective targets, which can exacerbate disease (15). Moreover, nucleoside-modified mRNA is known to be highly immunogenic and to induce high antibody titers when formulated with immune stimulatory lipid nanoparticles (16). We therefore analyzed anti-MOG<sub>35-55</sub> immunoglobulin G (IgG) antibody responses in the sera of EAE mice upon m1Ψ mRNA vaccination. First, we measured anti-MOG<sub>35-55</sub> levels in sera of MOG<sub>35-55</sub> peptide-induced EAE (C57BL/6 mice), which were vaccinated with MOG<sub>35-55</sub> m1Ψ mRNA on days 7 and 10 after EAE induction. Anti-MOG<sub>35-55</sub> IgG levels were not elevated in comparison with those of control animals treated

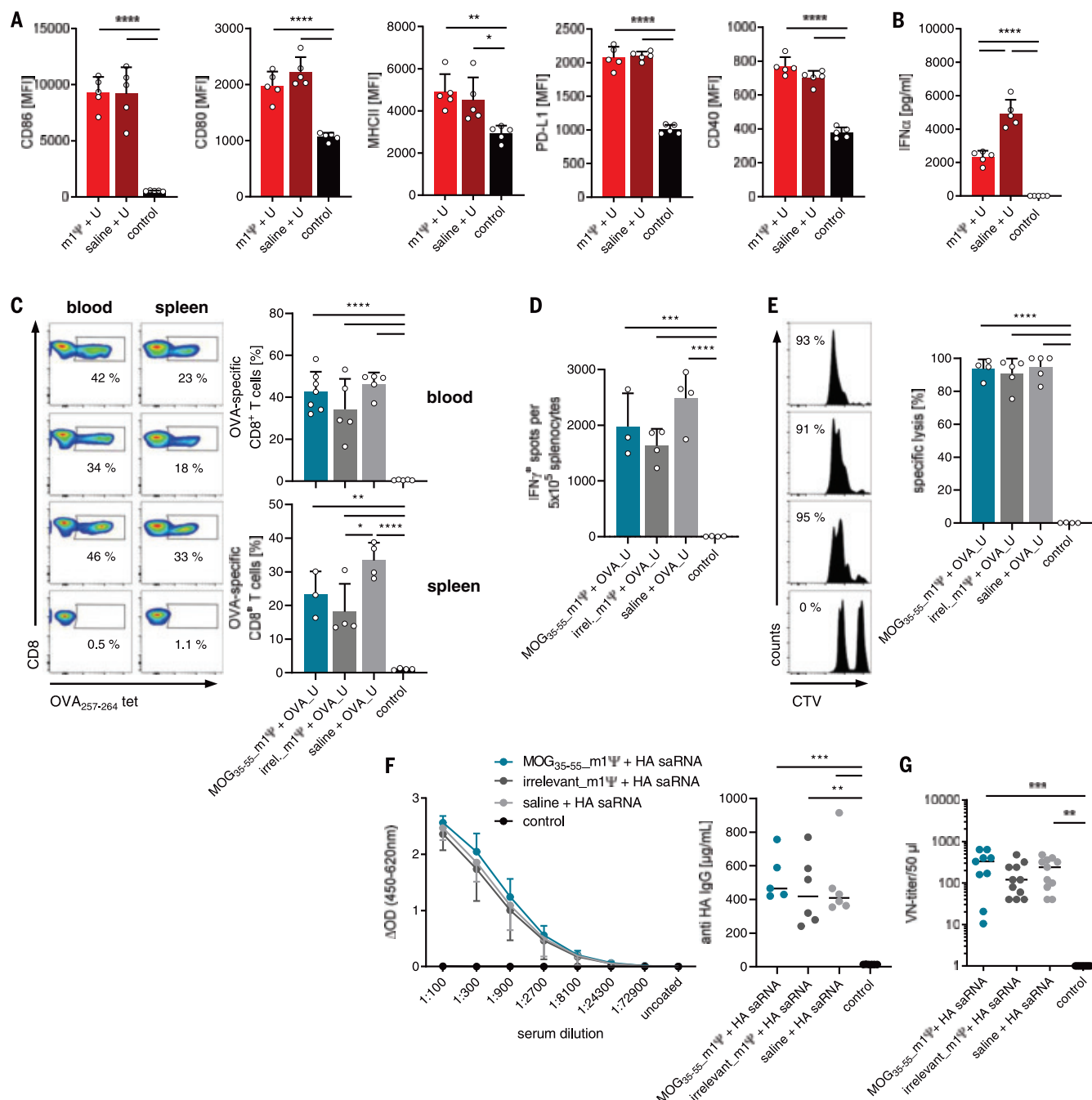


**Fig. 2. Exposure to m1Ψ mRNA does not impair the capability to mount immune responses.** (A) Activation of splenic CD11c<sup>+</sup> APCs 24 hours after ( $n = 3$ ) and (B) IFN-α serum levels 6 hours after intravenous injection (day 3) of LPX-formulated U mRNA or saline (control) in C57BL/6 mice ( $n = 6$ ), which were pretreated with m1Ψ mRNA or saline (control) at day 0. MHCII, major histocompatibility complex II. (C to E) De novo priming of SIINFEKL-specific CD8<sup>+</sup> T cells in C57BL/6 mice with prior exposure to MOG<sub>35-55</sub> or irrelevant m1Ψ mRNA or saline (days 0, 3, 7, and 10) to SIINFEKL U mRNA prime-boost vaccination (days 6 and 13). Controls only received saline. (C) Frequency of SIINFEKL-specific CD8<sup>+</sup> T cells (OVA<sub>257-264</sub> tet) in blood ( $n = 5$  to 7) and spleen ( $n = 3$  to 4). (D) IFN-γ secretion was measured by ELISpot upon restimulation of total splenocytes of mice from (C) ( $n = 3$  to 4) with SIINFEKL peptide and (E) in vivo antigen-specific killing of adoptively transferred CTV-labeled and peptide-loaded splenocytes of naive mice ( $n = 4$  to 5). For in vivo cytotoxicity

assays, mice were adoptively transferred on day 18 with 0.5 μM (low) or 5 μM (high) CTV-labeled naive splenocytes pulsed with peptide (6 μg/ml). Of these target cells,  $1.5 \times 10^6$  cells were adoptively transferred into immunized and control recipients at a ratio of 1:1 (irrelevant HA<sub>518-526</sub> peptide-loaded CTV<sub>low</sub>; SIINFEKL peptide-loaded CTV<sub>high</sub>). Recipient splenocytes were recovered and analyzed by flow cytometry 18 hours after transfer, and antigen-specific lysis was determined as follows: specific lysis (%) =  $[1 - (\text{percentage of cells pulsed with SIINFEKL} / \text{percentage of cells pulsed with HA}) \times 100]$ . (F) Total ( $n = 5$  to 6) and (G) neutralizing ( $n = 9$  to 11) anti-HA IgG in C57BL/6 mice with prior exposure to MOG<sub>35-55</sub> or irrelevant m1Ψ mRNA or saline (days 0, 3, 7, and 10). Controls only received saline. Protective immune responses were measured 28 days after mice were immunized with influenza HA-saRNA (1 μg intramuscularly) on day 6. Data were compared by using one-way ANOVA and post hoc Tukey's test. Error bars, mean ± SD. ΔOD, change in optical density; VN, virus neutralizing.



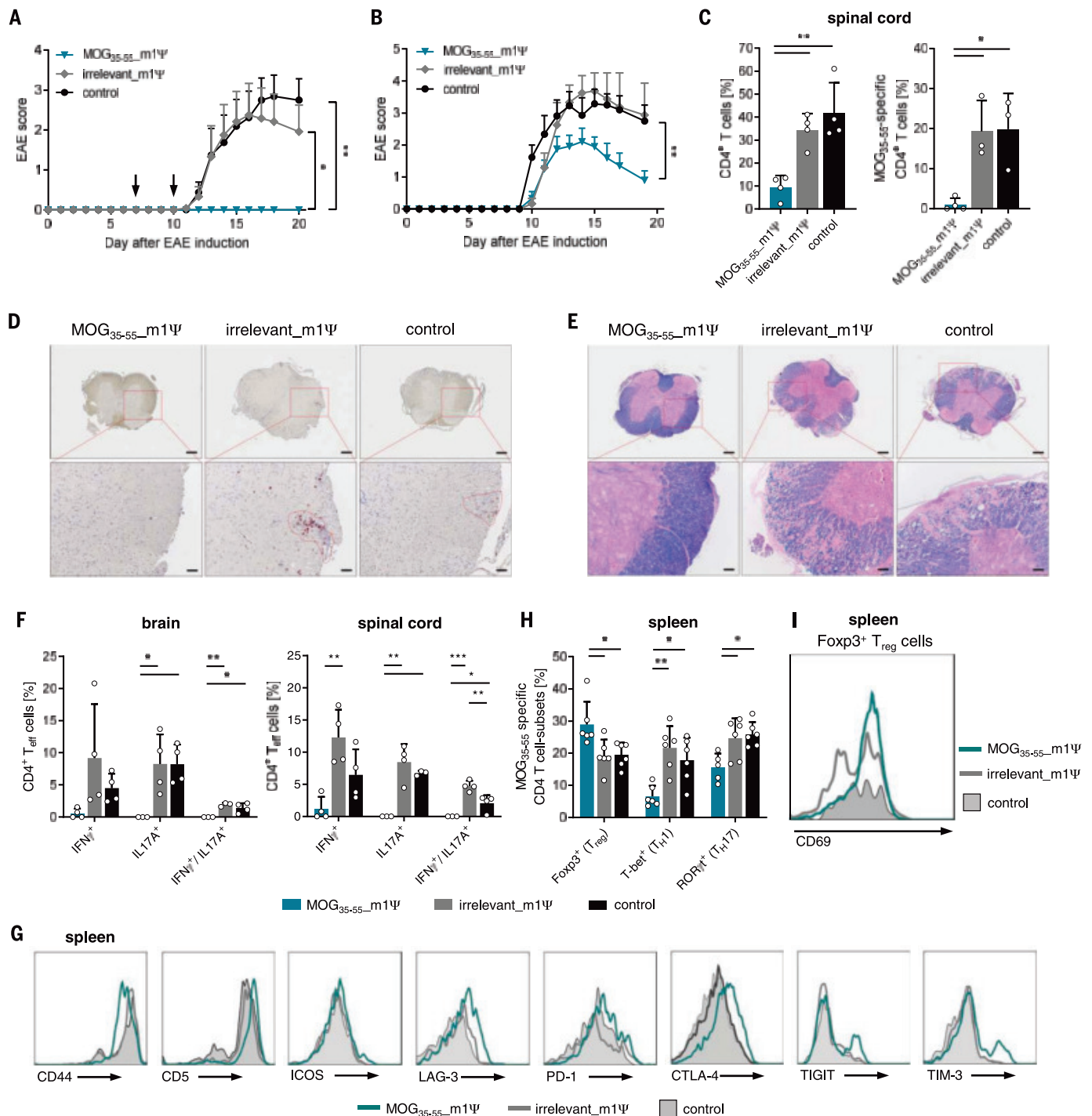


**Fig. 3. Treatment with antigen-encoding m1Ψ mRNA ameliorates EAE in mice.** (A and B) Disease severity in MOG<sub>35-55</sub>-induced EAE ( $n = 6$  to  $8$  C57BL/6 mice per group) treated with m1Ψ mRNA or saline (control) (A) on days 7 and 10 after disease induction or (B) when disease progressed to a score of 1 to 2. (C) Frequency of CD4<sup>+</sup> T cell and MOG<sub>35-55</sub>-specific CD4<sup>+</sup> T cells in the spinal cord of mice treated on days 7 and 10 after disease induction ( $n = 3$  to  $4$ ). Thy1.1<sup>+</sup> 2D2 CD4<sup>+</sup> T cells were transferred 1 day before EAE induction into Thy1.2<sup>+</sup> recipient mice and analyzed in the target organs on day 16 after disease induction. (D) Representative CD4 staining in the spinal cord of EAE mice treated with m1Ψ mRNAs or saline (control) ( $n = 3$ ) on days 7 and 10 after disease induction and analyzed at day 16 after EAE induction. (E) Representative Luxol fast blue (LFB) staining revealing areas of demyelination

in the spinal cord of mice from (D) ( $n = 3$ ). (F to I) Frequency of CD4<sup>+</sup> IFN- $\gamma$ - and IL-17A-secreting cells in brain and spinal cord ( $n = 3$  to  $4$ ) (F) and flow cytometry analysis of splenic tetramer<sup>+</sup> CD4<sup>+</sup> T cells ( $n = 4$  to  $6$ ) [(G) to (I)] of EAE mice treated with m1Ψ mRNAs or saline (control) on days 7 and 10 after disease induction and analyzed at day 16 after EAE induction. Area under the curve (AUC) was used to determine statistical significance through one-way ANOVA and Tukey's multiple comparison test of the different EAE disease development curves in (A) and (B). Data were compared by using one-way ANOVA and post hoc Tukey's test in (F) and (H). Error bars indicate mean  $\pm$  SEM in (A) and (B) or mean  $\pm$  SD in (C), (F), and (H). The scale bar in the upper row of (D) and (E) represents 200  $\mu$ m and, in the lower row of (D) and (E), represents 50  $\mu$ m.

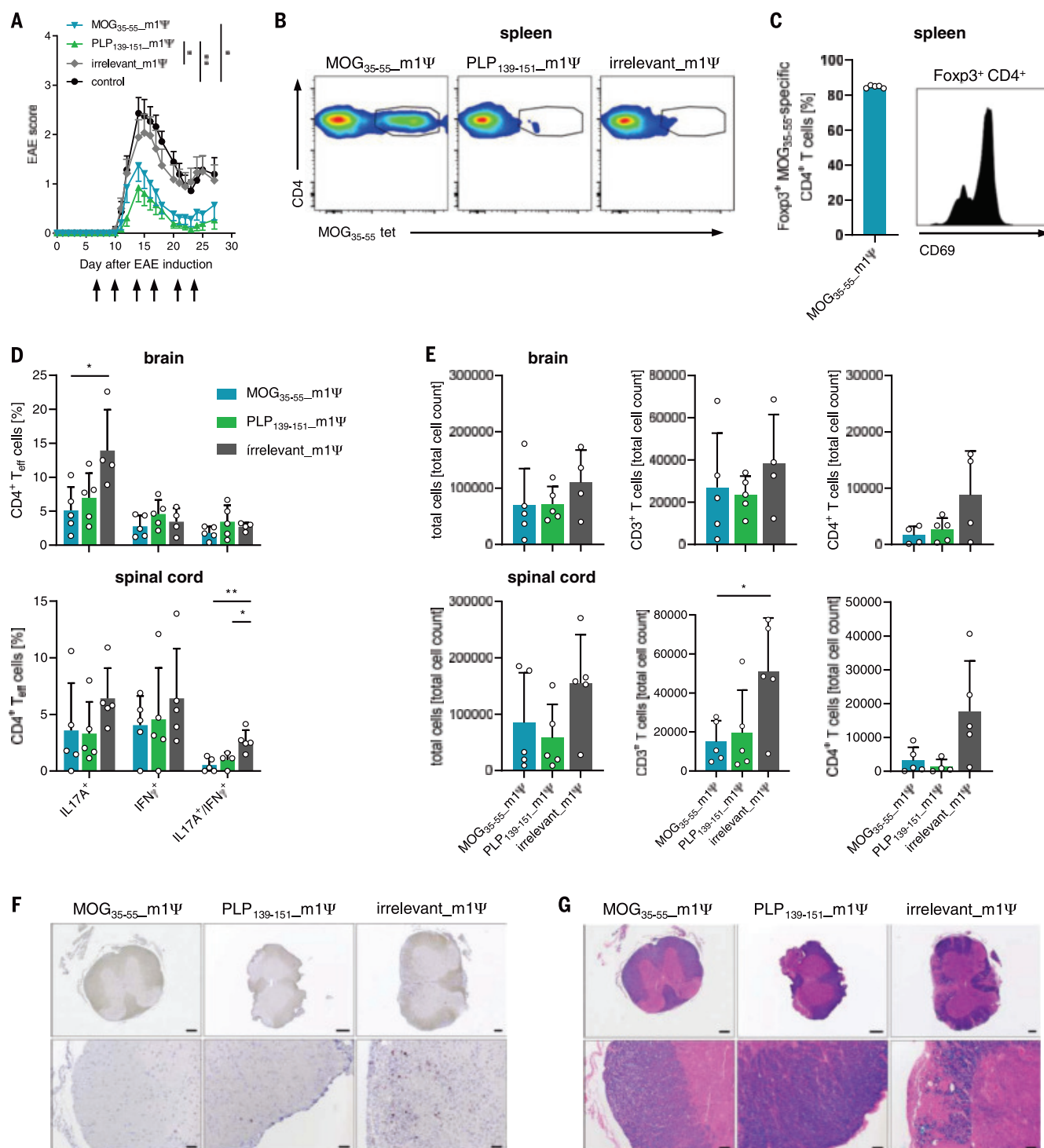


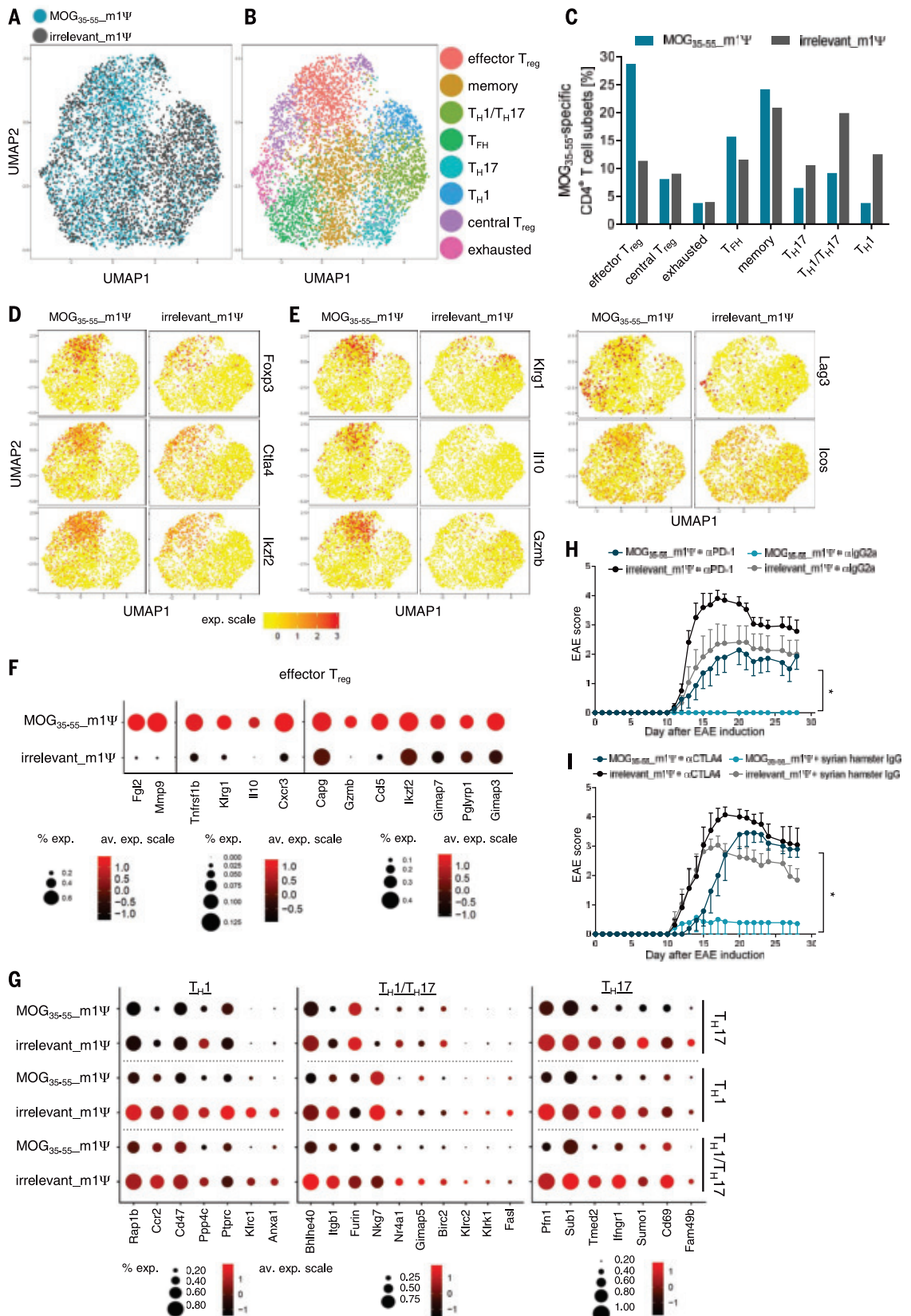
**Fig. 4. Treatment with m1Ψ mRNA leads to therapeutically effective bystander tolerance.** (A) Dynamics of EAE in PLP<sub>139-151</sub>-induced EAE mice (n = 13 to 15 F1 C57BL/6 x SJL mice) upon treatment with MOG<sub>35-55</sub> m1Ψ, PLP<sub>139-151</sub> m1Ψ, irrelevant m1Ψ mRNA, or saline (control) twice per week starting on days 7 and 10 after disease induction with 40 μg of m1Ψ mRNA. (B and C) Expansion of endogenous MOG<sub>35-55</sub>-specific CD4<sup>+</sup> T cells (B) and frequency of Tetramer<sup>+</sup> Fopx3<sup>+</sup> T<sub>reg</sub> cells and analysis of CD69 expression on respective cell population (C) upon treatment with m1Ψ mRNA measured in the spleen on day 28 after EAE induction (n = 5). (D) Frequency of CD4<sup>+</sup> IFN-γ- and IL-17A-secreting cells upon PLP<sub>139-151</sub>-peptide restimulation and (E) total cell count of

lymphocytes in brain and spinal cord of EAE mice treated with different m1Ψ mRNAs (n = 4 to 5) and analyzed on day 28 after EAE induction. (F) Representative CD4 staining in the spinal cord of EAE mice from (A) (n = 2). (G) Representative LFB staining revealing areas of demyelination in the spinal cord of mice from (A) (n = 2). AUC was used to determine statistical significance through one-way ANOVA and Tukey's multiple comparison test of the different EAE disease development curves (A). Data were compared by using one-way ANOVA and post hoc Tukey's test. Error bars indicate mean ± SEM in (A) or mean ± SD in (C) to (E). The scale bar in the upper row of (F) and (G) represents 200 μm and, in the lower row of (F) and (G), represents 50 μm.

**Fig. 5. Distinct splenic antigen-specific CD4<sup>+</sup> T cell subsets are expanded in EAE mice treated with antigen-encoding m1Ψ mRNA.** (A to G) MOG<sub>35-55</sub>-specific CD4<sup>+</sup> T cells isolated from mice with MOG<sub>35-55</sub>-induced EAE treated with m1Ψ mRNA on days 7 and 10 after disease induction and analyzed by single-cell RNA sequencing on day 15 or day 16, respectively.

(A) A two-dimensional uniform manifold approximation and projection (UMAP) projection of MOG<sub>35-55</sub>-specific CD4<sup>+</sup> T cells isolated from different treatment groups (each dot represents one cell) identified by unsupervised clustering. (B) UMAP projection of single cells, color-coded according to the identified cell subsets. (C) Frequency of different cell subsets. (D) and (E) depict a UMAP projection of classical T<sub>reg</sub> cell markers (D) and effector T<sub>reg</sub> cell markers (E). (F) Genes up-regulated in an effector T<sub>reg</sub> subpopulation upon MOG<sub>35-55</sub> m1Ψ mRNA treatment (adjusted *P* value < 0.05).

(G) Genes down-regulated upon MOG<sub>35-55</sub> m1Ψ mRNA treatment in T<sub>H</sub>1, T<sub>H</sub>17, and T<sub>H</sub>1/T<sub>H</sub>17 cell subsets (adjusted *P* value < 0.05). (H and I) MOG<sub>35-55</sub>-induced EAE in C57BL/6 mice (*n* = 8 per group) treated with m1Ψ mRNA on days 7 and 10 after disease induction in combination with (H), anti-PD-1, and (I) anti-CTLA-4 blocking antibodies or isotype controls administered twice per week. Statistical significance of AUC differences of EAE disease development curves was assessed by using one-way ANOVA and Tukey's multiple comparison test in (H) and (I). Error bars represent mean ± SEM in (H) and (I).





with irrelevant m1Ψ mRNA or saline (fig. S8A). This suggests that m1Ψ mRNA application does not exacerbate preformed autoantibody responses. Even after repetitive MOG<sub>35-55</sub> m1Ψ mRNA challenge (twice per week, 12 times in total) of F1 C57BL/6 x SJL mice, no anti-MOG<sub>35-55</sub> IgG antibodies were detected in those where EAE was induced with PLP<sub>139-151</sub>-peptide immunization (fig. S8B).

### Distinct antigen-specific CD4<sup>+</sup> T cell subsets are expanded in EAE mice treated with antigen-encoding m1Ψ mRNA

Next, we characterized the tolerized T cells by subjecting splenic tetramer<sup>+</sup> CD4<sup>+</sup> T cells from animals treated with MOG<sub>35-55</sub> m1Ψ mRNA or irrelevant m1Ψ mRNA to single-cell RNA sequencing (table S1). Clustering analysis revealed eight distinct antigen-specific CD4<sup>+</sup> T cell subsets in EAE mice (Fig. 5, A and B, and fig. S9). The CD4<sup>+</sup> T cell identity of all subsets was confirmed with canonical T cell markers (fig. S10). We used sets of genes characterizing different functional T cell subphenotypes for further analysis (figs. S11 and S12). We identified two distinct populations sharing common T<sub>reg</sub> cell markers (*Foxp3*, *Il27*, and *Ctla4*). One of these subpopulations displayed typical effector T<sub>reg</sub> cell markers (*Klrg1*, *Il10*, *Gzmb*, *Lag3*, and *Icos*), whereas the other subset were central T<sub>reg</sub> cells as defined by markers *Sell* and *Bcl2* and low expression of the common effector-associated molecules (*I7*, *I8*) (figs. S11, A and B, and S13A). We also identified T<sub>H1</sub> (*Ifnγ* and *Tbx21*), T<sub>H17</sub> (*Il17a*/f and *Tmem176a/b*), and T<sub>H1</sub>/T<sub>H17</sub> cells with combined expression of T<sub>H1</sub> and T<sub>H17</sub> markers (*Csf2*, *Tbx21*, *Ifnγ*, and *Il17a*). Moreover, we found exhausted antigen-specific T cells (*Lag3* and *Cd160*), T follicular helper (T<sub>FH</sub>) cells (*Il4*, *Il21*, and *Cxcr5*), and a T cell cluster with a memory phenotype (*Ccr7*<sup>high</sup> and *Tcf7*<sup>high</sup>) (figs. S11, C to H, and S13, B and C).

The relative frequencies of these antigen-specific CD4<sup>+</sup> T cell subpopulations changed in EAE mice treated with antigen-encoding m1Ψ mRNA. Most notably, in animals treated with MOG<sub>35-55</sub> m1Ψ mRNA, the effector T<sub>reg</sub> cells constituted the largest cluster by frequency and cell count (Fig. 5C). The T<sub>H1</sub>, T<sub>H17</sub>, and T<sub>H1</sub>/T<sub>H17</sub> T<sub>eff</sub> cell subpopulations were strongly reduced in comparison with those of control animals treated with irrelevant m1Ψ mRNA, whereas exhausted T cell and central T<sub>reg</sub> cell subpopulations were of similar size in both groups (Fig. 5C). We also found substantial differences in the expression levels of functionally relevant genes and activation markers. Common T<sub>reg</sub> cell markers such as *Foxp3*, *Il27*, and *Ctla4* were present in T<sub>reg</sub> cell subpopulations of both treatment groups (Fig. 5D), whereas transcripts characteristic for effector T<sub>reg</sub> cells and associated with T<sub>reg</sub> cell suppressive function, such as *Klrg1*, *Il10*,

*Gzmb*, *Lag3*, and *Icos*, were enriched in MOG<sub>35-55</sub> m1Ψ mRNA-treated EAE mice and almost completely absent in those treated with irrelevant m1Ψ mRNA (Fig. 5, E and F). Likewise, the transcript profiles of the T<sub>H1</sub>, T<sub>H17</sub>, and T<sub>H1</sub>/T<sub>H17</sub> T<sub>eff</sub> cell clusters differed considerably between the two treatment groups (Fig. 5G and fig. S14A). The most prominent examples of differentially regulated genes were those involved in differentiation (*Anxa1*, *Ppp4c*, and *Mid1*) (19–21), migration (*Ccr2*, *Itgb1*, *Wdr26*, and *Rap1b*) (22–26) or cytokine production of T<sub>eff</sub> cells (*Bhlhe40*) (27). In accordance with a previous study (28), we detected mainly down-regulation of genes associated with cell cycle and cell division in the mice treated with MOG<sub>35-55</sub> m1Ψ mRNA (fig. S14B). The number of genes up-regulated in T<sub>H1</sub>, T<sub>H17</sub>, and T<sub>H1</sub>/T<sub>H17</sub> T<sub>eff</sub> cell subpopulations from MOG<sub>35-55</sub> m1Ψ mRNA-treated mice was small (fig. S14A).

To visualize the relationships between the identified major cell populations, we performed single-cell trajectory analysis (fig. S15). Each state represents subpopulation structures of closely related transitory cellular states. T cells from mice treated with irrelevant m1Ψ mRNA appeared mainly as fully differentiated cells in state 5, representing T<sub>H1</sub>, T<sub>H17</sub>, and T<sub>H1</sub>/T<sub>H17</sub> T<sub>eff</sub> cells (fig. S15, B, D, and F). By contrast, T cells from the MOG<sub>35-55</sub> m1Ψ mRNA-treated group were in state 1 (memory) or mainly differentiated in state 2, representing effector T<sub>reg</sub> cells and T<sub>FH</sub> cells (fig. S15, B, C, and F). In sum, these findings indicate that m1Ψ mRNA treatment rather than deleting autoreactive T cells tips the immunological balance in favor of suppression of disease promoting MOG<sub>35-55</sub>-specific T<sub>H1</sub>, T<sub>H17</sub>, and T<sub>H1</sub>/T<sub>H17</sub> T<sub>eff</sub> cells by expanding effector T<sub>reg</sub> cells.

### PD-1 and CTLA-4 signaling contribute to the induction and maintenance of antigen-specific tolerance

Expression of coinhibitory receptors such as CTLA-4 and PD-1 on effector and T<sub>reg</sub> cells is a key mechanism of immune homeostasis. We therefore assessed the mechanistic contribution of these pathways to antigen-specific tolerance mediated by m1Ψ mRNA. Treatment of EAE mice with MOG<sub>35-55</sub> m1Ψ mRNA combined with anti-PD-1 or anti-CTLA-4 antibody on days 7 and 10 after EAE induction aggravated the disease in control groups in accordance with the known unleashing effect of checkpoint blockade on autoreactive T cells (29). Both CTLA-4 and PD-1 blockade almost completely abolished the EAE-protective effect of MOG<sub>35-55</sub> m1Ψ mRNA (Fig. 5, H and I). Flow cytometry and single-cell RNA sequencing revealed almost exclusive and high expression of *Ctla4* by MOG<sub>35-55</sub>-specific CD4<sup>+</sup> T<sub>reg</sub> cells (fig. S16, A and B), which supports a role of this population for mediating tolerance. The effect of PD-1 blockade may be driven by two inde-

pendent mechanisms, one being invigoration of preexistent T<sub>eff</sub> cells and the other being the inhibition of the de novo induction of antigen-specific T<sub>reg</sub> cells, which also depends crucially on PD-1 signaling (30). These findings suggest that disease-mediating T cells are suppressed but not deleted in mice treated with antigen-encoding m1Ψ mRNA and that both PD-1 and CTLA-4 signaling critically contribute to the induction and maintenance of antigen-specific tolerance.

### Discussion

Our study describes nanoparticulate delivery of nucleoside-modified autoantigen-encoding mRNA into lymphoid CD11c<sup>+</sup> APCs as a therapeutic approach for antigen-specific tolerization. We show, at single-cell resolution, the generation of different antigen-specific CD4<sup>+</sup> T cell subpopulations with distinct functional states.

Selective delivery of autoantigens into CD11c<sup>+</sup> APCs resident in lymphoid tissues exploits a highly effective natural mechanism for induction and maintenance of peripheral tolerance. The presentation of autoantigens in a noninflammatory context leads to expansion of antigen-specific CTLA-4<sup>+</sup>, ICOS<sup>+</sup>, IL-10<sup>+</sup>, and Foxp3<sup>+</sup> effector T<sub>reg</sub> cells (31) that not only suppress antigen-specific autoreactive T<sub>eff</sub> cells but also exert bystander immunosuppression, thereby enabling disease control even in a complex, polyclonal model of autoimmunity.

Bystander activity of T<sub>reg</sub> cells has been associated with noncognate mechanisms depending on cell-cell interaction, such as secretion of suppressive factors, e.g., IL-10 and transforming growth factor-β (TGF-β) (32). Thus, one would expect that MOG-specific T<sub>reg</sub> cells activated upon reexposure to their cognate antigen in the CNS would suppress immune responses that occur at that very location for a defined period of time. Because of its temporo-spatial nature, T<sub>reg</sub> cell activity exerts tissue-specific immune regulation rather than pan-immune suppression (33). This is in line with prior studies indicating that T cell tolerance to tissue-restricted self-antigens is actively mediated by antigen-specific T<sub>reg</sub> cells rather than deletion (34).

With the presented approach, key challenges for clinical translation of antigen-based treatment of autoimmune diseases can be addressed. Both the nucleoside-modified, purified mRNA and the liposomal nanoparticle formulation are pharmaceutically well-defined clinical-stage compounds and are currently being explored in human trials for various disease indications (35). The repetitive administration of m1Ψ mRNA is not compromised by induction of autoantigen-specific antibody responses, which usually causes safety-limiting constraints for other applications. Production of mRNA pharmaceuticals is fast and cost-efficient, and virtually any autoantigen can be encoded by

mRNA. Thus, tailoring the treatment for the disease-causing antigens of individual patients is conceivable, similar to that which has been successfully executed in the setting of personalized cancer vaccines (36, 37). Combination of m1P mRNAs encoding either multiple personalized autoantigens or autoantigens that confer bystander tolerance may enable control of even complex autoimmune diseases.

## REFERENCES AND NOTES

1. P. Serra, P. Santamaria, *Nat. Biotechnol.* **37**, 238–251 (2019).
2. A. Miller, O. Lider, H. L. Weiner, *J. Exp. Med.* **174**, 791–798 (1991).
3. L. M. Kranz et al., *Nature* **534**, 396–401 (2016).
4. K. Karikó, M. Buckstein, H. Ni, D. Weissman, *Immunity* **23**, 165–175 (2005).
5. K. Karikó et al., *Mol. Ther.* **16**, 1833–1840 (2008).
6. K. Karikó, H. Muramatsu, J. Ludwig, D. Weissman, *Nucleic Acids Res.* **39**, e142 (2011).
7. N. Yogeve et al., *Immunity* **37**, 264–275 (2012).
8. E. Bettelli et al., *J. Exp. Med.* **197**, 1073–1081 (2003).
9. I. S. Grewal et al., *Immunity* **14**, 291–302 (2001).
10. Y. Arima et al., *Cell* **148**, 447–457 (2012).
11. A. Reboli et al., *Nat. Immunol.* **10**, 514–523 (2009).
12. S. A. Apostolidis, T. Rauen, C. M. Hedrich, G. C. Tsokos, J. C. Crispin, *J. Biol. Chem.* **288**, 26775–26784 (2013).
13. L. R. Shiow et al., *Nature* **440**, 540–544 (2006).
14. R. Gold, C. Linington, H. Lassmann, *Brain* **129**, 1953–1971 (2006).
15. C. P. Genain et al., *Science* **274**, 2054–2057 (1996).
16. N. Pardi et al., *Nat. Commun.* **9**, 3361 (2018).
17. E. Cretney, A. Kallies, S. L. Nutt, *Trends Immunol.* **34**, 74–80 (2013).
18. R. J. Miragaia et al., *Immunity* **50**, 493–504.e7 (2019).
19. N. Paschalidis et al., *J. Neuroinflammation* **6**, 33 (2009).
20. S. A. Apostolidis, T. Rauen, C. M. Hedrich, G. C. Tsokos, J. C. Crispin, *J. Biol. Chem.* **288**, 26775–26784 (2013).
21. A. Collison et al., *Nat. Med.* **19**, 232–237 (2013).
22. E. E. Kara et al., *Nat. Commun.* **6**, 8644 (2015).
23. B. T. Fife, G. B. Huffnagle, W. A. Kuziel, W. J. Karpus, *J. Exp. Med.* **192**, 899–906 (2000).
24. S. Glatigny, R. Duhen, M. Oukka, E. Bettelli, *J. Immunol.* **187**, 6176–6179 (2011).
25. C. Runne, S. Chen, *Cell Adh. Migr.* **7**, 214–218 (2013).
26. T. Kinashi, K. Katagiri, *Immunol. Lett.* **93**, 1–5 (2004).
27. C. C. Lin et al., *Nat. Commun.* **5**, 3551 (2014).
28. B. R. Burton et al., *Nat. Commun.* **5**, 4741 (2014).
29. L. M. Yshii, R. Hohlfield, R. S. Liblau, *Nat. Rev. Neurol.* **13**, 755–763 (2017).
30. L. Wang et al., *Proc. Natl. Acad. Sci. U.S.A.* **105**, 9331–9336 (2008).
31. N. Ohkura, S. Sakaguchi, *Nat. Immunol.* **12**, 283–284 (2011).
32. A. M. Thornton, E. M. Shevach, *J. Immunol.* **164**, 183–190 (2000).
33. X. Clemente-Casares et al., *Nature* **530**, 434–440 (2016).
34. F. P. Legoux et al., *Immunology* **43**, 896–908 (2015).
35. N. Dammes, D. Peer, *Trends Pharmacol. Sci.* **41**, 755–775 (2020).
36. U. Sahin, Ö. Türeci, *Science* **359**, 1355–1360 (2018).
37. U. Sahin et al., *Nature* **547**, 222–226 (2017).

## ACKNOWLEDGMENTS

We thank V. Ames, K. Zwadlo, A. Plaschke, I. Beulshausen, E. Petscherschich, E. Daniel, R. Roth, B. Jesionek, M. Brkic, A. Selmi, M. Baidersdorfer, and S. Berl for technical assistance; S. Witzel, B. Tillmann, S. Wurzel, Z. Yildiz, and N. Blaumeuser for cloning of constructs; S. Fesser, K. Tillmann, J. Beckerle, E. Heintz, and C. Gollatz for mRNA production; and P. Guna, A.-L. Popa, and H. Haas for providing liposomes. Additional support was provided by S. Attig and A. Hoberger for cell sorting. Moreover, we acknowledge F. Vascotto for support and scientific discussion for the manuscript, T. Regen for experimental advice, and L. Giese for supporting single-cell RNA sequencing. Furthermore, we thank the NIH Tetramer Core Facility for providing the MOG<sub>35–55</sub> MHC class II tetramer. **Funding:** This work has been supported by grants from the Immunology Research Center (FZI) Mainz (FZI-TRP 2014–12 to U.S. and N.Y.) and the Deutsche Forschungsgemeinschaft DFG (SFB/CRC-TR 128 to A.W.). **Author contributions:** U.S. was responsible for conception and experimental strategy of the study. Planning and analysis of the experiments were done by C.K., L.M.K., M.D., S.Kr., H.B., and J.P., supported by N.Y. and A.W. C.K. and S.Kr. performed immunological experiments. Processing and analysis of scRNA-seq data was done by L.K., E.D., and M.S., supported by T.B. Ö.A.-Ö.

performed IHC experiments. C.K., Ö.T., and U.S. interpreted the data and drafted the manuscript. L.K., E.D., M.S., M.D., K.K., and A.W. supported writing of the manuscript. All authors edited and approved the final manuscript. **Competing interests:** L.M.K., H.B., K.K., Ö.T., and U.S. are employees at BioNTech SE (Mainz, Germany). M.D. and S.Kr. work as consultants for BioNTech SE (Mainz, Germany). C.K., J.P., L.M.K., M.D., S.Kr., K.K., and U.S. are inventors on patents and patent applications related to this study. Ö.T. and U.S. are stock owner and management board members of BioNTech SE (Mainz, Germany). All other authors declare no competing interests. **Data and materials availability:** Correspondence and request for materials should be addressed to U.S.

## SUPPLEMENTARY MATERIALS

science.sciencemag.org/content/371/6525/145/suppl/DC1  
Materials and Methods  
Figs. S1 to S16  
Tables S1 and S2  
References (38–52)

13 June 2019; resubmitted 27 April 2020  
Accepted 17 November 2020  
10.1126/science.aay3638

## NEUROSCIENCE

# Anterior cingulate inputs to nucleus accumbens control the social transfer of pain and analgesia

Monique L. Smith, Naoyuki Asada\*, Robert C. Malenka†

Empathy is an essential component of social communication that involves experiencing others' sensory and emotional states. We observed that a brief social interaction with a mouse experiencing pain or morphine analgesia resulted in the transfer of these experiences to its social partner. Optogenetic manipulations demonstrated that the anterior cingulate cortex (ACC) and its projections to the nucleus accumbens (NAc) were selectively involved in the social transfer of both pain and analgesia. By contrast, the ACC→NAc circuit was not necessary for the social transfer of fear, which instead depended on ACC projections to the basolateral amygdala. These findings reveal that the ACC, a brain area strongly implicated in human empathic responses, mediates distinct forms of empathy in mice by influencing different downstream targets.

Empathy plays an essential role in social communication and involves integrated behavioral, cognitive, and affective processes that facilitate the adoption of a sensory or affective state that is more appropriate to another's situation than one's own (1–3). Evolutionarily conserved behavioral antecedents of human empathy have been identified in a range of species (2–5), including rodents, which display emotional contagion (6, 7), socially transferred pain (8–11), observational fear (3, 5, 12), and prosocial behaviors such as consolation (13) and “helping” (14, 15).

The anterior cingulate cortex (ACC) is a principal node in the neural circuitry thought to mediate empathy (16–18). In both humans and rodents, the ACC is particularly critical for affective and motivational responses to direct and observed pain as well as the social transfer of pain (10, 13, 19, 20). The ACC is thought to communicate with a broad range of brain regions that regulate emotional and motivational states, including the thalamus, insula, amygdala, and nucleus accumbens (NAc) (16, 21–23). However, the roles of these specific ACC circuit elements in empathy-related behaviors are unknown.

## Rapid transfer of pain behavior to bystander mice

The presence of a conspecific in pain can modulate the expression of pain behavior in a test animal already experiencing pain (6) and cause hyperalgesia in “bystander” (BY) mice that have not been subjected to any pain-inducing stimuli (9, 10), a phenomenon known as the “social transfer of pain.” We examined whether a brief (1 hour), direct social interaction between a male BY mouse and a male cagemate experiencing inflammatory hyperalgesia [owing to intraplantar injection of complete Freund's adjuvant (CFA), which induces long-lasting arthritis-like pain, (24, 25)] would lead to the social transfer of pain (Fig. 1A). After this 1-hour social interaction, BY mice exhibited mechanical hypersensitivity [as measured by stimulation with von Frey hairs using the “up-down” technique (26)] equivalent to that of CFA mice, whereas control mice subjected to the same procedures (in the absence of a no-ciceptive stimulus in either mouse) exhibited no change in mechanical thresholds (Fig. 1, B and C). After von Frey testing, all mice were separated and housed with treatment-matched cagemates (fig. S1). Repeated mechanical testing revealed that the hyperalgesia in BY mice lasted 4 hours but not 24 hours (Fig. 1B), was not influenced by prolonging the social interaction to 2 hours (fig. S2A) or by delaying the start of the social interaction to 24 hours after CFA injection (fig. S2B), and still occurred

Nancy Pritzker Laboratory, Department of Psychiatry and Behavioral Sciences, Stanford University, Stanford, CA, USA.

\*Present address: Daiichi Sankyo Co., Ltd., Tokyo, Japan.

†Corresponding author. Email: malenka@stanford.edu

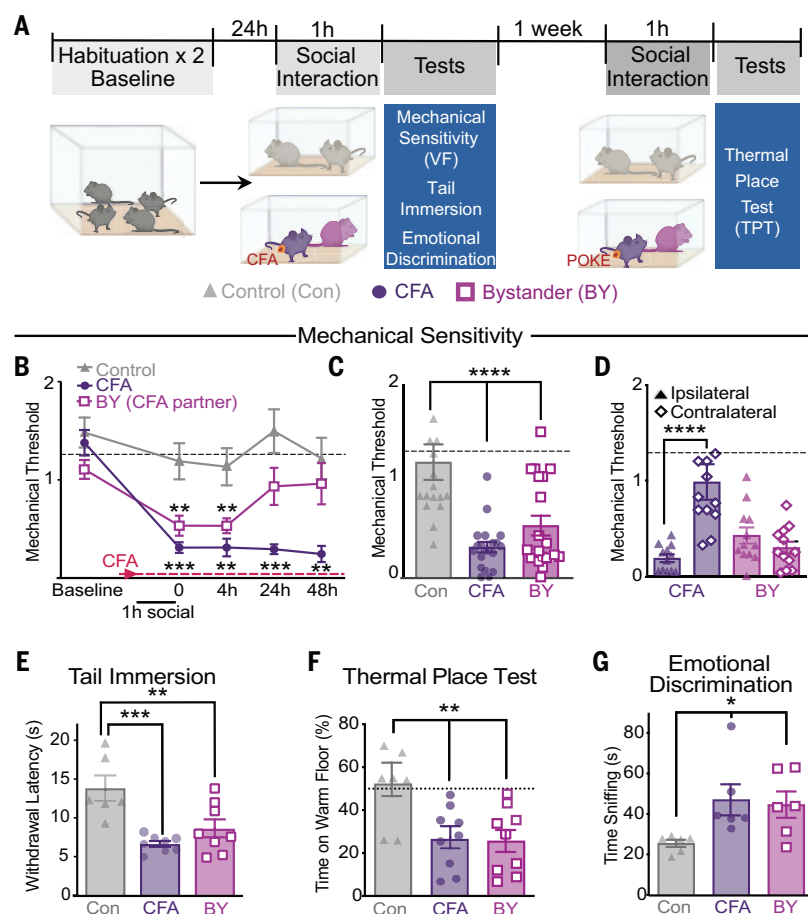


**Fig. 1. Rapid social transfer of pain to bystander mice.** (A) Timeline of social transfer of pain protocol. h, hour(s). (B) Time course of mechanical von Frey (VF) sensitivity at 0, 4, 24, and 48 hours after 1-hour social interaction in Control-Control (Con-Con) and CFA-BY pairs. (C) Mechanical thresholds immediately after the 1-hour social interaction. (D) Mechanical thresholds of the ipsilateral versus contralateral hindpaws. (E) Tail withdrawal latencies in the tail immersion test. (F) Time spent on the warm floor (40°C) in the TPT. (G) Time a stranger conspecific spent sniffing each group. For (B) to (G), data are means  $\pm$  SEM. In (B) to (D), dashed lines represent mean baseline thresholds for all groups. In (F), the dotted line represents 50% time on warm floor. Statistical tests included two-way repeated measures (A), one-way [(B) and (E) to (G)], and two-way (D) analysis of variance (ANOVA) with Holm-Sidak post hoc tests; \**P* < 0.05, \*\**P* < 0.01, \*\*\**P* < 0.001, and \*\*\*\**P* < 0.0001 representative of post hoc comparisons. All statistical measure details are presented in table S1A.

when capsaicin was used to induce pain and the social interaction was limited to 30 min (fig. S2C). Females demonstrated similar social transfer of pain (fig. S3A), although they expressed lower basal mechanical thresholds and enhanced CFA-induced hypersensitivity (fig. S3, A to C).

Whereas CFA mice exhibited hyperalgesia only in the ipsilateral, CFA-injected hindpaw, BY mice exhibited hyperalgesia in both hindpaws (Fig. 1D), suggesting the involvement of higher brain regions in mediating the pain transfer. Both CFA and BY mice also displayed thermal hypersensitivity to tail immersion in hot water (Fig. 1E) and thermal place aversion when given the choice between a warm (40°C) or room temperature (30°C) floor in a thermal place test (TPT; Fig. 1F). To determine whether the socially transferred pain experienced by

BY mice led to affective changes that could be detected by a conspecific, we conducted an emotional discrimination task (27), which demonstrated that a stranger mouse spent more time exploring both CFA and BY mice compared with controls (Fig. 1G).

#### Activation of an ACC-to-NAc core circuit by the social transfer of pain

To elucidate the brain regions potentially contributing to the social transfer of pain, we identified neurons activated during the social interaction using a reporter line generated by crossing FosCreER<sup>T2</sup> (TRAP2) mice with the Ai14-TdTomato reporter line (28, 29). Administering 4-hydroxytamoxifen (4-OHT) immediately before a 4-hour social interaction between BY and CFA mice (Fig. 2A) generated activated neurons in BY mice in brain regions

previously associated with empathy and social motivation, such as the ACC and NAc, as well as regions associated with pain transmission, such as the thalamus, central amygdala, and periaqueductal gray (Fig. 2, B and C). Because the numbers of activated neurons in the ACC and NAc were greater in BY mice than in both control and CFA mice (Fig. 2C) and because the ACC and NAc are important for social behaviors (30–33), we hypothesized that ACC neurons synapse onto NAc cells that are activated during the social transfer of pain. Thus, we first injected AAV-CaMKII $\alpha$ -YFP (AAV, adeno-associated virus; YFP, yellow fluorescent protein) into the ACC and verified that ACC pyramidal neurons send projections to the NAc, preferentially in its core region (Fig. 2D). To determine if there are direct synaptic connections between ACC neurons and activated NAc neurons during social transfer, we applied monosynaptic rabies virus tracing (34, 35) in TRAP2-BY and -CFA mice. Injection of AAVs expressing Cre-dependent rabies glycoprotein (RG) and avian tumor virus receptor A (TVA) into the NAc core followed by injection of EnvA-pseudotyped RG-deleted rabies virus expressing green fluorescent protein (GFP) (Fig. 2E), resulted in similar levels of GFP expression throughout the ACC in both CFA and BY mice (Fig. 2F and fig. S4).

#### ACC-to-NAc projections bidirectionally control social transfer of pain

To investigate if the ACC→NAc pathway is required for the social transfer of pain, we first tested the necessity of the ACC itself by injecting AAVs expressing the inhibitory opsin halorhodopsin (NpHR; AAV-DJ-CaMKII $\alpha$ -NpHR) or enhanced YFP (eYFP) as a control (YFP; AAV-DJ-CaMKII $\alpha$ -eYFP) and placing an optical fiber directly above the ACC (Fig. 3A). Activating NpHR during the social interaction between BY and CFA mice (Fig. 3A) attenuated the hyperalgesia in BY mice but not CFA mice, whereas YFP-expressing BY and CFA mice exposed to the same light stimulation displayed the expected mechanical hypersensitivity (Fig. 3B). Acute light exposure in the same mice during the mechanical testing had no consistent effect on mechanical thresholds (Fig. 3C), suggesting that acute inhibition of ACC neurons does not directly alter mechanical sensation.

To determine if the subset of ACC neurons activated during an initial social interaction is necessary for subsequent socially transferred pain, TRAP2: Ai14 mice that had received ACC injections of AAV-DIO-NpHR or AAV-DIO-eYFP were given 4-OHT before the social transfer of pain. One week later, optogenetic inhibition of the TRAP2 ACC neurons during a second social interaction prevented BY mice from developing mechanical hypersensitivity compared with control YFP-BY mice, which expressed robust hyperalgesia (Fig. 3D).



Immediately after the initial light-off test, the same mice were given light stimulation of the TRAPed neurons during the mechanical testing, and this manipulation had no consistent effect (Fig. 3E).

We next tested the necessity of ACC→Nac projections specifically by bilaterally injecting NpHR- or YFP-expressing AAVs in the ACC and placing optical fibers immediately above the Nac core. Similar to the effects of inhibiting the ACC, inhibition of ACC→Nac projections during the 1-hour social interaction strongly impaired the social transfer of mechanical hypersensitivity to BY mice but had no effects on CFA mice or YFP-expressing BY and CFA mice (Fig. 3F). Furthermore, repeated inhibition of the ACC→Nac projections during mechanical testing in the same mice had no consistent effect on mechanical thresholds (Fig. 3G).

To further evaluate the role of the ACC→Nac pathway in the social transfer of pain, we expressed channelrhodopsin-2 (ChR2) in the ACC and activated ACC→Nac projections during the 1-hour social transfer. This caused a robust prolongation of the duration of hyperalgesia in the BY mice, which lasted >72 hours as opposed to the expected 4 to 24 hours, as seen in YFP-expressing BY mice (Fig. 3H). Before any nociceptive stimulation, acute activation of ACC→Nac projections during mechanical testing had no consistent effect on mechanical sensitivity (fig. S5A) and also did not have acute aversive or reinforcing effects, as assayed by a real-time place preference test (fig. S5B).

### Distinct ACC projections control the social transfer of pain and fear

To examine the generalizability of ACC→Nac control over socially transferred behaviors, we examined the role of ACC→Nac projections in the well-established phenomenon of the social transfer of fear (5, 12). BY mice were exposed to shock 24 hours before placement in a distinct context, which allowed observation of a demonstrator (Shock) mouse being repeatedly shocked (Fig. 4A). Shock pre-exposure enhances the magnitude of freezing behavior in BY mice and is thought to more closely model human empathy (12, 20, 36). During the short observation period, BY mice exhibited significant increases in freezing (Fig. 4B), and this was maintained 24 hours later during reexposure to the shock observation context (“retrieval”; Fig. 4C). Inhibition of ACC→Nac projections in BY mice during the conditioning phase (Fig. 4D) had no effect on their acquisition of freezing behavior (Fig. 4E) and also did not affect freezing during the context-induced retrieval (Fig. 4F), where light was applied every other minute (fig. S6A). However, when the same mice were subjected to the social transfer of pain, inhibition of the ACC→Nac projections

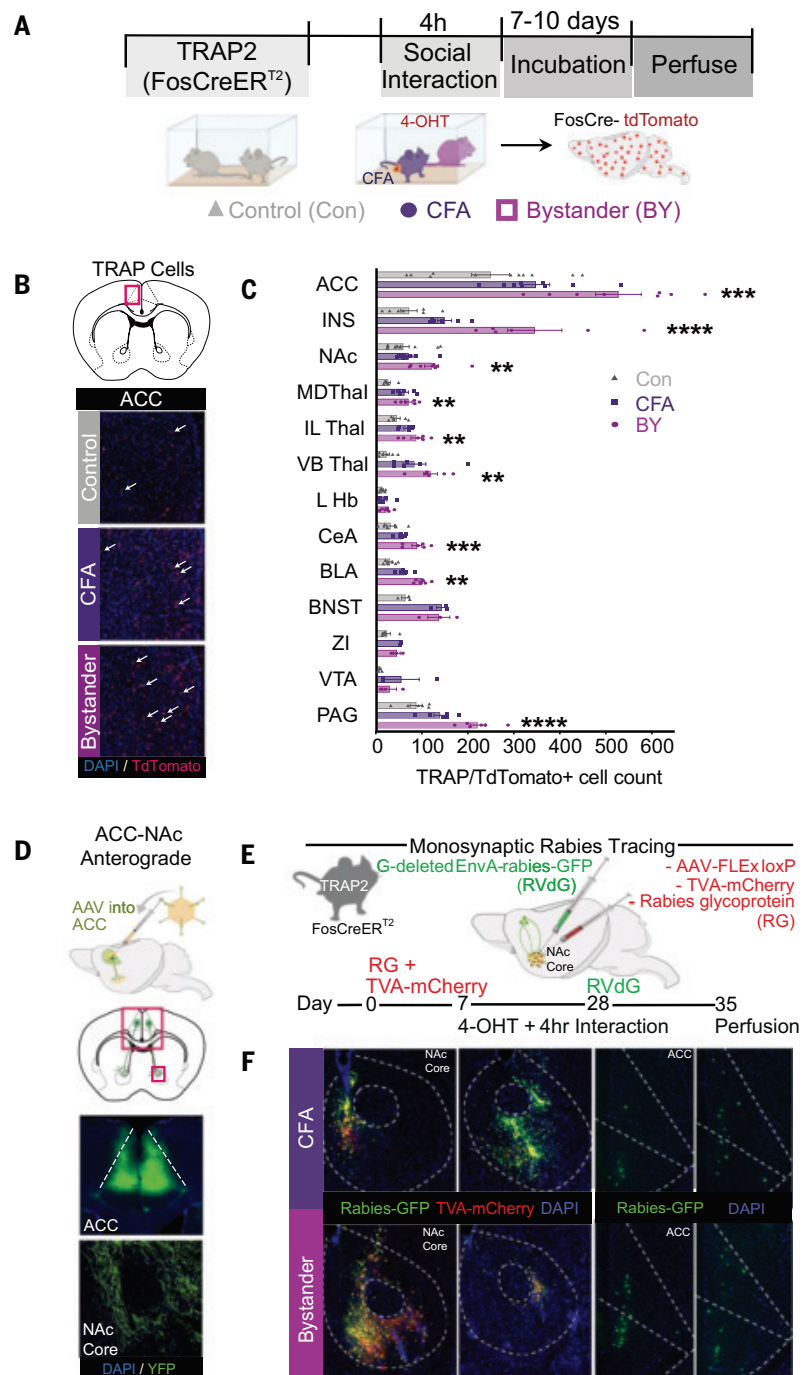


**Fig. 2. Activation of an ACC Nac core circuit by the social transfer of pain.** (A) Timeline to “TRAP” activated neurons during social transfer of pain. (B) Representative photomicrographs of TdTomato-positive cells (white arrows) in the ACC of Con, CFA, and BY mice after social transfer of pain. The red rectangle indicates the location of the photomicrographs. DAPI, 4',6-diamidino-2-phenylindole. (C) Quantification of Ai14-positive-TRAPed cells across 13 brain regions ( $n = 6$  to 9 mice per group). (D) Schematic of AAV injection and representative photomicrographs of ACC injection site and fibers in the Nac core. The large and small red rectangles indicated the location of the top and bottom micrographs, respectively. The dashed white lines indicate boundaries of the ACC. (E) Schematic and timeline of monosynaptic rabies tracing. (F) Representative photomicrographs of Nac core G-deleted EnvA-rabies-GFP (RVdG) and RG injection site and ACC GFP expression in CFA and BY mice. The dashed lines indicate boundaries of the Nac core and ACC. Data are means  $\pm$  SEM; one-way ANOVA with Holm-Sidak post hoc tests comparing Con versus BY; \*\* $P < 0.01$ , and \*\*\* $P < 0.001$ , and \*\*\*\* $P < 0.0001$ . All statistical measure details are presented in table S1B. INS, insula; MD Thal, mediodorsal thalamus; IL Thal, interlaminar thalamus; VB Thal, ventrobasal thalamus; L Hb, lateral habenula; CeA, central amygdala; BLA, basolateral amygdala complex; BNST, bed nucleus of the stria terminalis; ZI, zona inserta; VTA, ventral tegmental area; PAG, periaqueductal gray.

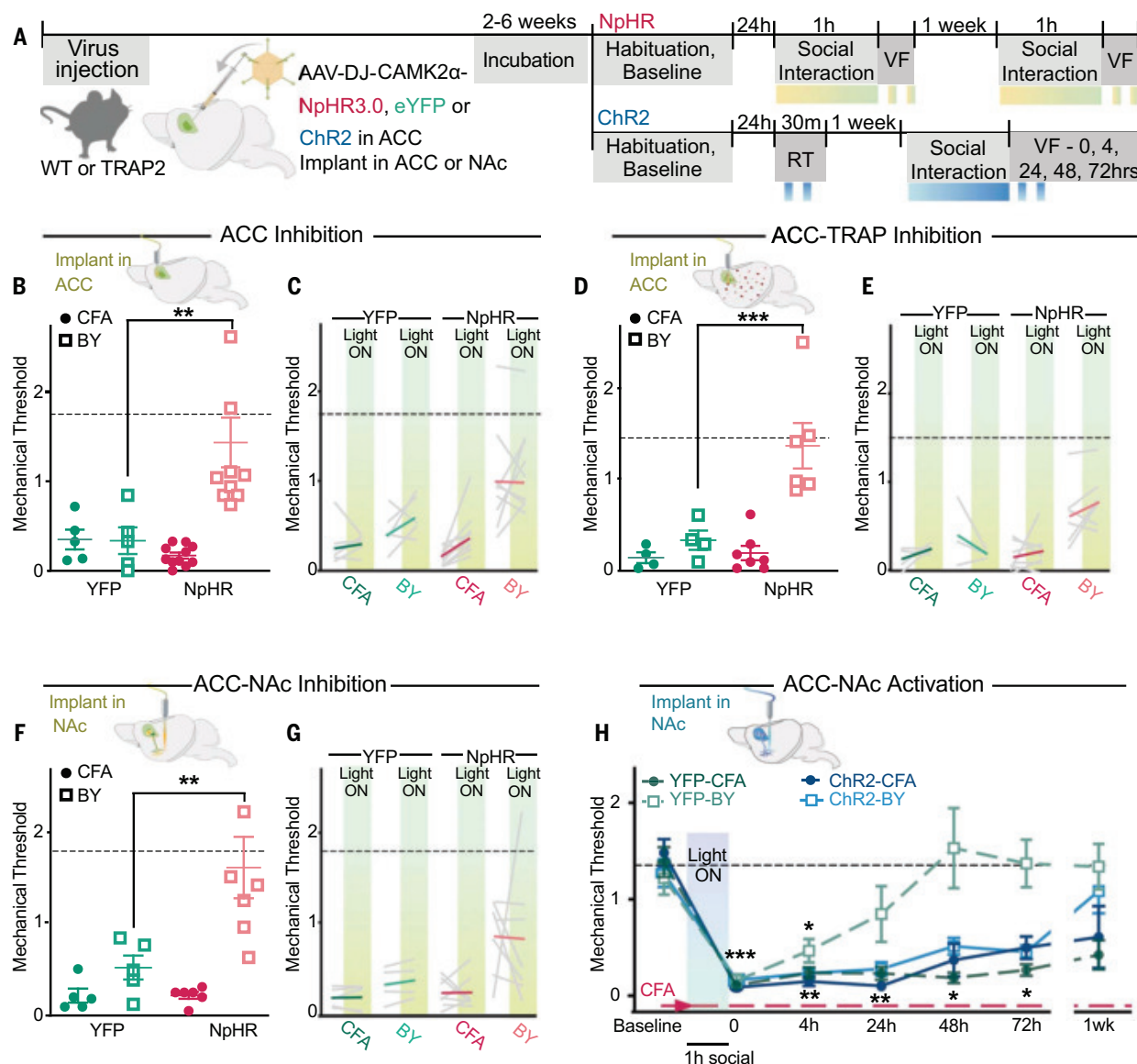


**Fig. 3. ACC NAc projections bidirectionally control social transfer of pain.**

(A) Schematic of viral injection and experimental timeline. Light stimulation periods are represented by yellow-green boxes for NpHR activation and by blue boxes for ChR2 activation. RT, real-time place preference. (B) Schematic shows fiber optic implant above the ACC. First light-off test of mechanical sensitivity (VF) of YFP- and NpHR-injected mice immediately after 1-hour social transfer with ACC inhibition. (C) Mechanical sensitivity during averaged ( $n = 2$ ) light-off and light-on sessions of ACC inhibition. (D) Schematic shows fiber optic implant above the ACC. First light-off test of mechanical sensitivity of YFP- and NpHR-injected TRAP2 mice immediately after 1-hour social transfer with ACC-TRAP inhibition. (E) Mechanical sensitivity during averaged ( $n = 2$ ) light-off and light-on sessions of ACC-TRAP inhibition. (F) Schematic of bilateral fiber

optic implants above the NAc core. First light-off test of mechanical sensitivity of YFP- and NpHR-injected mice immediately after 1-hour social transfer with ACC→Nac input inhibition. (G) Mechanical sensitivity during averaged ( $n = 2$ ) light-off and light-on sessions of ACC→Nac input inhibition. (H) First light-off test of mechanical sensitivity at 0, 4, 24, 48, and 72 hours and 1 week after 1-hour social interaction with ACC→Nac input inhibition. Data are means  $\pm$  SEM. Dashed lines represent mean baseline thresholds for all groups. One-way ANOVA with Holm-Sidak post hoc tests comparing YFP to matched NpHR groups [(B) to (G)] and two-way repeated measures ANOVA with Holm-Sidak post hoc tests comparing treatment groups to baseline at each time point, where notation is the least significant  $P$  value of all comparisons (H); \* $P < 0.05$ , \*\* $P < 0.01$ , and \*\*\* $P < 0.001$ . All statistical measure details are presented in table S1C.

during a 1-hour social interaction between CFA and BY mice impaired the acquisition of hyperalgesia in the BY mice (Fig. 4G), thereby providing evidence that the optogenetic inhibition of ACC→Nac input activity was effective in these mice.

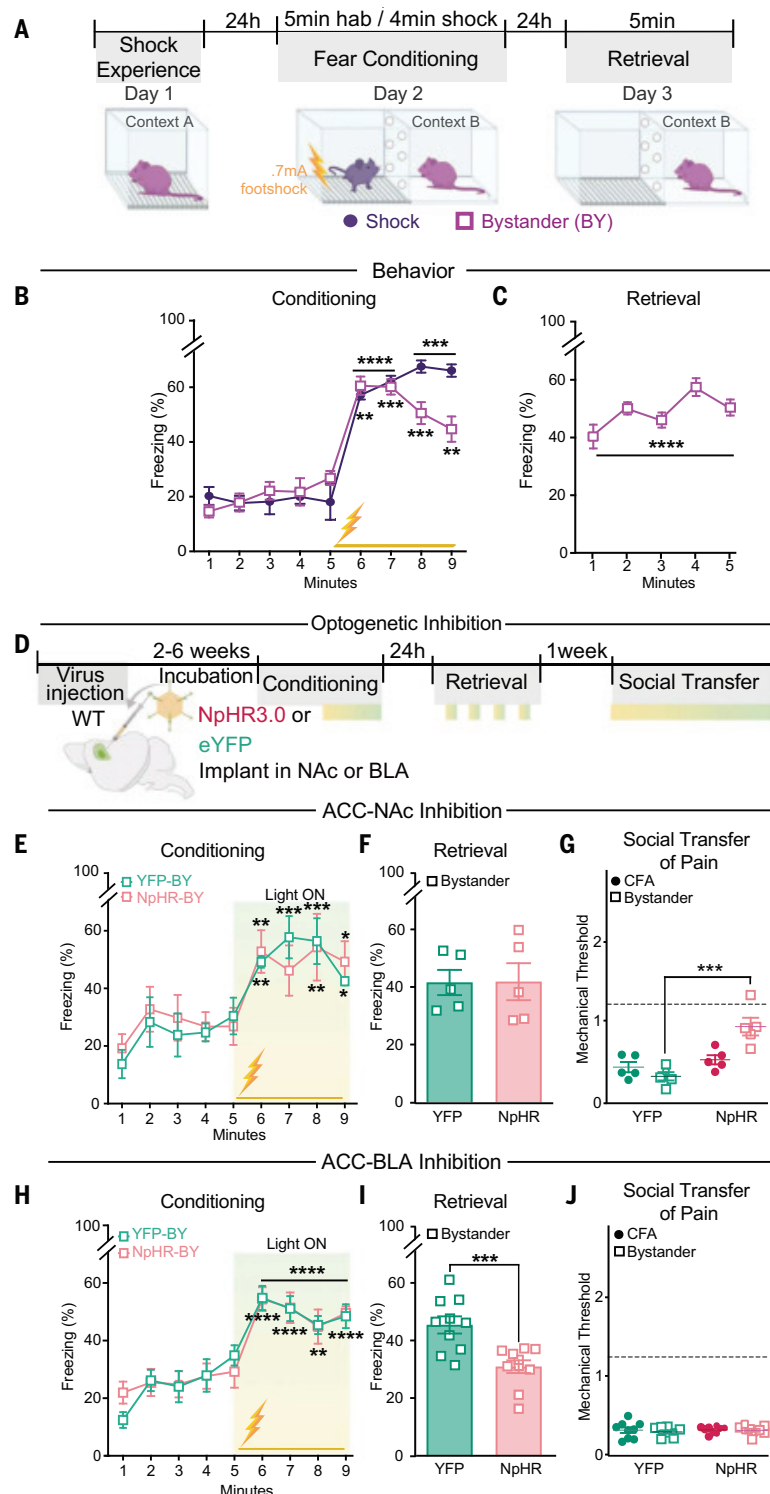
ACC projections to the basolateral amygdala (BLA) are necessary for cue-induced retrieval

of socially transferred fear (36). To evaluate if ACC→BLA projections are also necessary for context-induced retrieval of socially transferred fear behavior, we inhibited this pathway during acquisition of socially transferred fear and intermittently during retrieval (Fig. 4D). Inhibition of ACC→BLA projections in BY mice had no effect on their acquisition of freezing

behavior (Fig. 4H) but did attenuate freezing behavior during retrieval (Fig. 4I), regardless of whether the light was on or off (fig. S6B). By contrast, when the same mice were tested for the social transfer of pain, there was no effect of ACC→BLA input inhibition during the social interaction on their mechanical thresholds (Fig. 4J).

#### Fig. 4. Distinct ACC projections control the social transfer of pain and fear. (A) Schematic and timeline of social transfer of fear (shock experience: two at 0.7 mA, 2-s duration, 1-min intervals; shock conditioning: 24 at 0.7 mA, 2-s duration, 10-s intervals, total of 4 min).

hab, habituation. (B) Freezing behavior of Shock and BY mice during conditioning phase of socially transferred fear. (C) Freezing behavior of BY mice during retrieval phase of socially transferred fear. (D) Schematic of YFP and NpHR injection and experimental timeline of optogenetic stimulation in NAc or BLA. Light stimulation (~10 to 15 mW, 8-s on and 2-s off) periods are represented by yellow-green boxes. (E) Conditioning session with inhibition of ACC→NAc projections in YFP- and NpHR-BY mice during shock observation. (F) Freezing behavior of YFP- and NpHR-BY mice during retrieval phase. (G) First light-off session measuring mechanical sensitivity after NpHR inhibition of ACC→NAc projections during social transfer of pain in the same mice from (E) and (F). Dashed line represents mean baseline of all groups. (H) Conditioning session with inhibition of ACC→BLA projections in BY mice during shock observation. (I) Freezing behavior of YFP- and NpHR-BY mice during retrieval phase. (J) First light-off session measuring mechanical sensitivity after NpHR inhibition of ACC→BLA projections during social transfer of pain in the same mice from (H) and (I). Dashed line represents mean baseline of all groups. Data are means  $\pm$  SEM. Two-way repeated measures ANOVA with Holm Sidak post hoc tests comparing freezing to the first minute, where notation is the least significant  $P$  value of all comparisons [(B), (E), and (H)]; paired  $t$  test (C) or unpaired  $t$  test [(F) and (I)] comparing average baseline to average freezing during retrieval; or one-way ANOVA with Holm-Sidak post hoc tests [(G) and (J)]; \* $P < 0.05$ , \*\* $P < 0.01$ , \*\*\* $P < 0.001$ , \*\*\*\* $P < 0.0001$ . All statistical measure details are presented in table S1D.



#### ACC-to-NAc projections regulate the social transfer of analgesia

Although the social transfer of pain and fear in rodents is well established, it is unknown if the experience of pain relief [i.e., analgesia (Analg)] can be transferred socially. To examine this possibility, all mice were administered CFA to induce pain and then one-quarter of mice were also given an analgesic dose of

morphine [10 mg per kg of body weight (mg/kg)] at which time mice were paired for a 1-hour social interaction (Fig. 5A). Despite prior administration of CFA, CFA-Analg-BY mice paired with morphine-treated mice (CFA-Mor) exhibited diminished reductions in mechanical threshold (i.e., lessened pain responses) compared with CFA-CFA control pairs (CFA-Con; Fig. 5B). After separation

from CFA-Mor partners, the social transfer of analgesia in CFA-Analg-BY mice lasted 4 hours but not 24 hours (Fig. 5B). Because morphine causes hyperlocomotion, which prevents measurement of mechanical thresholds in CFA-Mor mice, we used the TPT to directly compare the magnitude of the analgesia in CFA-Analg-BY and CFA-Mor mice. In contrast to mechanical hyperalgesia, thermal



place aversion was not present 1 hour after CFA injection but was robust 1 week later (Fig. 5C), at which point one-quarter of CFA mice were again administered morphine immediately before a 1-hour social interaction with CFA-Analg-BY partners (Fig. 5A). CFA-induced thermal aversion (CFA-Con) was reduced in the CFA-Analg-BY mice to the same extent as morphine administration (CFA-Mor; Fig. 5D).

We next tested the necessity of ACC activity for the social transfer of analgesia. Optoge-

netic inhibition of ACC neurons using NpHR during the 1-hour social interaction (Fig. 5E) prevented the social transfer of analgesia in CFA-Analg-BY mice, as assayed by both mechanical sensitivity (Fig. 5F) and the TPT (Fig. 5G), but had no effect on acute mechanical thresholds, thermal place aversion, or the analgesic action of morphine during the testing of CFA-Con and CFA-Mor mice. Inhibition of ACC→Nac input activity specifically had essentially identical effects, also preventing the social transfer

of analgesia without affecting mechanical or thermal sensitivity directly (Fig. 5, H and I).

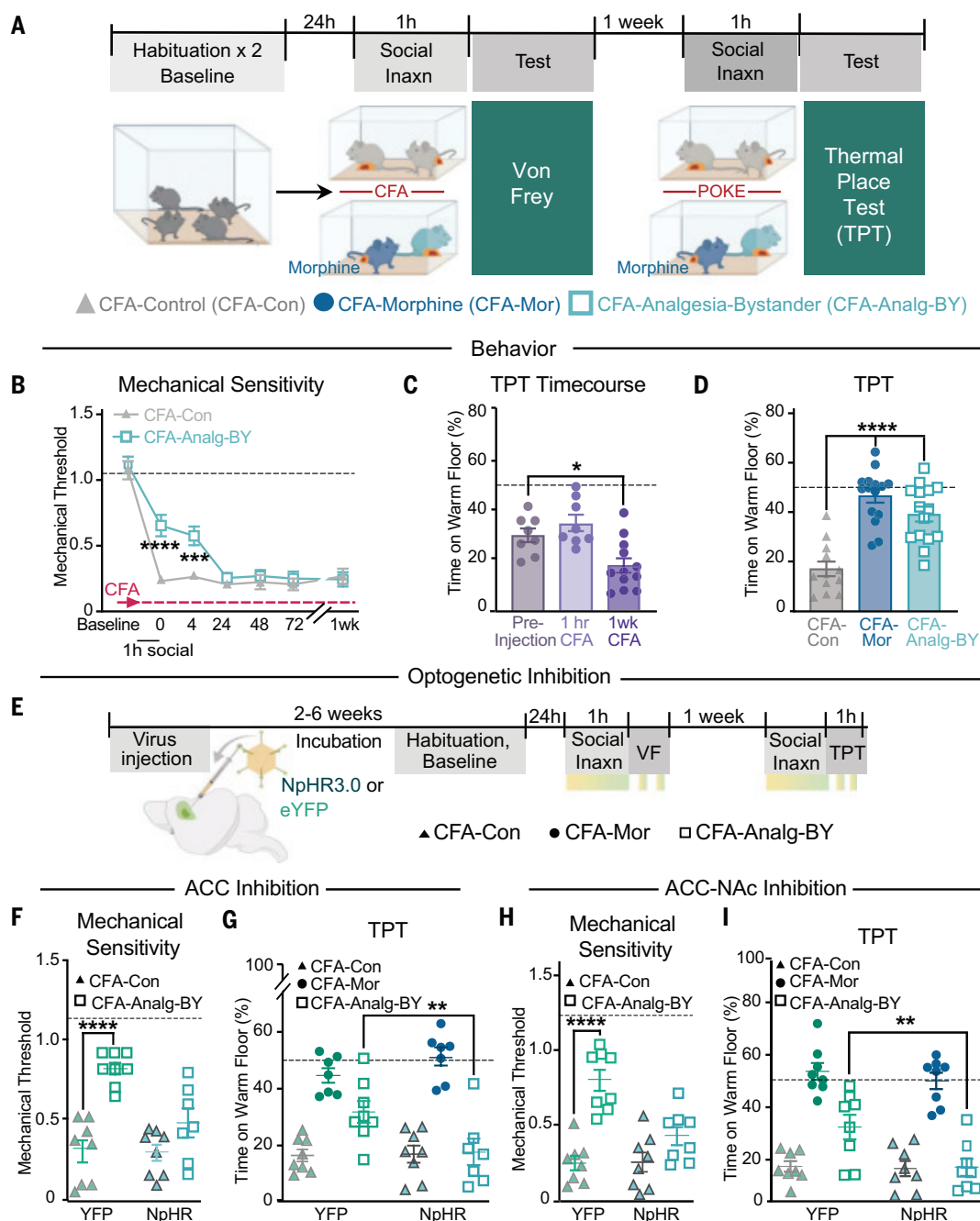
## Discussion

We investigated the neural mechanisms of simple forms of empathy in mice by establishing a protocol that results in the rapid social transfer of two types of pain behavior: hyperalgesia and analgesia. Although the definition of “empathy” is subject to debate (37), the BY mice in this bidirectional behavioral model appear

**Fig. 5. ACC Nac projections regulate social transfer of analgesia.** (A) Schematic of social transfer of analgesia protocol and timeline. Inaxn, interaction.

(B) Mechanical sensitivity at 0, 4, 24, 48, and 72 hours and 1 week after 1-hour social interaction in CFA-Con–CFA-Con pairs and CFA-Mor–CFA-Analg-BY pairs. (C) Time on the warm (40°C) floor in the TPT before and 1 hour and 1 week (wk) after CFA injection. (D) Time on the warm (40°C) floor in the TPT immediately after the second 1-hour social transfer of analgesia, 1 week after CFA injection.

(E) Schematic of YFP and NpHR injection and optogenetic stimulation in ACC or Nac. Light stimulation (~10 to 15 mW, 8-s on and 2-s off) periods are represented by yellow-green boxes. (F) First light-off session measuring mechanical sensitivity after light stimulation of ACC in YFP- and NpHR-expressing CFA-Con and CFA-Analg-BY mice during social transfer of analgesia. (G) Time on the warm (40°C) floor in the TPT after light stimulation of ACC in YFP- and NpHR-expressing CFA-Con, CFA-Mor, and CFA-Analg-BY mice during the second social transfer of analgesia test. (H) First light-off session measuring mechanical sensitivity after light stimulation of ACC→Nac projections in YFP- and NpHR-expressing CFA-Con and CFA-Analg-BY mice during social transfer of analgesia. (I) Time on the warm (40°C) floor in the TPT after ACC→Nac light stimulation in YFP- and NpHR-expressing CFA-Con, CFA-Mor, and CFA-Analg-BY mice during the second social transfer of analgesia test. Data are means ± SEM; dashed lines in (B), (F), and (H) represent baseline thresholds for all groups; dashed lines in (C), (D), (G), and (I) represent 50% time on warm floor. Two-way repeated measures (B) or one-way [(C), (D), and (F) to (I)] ANOVA with Holm-Sidak post hoc tests comparing between groups; \**P* < 0.05, \*\**P* < 0.01, \*\*\**P* < 0.001, \*\*\*\**P* < 0.0001. Not all significant post hoc analyses are displayed. All statistical measure details are presented in table S1E.



to fulfill one critical feature of the expression of empathy, the adoption of another's sensory and affective state (1–3, 37). The social transfer of hyperalgesia to BY mice required only 1 hour of social interaction, lasted 4 to 24 hours, and generalized to several different pain modalities. Notably, analgesia could also be transferred to a mouse in pain and lasted at least 4 hours. These results provide further evidence for the critical importance of the social environment to the experience of pain, including an innovative model for socially induced pain relief, which can be tested in human subjects.

The social interactions in mice resulted in increased activity in the ACC and several of its downstream targets, such as the NAc, a key node of the circuitry involved in a range of affective and motivated behaviors, including those triggered by pain (38–41). A critical role for ACC-to-NAc communication was established by demonstrating that bidirectional manipulation of activity in ACC→NAc inputs influences the acquisition of socially transferred pain but not the expression of mechanical sensitivity itself. Specifically, inhibiting this activity during the 1-hour social interaction reduced hyperalgesia in BY mice, whereas increasing activity in ACC→NAc inputs prolonged the duration of the hyperalgesia evoked by the brief social interaction. ACC→NAc input activity was also necessary for the social transfer of analgesia but not for the social transfer of fear, which requires activity in ACC projections to the BLA (36).

These results suggest that the ACC, which has been proposed to be a key brain area for mediating the emotional aspects of pain as well as encoding information about the affective state of others (23, 30, 42), generates a specific and appropriate empathic behavioral response by accessing distinct downstream targets. The specificity of the neural circuit and behavioral response generated during socially transferred pain and fear may be, at least in part, due to the sensory modalities required for these two forms of social transfer. The social transfer of pain does not require visual or auditory stimuli but can be generated by exposure to used bedding from mice experiencing pain, suggesting that olfactory cues are sufficient for this form of social transfer (9). By contrast, the social transfer of fear requires visual and/or auditory cues (3, 12). Further elucidation of the mechanisms by which this specificity in empathic neural and behavioral responses occurs will be important for developing interventions that promote social context-appropriate empathic responses. Furthermore, a better understanding of the neural circuits mediating specific empathic responses will greatly facilitate the development of therapies that target pathological forms of empathy, or its absence, in a variety of neuropsychiatric disorders.

Historically, empathy, as defined by the ability to experience and share the emotions of others, was often considered to be a high level, affective-cognitive process experienced almost exclusively by humans (1, 2, 43). However, most investigators now accept that empathy can be deconstructed into specifiable, evolutionarily conserved components, many of which can be studied in rodents to elucidate their underlying neural mechanisms (3–5, 12, 44). Our results provide additional evidence that mice can rapidly and reliably adopt the sensory-affective state of a social partner, regardless of the valence of the information (pain, fear, or pain relief). Although it is conceivable that the behavioral responses of our BY mice reflect “imitative” or “mimicry” behavior (45) rather than “empathy,” several findings suggest that at least for the social transfer of pain and analgesia, the BY mice manifest changes in their behavior because they are experiencing an altered sensory-affective state. Importantly, the BY mice were tested using several different behavioral assays and did not always have direct visual access to their social partners during testing. In addition, control mice spent more time interacting with a BY mouse that had recently been exposed to a CFA mouse than with another control mouse, indicating that the BY mouse is in an altered affective state that is sufficient to attract control mice. Finally, as mentioned above, the social transfer of pain can be generated by bedding (9), which provides no opportunity for imitative or mimicry-like behavior.

The behavioral protocols we established are relatively easy to implement and generate multifaceted empathy-like behavior in mice, a species that offers many advantages for rapid, direct, and highly specific manipulation of neural circuit activity. Mechanistic findings from rodents and other experimentally accessible species provide new hypotheses that researchers studying human empathy can explore using tools such as neuromodulation methods and brain imaging. Advancing our understanding of the evolutionarily conserved brain mechanisms of empathy will, hopefully, also expedite the development of new interventions that promote the empathic social interactions that the world, apparently, desperately needs.

## REFERENCES AND NOTES

- M. L. Hoffman, *Dev. Psychol.* **11**, 607–622 (1975).
- F. B. M. de Waal, *Annu. Rev. Psychol.* **59**, 279–300 (2008).
- J. B. Panksepp, G. P. Lahvis, *Neurosci. Biobehav. Rev.* **35**, 1864–1875 (2011).
- S. Sivaselvachandran, E. L. Acland, S. Abdallah, L. J. Martin, *Neurosci. Biobehav. Rev.* **91**, 130–137 (2018).
- S. Keum et al., *Genes Brain Behav.* **15**, 231–242 (2016).
- D. J. Langford et al., *Science* **312**, 1967–1970 (2006).
- D. Baptista-de-Souza et al., *Behav. Pharmacol.* **26**, 664–672 (2015).
- Z. Li et al., *Pain* **155**, 1253–1261 (2014).
- M. L. Smith, C. M. Hostetler, M. M. Heinricher, A. E. Ryabinin, *Sci. Adv.* **2**, e1600855 (2016).
- M. L. Smith, A. T. Walcott, M. M. Heinricher, A. E. Ryabinin, *eNeuro* **4**, ENEURO.0087-17.2017 (2017).

- Y.-F. Lu et al., *Neurosci. Lett.* **662**, 385–388 (2018).
- A. Kim, S. Keum, H.-S. Shin, *Genes Brain Behav.* **18**, e12521 (2019).
- J. P. Burkett et al., *Science* **351**, 375–378 (2016).
- H. Ueno et al., *Sci. Rep.* **9**, 5817 (2019).
- I. Ben-Ami Bartal, J. Decety, P. Mason, *Science* **334**, 1427–1430 (2011).
- C. Lamm, J. Decety, T. Singer, *Neuroimage* **54**, 2492–2502 (2011).
- I. Timmers et al., *Front. Behav. Neurosci.* **12**, 289 (2018).
- P. L. Jackson, E. Brunet, A. N. Meltzoff, J. Decety, *Neuropsychologia* **44**, 752–761 (2006).
- D. Jeon et al., *Nat. Neurosci.* **13**, 482–488 (2010).
- M. Carrillo et al., *Curr. Biol.* **29**, 1301–1312.e6 (2019).
- C. Fillinger, I. Yalcin, M. Barrot, P. Veinante, *Brain Struct. Funct.* **223**, 1747–1778 (2018).
- P. L. Jackson, A. N. Meltzoff, J. Decety, *Neuroimage* **24**, 771–779 (2005).
- F. L. Stevens, R. A. Hurley, K. H. Taber, *J. Neuropsychiatry Clin. Neurosci.* **23**, 121–125 (2011).
- A. A. Larson, D. R. Brown, S. el-Attrash, M. M. Walser, *Pharmacol. Biochem. Behav.* **24**, 49–53 (1986).
- K. Ren, R. Dubner, *ILAR J.* **40**, 111–118 (1999).
- S. R. Chaplan, F. W. Bach, J. W. Pogrel, J. M. Chung, T. L. Yaksh, *J. Neurosci. Methods* **53**, 55–63 (1994).
- V. Ferretti et al., *Curr. Biol.* **29**, 1938–1953.e6 (2019).
- C. J. Guenther, K. Miyamichi, H. H. Yang, H. C. Heller, L. Luo, *Neuron* **78**, 773–784 (2013).
- W. E. Allen et al., *Science* **357**, 1149–1155 (2017).
- M. A. J. Apps, M. F. S. Rushworth, S. W. C. Chang, *Neuron* **90**, 692–707 (2016).
- J. J. Walsh et al., *Nature* **560**, 589–594 (2018).
- L. W. Hung et al., *Science* **357**, 1406–1411 (2017).
- M. A. J. Apps, P. L. Lockwood, J. H. Balsters, *Front. Neurosci.* **7**, 251 (2013).
- E. M. Callaway, L. Luo, *J. Neurosci.* **35**, 8979–8985 (2015).
- E. J. Kim, M. W. Jacobs, T. Ito-Cole, E. M. Callaway, *Cell Rep.* **15**, 692–699 (2016).
- S. A. Allsop et al., *Cell* **173**, 1329–1342.e18 (2018).
- F. B. M. de Waal, S. D. Preston, *Nat. Rev. Neurosci.* **18**, 498–509 (2017).
- M. Watanabe, M. Narita, *Adv. Exp. Med. Biol.* **1099**, 201–210 (2018).
- H. N. Harris, Y. B. Peng, *Neural Regen. Res.* **15**, 597–605 (2020).
- A. M. Klawonn, R. C. Malenka, *Cold Spring Harb. Symp. Quant. Biol.* **83**, 119–129 (2018).
- N. Schwartz et al., *Science* **345**, 535–542 (2014).
- T. Singer et al., *Science* **303**, 1157–1162 (2004).
- S. D. Preston, F. B. M. de Waal, *Behav. Brain Sci.* **25**, 1–20 (2002).
- K. Z. Meyza, I. B.-A. Bartal, M. H. Monfils, J. B. Panksepp, E. Knapska, *Neurosci. Biobehav. Rev.* **76**, 216–234 (2017).
- H. Ueno et al., *BMC Neurosci.* **21**, 19 (2020).

## ACKNOWLEDGMENTS

We thank the Luo lab for generously providing the TRAP2 breeding pairs, M. Lenail for contributing to the cell counting in the TRAP2 analysis, the Sudhof lab for access to fear conditioning equipment, and B. Bentzley for aid in modifying the behavioral chambers used in the social transfer of fear experiments. **Funding:** This work was supported by the UCSF Dolby Family Center for Mood Disorders. M.L.S. was supported by the National Institute on Drug Abuse (T32DA035165-06) and a Stanford University School of Medicine Deans Fellowship. **Author contributions:** All studies were conceptualized and designed by M.L.S., N.A., and R.C.M. Experiments were performed and analyzed by M.L.S. and N.A. The paper was written by M.L.S. and R.C.M., with editorial comments by N.A. **Competing interests:** R.C.M. is a cofounder and scientific advisor of MapLight Therapeutics. R.C.M. is also on the scientific advisory board of Cerevance, Inc.; The Brave Neuroscience Co.; AZ Therapeutics; and Cognition Therapeutics. **Data and materials availability:** All data are available in the main text or the supplementary materials.

Materials and methods and references cited therein can be found in the main article online.

## SUPPLEMENTARY MATERIALS

science.sciencemag.org/content/371/6525/153/suppl/DC1  
Figs. S1 to S6  
Table S1  
MDAR Reproducibility Checklist

12 August 2020; accepted 5 November 2020  
10.1126/science.abe3040

## CHEMICAL PHYSICS

## Crossover from hydrogen to chemical bonding

Bogdan Dereka<sup>1</sup>, Qi Yu<sup>2,\*</sup>, Nicholas H. C. Lewis<sup>1</sup>, William B. Carpenter<sup>1</sup>, Joel M. Bowman<sup>2</sup>, Andrei Tokmakoff<sup>1†</sup>

Hydrogen bonds (H-bonds) can be interpreted as a classical electrostatic interaction or as a covalent chemical bond if the interaction is strong enough. As a result, short strong H-bonds exist at an intersection between qualitatively different bonding descriptions, with few experimental methods to understand this dichotomy. The  $[\text{F}\cdots\text{H}\cdots\text{F}]^-$  ion represents a bare short H-bond, whose distinctive vibrational potential in water is revealed with femtosecond two-dimensional infrared spectroscopy. It shows the superharmonic behavior of the proton motion, which is strongly coupled to the donor-acceptor stretching and disappears on H-bond bending. In combination with high-level quantum-chemical calculations, we demonstrate a distinct crossover in spectroscopic properties from conventional to short strong H-bonds, which identify where hydrogen bonding ends and chemical bonding begins.

Qualitatively, a hydrogen bond (H-bond) is an attractive interaction between an acceptor (A) and a hydrogen atom covalently bonded to a donor (D), but quantitative descriptions of H-bonds have been debated since their inception (1, 2). Conventional H-bonds are commonly described through the electrostatic attraction between the positive proton charge and the electronegative acceptor, and their presence is revealed in the separation and linearity of the D-H $\cdots$ A atoms and a decrease in D-H vibrational frequency. Questions about the adequacy of these classical concepts arise when considering short strong H-bonds (SHBs). They can have interaction strengths similar to those of covalent bonds, protons appearing shared between D and A, and could involve substantial electronic redistribution across the bonded atoms (3, 4). As a result, it may be better to describe SHBs as covalent three-center four-electron bonds, rather than as a classical electrostatic phenomenon (5). Where do hydrogen bonds end and covalent bonds begin? This question has implications in processes involving SHBs—for instance, in biomolecular processes such as enzymatic catalysis (3, 4, 6–8), signaling (9), and ligand binding (10, 11), as well as atmospheric and interstellar chemistry (12, 13), proton transport (9, 14, 15), and ion hydration (16–18). There is a debate about how large the SHB energies are and if they can survive the strong solvation interactions in water and polar environments (19–21). Therefore, experiments are needed to characterize the physical and chemical properties of SHBs.

H-bonding phenomena express themselves quantitatively in the shape of the electronic

potential energy experienced by the proton along the H-bond. In conventional H-bonds, the donor-acceptor separation is large ( $>2.7$  Å), and the potential minimum is localized near D at its covalent D-H bond length (Fig. 1A) (3, 4, 22). As the D $\cdots$ A distance shrinks and the H-bond strength increases, the barrier decreases until the zero-point energy of the proton exceeds it and ultimately yields a flat-bottom single-well potential. It corresponds to the SHB regime in which the proton becomes a confined particle delocalized between D and A. The potential energy surface is a key descriptor linking the underlying quantum-

mechanical electronic structure of the D-H $\cdots$ A H-bond to experimental observables.

Despite being the most common H-bond metric, the D $\cdots$ A distance cannot be easily related to the shape of the hydrogen bond potential, but infrared (IR) vibrational spectroscopy can directly characterize it. The D-H vibrational frequency decreases with increasing H-bond strength, a textbook property of an H-bond; however, the fundamental frequency itself is not a descriptor of the proton potential. The vibrations of protons in H-bonds deviate greatly from harmonic oscillations, and their anharmonicity and mode mixing with the D $\cdots$ A stretching and H-bond bending vibrations are major factors influencing the structure, dynamics, and reactivity of H-bonds. A more useful measurement is to observe how the vibrational transition frequencies depend on quantum numbers 0, 1, and 2 (Fig. 1A). Conventional H-bonds follow traditional rules for anharmonic vibrations, in which the vibrational energy splitting decreases as one ascends the vibrational ladder (positive anharmonicity). The  $|0\rangle$  to  $|1\rangle$  transition frequency  $\omega_{10}$  is larger than the  $|1\rangle$  to  $|2\rangle$  frequency  $\omega_{21}$ , as characterized by their ratio  $\gamma = \omega_{21}/\omega_{10} < 1$ . By contrast, when proton confinement dictates the potential shape in SHBs, the spacing between states increases up the vibrational ladder (analogous to a particle-in-a-box) and  $\gamma > 1$  (negative anharmonicity), yielding the effect called superharmonicity.

## Experimental results

We investigated an SHB in aqueous solution by characterizing the anharmonic potential of its multiple coupled vibrations, and we addressed how electronic structure becomes an important consideration in the transition from conventional to strong H-bonds. We used a combination of femtosecond two-dimensional infrared (2D IR) spectroscopy and high-level anharmonic quantum-chemical calculations to directly demonstrate the distinctive nature and characteristics of elusive SHBs in water using the bifluoride anion  $\text{HF}_2^-$  as a model system. Bifluoride is a linear symmetric ion with the proton bridging two fluorine atoms, which represents the ideal model of a bare H-bond and allows one to study SHBs in room-temperature liquid solution (23). The extremely short F-F separation puts it into the category of single-well H-bonds (Fig. 1 and fig. S3) and makes it the strongest H-bond, with an energy of 45.8 kcal/mol (24).

The infrared spectrum of aqueous  $\text{KHF}_2$  is shown in Fig. 2A with the assignment of vibrational modes that report on the principal geometric coordinates of any H-bond (Fig. 1B). On the basis of gas-phase, solid-state, and theoretical studies (23, 25, 26), one can assign the bands at 1215 and 1521  $\text{cm}^{-1}$  to the F-H-F bending modes,  $\delta$ , and the proton stretching

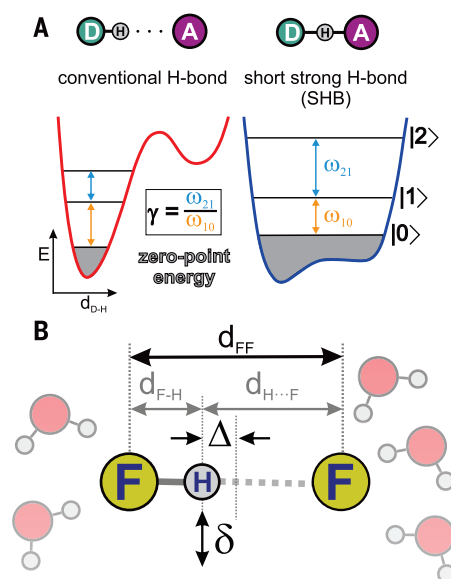


**Fig. 1. Hydrogen bonds.** (A) Types of hydrogen bonds depending on donor-acceptor distance. Potentials of proton motion are shown along with the first three quantum levels and the associated lowest-energy transitions. (B) Principal coordinates of any H-bond demonstrated with  $\text{HF}_2^-$  (aq): donor-acceptor distance ( $d_{\text{FF}}$ ), proton asymmetry ( $\Delta$ ), and linearity ( $\delta$ ).

<sup>1</sup>Department of Chemistry, Institute for Biophysical Dynamics, and James Franck Institute, The University of Chicago, Chicago, IL 60637, USA. <sup>2</sup>Department of Chemistry and Cherry L. Emerson Center for Scientific Computation, Emory University, Atlanta, GA 30322, USA.

\*Present address: Department of Chemistry, Yale University, New Haven, CT 06520, USA.

†Corresponding author. Email: tokmakoff@uchicago.edu



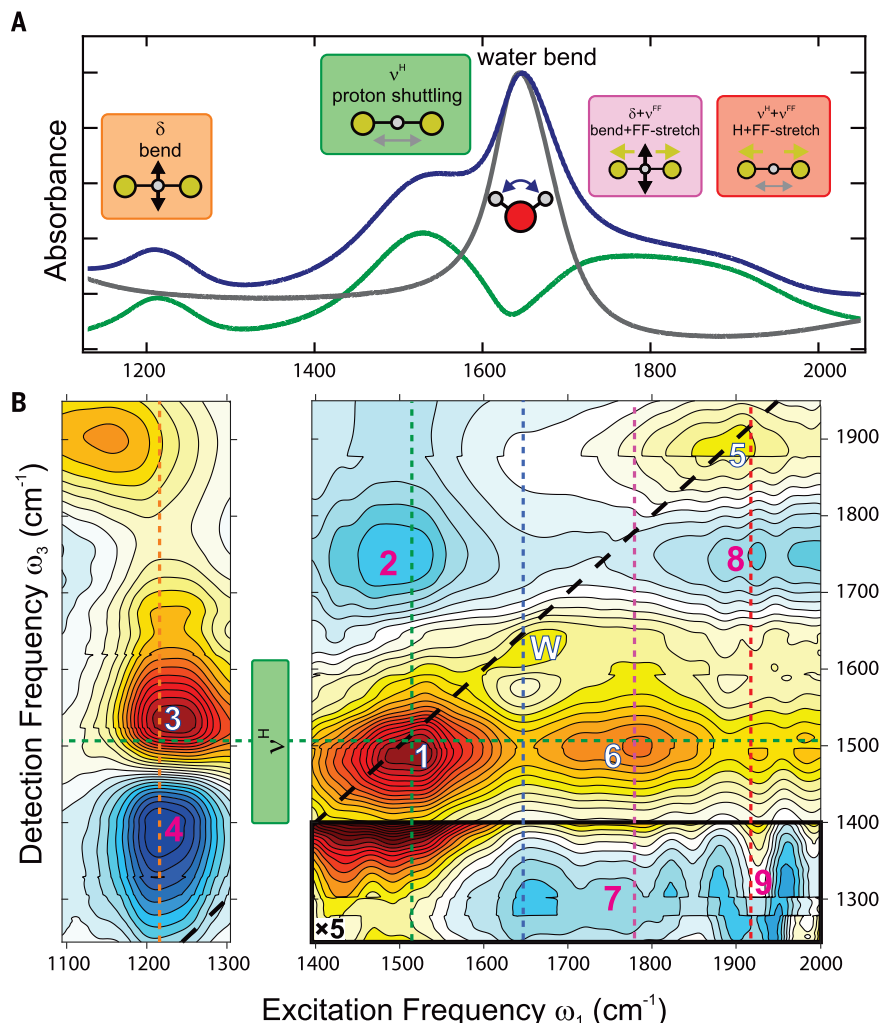


**Fig. 2. IR spectroscopy of short strong H-bonds.** (A) Linear infrared spectrum of aqueous 3.6 M  $\text{KHF}_2$  (blue), water (gray), and their difference (green). Cartoons represent molecular motions of the respective vibrational modes. (B) Early-time isotropic 2D IR spectrum of 3.6 M  $\text{KHF}_2$ . Waiting times  $\tau_2$  are 150 fs (left panel) and 100 fs (right panel).

(shuttling) mode,  $v^{\text{H}}$ . The H-O-H bending vibration of water appears at  $1652\text{ cm}^{-1}$ . The broad shoulder centered at  $1835\text{ cm}^{-1}$  shows two components in the difference spectrum. Solid-state spectrum (fig. S1B) indicates that the combination bands of F-F stretch and bending,  $\delta + v^{\text{FF}}$ , and F-F stretch and proton stretching,  $v^{\text{H}} + v^{\text{FF}}$ , are expected here. The strong anharmonicity and mode couplings have been observed in the gas-phase  $\text{HF}_2^-$  ion, where harmonic analysis at the CCSD(T) level of theory cannot even qualitatively reproduce the vibrational transitions, underestimating the proton shuttling mode by  $\sim 400\text{ cm}^{-1}$  (table S1). Considering the extreme anharmonicity of these short H-bonds in both gas-phase and condensed-phase systems, accurate experimental and theoretical investigations are required.

2D IR allows one to experimentally characterize the anharmonic nuclear potential by

measuring the change in absorption at a detection frequency  $\omega_3$  after exciting a vibration with frequency  $\omega_1$  (Fig. 2B). The method reveals sequential transitions up the vibrational ladder, both through a decrease in absorption corresponding to the negative  $|0\rangle \leftrightarrow |1\rangle$  ground-state bleach (yellow-red) and the positive  $|1\rangle \rightarrow |2\rangle$  excited-state absorption (ESA) (blue). The relative placement of these features characterizes the vibrational anharmonicity. Cross-peaks in a 2D spectrum characterize the anharmonic coupling between vibrations and provide a stringent test for vibrational assignments. 2D IR has been used in this context recently to characterize the strong H-bond potential of aqueous acids (17, 18).

Excitation of the proton shuttling  $v^{\text{H}}$  mode at  $\sim 1400$  to  $1600\text{ cm}^{-1}$  produced an intense bleach on the diagonal (1) (Fig. 2B) and a  $|1\rangle \rightarrow |2\rangle$  absorption peak (2) at higher detec-

tion frequencies ( $\omega_1, \omega_3$ ) = ( $1500, 1750\text{ cm}^{-1}$ ), indicating that  $\gamma = 1.17$ . This feature is a hallmark of the proton shared between two atoms in a single-well confined potential with steep walls that result in increased energy spacing between higher-lying vibrational levels. This feature is unusual because the excited-state absorption (2) is typically observed at lower frequencies than the bleach (1) and has been experimentally observed at higher frequencies only for the proton transfer mode ascribed to Zundel-like configurations of excess protons in water (17, 18).

Excitation of bifluoride bending modes  $\delta$  at  $\sim 1150$  to  $1280\text{ cm}^{-1}$  (Fig. 2B), followed by probing of  $v^{\text{H}}$ , revealed an intense cross-peak bleach at ( $1240, 1510\text{ cm}^{-1}$ ) (3), signifying strong coupling between the proton shuttling and bending motions. The ESA of this cross-peak at ( $1216, 1360\text{ cm}^{-1}$ ) (4) displayed an enormous downshift of  $150\text{ cm}^{-1}$  with respect to the bleach at  $1510\text{ cm}^{-1}$  ( $\gamma = 0.90$ ), an order of magnitude larger than typical molecular couplings of 10 to  $15\text{ cm}^{-1}$  (27). This feature illustrates how strongly the bending of the SHB reduces the proton's confinement and confirms that bending the ion transforms the proton potential from a single well toward a strongly anharmonic double well (fig. S3B). Excitation of the broad band in the  $1650$  to  $2000\text{ cm}^{-1}$  window revealed signs of two overlapping bands, which appear as peaks (5) and (6) with excitation frequencies of  $1920$  and  $1780\text{ cm}^{-1}$ . These peaks appear to correspond to the expected  $v^{\text{H}} + v^{\text{FF}}$  and  $\delta + v^{\text{FF}}$  bands, although the intense cross-peaks to the  $v^{\text{H}}$  at  $1500\text{ cm}^{-1}$  indicate strong anharmonicities that can mix the mode character. Indeed, given the assignment of the other resonances, peaks (8) and (9) may both result from the ESA of the  $v^{\text{H}}$  cross-peak. Peak (7) is the ESA corresponding to the  $v^{\text{H}}$  cross-peak bleach (6).

All these observations provided direct evidence of strong interactions between all H-bond coordinates that shape the potential for the shared proton (Fig. 1B). In linear SHBs, the proton is confined and its potential is superharmonic, but H-bond bending disrupts the confinement, making it strongly positively anharmonic. Modulation of the F...F distance affects the shared proton in the SHB, causing it to experience a large-amplitude variation of its confining potential from superharmonic to strongly anharmonic.

### Theoretical analysis

To quantitatively characterize the vibrational potential and spectral signatures of proton stretching in short H-bonds, we performed high-level quantum vibrational self-consistent field/virtual state configuration interaction (VSCF/VCI) calculations on  $(\text{HF}_2)^-(\text{H}_2\text{O})_6$  clusters using highly accurate many-body potential energy surface (see materials and methods)

(28). To reflect the asymmetric H-bonding environment of aqueous solution, the structure of the fully solvated  $(\text{HF}_2)^-(\text{H}_2\text{O})_6$  ion with three water H-bonds to each fluorine atom was optimized, and  $\sim 1100$  configurations were generated by varying F...F and F...H<sub>2</sub>O distances. For every configuration, the proton position was optimized by holding other atoms fixed, and VSCF/VCI calculations were performed within the local monomer framework (fig. S4). The key observations are summarized in Fig. 3.

First, the transition frequencies of the key infrared resonances (Fig. 3, A to D) followed a pronounced V-shape dependence on F-F distance ( $d_{\text{FF}}$ ). The calculations showed that this behavior arises from a shift between two qualitatively different types of H-bonds: SHBs for  $d_{\text{FF}} \leq 2.4$  Å (blue, Fig. 3, A to D) and conventional H-bonds at longer separations (red). The latter showcased a textbook behavior where decreasing F-F separation strengthens the H-bond, leading to softening of the stretch potential (Fig. 3, B and C) and increased stiffness of bending modes (Fig. 3D). In this regime, the correlation of F-F distance with frequency was diffuse ( $R^2 = 0.49$ ). Instead, the F-H distance provided a definitive correlation (Fig. 3E), corresponding to the near-linear

relation between O-H distance and frequency demonstrated for a vast variety of aqueous O-H...X H-bonds (29).

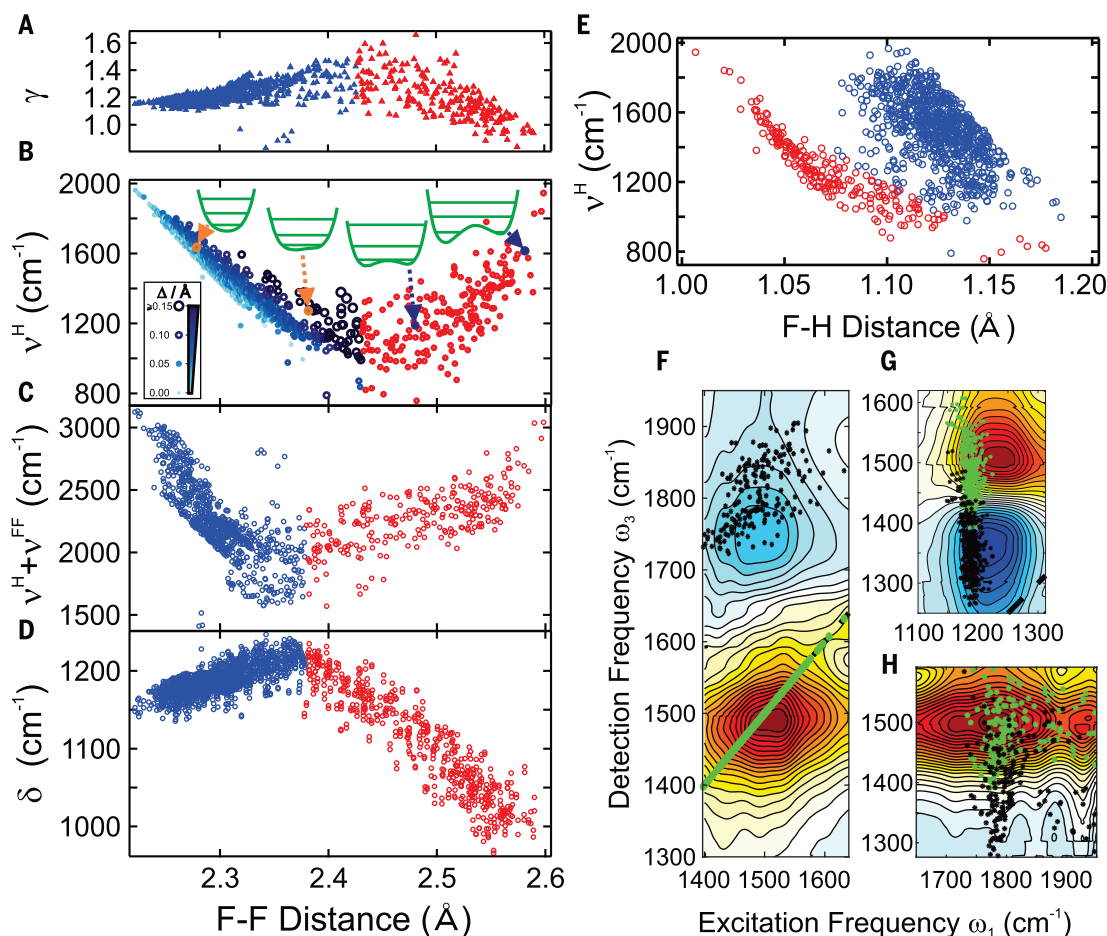
The SHBs demonstrated the opposite effect, showing a sharp anticorrelation of F-F distance with  $\nu^{\text{H}}$  frequency ( $R^2 = 0.89$ ): The stronger the H-bond, the higher the proton frequency. The  $\nu^{\text{H}} + \nu^{\text{FF}}$  frequency (Fig. 3C) followed a similar trend with the turning point at lower  $d_{\text{FF}}$ , because this mode includes F-F stretching that effectively decreases confinement compared to the  $\nu^{\text{H}}$  mode under identical separation. These dependences upon F-F expansion are a direct consequence of the emerging barrier that approaches and exceeds the zero-point energy of the proton and localizes it in a single F-H well (Fig. 1A).

Second, the highly anharmonic character of the SHB mixes the stretching and bending motions of the H-bond, and these interactions have the maximum effect near the crossover between SHBs and conventional H-bonds (fig. S11). In this region, the  $\nu^{\text{H}}$  potential has both steep walls and a flat bottom with the maximum value of  $\gamma$  reaching 1.6 (Fig. 3A), which renders it a classic example of a particle-in-a-box ( $\gamma = 1.67$ ); the combination bands of  $\nu^{\text{FF}}$  with  $\delta$  or  $\nu^{\text{H}}$  are quasi-degenerate and highly mixed, and solvation asymmetry governs the

mixing. Taking the trends in the vibrational frequencies for the transitions available to experiments, we selected all configurations that mapped onto the  $\nu^{\text{H}}$  2D IR data (Fig. 3, F to H) and observed a close correspondence to VSCF/VCI calculations over a narrow distribution of  $d_{\text{FF}} = 2.29$  to  $2.31$  Å in aqueous solution. This comparison indicates that peak (6) arose from the excitation of  $\delta + \nu^{\text{FF}}$ . ESA (7) is a unique transition to the state with all three modes excited and signifies a triple-mode coupling between all H-bond coordinates.

Third, the asymmetry of the solvent environment determines the structural asymmetry ( $\Delta$ ) of the  $\text{HF}_2^-$  proton position in SHBs (fig. S6) and thereby has a predictable effect on  $\nu^{\text{H}}$  frequency (Fig. 3B and fig. S9). Asymmetric ions absorb at higher frequencies for any given  $d_{\text{FF}}$ , and a strong linear  $\nu^{\text{H}}-d_{\text{FF}}$  anticorrelation ( $R^2 = 0.97$  to  $0.99$ ) existed for any given  $\Delta$ . As a result, it is the combination of changes in F-F distance and solvent asymmetry that determine  $\nu^{\text{H}}$  in the SHB regime. Although the experimentally observed frequencies for  $\nu^{\text{H}}$  can encompass a range of instantaneous solvent configurations, the water dynamics dictate that variations in these potentials may not be readily distinguished in these spectra. Nuclear magnetic resonance (NMR) experiments have

**Fig. 3. Crossover from conventional H-bonds to SHBs.** Influence of confinement on vibrational resonances: (A)  $\gamma$ ; (B)  $\nu^{\text{H}}$  (increasing proton asymmetry is mapped with color and marker size according to the legend). Proton potentials and energy levels in H-bonds at exemplary distances are shown; (C)  $\nu^{\text{H}} + \nu^{\text{FF}}$ ; (D)  $\delta$  modes. (E) Dependence of  $\nu^{\text{H}}$  on F-H distance. SHBs are blue, conventional H-bonds are red. (F to H) Experimental  $\nu^{\text{H}}$  bleach and ESA transitions upon excitation of (F)  $\nu^{\text{H}}$ , (G)  $\delta$ , and (H)  $\delta + \nu^{\text{FF}}$  overlaid with the corresponding VSCF/VCI transition frequency distributions (green for bleach, black for ESA) for  $d_{\text{FF}} = 2.29$  to  $2.31$  Å.



long pointed to  $\text{HF}_2^-$  ions as the exceptional example of a symmetric centered H-bond ( $\Delta = 0$ ) in solution (30, 31); however, these measurements average over the picosecond fluctuations in aqueous solvation environments. In principle, ultrafast 2D IR can observe a distribution of solvent environments as diagonal band elongation, but the lineshape of the  $\nu^{\text{H}}$  diagonal bleach (1) is round and homogeneous at the earliest waiting time (Fig. 2B), indicating that any differences in vibrational frequency due to distance and asymmetry of configurations are essentially indistinguishable by the lineshape on the time scale of the proton's vibrational motion.

The fluctuations in solvent-induced asymmetry do shape the single-well  $\text{HF}_2^-$  proton potential, but this perturbation was below its zero-point energy (fig. S10). This observation is similar to the recent interpretation of a homogeneous lineshape for the proton stretch ESA of aqueous acids (17), which was attributed to the fast electric field fluctuations shaping the potential below the zero-point energy. We found that the  $|1\rangle \rightarrow |2\rangle$  ESA transition was dominated by the confinement, whereas the  $|0\rangle \leftrightarrow |1\rangle$  bleach signal was sensitive to both the confinement and asymmetry (fig. S9). As a result, the  $(\text{F-H-F})^-$  can be considered as a model for the Zundel limiting form of the aqueous excess proton ( $\text{H}_2\text{O} \cdots \text{H}^+ \cdots \text{OH}_2$ ) devoid of flanking water OH-stretches.

### Nature of the strong H-bond

The crossover of H-bond character raises questions about when simple electrostatic descriptions of H-bonds (commonly accepted to dominate in formally ionic H-bonds, like  $\text{HF}_2^-$ ) (16, 21, 32) fail and explicit treatment of their electronic structure becomes important. Figure 4A shows that as  $d_{\text{FF}}$  shrank, the magnitude of the charges decreased continuously on the proton and acceptor fluorine, while increasing on the donor fluorine for the conventional H-bonds (navy) but decreasing in the SHB regime (green). For the shortest  $d_{\text{FF}}$ , the fluorine charges approached the same value. Both electrostatic  $\text{H} \cdots \text{F}$  attraction and  $\text{F} \cdots \text{F}$  repulsion counterintuitively decreased upon F-F reduction in the SHBs (fig. S12), but the net electrostatic bonding was weakly dependent on  $d_{\text{FF}}$ , with a clear preference of symmetric configurations (Fig. 4B). This result is in contrast with claims that symmetric SHBs bear a high-energy penalty and are anticatalytic compared to asymmetric bonds (20), or that a sudden jump in bonding energy occurs when crossing from conventional to SHBs (16).

Electrostatics accounted for only ~52 to 62% of the SHB bonding energy, and covalent, charge-transfer, and Pauli repulsion played an increasing role at short  $\text{D} \cdots \text{A}$  distances (fig. S13). A proper quantitative decomposition of these effects will require future work with

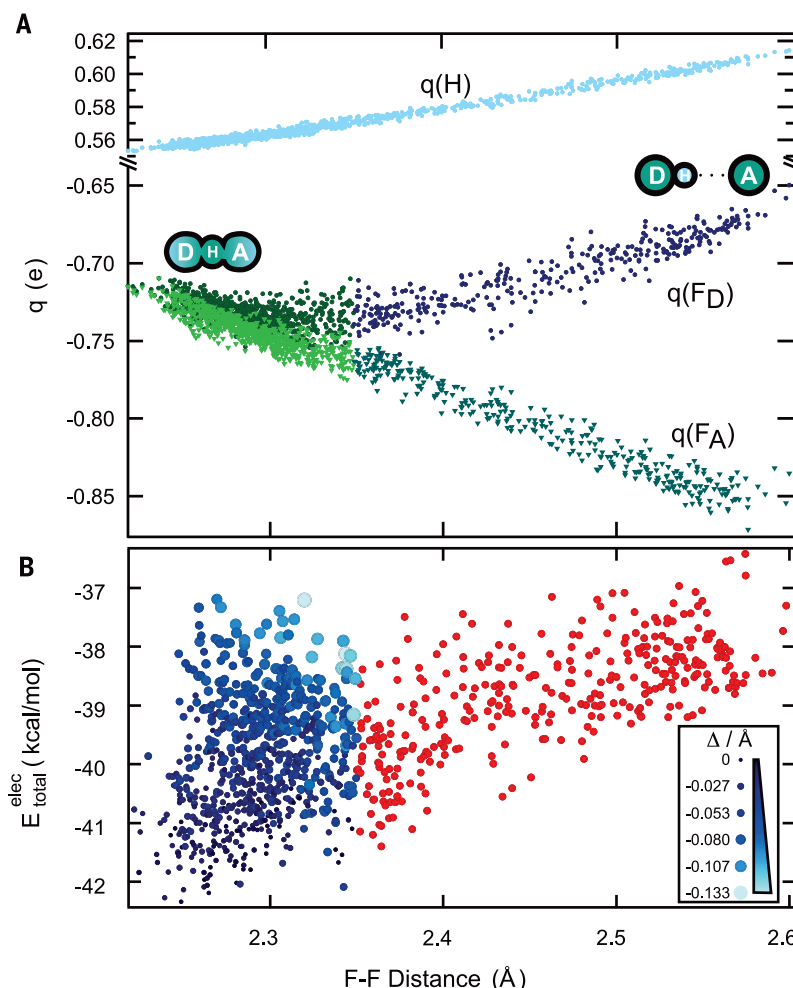


**Fig. 4. Crossover from the conventional H-bonding to H-mediated chemical bonding.** (A) Charge redistribution on constituent atoms upon donor-acceptor distance variation. (B) Electrostatic bonding component weakly increases with F-F distance with a preference for symmetric configurations. The proton asymmetry is encoded in the marker size and color. Conventional H-bonds are red, SHBs are blue.

advanced methods, like symmetry-adapted perturbation theory, although one can qualitatively understand the observed behavior with a simple molecular orbital picture. When  $d_{\text{FF}}$  decreased below 2.4 Å, F-F covalent bonding started to become a notable contributor to the SHB interactions (33). The hydrogen mediated this bonding, as the decreasing F-F distance enabled the overlap between the H 3s orbital and F 2p<sub>z</sub> orbitals, yielding a stabilization of the resulting  $\sigma_g$  molecular orbital (figs. S14 and S15). This chemical bonding, consistent with other three-center four-electron bonds (1, 5), is better characterized as a hydrogen-mediated donor-acceptor bond being qualitatively different from a conventional H-bond.

Our work sheds light on the distinctive and counterintuitive properties of SHBs: delocalization of the proton in the flat-bottom confined potential that yields H-bond superharmonicity; a blueshift of the proton stretch frequency upon H-bond strengthening; and major elec-

tron density redistributions that lead to the emergence of hydrogen-mediated donor-acceptor bonding. The structural simplicity of F-H-F system representing the bare H-bond atoms and its distinctive character as the “strongest H-bond” that one can readily describe as a chemical bond makes allowed one to identify spectroscopic trends and details of the SHB vibrational potential that will be applicable to all SHBs. Yet, F-H-F does not suffer from the complexities that hamper the interpretation of experimental data for larger molecular systems. These results suggest that the SHB lies at the tipping point where hydrogen bonding ends and chemical bonding begins.

### REFERENCES AND NOTES

1. G. C. Pimentel, *J. Chem. Phys.* **19**, 446–448 (1951).
2. A. C. Reiersolmoen et al., *Chem. Sci.* **68**, 42–61 (2020).
3. P. A. Frey, S. A. Whitt, J. B. Tobin, *Science* **264**, 1927–1930 (1994).
4. W. W. Cleland, M. M. Kreevoy, *Science* **264**, 1887–1890 (1994).
5. R. H. Crabtree, *Chem. Soc. Rev.* **46**, 1720–1729 (2017).



6. S. Yamaguchi *et al.*, *Proc. Natl. Acad. Sci. U.S.A.* **106**, 440–444 (2009).
7. P. Agback, T. Agback, *Sci. Rep.* **8**, 10078 (2018).
8. P. Kumar, E. H. Serpersu, M. J. Cuneo, *Sci. Adv.* **4**, eaas8667 (2018).
9. S. Dai *et al.*, *Nature* **573**, 609–613 (2019).
10. M. Elias *et al.*, *Nature* **491**, 134–137 (2012).
11. S. Zhou, L. Wang, *Chem. Sci.* **10**, 7734–7745 (2019).
12. K. Mackeprang, Z.-H. Xu, Z. Maroun, M. Meuwly, H. G. Kjaergaard, *Phys. Chem. Chem. Phys.* **18**, 24654–24662 (2016).
13. Q. Yu *et al.*, *J. Phys. Chem. A* **119**, 11623–11631 (2015).
14. A. Migliore, N. F. Polizzi, M. J. Therien, D. N. Beratan, *Chem. Rev.* **114**, 3381–3465 (2014).
15. G. A. Parada *et al.*, *Science* **364**, 471–475 (2019).
16. F. Hibbert, J. Emsley, “Hydrogen Bonding and Chemical Reactivity” in *Advances in Physical Organic Chemistry*, D. Bethell, Ed. (Elsevier, 1990), vol. 26, pp. 255–379.
17. F. Dahms, B. P. Fingerhut, E. T. J. Nibbering, E. Pines, T. Elsaesser, *Science* **357**, 491–495 (2017).
18. J. A. Fournier, W. B. Carpenter, N. H. C. Lewis, A. Tokmakoff, *Nat. Chem.* **10**, 932–937 (2018).
19. L. M. Oltrogge, S. G. Boxer, *ACS Cent. Sci.* **1**, 148–156 (2015).
20. A. Warshel, A. Papazyan, P. A. Kollman, *Science* **269**, 102–106 (1995).
21. C. L. Perrin, *Acc. Chem. Res.* **43**, 1550–1557 (2010).
22. B. L. Van Hoozen Jr., P. B. Petersen, *J. Chem. Phys.* **148**, 134309 (2018).
23. K. Kawaguchi, E. Hirota, *J. Chem. Phys.* **87**, 6838–6841 (1987).
24. P. G. Wenthold, R. R. Squires, *J. Phys. Chem.* **99**, 2002–2005 (1995).
25. R. Newman, R. M. Badger, *J. Chem. Phys.* **19**, 1207–1208 (1951).
26. G. Pérez-Hernández, J. González-Vázquez, L. González, *J. Phys. Chem. A* **116**, 11361–11369 (2012).
27. P. Hamm, M. T. Zanni, *Concepts and Methods of 2D Infrared Spectroscopy* (Cambridge Univ. Press, New York, 2011).
28. J. M. Bowman, S. Carter, X. Huang, *Int. Rev. Phys. Chem.* **22**, 533–549 (2003).
29. M. A. Boyer *et al.*, *J. Phys. Chem. Lett.* **10**, 918–924 (2019).
30. C. L. Perrin, Y. Wu, *J. Am. Chem. Soc.* **141**, 4103–4107 (2019).
31. P. Schah-Mohammadi *et al.*, *J. Am. Chem. Soc.* **122**, 12878–12879 (2000).
32. M. Meot-Ner (Mautner), *Chem. Rev.* **112**, PR22–PR103 (2012).
33. L. Bytautas, T. Nagata, M. S. Gordon, K. Ruedenberg, *J. Chem. Phys.* **127**, 164317 (2007).
34. B. Dereka, Q. Yu, N. H. C. Lewis, W. B. Carpenter, J. M. Bowman, A. Tokmakoff, Crossover from hydrogen to chemical bonding, Zenodo (2020). <https://doi.org/10.5281/zenodo.4060474>.

## ACKNOWLEDGMENTS

**Funding:** This work was supported by the U.S. Department of Energy grant DE-SC0014305 (B.D., N.H.C.L., W.B.C., A.T.) and the National Science Foundation grant CHE-1463552 (Q.Y., J.M.B.). Q.Y. and J.M.B. thank the Army Research Office (DURIP grant no. W911NF-14-1-0471) for funding a computer cluster where most of the calculations were performed. B.D. acknowledges the support from the Swiss National Science Foundation through Postdoc. Mobility fellowship grant P400P2\_180765. **Author contributions:** B.D. and A.T. conceived the idea and designed the research. B.D. performed the experiments and analyzed the experimental data. Q.Y. developed theoretical approaches and performed calculations. B.D. and Q.Y. analyzed the theoretical results. B.D., Q.Y., N.H.C.L., W.B.C., J.M.B., and A.T. discussed and interpreted the experimental and theoretical results. J.M.B. supervised theoretical work. A.T. supervised and guided the overall research. B.D. and A.T. wrote the paper with input from all authors.

**Competing interests:** None declared. **Data and materials**

**availability:** All other data needed to evaluate the conclusions in the paper are present in the paper or the supplementary materials. All the data have been uploaded to Zenodo (34).

## SUPPLEMENTARY MATERIALS

[science.sciencemag.org/content/371/6525/160/suppl/DC1](https://science.sciencemag.org/content/371/6525/160/suppl/DC1)

Materials and Methods

Supplementary Text

Figs. S1 to S22

Tables S1 to S3

References (35–56)

5 August 2020; accepted 20 October 2020

10.1126/science.abe1951

## REPORTS

### METEORITES

# Carbonaceous chondrite meteorites experienced fluid flow within the past million years

Simon Turner<sup>1\*</sup>, Lucy McGee<sup>1†</sup>, Munir Humayun<sup>2,3</sup>, John Creech<sup>1</sup>, Brigitte Zanda<sup>4,5</sup>

Carbonaceous chondritic meteorites are primordial Solar System materials and a source of water delivery to Earth. Fluid flow on the parent bodies of these meteorites is known to have occurred very early in Solar System history (first <4 million years). We analyze short-lived uranium isotopes in carbonaceous chondrites, finding excesses of <sup>234</sup>uranium over <sup>238</sup>uranium and <sup>238</sup>uranium over <sup>230</sup>thorium. These indicate that the fluid-mobile uranium ion U<sup>6+</sup> moved within the past few 100,000 years. In some meteorites, this time scale is less than the cosmic-ray exposure age, which measures when they were ejected from their parent body into space. Fluid flow occurred after melting of ice, potentially by impact heating, solar heating, or atmospheric ablation. We favor the impact heating hypothesis, which implies that the parent bodies still contain ice.

Carbonaceous chondritic meteorites are composed of material that formed in the early Solar System, perhaps beyond the orbit of Jupiter (1). Their elemental composition is similar to that of the Sun (2). Carbonaceous chondrites probably contain a record of early Solar System processes that have been modified or obscured to varying degrees by later processing (3). Some carbonaceous chondrites (the CI and CM subtypes) have undergone aqueous alteration (reactions with liquid water) as demonstrated by the presence of minerals, including hydrated silicates, magnetite, carbonates, sulfates, and halite (3, 4). Extinct radionuclide (<sup>53</sup>Mn–<sup>53</sup>Cr) dating of carbonates has shown that aqueous alteration began a few million years after the beginning of Solar System formation and persisted for at least 2 million to 4 million years (3, 5). Water ice has been observed on the surface of the asteroid (24) Themis (6), and the presence of radiogenic <sup>87</sup>Sr/<sup>86</sup>Sr in meteorite calcium sulfates indicates that fluid flow may have occurred recently (7).

The Th/U ratio of many chondrites and in the early Solar System (the current Solar System has a ratio Th/U = 3.72) are a subject of debate (8, 9). The present-day relative abundance of these radioactive elements provides information

on the time-integrated isotope evolution of the Solar System. However, variation of the Th/U ratio has been found even within chondrules from an individual sample of the carbonaceous chondrite Allende (10).

Radioactive uranium decays through a chain of reactions that produces a series of short-lived daughter nuclides. In a closed system, the activity ratio—the relative decay rates of two nuclides in the U-series chain—is exactly unity. The hexavalent uranium ion is fluid mobile, whereas thorium is not, so aqueous alteration is expected to fractionate U isotopes and the Th/U activity ratios, which we denote using parentheses—e.g., (<sup>230</sup>Th/<sup>238</sup>U)—to distinguish them from the weight or number ratios. Any resulting disequilibria persist for a time that depends on the half-life of the nuclides involved (11). The accessible time resolution of U-series isotope disequilibria is ~5 times the relevant half-life: ~1.25 million years ago for <sup>238</sup>U–<sup>234</sup>U and ~350,000 years ago for <sup>230</sup>Th–<sup>238</sup>U nuclide pairs. Many carbonaceous chondrites have cosmic-ray exposure ages <1 million years ago, indicating that they were only recently detached from their parent bodies (12, 13). Any fluid flow that occurred during their ejection, subsequent transport to Earth, and/or entry into the atmosphere is therefore potentially detectable using U-series disequilibria (14, 15).

We performed U-series measurements for a range of CV, CM, CI, and unclassified C-type meteorites (16). These include the Murray and Orgueil breccias, which contain numerous millimeter-sized clasts that have experienced more aqueous alteration than the surrounding host rock. This indicates that brecciation occurred after aqueous alteration. Figure 1A shows that these meteorites all have lower Th/U ratios than the bulk value of 3.72 inferred for the Solar System from time-integrated Pb isotope ratios

<sup>1</sup>Department of Earth and Environmental Sciences, Macquarie University, Sydney, NSW 2109, Australia.

<sup>2</sup>Department of Earth, Ocean & Atmospheric Science, Florida State University, Tallahassee, FL 32310, USA. <sup>3</sup>National High Magnetic Field Laboratory, Florida State University, Tallahassee, FL 32310, USA. <sup>4</sup>Institute de minéralogie, de physique des matériaux et de cosmochimie, Muséum National d'Histoire Naturelle, 75005 Paris, France. <sup>5</sup>Institute of celestial mechanics and ephemeris calculations, Observatoire de Paris, 75014 Paris, France.

\*Corresponding author. Email: [simon.turner@mq.edu.au](mailto:simon.turner@mq.edu.au)  
†Present address: Department of Earth Sciences, School of Physical Sciences, University of Adelaide, Adelaide, SA 5001, Australia.

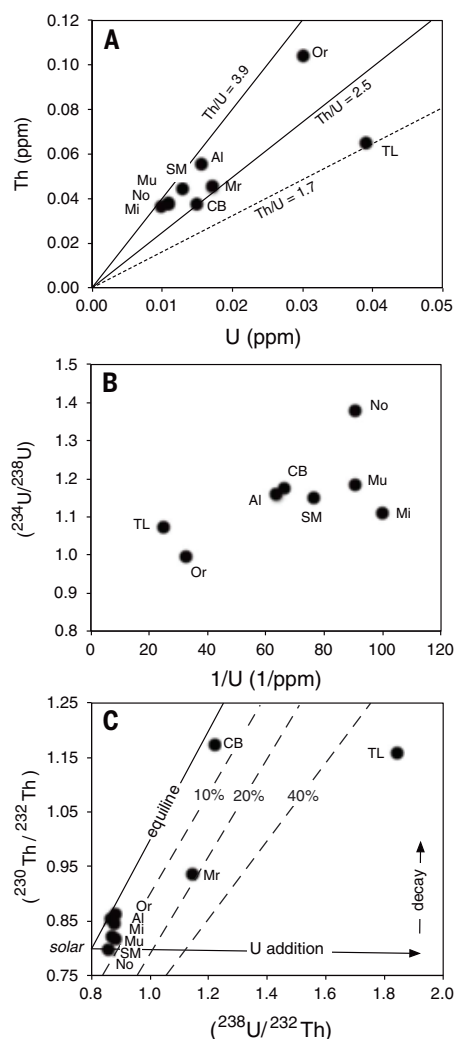


**Fig. 1. Elemental and isotopic U and Th variations.** (A) Abundances of U and Th in the nine carbonaceous chondrites we measured (black dots). The solid and dashed lines indicate constant Th/U ratios as labeled. Four samples have similar Th/U ratios, but Murray, Cold Bokkeveld, Orgueil, and Tagish Lake are enriched in U, i.e., appear below the solid line. (B)  $(^{234}\text{U}/^{238}\text{U})$  ratios plotted against  $1/\text{U}$ . The largest  $^{234}\text{U}$  excesses [ $(^{234}\text{U}/^{238}\text{U}) > 1$ ] occur in meteorites with the lowest U contents. (C) U-Th isotope diagram with equiline indicating U-Th secular equilibrium. Vectors illustrate the effects of U addition to a composition the same as that of the Solar System by fluid flow and subsequent decay of  $^{230}\text{Th}$  with time. Dashed lines indicate percentage of  $^{238}\text{U}$  excess. ppm, parts per million; Al, Allende; Mu, Murchison; CB, Cold Bokkeveld; SM, Sutter's Mill; No, Nogoya; TL, Tagish Lake; Or, Orgueil; Mi, Mighei; Mr, Murray. Error bars are smaller than the symbol sizes in all panels.

(17). Some of the carbonaceous chondrites have higher Th/U values than Earth's ratio of 3.4, as inferred from the geoneutrino flux (18). We measure a range of Th/U ratios from 3.60 to

1.64, with the lowest value being the Tagish Lake meteorite, which has a lower ratio than previously reported (19). We confirmed this result by repeating the Tagish Lake measurement. Variation in Th/U both between and within individual carbonaceous chondrites has been documented previously—for example, ratios in Orgueil range from 1.06 to 3.79, Murchison from 2.85 to 4.06, and Allende from 2.05 to 3.46 (8). We conclude that the Th/U ratios of carbonaceous chondrites vary substantially even within an individual meteorite (10).

We performed sequential leaching experiments (16), finding that the disequilibria are pervasive but heterogeneous. These experiments also confirm earlier studies that found that >50% of excess  $^{234}\text{U}$  is labile and located in low-temperature phases like calcium sulphates, whereas Th was likely contained in phosphates (20). We analyzed ~1-cm-sized samples that we expect to be representative of the bulk meteorites. This rules out an  $\alpha$ -particle recoil origin for the disequilibria because that effect occurs on ~50- $\mu\text{m}$  length scales. We find that carbonaceous chondrites all have excesses of  $^{234}\text{U}$  that range from 9 to 38%. The largest  $^{234}\text{U}$  excesses occur in those meteorites with the lowest U contents (Fig. 1B). Most samples have 4 to 8% deficits of  $^{230}\text{Th}$ , whereas the Tagish Lake sample has a 37% deficit of  $^{230}\text{Th}$ . Figure 1C compares these carbonaceous chondrites to the U-Th equiline [the line of equal activity ratios, where  $(^{230}\text{Th}/^{232}\text{Th}) = (^{238}\text{U}/^{232}\text{Th})$ ]. They all have excesses of  $^{238}\text{U}$ , implying either (i) variable recent U addition to materials that had a wide range of initial  $^{230}\text{Th}/^{238}\text{U}$  ratios or (ii) U addition over a range of times to materials with the same  $^{230}\text{Th}/^{238}\text{U}$ . We conclude that the carbonaceous chondrites we analyzed have all gained  $^{234}\text{U}$  relative to  $^{238}\text{U}$  and gained  $^{238}\text{U}$  relative to  $^{230}\text{Th}$  and that the resulting disequilibria have had insufficient time to decay back to equilibrium (Fig. 2A). Because many of the samples lie close to the equiline on Fig. 1C and the initial Th/U ratio is debated, it is difficult to estimate the timing of U addition from these results. An absolute age constraint is imposed by the half-lives of the nuclides. However, an upper limit for the age of the last U migration within these meteorites can be calculated by assuming no initial Th (21). This model is shown in Fig. 2A and indicates maximum ages of 80,000 to 180,000 years (assuming a single addition event followed by decay). In some cases, this estimate is less than the meteorite cosmic-ray exposure ages (Fig. 2B).

There are several possible explanations for the observed U-series disequilibria. We first consider terrestrial contamination, even though all of the samples were from meteorite falls collected soon after landing on Earth. Uranium is fluid mobile in the hexavalent state and  $^{234}\text{U}$

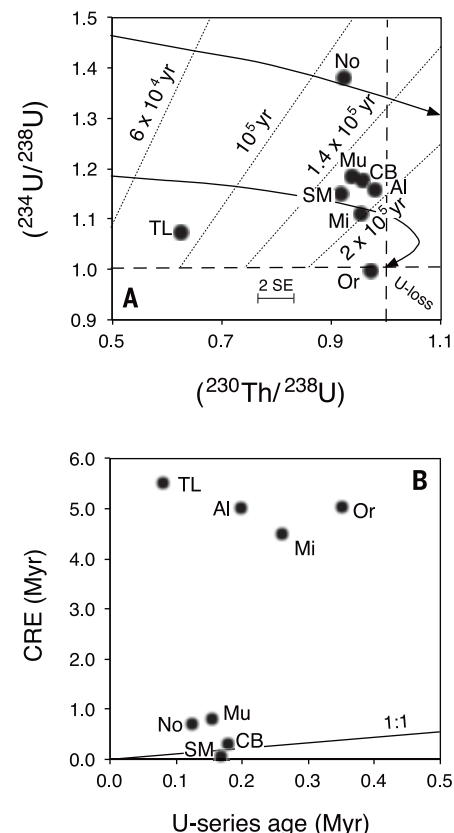


**Fig. 2. Uranium-series disequilibria diagrams for carbonaceous chondrites.** (A)  $(^{234}\text{U}/^{238}\text{U})$  ratios plotted against  $(^{230}\text{Th}/^{238}\text{U})$  ratios with age calculations; dotted diagonal lines indicate ages for samples that have the same initial disequilibria. Curved lines with arrows indicate time-evolution for samples with different initial activity ratios, and dashed lines indicate equilibrium values [after (21)]. The data imply that U mobility (addition) occurred between 140,000 and 200,000 years ago (maximum ages). yr, years. (B) U-Th isotope ages inferred from (A) plotted against cosmic-exposure ages (CRE) (table S1). For most meteorites, the CRE age is well above the 1:1 ratio (solid line). Meteorite labels are the same as in Fig. 1. Error bars are smaller than the symbol size, except for  $(^{230}\text{Th}/^{238}\text{U})$  in (A), which is shown as 2 standard errors (2 SE). Myr, million years.

resides in recoil-damaged crystallographic sites, but rain does not contain U (11). Therefore, if some of the samples were exposed to rainfall before collection (which we cannot exclude), then the result would be loss of U relative to Th, forming a horizontal distribution on the equiline diagram and preferential loss of  $^{234}\text{U}$ . However, neither effect is observed in Fig. 1C. River and ground waters contain trace abundances of  $^{234}\text{U} > ^{238}\text{U} > \text{Th}$  (11), but none of the samples are known to have interacted with such waters. Allende has excess  $^{234}\text{U}$  yet equilibrium  $^{238}\text{U}$ - $^{230}\text{Th}$ , which is not consistent with

acquiring U from surface waters, and it was recovered from a desert environment (22). The Tagish Lake sample was collected from a frozen lake surface within a few days of falling and so was never in contact with terrestrial soils, rainfall, or melt water. This sample

has the largest disequilibrium we measured [and replicated (16)]. Calcium sulfate veins in Orgueil (CI) have been suggested to have a terrestrial origin, in reactions with atmospheric humidity that lead to repeated dissolution and precipitation during sample storage (23). Such

veins are not a common feature of the other meteorites we have analyzed, and this process would result in alteration areas similar in size to the dimensions of the sulfate veins (<1 mm), with both excesses and deficits of  $^{234}\text{U}$ , whereas at the larger scale (~1 cm) measured in our experiments, the U-series would be in equilibrium. We do not measure any samples with deficits of  $^{234}\text{U}$  or in equilibrium, though Orgueil is close. We conclude that the disequilibria do not have a terrestrial origin.

Cosmic-ray irradiation cannot produce  $^{234}\text{U}$  either by spallation or by neutron capture (24). Nor can it explain the observed excesses of  $^{238}\text{U}$  activity over  $^{230}\text{Th}$  activity. We verified this using numerical calculations and measurements of  $^{150}\text{Sm}/^{149}\text{Sm}$  as a neutron dosimeter (16). Our results indicate that fluid-assisted U migration occurred. This implies that ice persists on carbonaceous chondrite parent bodies to the present day. This is consistent with the occurrence of evaporite minerals like halite in carbonaceous chondrites (4) and the presence of water ice on the surface of the asteroid (24) Themis (6).

Our results demonstrate that recent fluid flow extended beyond the local scale (>1 cm, the size of our samples). We favor fluid flow similar to that proposed for primordial alteration (3). We estimate the scale of recent fluid flow as greater than that of the present diameters of carbonaceous chondrites (>1 m). Continuous fluid flow on the parent bodies of these meteorites since their formation would have destroyed the carbonates that formed in the first 10 million years after Solar System formation (3, 5). We have not found any materials with  $^{234}\text{U}$  deficits and  $^{230}\text{Th}$  excesses. We consider three alternative hypotheses to explain the U-series disequilibria.

The first possibility is solar heating (25), in which meteoroids are warmed above the melting point of ice when their orbits pass close to the Sun (Fig. 3A). We calculate (16) that some carbonaceous parent asteroids may retain primordial ice but find that an object that spends a few months warming up at perihelion (the point of closest approach to the Sun) would quickly melt its ice. This would result in a film of fluid evaporating at the surface of the meteoroid, transporting any dissolved U to the exterior of the object. This exterior would be lost during atmospheric entry, so the observed low Th/U, high  $^{234}\text{U}$ , and high  $^{238}\text{U}$  would not be expected in any chondrite.

The second possibility is ablation of a porous carbonaceous chondrite during atmospheric entry, which could drive an ice melt front ahead of the ablation front before the fusion crust forms, leading to  $(^{234}\text{U}/^{238}\text{U}) > 1$  and  $(^{230}\text{Th}/^{238}\text{U}) < 1$  (compare Figure 2A) in the meteorite interior (Fig. 3B). Although atmospheric entry is too short (a few seconds) for substantial heating to occur, the total mass

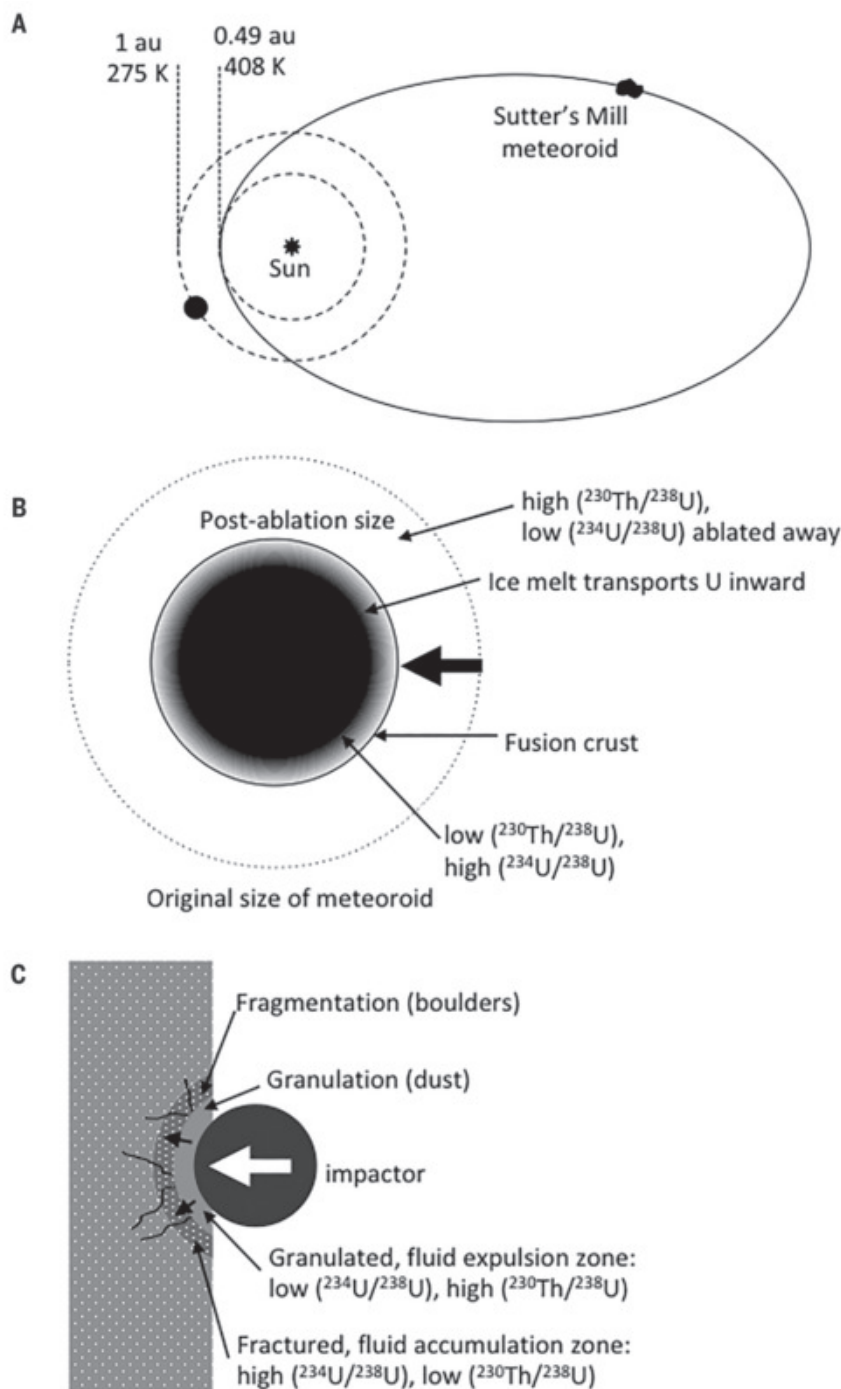


**Fig. 3. Hypotheses that could explain the uranium-series disequilibria in carbonaceous chondrites.** (A) Solar heating scenario with illustration of the orbit of the Sutter's Mill meteoroid, the orbit of Earth, and their respective perihelion temperatures. au, astronomical units. (B) Atmospheric ablation scenario. (C) Collisional ice melting scenario. See text for descriptions of each scenario.



loss by ablation could be 50 to 80% in the atmosphere. We assume that the porous object has ice partially filling the pores. As the fusion crust migrates inward, silicate melting would be restricted to the outer ~1 mm, but a warm region with liquid water (melted ice) would extend inward about 2 to 3 mm behind the fusion crust. This moving boundary layer (melt front) would eventually traverse about 50 to 80% of the mass of the meteoroid, transporting  $^{234}\text{U}$  and  $^{238}\text{U}$  inward ahead of the fusion crust. This would leave behind a residue with complementary fractionations that is then removed by ablation, forming ablation melt spherules. These ablation melt spherules would show systematic deficits of  $^{234}\text{U}$  and excesses of  $^{230}\text{Th}$ . Fusion crusts would show similar disequilibrium, complementary to the chondritic interior. To produce variable disequilibria throughout the chondrite, the U-enriched fluid would need to percolate throughout the interior of the meteorite after the fall, as it warms up. The fluid flow and U migration would then date from entry into the atmosphere. Testing this scenario would require analysis of very short-lived U-series isotopes such as  $^{210}\text{Po}$  (half-life of 138 days) in samples collected within days of falling, which was not possible. This hypothesis could explain why the apparent U-series ages are in some cases less than the cosmic-ray exposure ages (Fig. 2B). However, it should also result in a horizontal array on Fig. 1C for Tagish Lake and Murray [using the ( $^{230}\text{Th}/^{232}\text{Th}$ ) ratio, we calculate that the original Th/U = 2.6 and 3.3, respectively]. Most other chondrites lie close to the equiline, i.e., show no disequilibria in ( $^{230}\text{Th}/^{238}\text{U}$ ), implying that the ( $^{234}\text{U}/^{238}\text{U}$ ) ratio must have been perturbed more than 350,000 years ago. Solar heating would result in loss of any ice during the multiple perihelion approaches made by a meteoroid before Earth atmospheric entry, precluding the ablation hypothesis (16).

The third scenario is collisional melting (Fig. 3C) by impact heating when these meteorites were broken off their parent bodies (26), melting ice and producing the fluid flow required to explain the observed disequilibria. There is petro-fabric (petrologic alignment of minerals) evidence for impact-related deformation in these meteorites, and the degree of aqueous alteration correlates with the strength of, and may in some cases postdate, fabric formation (27). Moderate velocity (~1 km/s) impacts are sufficient to melt ice (14). Our observations are consistent with postaccretionary surface regolith fluid flow on the parent bodies (28) and indicate that they still contain substantial quantities of ice. Large carbonaceous asteroids may have initially experienced convection of their interiors (29). After an early sharp burst of aqueous activity (indicated by the  $^{53}\text{Mn}$ - $^{53}\text{Cr}$  data), the exhaustion of radio-

active heat-producing  $^{26}\text{Al}$  would have left them frozen, ending fluid flow until episodic impacts ejected parts of the parent bodies. This collisional melting hypothesis relates the observed U-series disequilibria to their ejection from the parent body. Material immediately in front of the impactor would be crushed to dust (granulated), and any ice in it would melt. The resulting fluid would be driven into the porous fractured rock behind the granulated zone. As illustrated in Fig. 3C, this process transports U (and other materials, including organics) into the porous fragments that are then accelerated away from the parent body, some into Earth-crossing orbits. Because impacts can occur at any time, this scenario could explain the wide and nonzero range of apparent U-series ages. Direct samples of solid carbonaceous asteroid material would then show no U-series disequilibria.

Recent fluid transport of U implies potential recent effects on other fluid-mobile species, including organics, alkalis, boron, and other elements. This could potentially affect the radiogenic parent-daughter Rb/Sr ratios—for example, a 10% recent change in a present-day Rb/Sr ratio would be equivalent to a 0.01 difference in a time-integrated  $^{87}\text{Sr}/^{86}\text{Sr}$  ratio at 4.56 billion years ago (7). Differences in initial U isotope and U/Pb ratios could change the dating of the age of the Solar System by 1 million to 2 million years (13, 14). The continuing presence of ice in carbonaceous chondrites could deliver water (30) and methane (31) to Earth.

## REFERENCES AND NOTES

1. T. S. Kruijer, C. Burkhardt, G. Budde, T. Kleine, *Proc. Natl. Acad. Sci. U.S.A.* **114**, 6712–6716 (2017).
2. H. Palme, H. S. C. O'Neill, in *Treatise on Geochemistry*, vol. 2, H. D. Holland, K. K. Turekian, Eds. (Elsevier, 2014), pp. 1–38.
3. A. J. Brearley, in *Treatise on Geochemistry*, vol. 1, H. D. Holland, K. K. Turekian, Eds. (Elsevier, 2003), pp. 247–268.
4. D. J. Barber, *Geochim. Cosmochim. Acta* **45**, 945–970 (1981).
5. G. K. MacPherson, K. Nagashima, A. N. Krot, P. M. Doyle, M. A. Ivanova, *Geochim. Cosmochim. Acta* **201**, 260–274 (2017).
6. H. Campins et al., *Nature* **464**, 1320–1321 (2010).
7. J. D. Macdougall, G. W. Lugmair, J. F. Kerridge, *Nature* **307**, 249–251 (1984).
8. A. Rocholl, K. P. Jochum, *Earth Planet. Sci. Lett.* **117**, 265–278 (1993).
9. J. S. Goreva, D. S. Burnett, *Meteorit. Planet. Sci.* **36**, 63–74 (2001).
10. J. Blichert-Toft, C. Gopel, M. Chaussidon, F. Albarède, *Geochim. Cosmochim. Acta* **280**, 378–394 (2020).
11. B. Bourdon, S. Turner, G. M. Henderson, C. C. Lundstrom, *Rev. Mineral. Geochem.* **52**, 1–21 (2003).
12. O. Eugster, S. Lorenzetti, U. Krahenbuhl, K. Marti, *Meteorit. Planet. Sci.* **42**, 1351–1371 (2007).
13. P. Scherer, L. Schultz, *Meteorit. Planet. Sci.* **35**, 145–153 (2000).
14. A. Bouvier, J. Blichert-Toft, F. Moynier, J. D. Vervoort, F. Albarède, *Geochim. Cosmochim. Acta* **71**, 1583–1604 (2007).
15. Y. Amelin et al., *Geochim. Cosmochim. Acta* **73**, 5212–5223 (2009).

16. Materials and methods are available as supplementary materials.
17. J. Blichert-Toft, B. Zanda, D. S. Ebel, F. Albarède, *Earth Planet. Sci. Lett.* **300**, 152–163 (2010).
18. M. Javoy, E. Kaminski, *Earth Planet. Sci. Lett.* **407**, 1–8 (2014).
19. J. M. Friedrich, M.-S. Wang, M. E. Lipschutz, *Meteorit. Planet. Sci.* **37**, 677–686 (2002).
20. C. H. Stirling, A. N. Halliday, E.-K. Potter, M. B. Andersen, B. Zanda, *Earth Planet. Sci. Lett.* **251**, 386–397 (2006).
21. K. Thiel, R. Vorwerk, R. Saager, H. D. Stupp, *Earth Planet. Sci. Lett.* **65**, 249–262 (1983).
22. R. S. Clarke Jr., E. Jarosewich, B. Mason, J. Nelsen, M. Gómez, J. R. Hyde, *The Allende, Mexico, Meteorite Shower* (Smithsonian Institution Press, 1970).
23. M. Gounelle, M. E. Zolensky, *Meteorit. Planet. Sci.* **36**, 1321–1329 (2001).
24. E. R. Toth, M. A. Fehr, M. Friebe, M. Schonbachler, *Geochim. Cosmochim. Acta* **274**, 286–301 (2020).
25. N. Chaumard, B. Devouard, M. Delbo, A. Provost, B. Zanda, *Icarus* **220**, 65–73 (2012).
26. E. Amsellem, F. Moynier, B. Mahan, P. Beck, *Icarus* **339**, 113593 (2020).
27. A. W. Tait, K. R. Fisher, P. Srinivasan, J. I. Simon, *Earth Planet. Sci. Lett.* **454**, 213–224 (2016).
28. R. E. Grimm, H. Y. McSweeney Jr., *Icarus* **82**, 244–280 (1989).
29. P. A. Bland, B. J. Travis, *Sci. Adv.* **3**, e1602514 (2017).
30. A. Morbidelli et al., *Meteorit. Planet. Sci.* **35**, 1309–1320 (2000).
31. W. Guo, J. M. Eiler, *Geochim. Cosmochim. Acta* **71**, 5565–5575 (2007).

## ACKNOWLEDGMENTS

We thank the U.S. National Museum of Natural History (Smithsonian Institution, Washington, DC), the Field Museum (Chicago), and the Muséum National d'Histoire Naturelle (Paris) for providing chondrite samples. T. Irving, T. McCoy, G. Hupé, and Y. Amelin provided assistance with sourcing samples. D. Krietsch kindly provided the cosmic-ray exposure ages for Murray and Mighei. We thank four reviewers for their constructive comments. We also thank the organizers and participants of the 2017 Accrete meeting in Nice for their feedback and H. O'Neill for reading and commenting on the manuscript. We thank G. Hupé, B. Fectay, and C. Fectay for providing field collection details on the Tagish Lake sample. B.Z. thanks F. Colas for information about the physics of meteoroids. **Funding:** S.T. acknowledges a Distinguished Professors award at Macquarie University and the support from staff in the Macquarie GeoAnalytical Laboratories. M.H. acknowledges the National High Magnetic Field Laboratory that is supported by the National Science Foundation through NSF/DMR-1644779 and the state of Florida. **Author contributions:** S.T. and M.H. conceived the project. S.T. and L.M. performed the U-series analyses, and J.C. undertook the Sm analyses. All authors contributed to writing and reviewing the manuscript. **Competing interests:** The authors declare no competing interests. **Data and materials availability:** The U and Th measurements are listed in tables S1 and S2, and the Sm measurements used for neutron fluence calculations are in table S3. The meteorite samples were sourced from a variety of museums and collections, as listed in the supplementary materials. These samples were consumed during the analysis process. Each meteorite has at least one other sample archived in a museum, as listed in the supplementary materials.

## SUPPLEMENTARY MATERIALS

science.sciencemag.org/content/371/6525/164/suppl/DC1  
Materials and Methods  
Supplementary Text  
Figs. S1 to S3  
Tables S1 to S3  
References (32–43)

14 May 2020; accepted 1 December 2020  
10.1126/science.abc8116

## STELLAR ASTROPHYSICS

# Lithium pollution of a white dwarf records the accretion of an extrasolar planetesimal

B. C. Kaiser<sup>1\*</sup>, J. C. Clemens<sup>1</sup>, S. Blouin<sup>2</sup>, P. Dufour<sup>3,4</sup>, R. J. Hegedus<sup>1</sup>, J. S. Reding<sup>1</sup>, A. Bédard<sup>3</sup>

Tidal disruption and subsequent accretion of planetesimals by white dwarfs can reveal the elemental abundances of rocky bodies in exoplanetary systems. Those abundances provide information on the composition of the nebula from which the systems formed, which is analogous to how meteorite abundances inform our understanding of the early Solar System. We report the detection of lithium, sodium, potassium, and calcium in the atmosphere of the white dwarf Gaia DR2 4353607450860305024, which we ascribe to the accretion of a planetesimal. Using model atmospheres, we determine abundance ratios of these elements, and, with the exception of lithium, they are consistent with meteoritic values in the Solar System. We compare the measured lithium abundance with measurements in old stars and with expectations from Big Bang nucleosynthesis.

**W**hite dwarfs are remnants of main-sequence stars that have exhausted their available nuclear fuel and have expelled their outer layers to leave a hot, planet-sized object, which cools over billions of years. Their high surface gravities cause stratification of elements by mass, so undisturbed white dwarf atmospheres should exhibit spectral lines of only the lightest element present, usually hydrogen or helium. However, many white dwarf spectra show evidence of atmospheric contamination by heavier elements (referred to as pollution), which in some cases is accompanied by an excess in infrared emission caused by a surrounding dust disk. These are attributed to the tidal disruption and accretion of extrasolar planetesimals (1–4).

Surveys indicate that up to half of hot white dwarfs show atmospheric pollution (2, 5, 6) by elements that are expected to sink below the surface on time scales of approximately days to approximately millions of years (7), so planetesimal disruption and accretion must be a frequent event. In white dwarf atmospheres where the abundances of all major rock-forming elements have been measured, the extrasolar planetesimal compositions resemble those of the bulk Earth or other rocky Solar System bodies (8–10). Abundances have mostly been measured from white dwarfs with effective temperatures >4500 K, as cooler (therefore older) white dwarfs are faint and difficult to study (9, 11, 12). A sample of 230 metal-polluted white dwarfs included only two with cooling ages >7 billion years (Gyr), and most were younger than 4 to 5 Gyr (11). The Solar System is 4.5 Gyr old, so the

compositions of exoplanets that formed at earlier times are unknown.

We observed the white dwarf (WD) Gaia DR2 4353607450860305024 (WD J1644–0449, hereafter referred to as WD J1644–0449) as part of a survey of ultracool objects selected from the Gaia Data Release 2 (DR2) catalog (13, 14), chosen to have temperatures <4500 K and total (main-sequence plus white dwarf cooling) ages ≥7 Gyr. We expect elemental abundances of these systems to reflect Galactic chemical enrichment at their epoch of formation, as has been measured in the atmospheres of similarly old stars (15). WD J1644–0449 is not in previous white dwarf catalogs derived from Gaia data (16, 17) be-

cause its color is redder than the usual selection criteria. We obtained optical spectra of WD J1644–0449 using the Goodman Spectrograph mounted on the 4.1-m Southern Astrophysical Research (SOAR) telescope (18). We examined archival infrared photometry (18) and found no infrared excess indicative of a cool companion or dust disk.

Our spectra show (Fig. 1) that WD J1644–0449 is a white dwarf of spectral type DZ that exhibits several heavy element absorption features. The effective temperature is too low for the spectrum to show optical absorption lines of atomic H or He even if they dominate the atmosphere (as we expect). The dominant spectral feature is a broad and deep Na I D absorption line reminiscent of two previously known white dwarfs: WD J2356–209 and (Sloan Digital Sky Survey) SDSS J133001.13+643523.7 (hereafter SDSS J1330+6435) (19, 20). Broad Ca II H and K lines overlap a broad Ca I line, and a further broad dip is present at the wavelength of a molecular band of MgH. We also identified a K I line, and, in two different instrument modes, we detected an absorption feature centered at 6710 Å, which we identify as a Li I line with a rest wavelength of 6708 Å.

We examined published spectra of other white dwarfs known to have broad Na I D lines (19, 20) and found that SDSS J1330+6435 also shows an absorption line at the location of the same Li line. This line was visible in a prior publication but was not identified, perhaps because of the low signal-to-noise ratio of the spectrum (21). WD J2356–209 does not show

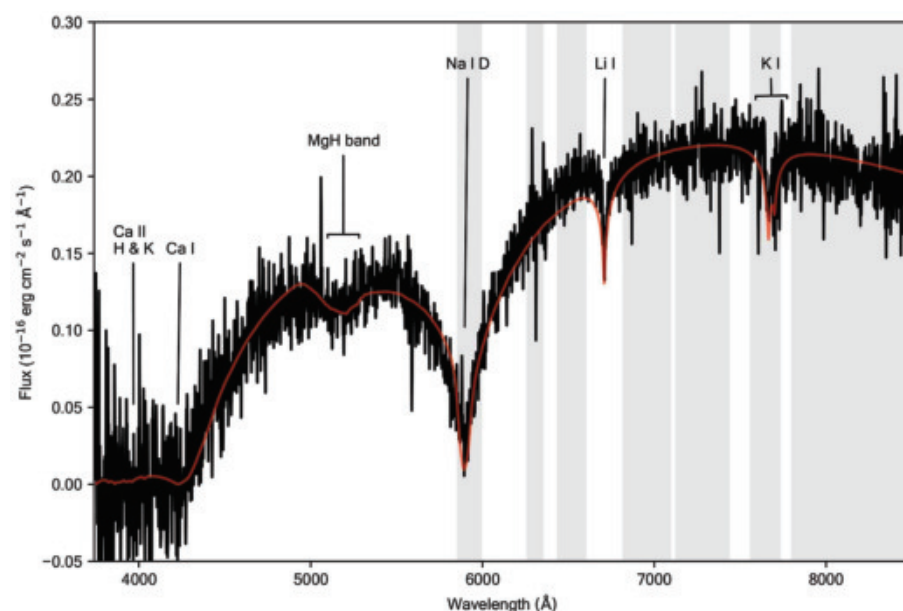


**Fig. 1. Spectrum of WD J1644–0449.** Data (black) are overlaid with the best-fitting model (red line). The spectrum was constructed by combining two observations above and below 6800 Å (18). Gray bands show regions of telluric absorption from Earth's atmosphere (31); we applied telluric corrections at wavelengths >6800 Å. Labeled absorption lines include Ca II H and K (3934 and 3969 Å), Ca I (4226 Å), MgH band (5190 Å), Na I D (5893 Å), Li I (6708 Å), and K I (7665 and 7699 Å).

<sup>1</sup>Department of Physics and Astronomy, University of North Carolina, Chapel Hill, NC, USA. <sup>2</sup>Los Alamos National Laboratory, Los Alamos, NM, USA. <sup>3</sup>Département de Physique, Université de Montréal, Montréal, QC, Canada. <sup>4</sup>Institut de Recherche sur les Exoplanètes, Université de Montréal, Montréal, QC, Canada.

\*Corresponding author. Email: ben.kaiser@unc.edu

any evidence for Li absorption (19). We re-observed WD J2356–209 with the Goodman Spectrograph and again did not detect any Li or K lines (fig. S3), but we placed upper limits on their abundances that are tighter than previously available (12).

To determine atmospheric abundances, we calculated a grid of white dwarf atmosphere models by adding Li to previously published models (22). We also used models to evaluate the mass contained in the surface convection layer and the masses of accreted elements that are expected to be mixed in this convection zone. We used a theoretical mass-radius relation to estimate the stellar mass and radius consistently with all the data (18, 23). We estimated the temperature of WD J1644–0449 to be  $3830 \pm 230$  K—very cool for a metal-polluted white dwarf.

The detection of Li allows us to investigate the Li abundance of extrasolar planetesimals and compare them with both the atmospheres of stars with similar ages (24) and the expectations of Li formation during Big Bang nucleosynthesis (BBN) (25). Li can be strongly depleted in stellar atmospheres, including in the Sun, because it is consumed by nuclear reactions at a lower temperature than H. However, Li is incorporated into meteorites and planetesimals because it is only moderately volatile—condensing at higher temperatures than either Na or K (26). Thus, measurements of Li-polluted white dwarfs may offer a record of ancient Li abundances. However, the measurements must be corrected for a possible bias introduced by the different rates at which elements sink in a white dwarf atmosphere.

Planetesimal accretion onto a white dwarf occurs in three phases. In the increasing phase, the star is actively accreting material from one or more planetesimals, and the atmospheric abundance ratios equal those of the accreted body. If accretion continues for several elemental sinking time scales, an equilibrium between accretion and diffusion is reached in which atmospheric abundance ratios approach a steady-state value that differs from that of the accreted body, but which can be corrected using the ratio of the sinking time scales (7, 10, 18). Once all accretion stops, the atmospheric abundances decrease exponentially at rates that are generally slower for lighter elements; abundance ratios then depend on both sinking times and the time elapsed since steady state accretion halted (7, 18). Figure 2 shows our measured abundance ratios and corrected ratios calculated using the sinking times for Na, K, and Ca. For reference, we have also plotted abundance ratios for meteorites and a selection of Solar System bodies.

The K/Ca ratio in WD J1644–0449 remains nearly constant over accretion phases owing to the similar atomic masses and sinking times

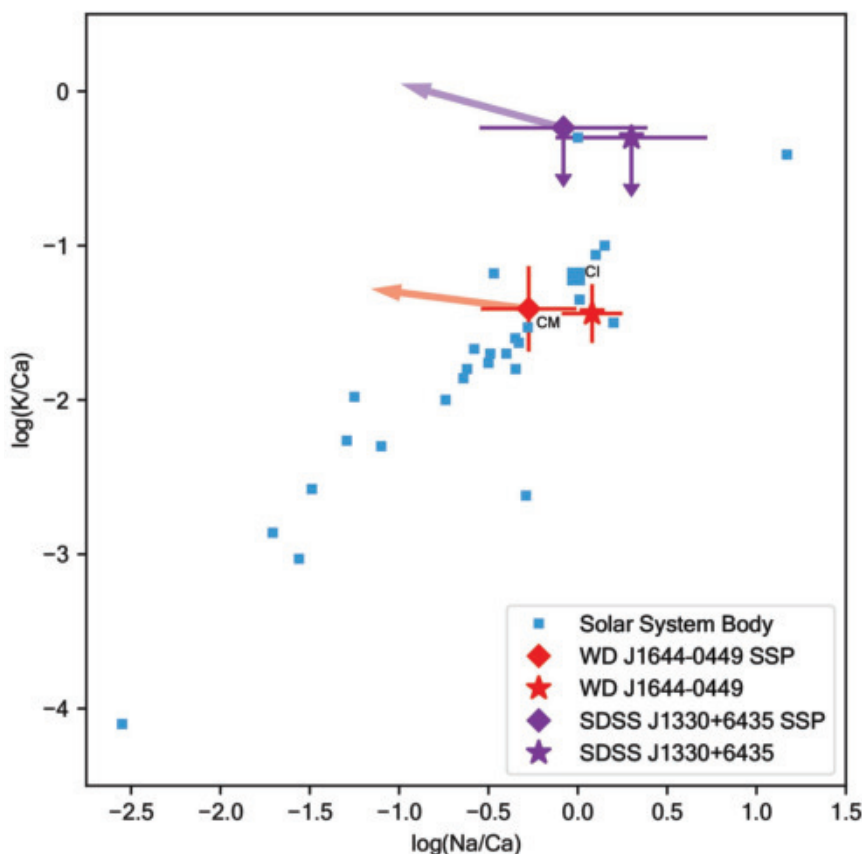


**Fig. 2. Abundance ratios K/Ca and Na/Ca in the white dwarf planetesimals and Solar System bodies.**

Logarithmic number abundances for the white dwarfs WD J1644–0449 (red) and SDSS J1330+6435 (purple) are compared with Solar System bodies (blue), including meteorites (18). The two chondrite groups discussed in the text (CI and CM) are labeled. Star symbols show the measured atmospheric abundances, and diamond symbols show the inferred accreted body abundances, assuming steady-state accretion phase (SSP). Downward arrows indicate upper limits. Leftward arrows show corrections to the inferred abundance ratios if the accretion has been in the decreasing phase for five Ca sinking times (see table S4), in the style of previous work (10). Error bars show  $1\sigma$  uncertainties (18).

of these elements. Thus, the accreted body had a K/Ca ratio that falls in a region centered between the carbonaceous Ivuna-type (CI) and the carbonaceous Mighei-type (CM) chondrite meteorites shown in Fig. 2, regardless of the accretion phase. Chondrites are the most primitive meteorites in the Solar System, and CI chondrites are used to establish the initial composition of the Solar nebula on the basis of their abundance similarities to many elements in the Solar atmosphere (26). Unlike K, Na sinks more slowly than Ca, so the Na/Ca ratio would be enhanced in the atmosphere during a decreasing phase of accretion. Figure 2 shows that the inferred Na/Ca ratio would, in this case, be lower than that of CI or CM chondrites and would deviate from the sequence defined by Solar System bodies. This sequence arises because K and Na have nearly identical condensation temperatures and are both lithophile elements (i.e., they accumulate in the crust of differentiated bodies). On the basis of measurements of Na/Ca in the atmo-

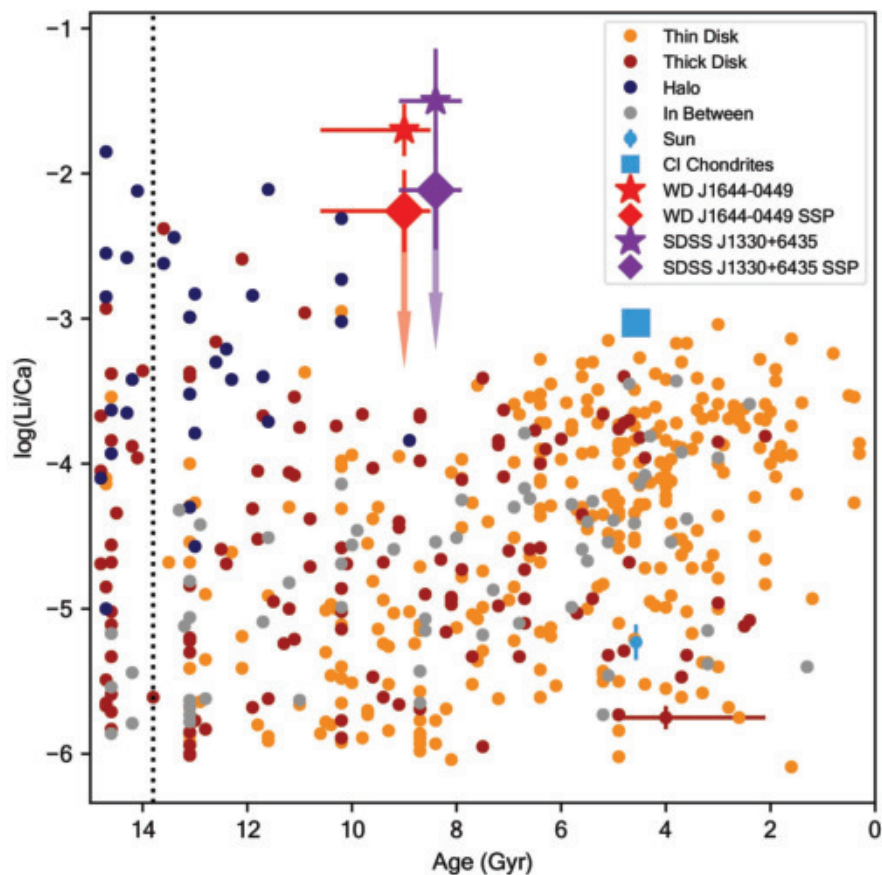
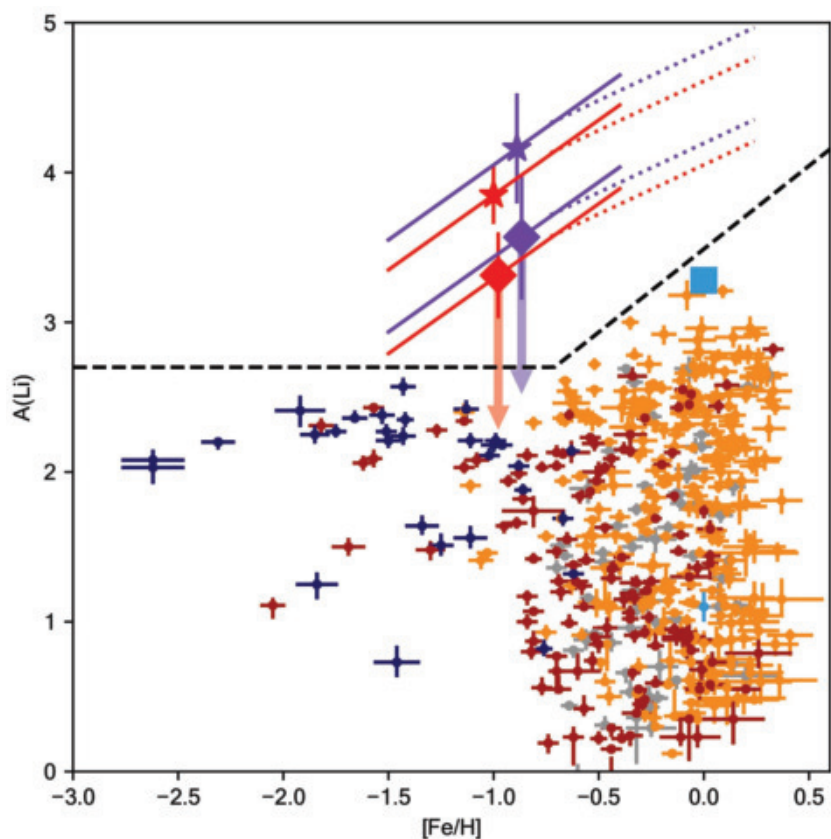
spheres of old stars in the solar neighborhood, which show mean deviations of  $<0.2$  dex from Solar ratios (27), we expect that the Na/Ca abundance ratio in the gas from which WD J1644–0449 and its planetesimals formed is consistent with the Solar System value, within the uncertainties. Thus, we expect the planetesimal abundances for K/Ca and Na/Ca to fall along the same sequence as that defined by rocky bodies in the Solar System. This implies that the accretion is currently in a steady-state or early decreasing phase for WD J1644–0449. However, we also consider other accretion phases in our subsequent analysis.

The history of Li in the Galaxy is different from other elements and is more uncertain because of its destruction by nuclear burning in stars; in the solar atmosphere, Li is depleted by two orders of magnitude compared with the CI chondrites (26). BBN theory predicts that a substantial amount of Li formed in the first 5 min after the Big Bang. The



**Fig. 3. Li/Ca evolution in the solar neighborhood.**

Logarithmic Li/Ca is shown as a function of age for a sample of typical stars from the Solar neighborhood (circles), and error bars in the lower right show typical  $1\sigma$  uncertainties (15, 29). Because Li is consumed in stars, the highest values of  $\log(\text{Li}/\text{Ca})$  at each age represent the best proxy for interstellar gas values (32). The atmospheric values for the Li-polluted white dwarfs are shown with the same symbols as in Fig. 2 (18). White dwarf vertical error bars correspond to  $1\sigma$  uncertainties; horizontal error bars correspond to the 68% confidence intervals. CI chondrites (blue square;  $1\sigma$  vertical error bars are smaller than the symbol) represent the initial value for the Solar System, which is greater than the Sun's atmosphere (blue circle; vertical error bars correspond to  $1\sigma$  uncertainties) (26, 33). The age of the Universe is marked with the vertical dotted line (34).

**Fig. 4. Spite diagram for the same sources as shown in previous figure.** Li abundance  $A(\text{Li})$  is shown as a function of iron abundance  $[\text{Fe}/\text{H}]$ . Predicted values for BBN and expected Galactic Li enrichment history are shown as the dashed line (25, 28). Symbols are the same as in Fig. 3. Sloped lines for each white dwarf represent abundances rescaled to  $A(\text{Li})$  using  $\log(\text{Ca}/\text{Fe})$  relations for thick disk (solid lines) and thin disk (dotted lines) Galactic stellar populations, extending over the full range of those populations (18). The white dwarf symbol placement in  $[\text{Fe}/\text{H}]$  is representative and does not depict a preferred value (18).

interstellar medium (ISM) abundance remained close to the BBN value until the ISM Fe content was enriched by explosions of massive stars to a value of  $-1.0 < [\text{Fe}/\text{H}] < -0.5$ , where  $[\text{Fe}/\text{H}]$  is the logarithm of the Fe-to-H ratio relative to the solar value (28). After that time, Li production by other nucleosynthetic processes increased the Li in the ISM (28). Ca was not produced during BBN, but rather formed by subsequent stellar nucleosynthesis and injection into the ISM. Consequently, we expect the Li/Ca ratio to be highest in the very early Universe because the Ca abundance was negligible, whereas the Li abundance reflected the BBN value. Figure 3 shows Li/Ca measurements in atmospheres of typical stars in the solar neighborhood (15, 29) compared with the two Li-bearing white dwarfs. As expected, the highest Li/Ca values measured are in the atmospheres of the oldest stars.

Figure 3 shows the inferred abundance ratios for the accreted bodies in WD J1644–0449 and SDSS J1330+6435 under the assumptions of steady-state and decreasing accretion phases (18). The steady state Li/Ca is higher than that of stars of a similar age, which could reflect Li depletion by nuclear reactions in the main-sequence stars. We also cannot rule out systematic differences in the age determination methods for white dwarfs and the nearby sample of stars. The latter are, in some cases, unphysically old; Fig. 3 includes several stars with inferred ages that are greater than the age of the Universe. Our white dwarf ages were calculated using published parameterizations of stellar lifetimes and white dwarf cooling ages, under the assumption of single-star evolution (18). The most likely mass of WD J1644–0449 is  $0.45 \pm 0.12$  solar masses, which suggests that it may have lost mass through binary-star evolution, but there is no evidence of a companion. The Li/Ca measurements are also higher than the CI chondrites, which reflects the lower abundance of Ca that prevailed at earlier times rather than an excess of Li over solar values.

The Li abundance history of the Galaxy is conventionally plotted on a Spite diagram (Fig. 4), which shows the Li abundance [defined as  $A(\text{Li}) \equiv 12 + \log(\text{Li}/\text{H})$ ] as a function of the iron abundance  $[\text{Fe}/\text{H}]$ , a proxy for age with lower values reflecting earlier epochs (30). Figure 4 shows a plateau at the expected BBN value of  $A(\text{Li})$ , followed by a rising segment that reflects later enrichment. The measured  $A(\text{Li})$  in the old, low- $[\text{Fe}/\text{H}]$  local stars under the plateau is lower than the  $A(\text{Li})$  predicted by BBN. The origin of this deficit is unknown, so it is commonly referred to as the cosmological Li problem (24).

As with Solar System meteorites (26), for the accreted planetesimals, we cannot measure the Li-to-H ratio to get  $A(\text{Li})$  directly.

We used published Ca/Fe values measured from the atmospheres of the main Galactic stellar populations to convert our Li/Ca into Li/Fe values (18). Unlike Li/Ca ratios, the Ca/Fe values measured from main-sequence stellar atmospheres reflect the gas from which these stars formed, which provides a sound basis for translating Li/Ca to Li/Fe. Figure 4 shows  $A(\text{Li})$  for each accreted extrasolar planetesimal as lines extending from  $-1.5 < [\text{Fe}/\text{H}] < 0.24$ . We have included representative lines for the inferred  $A(\text{Li})$  for WD J1644–0449 and SDSS J1330+6435 for two possible Galactic stellar populations (18). Each population line has a different transformation for Ca/Fe, but both have an upward slope reflecting the increase in our calculated  $A(\text{Li})$  that results from increasing  $[\text{Fe}/\text{H}]$ . We also illustrate the differing  $A(\text{Li})$  inferred for steady-state accretion or decreasing phase accretion.

The accreted bodies in Fig. 4 extend at low metallicities to  $A(\text{Li})$  values compatible with BBN, but they do not extend below that prediction. They do not show evidence for the cosmological Li problem exhibited by the local stars. Thus, these Li-bearing extrasolar planetesimals represent an alternative to old stars for gaining insight into the primordial Li abundance, the earliest epochs of chemical enrichment in our Galaxy, and the properties of ancient exoplanets.

## REFERENCES AND NOTES

1. M. Jura, *Astrophys. J.* **584**, L91–L94 (2003).
2. B. Zuckerman, D. Koester, I. N. Reid, M. Hünsch, *Astrophys. J.* **596**, 477–495 (2003).
3. M. Jura, E. D. Young, *Annu. Rev. Earth Planet. Sci.* **42**, 45–67 (2014).
4. J. Farihi, *New Astron. Rev.* **71**, 9–34 (2016).
5. B. Zuckerman, C. Melis, B. Klein, D. Koester, M. Jura, *Astrophys. J.* **722**, 725–736 (2010).
6. D. Koester, B. T. Gänsicke, J. Farihi, *Astron. Astrophys.* **566**, A34 (2014).
7. D. Koester, *Astron. Astrophys.* **498**, 517–525 (2009).
8. B. Klein, M. Jura, D. Koester, B. Zuckerman, C. Melis, *Astrophys. J.* **709**, 950–962 (2010).
9. S. Xu et al., *Astron. J.* **158**, 242 (2019).
10. A. Swan et al., *Mon. Not. R. Astron. Soc.* **490**, 202–218 (2019).
11. M. A. Hollands, D. Koester, V. Alekseev, E. L. Herbert, B. T. Gänsicke, *Mon. Not. R. Astron. Soc.* **467**, 4970–5000 (2017).
12. S. Blouin et al., *Astrophys. J.* **872**, 188 (2019).
13. T. Prusti et al., *Astron. Astrophys.* **595**, A1 (2016).
14. L. Lindegren et al., *Astron. Astrophys.* **616**, A2 (2018).
15. T. Bensby, S. Feltzing, M. S. Oey, *Astron. Astrophys.* **562**, A71 (2014).
16. F. M. Jiménez-Esteban et al., *Mon. Not. R. Astron. Soc.* **480**, 4505–4518 (2018).
17. N. P. Gentile Fusillo et al., *Mon. Not. R. Astron. Soc.* **482**, 4570–4591 (2019).
18. Materials and methods are available as supplementary materials.
19. B. R. Oppenheimer, N. C. Hambly, A. P. Digby, S. T. Hodgkin, D. Saumon, *Science* **292**, 698–702 (2001).
20. H. C. Harris et al., *Astron. J.* **126**, 1023–1040 (2003).
21. D. Homeier et al., in *14th European Workshop on White Dwarfs*, vol. 334 of *Astronomical Society of the Pacific (ASP) Conference Series*, D. Koester, S. Moehler, Eds. (ASP, 2005), pp. 209–214.
22. S. Blouin, P. Dufour, N. F. Allard, *Astrophys. J.* **863**, 184 (2018).

23. G. Fontaine, P. Brassard, P. Bergeron, *Publ. Astron. Soc. Pac.* **113**, 409–435 (2001).
24. M. Spite, F. Spite, *Nature* **297**, 483–485 (1982).
25. A. Coc, J.-P. Uzan, E. Vangioni, *J. Cosmol. Astropart. Phys.* **2014**, 050 (2014).
26. K. Lodders, H. Palme, H. P. Gail, in *Astronomy, Astrophysics, and Cosmology: Solar System*, vol. 4B, *Landolt-Börnstein - Group VI Astronomy and Astrophysics*, J. E. Trümper, Ed. (Springer, 2009), chap. 4.4.
27. N. R. Hinkel, F. X. Timmes, P. A. Young, M. D. Pagano, M. C. Turnbull, *Astron. J.* **148**, 54 (2014).
28. V. Grisoni, F. Matteucci, D. Romano, X. Fu, *Mon. Not. R. Astron. Soc.* **489**, 3539–3546 (2019).
29. T. Bensby, K. Lind, *Astron. Astrophys.* **615**, A151 (2018).
30. R. Rebolo, P. Molero, J. E. Beckman, *Astron. Astrophys.* **192**, 192–205 (1988).
31. S. Moehler et al., *Astron. Astrophys.* **568**, A9 (2014).
32. X. Fu, A. Bressan, P. Molero, P. Marigo, *Mon. Not. R. Astron. Soc.* **452**, 3256–3265 (2015).
33. A. Bouvier, M. Wadhwa, *Nat. Geosci.* **3**, 637–641 (2010).
34. P. A. R. Ade et al., *Astron. Astrophys.* **594**, A13 (2016).
35. B. C. Kaiser, Lithium pollution of a white dwarf records the accretion of an extrasolar planetesimal (Reduction and Analysis Code), version 2, Zenodo (2020); <http://doi.org/10.5281/zenodo.4244680>.
36. S. Blouin et al., Lithium pollution of a white dwarf records the accretion of an extrasolar planetesimal (Atmosphere/envelope code), version 1, Zenodo (2020); <http://doi.org/10.5281/zenodo.4244665>.

## ACKNOWLEDGMENTS

We benefited from conversations with M. Wadhwa and A. Mann. This work is based on observations obtained at the SOAR telescope, which is a joint project of the Ministério da Ciência, Tecnologia, Inovações e Comunicações do Brasil (MCTIC/LNA); the U.S. National Science Foundation's National Optical-Infrared Astronomy Research Laboratory (NOIRLab); the University of North Carolina at Chapel Hill (UNC); and Michigan State University (MSU). This work has made use of data from the European Space Agency (ESA) mission Gaia ([www.cosmos.esa.int/gaia](http://www.cosmos.esa.int/gaia)), processed by the Gaia Data Processing and Analysis Consortium (DPAC) ([www.cosmos.esa.int/web/gaia/dpac/consortium](http://www.cosmos.esa.int/web/gaia/dpac/consortium)). Funding for DPAC has been provided by national institutions, in particular the institutions participating in the Gaia Multilateral Agreement. The Pan-STARRS1 Surveys (PS1) and the PS1 public science archive have been made possible through contributions by the Institute for Astronomy, the University of Hawaii; the Pan-STARRS Project Office; the Max-Planck Society and its participating institutes, the Max Planck Institute for Astronomy, Heidelberg, and the Max Planck Institute for Extraterrestrial Physics, Garching; The Johns Hopkins University; Durham University; the University of Edinburgh; the Queen's University Belfast; the Harvard-Smithsonian Center for Astrophysics; the Las Cumbres Observatory Global Telescope Network Incorporated; the National Central University of Taiwan; the Space Telescope Science Institute; the National Aeronautics and Space Administration (NASA) under grant no. NNX08AR22G issued through the Planetary Science Division of the NASA Science Mission Directorate; the National Science Foundation grant no. AST-1238877; the University of Maryland; Eotvos Lorand University (ELTE); the Los Alamos National Laboratory; and the Gordon and Betty Moore Foundation. Funding for the Sloan Digital Sky Survey (SDSS) has been provided by the Alfred P. Sloan Foundation, the Participating Institutions, NASA, the National Science Foundation, the U.S. Department of Energy, the Japanese Monbukagakusho, and the Max Planck Society. The SDSS is a joint project of the University of Chicago, Fermilab, the Institute for Advanced Study, the Japan Participation Group, the Johns Hopkins University, Los Alamos National Laboratory, the Max Planck Institute for Astronomy (MPIA), the Max Planck Institute for Astrophysics (MPA), New Mexico State University, the University of Pittsburgh, Princeton University, the U.S. Naval Observatory, and the University of Washington. **Funding:** S.B. acknowledges support from the Laboratory Directed Research and Development program of Los Alamos National Laboratory under project no. 20190624PRD2. A.B. acknowledges support from NSERC (Canada) and the FRQNT (Québec). **Author contributions:** B.C.K. cowrote the manuscript, obtained observations, coidentified the Li line, and performed all calculations except the atmospheric and envelope modeling. J.C.C. cowrote the manuscript, coidentified the Li line, and supervised all

calculations except the atmospheric and envelope modeling. S.B. performed the atmospheric modeling calculations and cowrote the manuscript. P.D. assisted with the atmospheric modeling calculations. R.J.H. obtained observations and assisted with the Li line identification. J.S.R. obtained observations. A.B. performed the envelope modeling and cowrote the supplement. **Competing interests:** The authors declare no competing interests. **Data and materials availability:** The reduced Goodman spectra of WD J1644–0449 and WD J2356–209 are available in data S1 to S5. The SDSS J1330+6435 spectra are available from the SDSS archive

(<https://dr9.sdss.org/basicSpectra>) with plate 0603, modified Julian date 52056, and fiber 0510. Our data reduction and analysis code is available on Zenodo (35). The atmosphere and envelope modeling software was written by a combination of authors (S.B. and P.D.) and nonauthors (G. Fontaine, P. Brassard, and P. Bergeron), so we cannot distribute the source code. An executable version with adjustable input parameters is available on Zenodo (36).

#### SUPPLEMENTARY MATERIALS

[science.sciencemag.org/content/371/6525/168/suppl/DC1](https://science.sciencemag.org/content/371/6525/168/suppl/DC1)

Materials and Methods  
Supplementary Text  
Figs. S1 to S7  
Tables S1 to S5  
References (37–77)  
Data S1 to S5

30 June 2020; accepted 4 December 2020  
Published online 17 December 2020  
10.1126/science.abd1714

## CORONAVIRUS

# Transmission of SARS-CoV-2 on mink farms between humans and mink and back to humans

Bas B. Oude Munnink<sup>1\*</sup>, Reina S. Sikkema<sup>1</sup>, David F. Nieuwenhuijse<sup>1</sup>, Robert Jan Molenaar<sup>2</sup>, Emmanuelle Munger<sup>1</sup>, Richard Molenkamp<sup>1</sup>, Arco van der Spek<sup>3</sup>, Paulien Tolsma<sup>4</sup>, Ariene Rietveld<sup>5</sup>, Miranda Brouwer<sup>5</sup>, Noortje Bouwmeester-Vincken<sup>6</sup>, Frank Harders<sup>7</sup>, Renate Hakze-van der Honing<sup>7</sup>, Marjolein C. A. Wegdam-Blans<sup>8</sup>, Ruth J. Bouwstra<sup>2</sup>, Corine GeurtsvanKessel<sup>1</sup>, Annemiek A. van der Eijk<sup>1</sup>, Francisca C. Velkers<sup>9</sup>, Lidwien A. M. Smit<sup>10</sup>, Arjan Stegeman<sup>9</sup>, Wim H. M. van der Poel<sup>7</sup>, Marion P. G. Koopmans<sup>1</sup>

Animal experiments have shown that nonhuman primates, cats, ferrets, hamsters, rabbits, and bats can be infected by severe acute respiratory syndrome coronavirus 2 (SARS-CoV-2). In addition, SARS-CoV-2 RNA has been detected in felids, mink, and dogs in the field. Here, we describe an in-depth investigation using whole-genome sequencing of outbreaks on 16 mink farms and the humans living or working on these farms. We conclude that the virus was initially introduced by humans and has since evolved, most likely reflecting widespread circulation among mink in the beginning of the infection period, several weeks before detection. Despite enhanced biosecurity, early warning surveillance, and immediate culling of animals in affected farms, transmission occurred between mink farms in three large transmission clusters with unknown modes of transmission. Of the tested mink farm residents, employees, and/or individuals with whom they had been in contact, 68% had evidence of SARS-CoV-2 infection. Individuals for which whole genomes were available were shown to have been infected with strains with an animal sequence signature, providing evidence of animal-to-human transmission of SARS-CoV-2 within mink farms.

In late December 2019, severe acute respiratory syndrome coronavirus 2 (SARS-CoV-2) was identified as the cause of a viral pneumonia outbreak, possibly related to a seafood and live animal market in Wuhan, China (1). Since then, SARS-CoV-2 has spread across the world. By 8 October 2020, more than 36.1 million people had been infected with SARS-CoV-2, resulting in more than 1 million deaths (2). In the Netherlands, more than 155,000 infections have been con-

firmed, more than 6500 SARS-CoV-2–related deaths have been reported, and nonpharmaceutical interventions have been put into place to prevent further spread of SARS-CoV-2 (3).

In view of the similarities of the new virus and SARS-CoV-1, a zoonotic origin of the outbreak was suspected and linked to a Wuhan fresh market where various animals—including fish, shellfish, poultry, wild birds, and exotic animals—were sold. However, other cases with onset well before the period correlated with the Wuhan market-associated cluster were observed, which suggests the possibility of other sources (4). Although closely related coronaviruses found in bats (5, 6) and pangolins (7, 8) have the greatest sequence identity to SARS-CoV-2, the most likely divergence of SARS-CoV-2 from the most closely related bat sequence is estimated to have occurred between 1948 and 1982 (9). Therefore, the animal reservoir(s) of SARS-CoV-2 is(are) yet to be identified.

Similarly to SARS-CoV-1, SARS-CoV-2 binds to the host angiotensin-converting enzyme 2

(ACE2) receptor. On the basis of ACE2 similarities, a range of different animals have been used as models. Experimental infections in dogs (10), cats (10–13), ferrets (10, 14), hamsters (15, 16), rhesus macaques (17), tree shrews (18), cynomolgus macaques (19), African green monkeys (20), common marmosets (21), rabbits (22), and fruit bats (23) have shown that these species are susceptible to SARS-CoV-2, and experimentally infected cats, tree shrews, hamsters, and ferrets could also transmit the virus. By contrast, experimental infection of pigs and several poultry species with SARS-CoV-2 proved to be unsuccessful (10, 23, 24). SARS-CoV-2 has also sporadically been identified in naturally infected animals. In the United States and Hong Kong, SARS-CoV-2 RNA has been detected in dogs (25). In the Netherlands, France, Hong Kong, Belgium, Spain, and the United States, cats have tested positive for SARS-CoV-2 by reverse transcription polymerase chain reaction (RT-PCR) (26–30). Furthermore, SARS-CoV-2 has been detected in four tigers and three lions in a zoo in New York (31). In Italy, the Netherlands, and Wuhan, China, antibodies to SARS-CoV-2 have been detected in cats (29, 32, 33). Recently, SARS-CoV-2 was detected in farmed mink (*Neovison vison*), resulting in signs of respiratory disease and increased mortality (29, 34).

In response to the outbreaks in mink farms, the Dutch national response system for zoonotic diseases was activated. Although the public health risk of exposure to animals with SARS-CoV-2 was determined to be low, increased awareness of animals' possible involvement in the COVID-19 epidemic was needed. Therefore, from 20 May 2020 onward, mink farmers, veterinarians, and laboratories were obliged to report symptoms in mink (family Mustelidae) to the Netherlands Food and Consumer Product Safety Authority (NFCPSA), and an extensive surveillance system was established (35).

Whole-genome sequencing (WGS) can be used to monitor the emergence and spread of pathogens (36–39). As part of the surveillance effort in the Netherlands, more than 1750 SARS-CoV-2 viruses have been sequenced to date from patients from different parts of the country (40). Here, we describe an in-depth investigation into the SARS-CoV-2 outbreak in mink farms and mink farm employees

<sup>1</sup>Department of Viroscience, Erasmus MC, WHO Collaborating Centre for Arbovirus and Viral Hemorrhagic Fever Reference and Research, Rotterdam, Netherlands. <sup>2</sup>Royal GD, Deventer, Netherlands. <sup>3</sup>Netherlands Food and Consumer Product Safety Authority (NVWA), Utrecht, Netherlands. <sup>4</sup>Municipal Health Services GGD Brabant-Zuidoost, Eindhoven, Netherlands. <sup>5</sup>Municipal Health Services GGD Hart voor Brabant, 's-Hertogenbosch, Netherlands. <sup>6</sup>Municipal Health Services GGD Limburg-Noord, Venlo, Netherlands. <sup>7</sup>Wageningen Bioveterinary Research, Lelystad, Netherlands. <sup>8</sup>Stichting PAMM, Veldhoven, Netherlands. <sup>9</sup>Division of Farm Animal Health, Department of Population Health Sciences, Utrecht University, Utrecht, Netherlands. <sup>10</sup>Institute for Risk Assessment Sciences (IRAS), Utrecht University, Utrecht, Netherlands. \*Corresponding author: Email: [b.oudemunnink@erasmusmc.nl](mailto:b.oudemunnink@erasmusmc.nl)



in the Netherlands, combining epidemiological information, surveillance data, and WGS on the human-animal interface.

SARS-CoV-2 was first diagnosed on two mink farms (designated NB1 and NB2) in the Netherlands on 23 and 25 April 2020, respectively. After the initial detection of SARS-CoV-2 on these farms, a thorough investigation was initiated to identify potential transmission routes and to perform an environmental and occupational risk assessment. Here, we de-

scribe the results of the investigation of the first 16 SARS-CoV-2-affected mink farms by combining SARS-CoV-2 diagnostics, WGS, and in-depth interviews.

Owners and employees of the 16 mink farms with SARS-CoV-2-positive animals were included in the contact tracing investigation by the Dutch Municipal Health Services and were tested according to national protocol. Ninety-seven individuals were tested by either serological assays and/or RT-PCR.

Forty-three of 88 (49%) upper respiratory tract samples tested positive by RT-PCR, whereas 38 of 75 (51%) serum samples tested positive for SARS-CoV-2-specific antibodies. In total, 66 of 97 (68%) tested individuals had evidence for SARS-CoV-2 infection (Table 1).

During the interview on 28 April, four of five employees from NB1 reported that they had experienced respiratory symptoms before the outbreak was detected in minks, but none of them had been tested for SARS-CoV-2. Their symptom-onset dates ranged from 1 April to 9 May. For 16 of the mink (sampled on 28 April) and one farm employee (sampled on 4 May), a whole-genome sequence was obtained (hCov-19/Netherlands/NoordBrabant\_177/2020). The human sequence clusters within the mink sequences, although it differs from the closest mink sequence by 7 nucleotides (nts) (Fig. 1 and cluster A in Figs. 2 and 3). On farm NB2, SARS-CoV-2 was diagnosed on 25 April. Retrospective analysis showed that one employee from NB2 had been hospitalized with SARS-CoV-2 on 31 March. All samples from the eight employees taken on 30 April were negative by RT-PCR but tested positive for SARS-CoV-2 antibodies. The virus sequence obtained from NB2 animals was distinct from that of NB1 animals, indicating a separate introduction (Figs. 2 and 3, cluster B).

On mink farm NB3, SARS-CoV-2 infection was diagnosed on 7 May. Initially, all seven employees tested negative for SARS-CoV-2, but when retested between 19 and 26 May after developing COVID-19-related symptoms, five of seven individuals working or living on the farm tested positive for SARS-CoV-2 RNA.

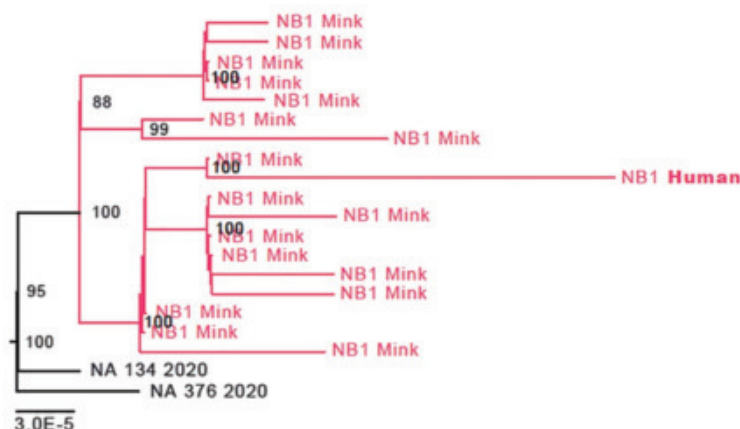


**Fig. 1. Phylogenetic analysis of mink farm NB1.** A maximum likelihood analysis was performed using all available SARS-CoV-2 sequences from the Netherlands. Sequences from NB1 are depicted in red, and the employee of NB1 is shown in bold. The two sequences in black at the root of the cluster are the closest-matching human genome sequences from the national SARS-CoV-2 sequence database. The scale bar represents units of substitutions per site.

**Table 1. Overview of human sampling on SARS-CoV-2-affected mink farms.**

Farm	First diagnosis in animals	Date(s) of sampling of employees and family members	PCR-positive individuals/tested individuals (%)	Serology-positive individuals/tested individuals (%)	Positive employees and family members/tested individuals (PCR and/or serology)
NB1	23 April 2020	28 April 2020 to 11 May 2020	5/6 (83%)	5/5 (100%)	6/6 (100%)
NB2	25 April 2020	31 March 2020 to 30 April 2020	1/2 (50%)	7/8 (88%)	7/8 (88%)
NB3	7 May 2020	11 May 2020 to 26 May 2020	5/7 (71%)	0/6 (0%)*	5/7 (71%)
NB4	7 May 2020	8 May 2020	1/3 (33%)	2/2 (100%)	2/3 (66%)
NB5	31 May 2020	1 June 2020	2/7 (29%)	3/6 (50%)	3/7 (43%)
NB6	31 May 2020	1 June 2020	1/6 (17%)	4/6 (66%)	4/6 (66%)
NB7	31 May 2020	10 June 2020 to 1 July 2020	8/10 (80%)	NA†	8/10 (80%)
NB8	2 June 2020	3 June 2020	5/10 (50%)	5/9 (56%)	8/10 (80%)
NB9	4 June 2020	7 June 2020	1/7 (14%)	1/7 (14%)	2/7 (29%)
NB10	8 June 2020	11 June 2020	1/8 (13%)	3/8 (38%)	4/8 (50%)
NB11	8 June 2020	11 June 2020	1/3 (33%)	0/2 (0%)	1/3 (33%)
NB12	9 June 2020	11 June 2020	6/9 (66%)	2/8 (25%)	7/9 (78%)
NB13	14 June 2020	11 June 2020 to 18 June 2020	3/3 (100%)	0/2 (0%)	3/3 (100%)
NB14	14 June 2020	14 June 2020	1/3 (33%)	5/6 (83%)	5/6 (83%)
NB15	21 June 2020	10 June 2020 to 30 June 2020	2/2 (100%)	NA†	2/2 (100%)
NB16	21 June 2020	23 June 2020	0/2 (0%)	NA†	0/2 (0%)
Total			43/88 (49%)	37/75 (49%)	66/97 (68%)

\*Serology was performed ~1 week before the positive PCR test.

†No serology was performed (NA, not applicable).

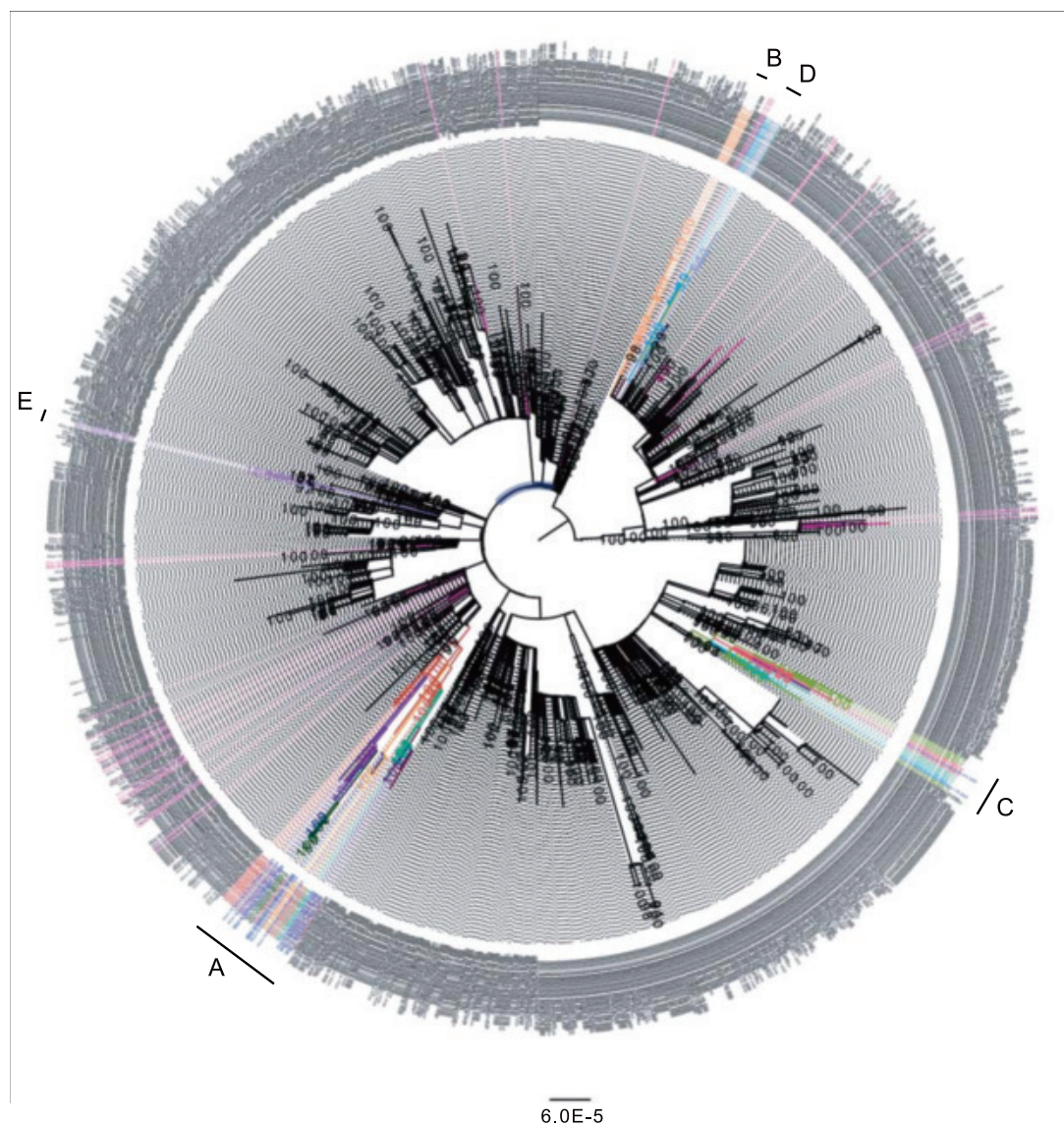


**Fig. 2. Maximum likelihood analysis of all SARS-CoV-2 sequences from the Netherlands.** Sequences derived from minks from different farms are indicated with different colors, human sequences related to the mink farms are shown in blue, and samples from similar areas (as determined by four-digit postal code) are shown in magenta. The scale bar represents units of substitutions per site.

Whole-genome sequences were obtained from these five individuals. The clustering of these sequences with the sequences derived from NB3 mink, together with initial negative test results and subsequent symptom onset, indicate that the employees were infected with SARS-CoV-2 after mink on the farm became infected. An additional infection was identified from contact tracing: An individual who did not visit the farm but had close contact with one of the employees became infected with the SARS-CoV-2 strain found on farm NB3. Animal and human sequences from farm NB3 were close to those from farm NB1, and both were categorized in cluster A.

Similarly, on mink farm NB7, zoonotic transmission from mink to humans likely occurred.

On this farm, SARS-CoV-2 infection in mink was diagnosed on 31 May. NB7 employees initially tested negative for SARS-CoV-2, but several of them subsequently began to show symptoms. Between 10 June and 1 July, samples were taken from 10 employees, 8 of which tested positive for SARS-CoV-2 RNA. WGS of two NB7 employee samples showed that their virus sequences clustered with the sequences from the mink at this farm.

The sequences generated from animals and employees of mink farms were compared with ~1775 whole-genome sequences in the national database. To discriminate between community-acquired and mink farm-related infections and to determine the potential risk for people who live near mink farms, WGS was

also performed on 34 SARS-CoV-2-positive samples (collected from 4 March until 29 April 2020) from individuals who live in the same geographic area (as determined by four-digit postal code) in which farms NB1 to NB4 are located. These local sequences, sampled in a proxy of ~19 km<sup>2</sup>, reflected the general diversity of SARS-CoV-2 seen in the Netherlands and were not related to the clusters of mink sequences found on the mink farms, thereby indicating that no spillover to people living in close proximity to mink farms had occurred and that the sequences from SARS-CoV-2-infected animals and farm workers clustered by farm (Fig. 2; sequences from community shown in magenta). The sequences from the mink farm investigation were also compared with sequences

from Poland ( $n = 65$ ) because many of the mink farm workers were seasonal migrants from Poland, but the Polish sequences were more divergent.

Phylogenetic analysis of the mink SARS-CoV-2 genomes showed that mink sequences of 16 farms were grouped into five different clusters (Figs. 2 and 3). Viruses from farms NB1, NB3, NB4, NB8, NB12, NB13, and NB16 belonged to cluster A; sequences from NB2 formed a distinct cluster (cluster B); those from farms NB6, NB7, NB9, and NB14 formed cluster C; those from NB5, NB8, NB10, and NB15 formed cluster D; and those from NB11 were designated as cluster E. On farm NB8, SARS-CoV-2 viruses from clusters A and D were found. A detailed inventory of possible common characteristics—including farm owner, shared personnel, feed supplier, and veterinary service provider—was made. Multiple farms within a cluster shared the same owner; however, in most cases no common factor could be identified for most farms, and clustering could not be explained by geographic distance (Table 2 and Fig. 4).

In total, 18 sequences from mink farm employees or their close contacts were generated from seven different farms. In most cases, these human sequences were nearly identical to the mink sequences from the same farm. For NB1, the situation was different: The human sequence clusters deeply within the sequences derived from mink (Fig. 1), differing from the closest related mink sequence by 7 nts. This was also the case on farm NB14, with a 4-nt difference from the closest related mink sequence. Sequences of employees at mink farm NB8 clustered with those of animals from NB12, likely because personnel were exchanged between these two farms.

SARS-CoV-2 was detected on mink farms NB1 to NB4 after reports of respiratory symptoms and increased mortality in mink. The sequences from farm NB1 showed a difference of 0 to 9 single-nucleotide polymorphisms (SNPs) (average of 3.9 nts) and sequences from NB2 had a difference of 0 to 8 SNPs (average of 3.6 nts), which is more than is generally observed in outbreaks in human settings. In addition, two deletions (one of 12 nts and one of 134 nts) were observed in a single sequence from NB1. The sequences of mink at NB6 had differences of 0 to 12 SNPs, and a deletion of 9 nts was observed in one sequence, whereas diversity was lower for the subsequent farm sequences (Table 2). After the initial detection of SARS-CoV-2, farms were screened weekly. The first, second, fifth, and sixth weekly screening yielded new positive cases.

Several nonsynonymous mutations were identified among the mink sequences when compared with the Wuhan reference sequence NC\_045512.2. However, no particular amino acid substitutions were found in all mink

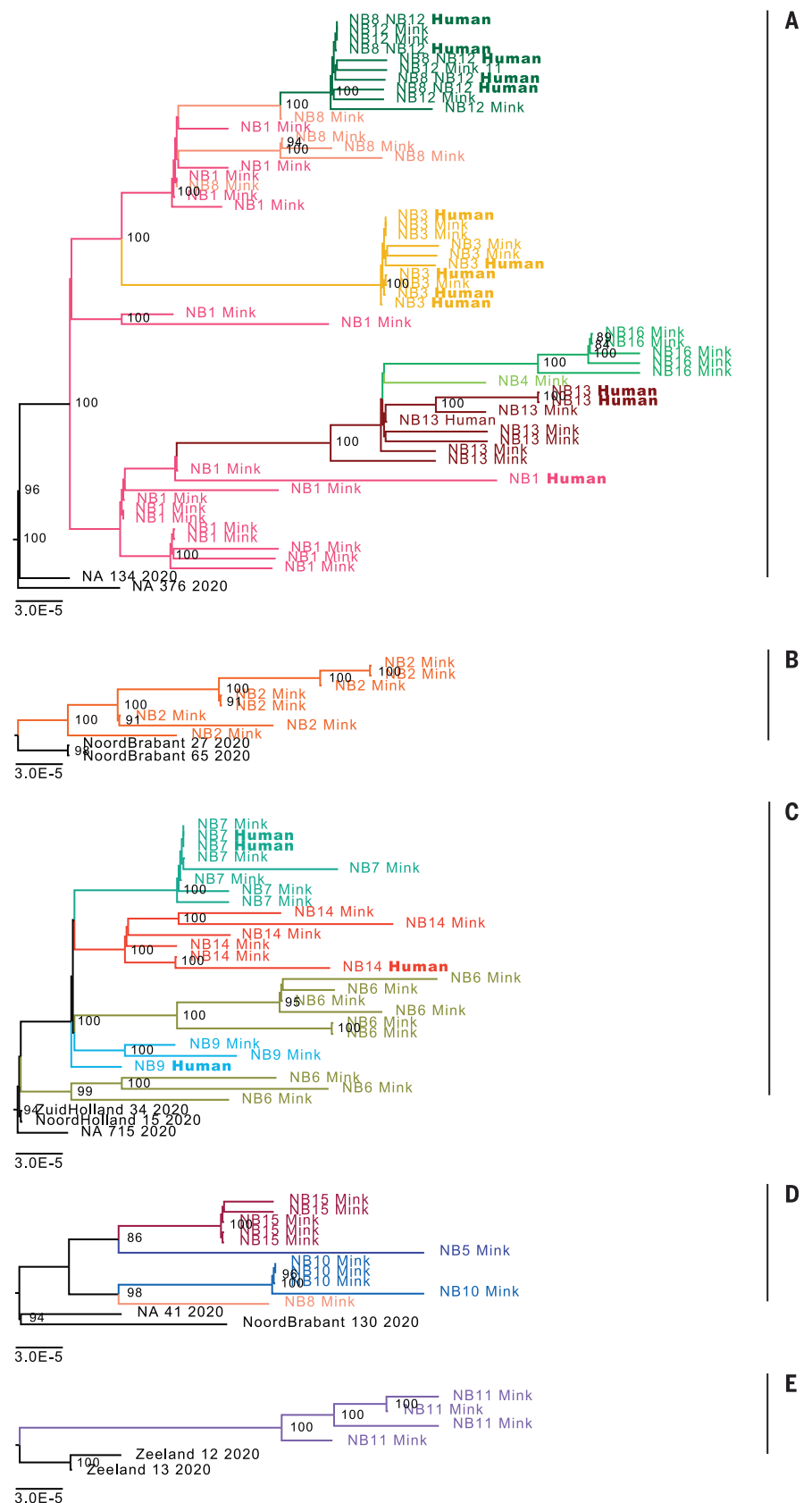


**Fig. 3. Phylogenetic analysis of 88 mink and 18 mink-related human SARS-CoV-2 sequences detected in the five mink farm clusters.** Sequences derived from different farms are depicted in different colors. The scale bar represents units of substitutions per site.



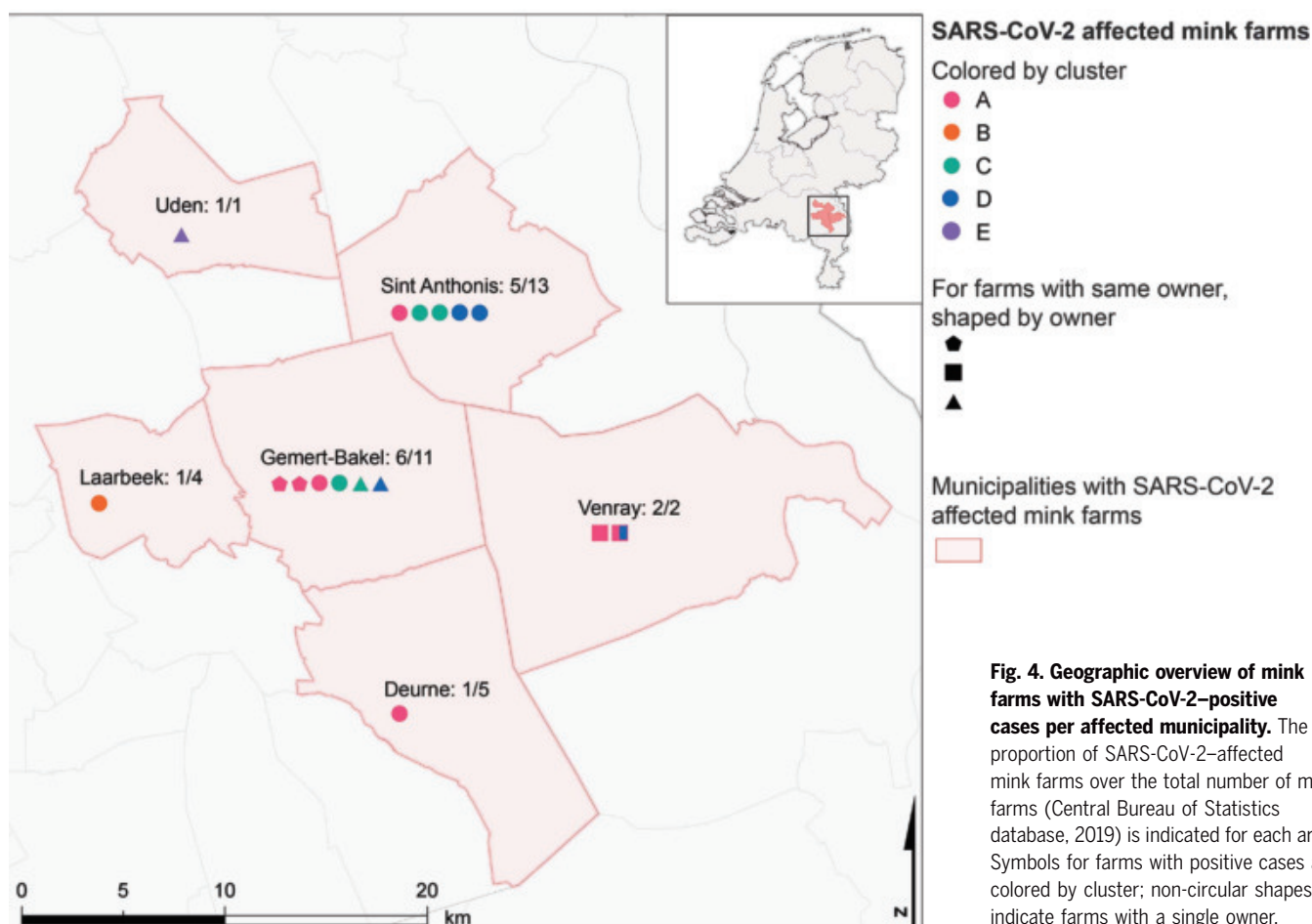


**Table 2. Overview of the clusters detected on the different farms.** Note that veterinarians II and V were from the same veterinary practice. In regard to detection, notification was based on reporting of clinical signs, which was required from 26 April onward. EWS-Ser detection was based on a one-time nationwide compulsory serological screening of all mink farms at the end of May or early June by GD Animal Health. EWS-PM detection was based on the early warning monitoring system (EWS) for which carcasses of animals that died of natural causes were submitted weekly for PCR testing by GD Animal Health from the end of May onward [EWS-PM-1st to -6th postmortem (PM) screening]. NA, not applicable.

Farm	Date of diagnosis	Sequence cluster	Same owner	Feed supplier	Vet	No. of mink sequences (+no. of human sequences)	SNP differences (average)	Mink population size	Detection
NB1	24 April 2020	A	NB1, NB4	1	I	17 (+1)	0 to 9 (3.9)	75,711	Notification
NB2	25 April 2020	B	NA	1	II	8	0 to 8 (3.6)	50,473	Notification
NB3	7 May 2020	A	NA	2	III	5 (+5)	0 to 2 (0.6)	12,400	Notification
NB4	7 May 2020	A	NB1, NB4	1	I	1	NA	67,945	Contact tracing NB1
NB5	31 May 2020	D	NA	1	IV	1	NA	38,936	EWS-Ser+PM-1st
NB6	31 May 2020	C	NA	3	V	9	0 to 12 (6.8)	54,515	EWS-Ser+PM-1st
NB7	31 May 2020	C	NB7, NB11, NB15	3	II	6 (+2)	0 to 4 (1.4)	79,355	EWS-PM-1st
NB8	2 June 2020	A and D	NB8, NB12*	3	V	6 (+5)	0 to 6 (2.6)	39,144	EWS-Ser+PM-1st
NB9	4 June 2020	C	NA	2	V	2 (+1)	0 to 3 (1.5)	32,557	EWS-Ser+PM-2nd
NB10	8 June 2020	D	NA	3	II	4	0 to 3 (1.1)	26,824	EWS-Ser+PM-2nd
NB11	8 June 2020	E	NB7, NB11, NB15	3	II	4	0 to 4 (2.2)	38,745	EWS-PM-2nd
NB12	9 June 2020	A	NB8, NB12*	3	II	5	0 to 3 (1.2)	55,352	Notification
NB13	14 June 2020	A	NA	3	V	5 (+3)	0 to 5 (3.2)	20,366	EWS-PM-5th
NB14	14 June 2020	C	NA	3	II	5 (+1)	0 to 7 (3.7)	28,375	EWS-PM-5th
NB15	21 June 2020	D	NB7, NB11, NB15	3	II	5	0 to 2 (0.6)	35,928	EWS-PM-6th
NB16	21 June 2020	A	NA	3	II	5	0 to 4 (1.6)	66,920	EWS-PM-6th

\*There was exchange of personnel in these two locations.

samples (fig. S1). Of note, three clusters had the position 614G variant (clusters A, C, and E), and two had the original variant. On the basis of the data available at this stage, there were no obvious disease presentation differences in animals or humans between clusters, but data collection and analysis are ongoing for cases after NB16. This D614G mutation that we observed can also be found in the general human population, and the same mutation was found in human cases related to the mink farms.

Our work shows evidence of ongoing SARS-CoV-2 transmission in mink farms and spillover events to humans. More research in minks and other mustelid species will be needed to determine whether these species are at risk of becoming reservoirs of SARS-CoV-2. After the detection of SARS-CoV-2 on mink farms, 68% of the tested farm workers and/or relatives or contacts would later become or had been infected with SARS-CoV-2, indicating that contact with SARS-CoV-2-infected mink is a risk factor for contracting COVID-19. Recently, an eightfold increase in cytidine-to-uridine (C→U) substitutions compared with uridine-to-cytidine (U→C) substitutions was described, suggestive of host adaptation (41). In the mink sequences, we observed a 3.5-fold increase in C→U compared with U→C substitutions, but the number of substitutions (185) was limited.

A high diversity was observed in the sequences from some mink farms, which is likely explained by multiple generations of viral infections in animals before the increase in mortality was detected. Current estimates indicate that the substitution rate of SARS-CoV-2 is around  $1.16 \times 10^{-3}$  substitutions per site per year in the human population (42), which corresponds to around one mutation per 2 weeks. This could mean that the virus was already circulating in mink farms for some time before it was identified. However, a relatively high sequence diversity was also observed on farms where dead animals tested under the early warning surveillance system tested negative 1 week before a positive test, hinting toward a faster evolutionary rate of the virus in the mink population. Mink farms have large populations of animals, living at high density, which may promote virus transmission. However, the moment of viral introduction was not known, which makes it difficult to draw definite conclusions about the substitution rate in mink farms. The generation interval for SARS-CoV-2 in humans has been estimated to be around 4 to 5 days (43), but with high-dose exposure in a farm with a high number and density of animals, this interval could potentially be shorter.

Further evidence that animals were the most likely source of human infection was provided by the clear phylogenetic separation between

mink farm-related human and animal sequences and sequences from human cases within the same geographic area (as determined by four-digit postal code). However, some of the farm-related humans may have been infected within their household, not directly from mink. Spillover into the local community was not observed in our sequence data.

Thus far, the investigation has failed to identify common factors that might explain farm-to-farm spread, possibly via temporary workers who were not included in testing. Since our observations were made, SARS-CoV-2 infections have also been described in mink farms elsewhere (44–46). Additional research efforts are needed, as it is imperative that the fur production and trading sector should not become a reservoir for future spillover of SARS-CoV-2 to humans.

## REFERENCES AND NOTES

- N. Zhu et al., *N. Engl. J. Med.* **382**, 727–733 (2020).
- E. Dong, H. Du, L. Gardner, *Lancet Infect. Dis.* **20**, 533–534 (2020).
- B. B. Oude Munnink et al., *Nat. Med.* **26**, 1405–1410 (2020).
- F. Wu et al., *Nature* **579**, 265–269 (2020).
- H. Zhou et al., *Curr. Biol.* **30**, 3896 (2020).
- P. Zhou et al., *Nature* **579**, 270–273 (2020).
- T. T. Y. Lam et al., *Nature* **583**, 282–285 (2020).
- G. Z. Han, *Trends Microbiol.* **28**, 515–517 (2020).
- M. F. Boni et al., *Nat. Microbiol.* **5**, 1408–1417 (2020).
- J. Shi et al., *Science* **368**, 1016–1020 (2020).
- P. J. Halfmann et al., *N. Engl. J. Med.* **383**, 592–594 (2020).
- GOV.UK, COVID-19 confirmed in pet cat in the UK (2020); [www.gov.uk/government/news/covid-19-confirmed-in-pet-cat-in-the-uk](https://www.gov.uk/government/news/covid-19-confirmed-in-pet-cat-in-the-uk).
- I. Ruiz-Arrondo et al., *Transbound. Emerg. Dis.* **10**, 1111/tbed.13803 (2020).
- M. Richard et al., *Nat. Commun.* **11**, 3496 (2020).
- S. F. Sia et al., *Nature* **583**, 834–838 (2020).
- J. F.-W. Chan et al., *Clin. Infect. Dis.* **71**, 2428–2446 (2020).
- V. J. Munster et al., *Nature* **585**, 268–272 (2020).
- Y. Zhao et al., *Sci. Rep.* **10**, 16007 (2020).
- B. Rockx et al., *Science* **368**, 1012–1015 (2020).
- bioRxiv 2020.05.17.100289 [Preprint]. 17 May 2020. <https://doi.org/10.1101/2020.05.17.100289>.
- S. Lu et al., *Signal Transduct. Target. Ther.* **5**, 157 (2020).
- bioRxiv 2020.08.24.264630 [Preprint]. 24 August 2020. <https://doi.org/10.1101/2020.08.24.264630>.
- SSRN 3578792. 15 April 2020. <https://doi.org/10.2139/ssrn.3578792>.
- D. L. Suarez et al., *Emerg. Infect. Dis.* **26**, 3074–3076 (2020).
- T. H. C. Sit et al., *Nature* **586**, 776–778 (2020).
- C. Sailleau et al., *Transbound. Emerg. Dis.* **67**, 2324–2328 (2020).
- A. Newman et al., *MMWR Morb. Mortal. Wkly. Rep.* **69**, 710–713 (2020).
- ProMED, “COVID-19 update (166): China (Hong Kong) animal, cat, OIE, resolved,” 20200508.7314521 (2020); <https://promedmail.org/promed-post/?id=7314521>.
- N. Oreshkova et al., *Euro Surveill.* **25**, 2001005 (2020).
- J. Segalés et al., *Proc. Natl. Acad. Sci. U.S.A.* **117**, 24790–24793 (2020).
- R. Gollakner, I. Capua, *Vet. Ital.* **56**, 7–8 (2020).
- bioRxiv 2020.04.01.021196 [Preprint]. 3 April 2020. <https://doi.org/10.1101/2020.04.01.021196>.
- bioRxiv 2020.07.21.214346 [Preprint]. 23 July 2020. <https://doi.org/10.1101/2020.07.21.214346>.

- R. J. Molenaar et al., *Vet. Pathol.* **57**, 653–657 (2020).
- NVWA, Bedrijfsmatig gehouden dieren en SARS-CoV-2; [www.nvwa.nl/nieuws-en-media/actuele-onderwerpen/corona/g/bedrijfsmatig-gehouden-dieren-en-corona](https://www.nvwa.nl/nieuws-en-media/actuele-onderwerpen/corona/g/bedrijfsmatig-gehouden-dieren-en-corona).
- B. B. Oude Munnink et al., *Sci. Rep.* **10**, 2798 (2020).
- A. Arias et al., *Virus Evol.* **2**, vew016 (2016).
- N. R. Faria et al., *Science* **361**, 894–899 (2018).
- J. Quick et al., *Nature* **530**, 228–232 (2016).
- R. S. Sikkema et al., *Lancet Infect. Dis.* **20**, 1273–1280 (2020).
- P. Simmonds, *mSphere* **5**, e00408-20 (2020).
- D. S. Candido et al., *Science* **369**, 1255–1260 (2020).
- T. Ganyani et al., *Euro Surveill.* **25**, 2000257 (2020).
- E. Cahán, *Science* **10.1126/science.abe3870** (2020).
- ProMED, “COVID-19 update (319): Spain (AR) animal, farmed mink, 1st rep,” 20200717.7584560 (2020); <https://promedmail.org/promed-post/?id=7584560>.
- ProMED, “COVID-19 update (266): Denmark (ND) animal, farmed mink, 1st rep,” 20200617.7479510 (2020); <https://promedmail.org/promed-post/?id=20200617.7479510>.

## ACKNOWLEDGMENTS

We would like to acknowledge R. van Houdt, J. Schinkel, J. Koopsen, and R. Zonneveld (Amsterdam UMC); B. Wintermans (ARDZ); E. Schmid (GGD Goes); B. Rump (GGD Zeeland); J. Filipse and C. Oliveira dos Santos (Isala Hospital, Laboratory of Clinical Microbiology and Infectious Diseases); T. Schuurs (Izore); R. Nijhuis (Meander Medisch Centrum); S. Pas (Microvida); B. de Leeuw (RLM Microbiologie); and R. Jansen, J. Kalpoe, and W. van der Reijden (Streeklab Haarlem) for sample provision and A. van der Linden, M. Boter, and I. Chestakova (Erasmus MC) for technical assistance. **Funding:** This work has received funding from the European Union’s Horizon 2020 research and innovation program under grants 874735 (VEO), 848096 (SHARP JA), and 101003589 (RECOVER); from ZonMW under grant 10150062010005; and from the Netherlands Ministry of Agriculture, Nature and Food Quality. **Author contributions:** Conceptualization: B.B.O.M., R.S.S., A.S., and M.P.G.K.; Investigation: B.B.O.M., D.F.N., R.S.S., A.S., M.P.G.K., L.A.M.S., W.H.M.v.d.P., R.J.M., R.J.B., E.M., R.M., A.v.d.S., P.T., A.R., M.B., N.B.-V., F.H., R.H.-v.d.H., M.C.A.W.-B., R.J.B., C.G., A.A.v.d.E., F.C.V., and L.A.M.S.; Supervision: M.P.G.K.; Writing – original draft: B.B.O.M., R.S.S., and M.P.G.K.; Writing – review & editing: all authors. **Competing interests:** The authors declare no competing interests. **Data and material availability:** All data, code, and materials used in this work are publicly available. All sequences are publicly available in the GISAID database under accession numbers EPI\_ISL\_461190 to EPI\_ISL\_461192, EPI\_ISL\_461200, EPI\_ISL\_461202, EPI\_ISL\_461203, EPI\_ISL\_522987 to EPI\_ISL\_523034, EPI\_ISL\_523040, EPI\_ISL\_523046, EPI\_ISL\_523068, EPI\_ISL\_523070, EPI\_ISL\_523072, EPI\_ISL\_523073, EPI\_ISL\_523075, EPI\_ISL\_523085, EPI\_ISL\_523089 to EPI\_ISL\_523120, EPI\_ISL\_523282 to EPI\_ISL\_523286, EPI\_ISL\_523301, EPI\_ISL\_523310 to EPI\_ISL\_523312, EPI\_ISL\_523333, EPI\_ISL\_523493, and EPI\_ISL\_523494. Ethical approval was not required for this study, as anonymous aggregated data were used, and no medical interventions were made on animal or human subjects. This work is licensed under a Creative Commons Attribution 4.0 International (CC BY 4.0) license, which permits unrestricted use, distribution, and reproduction in any medium, provided the original work is properly cited. To view a copy of this license, visit <https://creativecommons.org/licenses/by/4.0/>. This license does not apply to figures/photos/artwork or other content included in the article that is credited to a third party; obtain authorization from the rights holder before using such material.

## SUPPLEMENTARY MATERIALS

science.sciencemag.org/content/371/6525/172/suppl/DC1  
Materials and Methods  
Fig. S1  
Table S1  
References (47–63)  
MDAR Reproducibility Checklist

1 September 2020; accepted 5 November 2020  
Published online 10 November 2020  
10.1126/science.abe5901

## OCEAN ANOXIA

## Microbial sulfate reduction and organic sulfur formation in sinking marine particles

M. R. Raven<sup>1\*</sup>, R. G. Keil<sup>2</sup>, S. M. Webb<sup>3</sup>

Climate change is driving an expansion of marine oxygen-deficient zones, which may alter the global cycles of carbon, sulfur, nitrogen, and trace metals. Currently, however, we lack a full mechanistic understanding of how oxygen deficiency affects organic carbon cycling and burial. Here, we show that cryptic microbial sulfate reduction occurs in sinking particles from the eastern tropical North Pacific oxygen-deficient zone and that some microbially produced sulfide reacts rapidly to form organic sulfur that is resistant to acid hydrolysis. Particle-hosted sulfurization could enhance carbon preservation in sediments underlying oxygen-deficient water columns and serve as a stabilizing feedback between expanding anoxic zones and atmospheric carbon dioxide. A similar mechanism may help explain more-extreme instances of organic carbon preservation associated with marine anoxia in Earth history.

The oxygen-deficient zones (ODZs) of the eastern tropical Pacific and Arabian Sea, which currently represent ~0.35% of the total volume of the ocean (1), are expanding rapidly in apparent response to anthropogenic climate change (2–5). Concentrations of dissolved O<sub>2</sub> in ODZs are below ~1 μM and may be effectively zero [ $<10$  nM (6)]. Without available O<sub>2</sub>, animals are largely excluded, and microorganisms must rely on alternative electron acceptors like nitrate, ferric iron, and sulfate to respire organic matter (OM). Microbial sulfate reduction (MSR), which produces sulfide, is canonically expected to occur only when more-energetically favorable electron acceptors like nitrate have been locally depleted (7). However, there is emerging molecular and geochemical evidence that suggests MSR may occur in ODZs despite plentiful dissolved nitrate (8, 9). Active MSR in ODZs could fundamentally alter the biogeochemical cycles of other elements because any sulfide produced could react rapidly with both metals (10) and organics (11)—a process called sulfurization. During more-severe periods of ocean deoxygenation in Earth history, like the Cretaceous ocean anoxic events, reactions with sulfide were globally consequential sinks for both dissolved trace metals (12) and potentially atmospheric CO<sub>2</sub> (13). Still, we do not yet know whether MSR is a substantial contributor to the biogeochemistry of ODZs and how it affects fluxes of organic carbon to the sediments.

Because of its potential to affect global geochemistry, a great deal of effort has been devoted in recent years to finding evidence of active microbial sulfur cycling within ODZs. Sulfur-cycling transcripts and gene sequences have

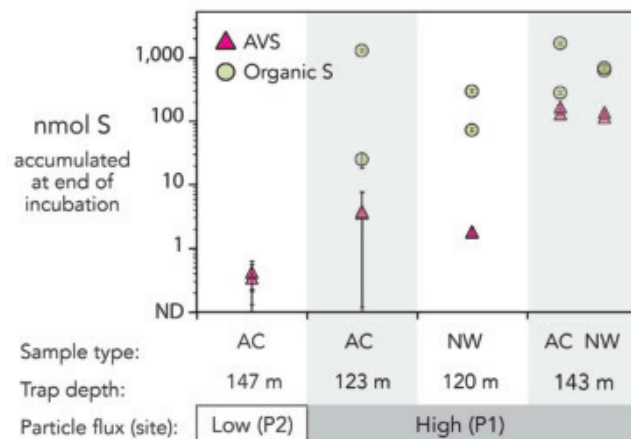
been detected in ODZs of the eastern Pacific (8, 9, 14), the Washington margin (15), and the Arabian Sea (16), and cadmium loss—attributed to CdS formation—has been reported in the Northeast Pacific (17). Sulfide has been detected in large marine snow from the San Juan Islands (18), and low rates of sulfide production in the ODZ offshore Chile have been measured in the water column by means of radiolabeling experiments (9). Despite this progress, none of this work has yet yielded rates of MSR in the large, sinking particles that are the most probable locations for this metabolism (19), nor has any of this work explored the effects of sulfide on the composition of sinking OM. To predict how expanding ODZs will affect the cycles of carbon and metals in the ocean, we need to know whether MSR and OM sulfurization occur at appreciable rates in sinking ODZ particles.

We tested the hypothesis that MSR occurs in large particles sinking through the eastern tropical North Pacific (ETNP) ODZ by concentrating sinking particles, incubating them with radiolabeled sulfate, and characterizing the

products of reactions with any resulting sulfide (20). We deployed a surface float–tethered particle trap with a 2-m-diameter, 50-μm-mesh net (21) from the R/V Roger Revelle four times in April and May of 2018: once at a relatively low particle flux site (P2; 200 km from the Mexican coast, 17.0°N × 107.0°W, ~3500-m water depth), which included a large-particle-free control, and three times at a relatively high-particle flux site (P1; ~50 km from shore, 20.3°N × 106.1°W, ~1500-m water depth). Particles were trapped at the depth of the secondary nitrite maximum (120 to 143 m at P1 and 147 m at P2; fig. S1), which represents the depth of most-intense nitrate reduction and thus the highest expected rates of anaerobic OM cycling (19). Particles for MSR (sulfide production) rate measurements were transferred from the anoxic particle collector and the net wash to serum bottles and incubated for ~24 hours in the dark with radiolabeled sulfate. After stopping microbial activity in the incubations with excess zinc acetate, we isolated acid-volatile sulfides (AVS) (including both dissolved H<sub>2</sub>S and metal monosulfides) and measured radioactivity in sulfate, AVS, and hydrolysis-resistant solids. This sampling approach allows us to focus specifically on processes in large, fast-sinking particles, which have been shown to develop internal redox gradients (18, 22, 23) and therefore have the highest probability of supporting MSR. If rates of nitrate utilization in large particles exceed the diffusive resupply of nitrate from the water column, microenvironments within the particle can theoretically support MSR.

Most of the radiolabeled sulfide produced by MSR in our incubations is expected to either reoxidize or react with metals or organics to form solids (24). Because we did not add sulfide to our incubations as a trap (9), the AVS we measured (Fig. 1 and table S1) is likely composed mostly of iron monosulfides rather than dissolved sulfide. Given our processing

**Fig. 1. Accumulation of radiolabeled S as AVS and organic sulfur in particle incubations.** Samples are arranged arbitrarily along the x axis, and the y axis is log scale. Sample type describes whether particles were obtained from the strictly anoxic collector (AC) or recovered from the net wash (NW). Shading groups samples from individual deployments (table S1). Error bars that reach the x axis indicate results that are not significantly different from zero. See fig. S1 for hydrographic context. ND, not detected.



<sup>1</sup>Department of Earth Science, University of California Santa Barbara, Santa Barbara, CA 93106, USA. <sup>2</sup>School of Oceanography, University of Washington, Seattle, WA 98195, USA. <sup>3</sup>Stanford Synchrotron Radiation Lightsource, Stanford University, Menlo Park, CA 94025, USA.

\*Corresponding author. Email: raven@ucsb.edu

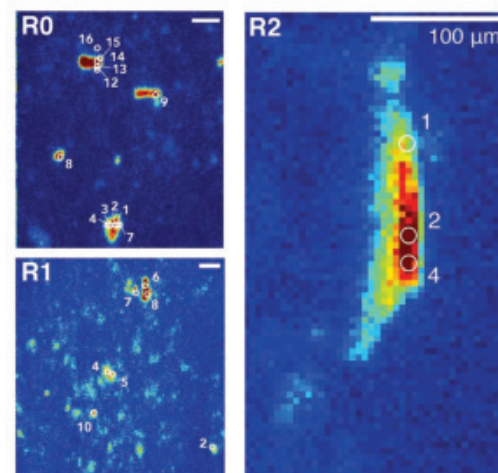


methods, the radiolabeled S that accumulated in the hydrolysis-resistant residual solid phase could potentially include elemental S, organic S, and/or pyrite. Below, we show that this phase is organic S, so we use that term throughout. P1 experiments (Fig. 1) accumulated as much as  $171 \pm 10.8$  (2 $\sigma$ ) nmol AVS or  $1711 \pm 100$  nmol organic S in 24 hours. P2 experiments contained fewer macroscopic aggregates and did not accumulate any resolvable AVS. The ratio of organic S to AVS produced was variable, which could reflect differences in the reactive iron content of different particle populations. These results also highlight that organic S, which is traditionally not measured as part of radiosulfur incubations, can be a major sink for MSR-derived sulfide.

To scale the S cycling rates in our bottles to the water column, we need to assess particle settling rates. Cavan *et al.* found near-shore particle sinking rates in the ETNP that ranged from  $\sim 2$  to  $\sim 120$  m/day (25), although most of the particle mass was present in the slow-sinking pool with fluxes closer to 6.5 m/day. An average sinking rate of 6.5 m/day—for a 2-m-diameter net and 1-liter collector—would imply a concentration factor of 20,420; an average sinking rate of 30 m/day would imply a concentration factor of 94,245. Volume-corrected minimum MSR rates at P1 (average,  $n = 8$ ) are thus  $\sim 14$  pM/hr (for 6.5 m/day), or 3.0 pM/hr (for 30 m/day). For comparison, measured MSR rates were  $\sim 26$  times as high ( $\leq 360$  pM/hr) for water samples from the highly productive,  $O_2$ -deficient Chilean margin, where surface chlorophyll a concentrations were correspondingly  $\sim 22$  times as high [ $\sim 16$   $\mu\text{g}$  of chlorophyll a per liter off Chile (9) versus  $\sim 0.7$   $\mu\text{g}$  of chlorophyll a per liter at P1]. Particle-hosted MSR rates in the ETNP are therefore roughly comparable to previously reported water-column MSR rates (9) after scaling for local productivity.

By assuming that two organic carbon atoms are oxidized for each sulfate molecule reduced (7), we can also estimate the contribution of MSR to carbon oxidation rates in sinking ETNP particles. An average of at least 0.68  $\mu\text{mol}$  sulfide per day was produced in bottles from the high-flux site P1 (average,  $n = 8$ ), which is equivalent to  $\sim 1.4$   $\mu\text{mol}$ /day organic C respiration. The exact mass of carbon in these bottles is not known, so we report calculations for both our best estimate (5 mg of C per bottle; see fig. S2) and the flux measured at another near-shore ETNP site [equivalent to  $\sim 20$  mg of C per bottle (25)]. We assume an organic carbon turnover rate for fast-sinking particles of 12% per day (25, 26). For 5 mg (20 mg) of organic carbon in each bottle, this turnover rate would suggest a total organic carbon respiration of 50  $\mu\text{mol}$  C per day (200  $\mu\text{mol}$  C per day), which would mean that MSR accounts for 2.8% (0.7%) of the total expected respiration.

**Fig. 2. Sinking particles on glass microfiber filters after high-temperature acid treatment.** Selected map regions 0, 1, and 2 (R0, R1, and R2) show the spatial distribution of reduced S (2473.0 eV) on filters, with color indicating relative absorbance from low (blue) to high (red). Numbered white circles show locations at which full spectra were collected; see fig. S3 and table S2 for full maps and data. All scale bars are 100  $\mu\text{m}$ , and pixels represent  $\sim 5$   $\mu\text{m}^2$ .



Bianchi *et al.* (19) have predicted that  $\sim 1\%$  of depth-integrated respiration in the ETNP ODZ may be driven by MSR; our estimates for the contribution of MSR to total carbon respiration at our high-particle flux site (0.7 to 2.8%) are consistent with these theoretical predictions.

We identified the speciation of sulfur in sinking ETNP ODZ particles using sulfur K-edge x-ray absorption spectroscopy (XAS). During incubations, sinking aggregates were macroscopic ( $>1$  mm) and composed of dark particles bound in a fluffy, near-transparent matrix (fig. S2). This fluffy matrix dissolved during acid hydrolysis, leaving behind both discrete,  $\sim 100$ - $\mu\text{m}$ -long particles as well as more-diffuse solids (Fig. 2). Sulfur in the hydrolysable matrix is relatively oxidized and is in the form of sulfate esters and some sulfonates (Fig. 3). This material is consistent with the presence of sulfated polysaccharides, which are abundant constituents of exocellular polymers exuded by diatoms and other algae (27) and have been implicated in marine snow formation (28, 29). Polysaccharide exopolymers are likely sinks for sulfide in sinking particles, as sulfide can convert them to more-hydrolysis-resistant forms (30).

The speciation of sulfur in the discrete, hydrolysis-resistant particles contrasts the largely oxidized organic sulfur in the hydrolysable matrix. Hydrolysis-resistant S is present primarily as organic sulfides, with smaller amounts of aromatics, disulfides, and more-oxidized forms (table S2). We found no evidence of elemental S, pyrite, or a sulfate background within the filters, which demonstrates that the radiolabeled S product from shipboard incubations is predominantly organic sulfur. Discrete particles in regions 0 and 2 consist mostly of alkyl sulfides ( $75.4 \pm 5.9\%$ , mean  $\pm 1\sigma$ , for type 1; see table S2) with only a few percent each of sulfonates, esters, and disulfides. By contrast, diffuse materials in region 1 and a spot within the large particle from region 2

(type 2) are more enriched in sulfonates, sulfate esters, and disulfides, with only 40.4% ( $\pm 2.7\%$ ) sulfides.

Spatial differences in the speciation of organic sulfur likely reflect heterogeneities in the sources and types of OM that combine to form large marine particles. Sources of organic sulfides include both S-bearing amino acids in proteins that survived strong acid hydrolysis and OM sulfuration reactions (31). Similarly, sulfonates and esters can represent primary biogenic sulfur from organisms in the surface ocean (32, 33), like the hydrolyzable exopolymers, or they can also be produced during OM sulfuration reactions alongside organic sulfides, disulfides, and aromatics (34). XAS results integrate organic S formed both before and during field incubations, so any combination of these organic S forms could be the products of de novo sulfuration during shipboard incubations. Still, it is clear that that hydrolysis-resistant OM can be a sink for the sulfide produced during particle-hosted MSR.

The organic S production we observe in sinking particles is sufficient to drive consequential changes in the properties of the OM sinking to, and potentially preserved in, underlying marine sediments. Sulfuration involves cross-linking and rearrangement of organic molecules, which is thought to enhance the preservation potential of OM by reducing its compatibility with exoenzymes (35, 36). The extent of sulfuration is reflected in the molar S:C ratio of OM, which ranges from typically  $\leq 1\%$  for fresh algal biomass to 3 to 5% in many black shales (13, 37, 38). If we assume that  $\sim 80\%$  of the original 5 mg (20 mg) of C in each bottle from the 143-m high-flux trap ( $n = 4$ ) dissolved during hydrolysis (32), then an average of 0.83  $\mu\text{mol}$  organic S accumulated in a pool of  $\sim 80$  to 340  $\mu\text{mol}$  C over the course of the 24-hour incubation. By this calculation, the molar S:C ratio of nonhydrolyzable OM increased by  $\sim 0.3$  to 1.1% per day, which is the

right order of magnitude to generate strongly sulfurized OM (S:C  $\geq 3$  mol %) within a few days of sinking through the water column. Particles therefore appear to be a feasible source of sulfurized OM to marine sediments, at least under sufficiently reducing and high-particle flux conditions. Most of the hydrolysable, unsulfurized biomass is then remineralized by microbial processes before deeper burial (39), leaving behind the sulfurized component. Particle-hosted sulfurization could thus provide an explanation for observations of high OM burial in sediments underlying ODZs that do not intersect the sediment-water interface (40).

The organic S speciation in modern ODZ particles is also very similar to that reported from ancient kerogens in black shales from Ocean Anoxic Event 2 (13) (Fig. 3), which have sequestered vast amounts of OM for the past 94 million years (41). During this event, much of the southern proto-North Atlantic was sulfidic and preserved particularly S-rich OM, which could be the result of rapid sulfurization in sinking particles (13). The hydrolysis-resistant organic S in these shales, like that

in ODZ particles, consists mostly of organic sulfides, with ~10% contributions each from disulfides, aromatics, and sulfonates. The notable resemblance between actively sulfurizing particulate OM and ancient OM in shales allows for the interpretation that the same reactions that sulfurize OM in modern ODZ particles also facilitated elevated OM burial during periods of much more intense O<sub>2</sub> depletion in Earth history. Particle-hosted OM sulfurization is therefore a potentially powerful mechanism to enhance OM preservation in sediments under anoxic conditions.

In modern ODZs, rates of particle-hosted MSR and OM sulfurization appear to be highly variable in both time and space, which makes any attempt to estimate the global scale of their effects on organic carbon burial premature. Mechanistically, however, we might expect expanding ODZs to likewise expand the scale of marine particle-hosted OM sulfurization in the ocean. This would represent a negative feedback with climate and atmospheric CO<sub>2</sub>: Elevated CO<sub>2</sub> leads to ODZ expansion that then drives enhanced CO<sub>2</sub> sequestration

in the form of sedimentary OM. Future research using this sampling approach will allow us to quantify the scale and environmental sensitivities of particle-hosted MSR and OM sulfurization globally.

## REFERENCES AND NOTES

1. J. Karstensen, L. Stramma, M. Visbeck, *Prog. Oceanogr.* **77**, 331–350 (2008).
2. L. Stramma et al., *Nat. Clim. Chang.* **2**, 33–37 (2011).
3. S. Schmidtke, L. Stramma, M. Visbeck, *Nature* **542**, 335–339 (2017).
4. C. Deutsch, H. Brix, T. Ito, H. Frenzel, L. Thompson, *Science* **333**, 336–339 (2011).
5. Y. Takano, T. Ito, C. Deutsch, *Global Biogeochem. Cycles* **32**, 1329–1349 (2018).
6. N. P. Revsbech et al., *Limnol. Oceanogr. Methods* **7**, 371–381 (2009).
7. P. N. Froelich et al., *Geochim. Cosmochim. Acta* **43**, 1075–1090 (1979).
8. M. T. Carolan, J. M. Smith, J. M. Beman, *Front. Microbiol.* **6**, 334 (2015).
9. D. E. Canfield et al., *Science* **330**, 1375–1378 (2010).
10. T. M. Conway, S. G. John, *Geochim. Cosmochim. Acta* **164**, 262–283 (2015).
11. M. R. Raven, A. L. Sessions, J. F. Adkins, R. C. Thunell, *Geochim. Cosmochim. Acta* **190**, 175–190 (2016).
12. J. D. Owens, C. T. Reinhard, M. Rohrsen, G. D. Love, T. W. Lyons, *Earth Planet. Sci. Lett.* **449**, 407–417 (2016).
13. M. R. Raven et al., *Earth Planet. Sci. Lett.* **512**, 27–38 (2019).
14. O. Ulloa, D. E. Canfield, E. F. DeLong, R. M. Letelier, F. J. Stewart, *Proc. Natl. Acad. Sci. U.S.A.* **109**, 15996–16003 (2012).
15. M. W. Smith, L. Zeigler Allen, A. E. Allen, L. Herfort, H. M. Simon, *Front. Microbiol.* **4**, 120 (2013).
16. B. M. Fuchs, D. Woebken, M. V. Zubkov, P. Burkil, R. Amann, *Aquat. Microb. Ecol.* **39**, 145–157 (2005).
17. D. J. Janssen et al., *Proc. Natl. Acad. Sci. U.S.A.* **111**, 6888–6893 (2014).
18. A. L. Shanks, M. L. Reeder, *Mar. Ecol. Prog. Ser.* **96**, 43–47 (1993).
19. D. Bianchi, T. S. Weber, R. Kiko, C. Deutsch, *Nat. Geosci.* **11**, 263–268 (2018).
20. Details are provided in the materials and methods section of the supplementary materials available online.
21. B. A. S. Van Mooy, R. G. Keil, Aquatic sample analysis system, U.S. Patent 9,188,512 (2015).
22. H. Ploug, *Limnol. Oceanogr.* **46**, 1624–1631 (2001).
23. A. L. Alldredge, Y. Cohen, *Science* **235**, 689–691 (1987).
24. B. B. Jørgensen, *Limnol. Oceanogr.* **22**, 814–832 (1977).
25. E. L. Cavan, M. Trimmer, F. Shelley, R. Sanders, *Nat. Commun.* **8**, 14847 (2017).
26. M. H. Iversen, H. Ploug, *Biogeochemistry* **10**, 4073–4085 (2013).
27. E. L. McCandless, J. S. Craigie, *Annu. Rev. Plant Physiol.* **30**, 41–53 (1979).
28. U. Passow, A. L. Alldredge, B. E. Logan, *Deep Sea Res. Part I Oceanogr. Res. Pap.* **41**, 335–357 (1994).
29. A. L. Alldredge, M. W. Silver, *Prog. Oceanogr.* **20**, 41–82 (1988).
30. M. D. Kok, S. Schouten, J. S. Sinninghe Damsté, *Geochim. Cosmochim. Acta* **64**, 2689–2699 (2000).
31. A. Amrani, Z. Aizenshtat, *Organic Geochem.* **35**, 1319–1336 (2004).
32. A. Vairavamurthy, W. Zhou, T. Eglinton, B. Manowitz, *Geochim. Cosmochim. Acta* **58**, 4681–4687 (1994).
33. M. R. Raven, D. A. Fike, M. L. Gomes, S. M. Webb, *Front. Earth Sci.* **7**, 98 (2019).
34. A. M. Pohlmann, G. V. Gomez-Saez, B. E. Noriega-Ortega, T. Dittmar, *Front. Mar. Sci.* **4**, 364 (2017).
35. S. C. Brassell, C. A. Lewis, J. W. De Leeuw, F. de Lange, J. S. Damsté, *Nature* **320**, 160–162 (1986).
36. M. Boussafir et al., *Geochim. Cosmochim. Acta* **59**, 3731–3747 (1995).
37. D. Dinur, B. Spiro, Z. Aizenshtat, *Chem. Geol.* **31**, 37–51 (1980).
38. D. A. Zback, L. M. Pratt, *Geochim. Cosmochim. Acta* **56**, 763–774 (1992).
39. H. E. Hartnett, R. G. Keil, J. I. Hedges, A. H. Devol, *Nature* **391**, 572–575 (1998).
40. T. F. Pedersen, G. B. Shimmield, N. B. Price, *Geochim. Cosmochim. Acta* **56**, 545–551 (1992).
41. J. D. Owens, T. W. Lyons, C. M. Lowery, *Earth Planet. Sci. Lett.* **499**, 83–94 (2018).
42. A. H. Devol, R. Keil, G. Rocap, C. Haskins, “CTD bottle data for all CTD casts during R/V Roger Revelle R1804, R1805 cruises in the Eastern Tropical North Pacific Ocean, from March to April 2018” (2019); [www.bco-dmo.org/dataset/779185/data](http://www.bco-dmo.org/dataset/779185/data).

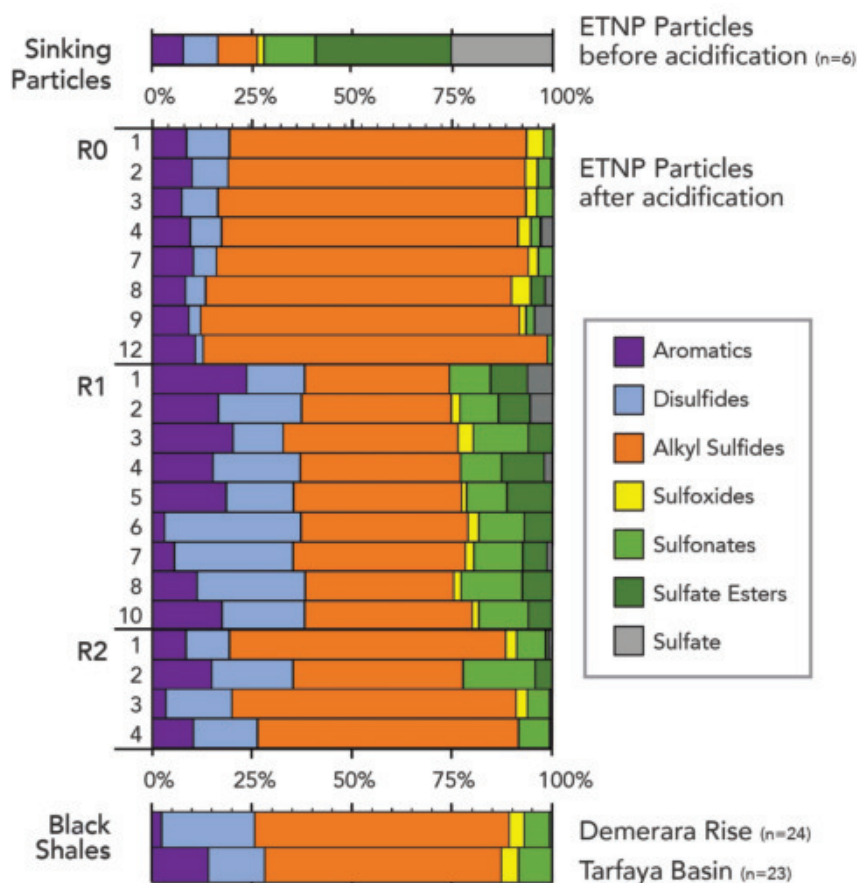


**Fig. 3. Speciation of sulfur in ETNP particles and 94-million-year-old black shales.** Bars represent the relative abundances of different sulfur moieties by linear deconvolution fitting in SIXPACK. Only high-quality spot fits ( $X^2 < 2$ ) are shown; see table S2 for uncertainties and fit parameters. Bars for black shales (13) and particles before acidification represent averages of all available data. Figure 2 includes a key to spot locations for acidified ETNP particles from R0, R1, and R2.

## ACKNOWLEDGMENTS

This work was made possible through the support and generosity of A. Devol, G. Rocap, J. Neibauer, and M. Duffy at the University of Washington; D. Fike at Washington University in St. Louis; and V. Orphan and S. Connon at Caltech. Special thanks are also owed to M. O'Beirne (University of Pittsburgh) and the full science party and crew of the R/V Roger Revelle (RR1805). **Funding:** Financial support was provided under NSF Dimensions of Biodiversity award no. 1542240 (to R.G.K.) and the Agouron Institute Geobiology Postdoctoral Fellowship (to M.R.R.). Use of the Stanford Synchrotron Radiation Lightsource, SLAC National Accelerator Laboratory (proposal 5359) is supported by the U.S. Department of Energy, Office of Science, Office of Basic Energy Sciences under contract no. DE-AC02-76SF00515. The

SSRL Structural Molecular Biology Program is supported by the DOE Office of Biological and Environmental Research and by the National Institutes of Health, National Institute of General Medical Sciences (P30GM133894). The contents of this publication are solely the responsibility of the authors and do not necessarily represent the official views of NIGMS or NIH. **Author contributions:** M.R.R. designed the study, conducted experiments, analyzed results, and wrote the text; R.G.K. designed the field expedition and collected particle material; S.M.W. helped collect and interpret x-ray absorption spectrometric data; and all authors contributed to the final manuscript. **Competing interests:** The authors declare no competing interests. **Data and materials availability:** All of the processed data analyzed in this study are included in this article, its supplementary materials, and the

referenced public database (42). Raw data files (XAS spectra and map files) are available from the corresponding author on request.

## SUPPLEMENTARY MATERIALS

science.sciencemag.org/content/371/6525/178/suppl/DC1  
Materials and Methods  
Figs. S1 to S3  
Tables S1 and S2  
References (43, 44)

3 May 2020; accepted 3 December 2020  
Published online 17 December 2020  
10.1126/science.abc6035

## IMMUNOLOGY

# Pre-T cell receptors topologically sample self-ligands during thymocyte $\beta$ -selection

Xiaolong Li<sup>1,2,3\*</sup>, Réka Mizsei<sup>1\*</sup>, Kemin Tan<sup>4</sup>, Robert J. Mallis<sup>1,5,6</sup>, Jonathan S. Duke-Cohan<sup>1,2,3</sup>, Aoi Akitsu<sup>1,2,3</sup>, Paul W. Tetteh<sup>1,2</sup>, Abhinav Dubey<sup>6,7</sup>, Wonmuk Hwang<sup>8,9,10,11</sup>, Gerhard Wagner<sup>6</sup>, Matthew J. Lang<sup>12,13</sup>, Haribabu Arthanari<sup>6,7</sup>, Jia-huai Wang<sup>1,2,6,7,14†</sup>, Ellis L. Reinherz<sup>1,2,3†</sup>

Self-discrimination, a critical but ill-defined molecular process programmed during thymocyte development, requires myriad pre-T cell receptors (preTCRs) and  $\alpha\beta$ TCRs. Using x-ray crystallography, we show how a preTCR applies the concave  $\beta$ -sheet surface of its single variable domain ( $V\beta$ ) to “horizontally” grab the protruding MHC  $\alpha 2$ -helix. By contrast,  $\alpha\beta$ TCRs purpose all six complementarity-determining region (CDR) loops of their paired  $V\alpha V\beta$  module to recognize peptides bound to major histocompatibility complex molecules (pMHCs) in “vertical” head-to-head binding. The preTCR topological fit ensures that CDR3 $\beta$  reaches the peptide’s featured C-terminal segment for pMHC sampling, establishing the subsequent  $\alpha\beta$ TCR canonical docking mode. “Horizontal” docking precludes germline CDR1 $\beta$ - and CDR2 $\beta$ -MHC binding to broaden  $\beta$ -chain repertoire diversification before  $\alpha\beta$ TCR-mediated selection refinement. Thus, one subunit successively attunes the recognition logic of related multicomponent receptors.

**P**luripotent progenitors seed the thymus and undergo massive expansion in a precisely orchestrated manner (1). Proliferation at the early CD4<sup>+</sup>CD8<sup>+</sup> double-negative (DN) thymocyte stages (DN1,

DN2, and DN3a) is driven by stem cell factor, interleukin-7, and Notch (2, 3). Productive T cell receptor (TCR)- $\beta$ -chain rearrangement and surface pre-T cell receptor (preTCR) expression begins a second stage of proliferation at DN3b with transitioning to DN4, immature single-positive thymocytes, and early CD4<sup>+</sup>CD8<sup>+</sup> double-positive (DP) thymocyte blasts. This second stage, referred to as  $\beta$ -selection, is required for  $\alpha\beta$  T-lineage commitment, allelic exclusion to restrict  $\beta$ -chain clonotypes to one per cell, and the development of thymocytes expressing  $\alpha\beta$ TCRs (4, 5).

PreTCRs each comprise a unique somatically rearranged TCR $\beta$  gene product disulfide-linked to an invariant transmembrane glycoprotein, pT $\alpha$ , which is thymocyte-specific. pT $\alpha$  lacks a ligand-binding variable domain, but has one membrane-proximal constant domain, which pairs with the  $\beta$ -chain constant domain (6). Although early studies suggested that preTCRs do not require ligands (7–10), instead signaling autonomously through site-specific self-oligomerization (11, 12), sequence analysis across mammalian species has refuted this model (13, 14). Notch signaling, in part, mimics

preTCR signaling to explain this paradox (15). More recently, it has been shown that peptides bound to major histocompatibility complex molecules (pMHCs) are preTCR ligands, promoting thymocyte development through interactions with  $V\beta$  (16–20). After preTCR triggering, pT $\alpha$  transcription is shut off, Notch signaling is blunted, and TCR $\alpha$  transcription is initiated such that each pT $\alpha\beta$  heterodimer can be replaced by a TCR $\alpha\beta$  heterodimer (21). Consequently, the same  $\beta$ -chain is paired with an  $\alpha$ -chain at the major DP thymocyte stage. Each TCR $\alpha\beta$  clonotype creates a cognate pMHC ligand specificity with its  $V\alpha V\beta$  module. Desirable TCRs foster thymocyte survival, whereas autoreactive TCRs induce thymocyte apoptosis consequent to self-pMHC interaction (22).

Both the recognition logic for the obligate preTCR to  $\alpha\beta$ TCR transition and the impact of the preTCR-self-pMHC interaction on T-lineage repertoire formation have been elusive. In this report, we present crystal structures of a preTCR $\beta$  chain, the sole ligand-binding subunit of the preTCR, in complex with pMHC ligands, and accompanying functional data. The  $\beta$  chain used was N15 $\beta$  and its ligand vesicular stomatitis virus octapeptide (VSV8) or variant bound to a truncated version of a class I MHC (MHC-I) K<sup>b</sup> molecule (called K<sup>b</sup>-t2) comprising the peptide-binding  $\alpha 1\alpha 2$  domains. To facilitate N15 $\beta$ -pMHC cocrystallization, we covalently linked N15 $\beta$  with K<sup>b</sup>-t2 (figs. S1 and S2). The representative structure of N15 $\beta$ -VSV8-K<sup>b</sup>-t2 revealed the topological fitting by which the concave C<sup>′</sup>C<sup>′</sup>CFG  $\beta$ -sheet face of the Ig-like N15V $\beta$  domain grabs the apex of the convex  $\alpha 2$  helical region of K<sup>b</sup>-t2 (Fig. 1A). Closed- and open-book surface views (Fig. 1B) as well as detailed sample-related analyses (figs. S2 to S5 and tables S1 to S3) further delineated this fitting.

TCR $\alpha\beta$  heterodimers “vertically” bind a pMHC molecule in a canonical mode, with  $V\alpha$  and  $V\beta$  domains contacting N- and C-terminal segments of a peptide, respectively (23, 24). By contrast, in the structure of the N15 $\beta$ -VSV8-K<sup>b</sup>-t2 complex, N15 $\beta$  bound to pMHC in a “horizontal” docking mode (Fig. 2A) with the CDR3 $\beta$  loop contacting the C terminus of the

<sup>1</sup>Laboratory of Immunobiology, Dana-Farber Cancer Institute, Boston, MA, USA. <sup>2</sup>Department of Medical Oncology, Dana-Farber Cancer Institute, Boston, MA, USA. <sup>3</sup>Department of Medicine, Harvard Medical School, Boston, MA, USA.

<sup>4</sup>Structural Biology Center, X-ray Science Division, Advanced Photon Source, Argonne National Laboratory, Lemont, IL, USA. <sup>5</sup>Department of Dermatology, Harvard Medical School, Boston, MA, USA. <sup>6</sup>Department of Biological Chemistry and Molecular Pharmacology, Harvard Medical School, Boston, MA, USA. <sup>7</sup>Department of Cancer Biology, Dana-Farber Cancer Institute, Boston, MA, USA. <sup>8</sup>Department of Biomedical Engineering, Texas A&M University, College Station, TX, USA. <sup>9</sup>Department of Materials Science & Engineering, Texas A&M University, College Station, TX, USA. <sup>10</sup>Department of Physics & Astronomy, Texas A&M University, College Station, TX, USA. <sup>11</sup>School of Computational Sciences, Korea Institute for Advanced Study, Seoul, Republic of Korea. <sup>12</sup>Department of Chemical and Biomolecular Engineering, Vanderbilt University, Nashville, TN, USA. <sup>13</sup>Department of Molecular Physiology and Biophysics, Vanderbilt University, Nashville, TN, USA. <sup>14</sup>Department of Pediatrics, Harvard Medical School, Boston, MA, USA.

\*These authors contributed equally to this work.  
†Corresponding author. Email: jwang@crystal.harvard.edu (J.W.); ellis\_reinherz@dfci.harvard.edu (E.L.R.)



peptide. In the vertical N15 $\alpha\beta$ -VSV8-K<sup>b</sup> binding, all six complementarity-determining region (CDR) loops from both  $\alpha$  and  $\beta$  subunits made contact in a head-on fashion (Fig. 2A). The TCR $\alpha\beta$ -pMHC interface is generally flat with an  $\sim 1240$ - to  $2020$ -Å<sup>2</sup> buried surface area (BSA) (23). Had a single TCR $\beta$  subunit assumed the same vertical binding to pMHC using its three CDR loops, the BSA would be only around  $900$ - $1000$  Å<sup>2</sup>, considerably less than the average protein-protein interaction (PPI) value of  $1600 \pm 400$  Å<sup>2</sup> (25). Horizontal topological

fitting offered a BSA of  $1379$  Å<sup>2</sup> (table S4). A composite view of the distribution of CDR loops and footprints of a preTCR $\beta$  versus TCR $\alpha\beta$  binding on the same K<sup>b</sup> molecule was then generated (Fig. 2B). Despite different approaches to pMHC (Fig. 2C), both preTCR and TCR $\alpha\beta$  were capable of associating with the same CD3 signaling subunits (fig. S6).

The inherent left-handed twist of the  $\beta$ -sheet platform of an MHC-I molecule caused the  $\alpha 1$  and  $\alpha 2$  helices on top of the sheet to form a convex point on the peptide-binding groove,

most prominently for the  $\alpha 2$ -helix (Fig. 1A) (24). The twisted C<sup>''</sup>C'CFG  $\beta$  sheet of the N15 $\beta$  V-domain contoured as a concavity (Fig. 1A). Convex/concave topological fitting should be a feature of all preTCRs binding to pMHC. The binding-geometry positions CDR3 $\beta$  to contact the pMHC while orienting CDR1 $\beta$  and CDR2 $\beta$  loops away from the interface (Figs. 1A, 2C, and 3A and table S5). Only after TCR $\beta$  pairs with TCR $\alpha$  at the DP thymocyte stage does the resultant TCR $\alpha\beta$  heterodimer mediate potential CDR1 and CDR2 interactions with pMHC.

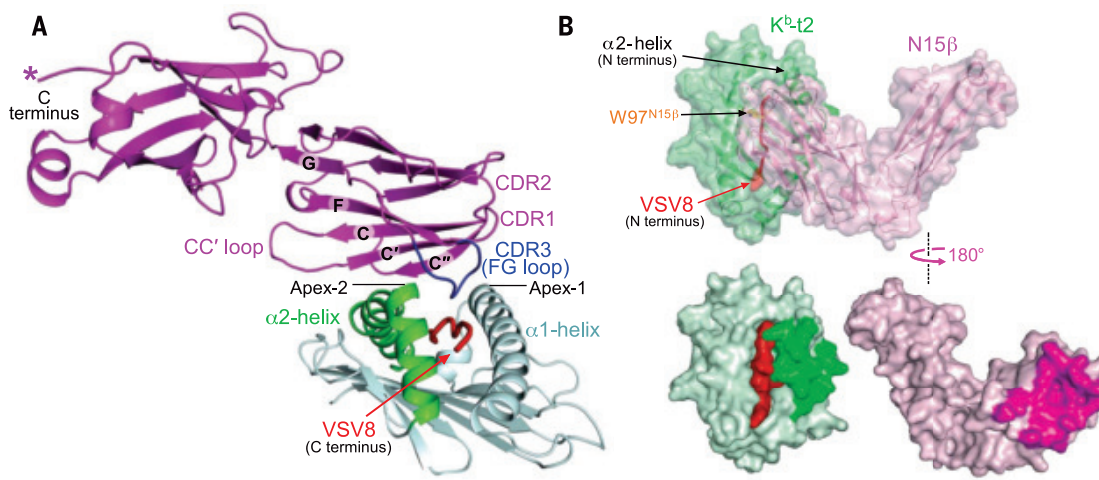


**Fig. 1. The structure of N15 $\beta$ -VSV8-K<sup>b</sup>-t2.** (A) Ribbon drawing of one representative structure of N15 $\beta$ -VSV8-K<sup>b</sup>-t2. The twisted concave C<sup>''</sup>C'CFG  $\beta$  sheet of the N15 $\beta$  V-domain topologically fits the protruding  $\alpha 2$ -helix of K<sup>b</sup>-t2, with the N15 $\beta$  CDR3 loop reaching the C-terminal VSV8 segment. Note that CDR1 and CDR2 point away from pMHC. (B) Surface representation of the "closed-book" view (top panel) and "open-book" view (bottom panel) of N15 $\beta$ -VSV8-K<sup>b</sup>-t2.

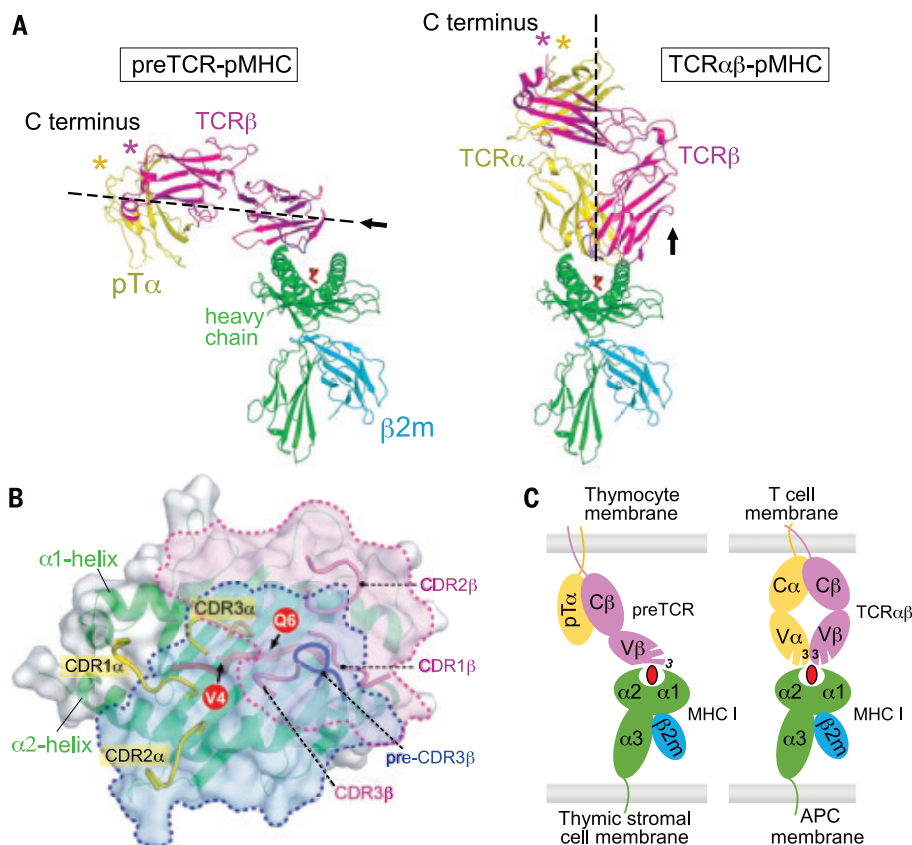


**Fig. 2. Distinct pMHC-binding mode of preTCR versus TCR $\alpha\beta$ .** (A) Side-by-side ribbon drawings of the "horizontal" N15preTCR-VSV8-K<sup>b</sup> complex model (left) and "vertical" N15TCR $\alpha\beta$ -VSV8-K<sup>b</sup> complex structure (right) (31). The former was constructed by overlaying structures of human preTCR (PDB: 3OF6) and mouse VSV8-K<sup>b</sup> (PDB: 1KPU) onto the current structure of N15 $\beta$ -VSV8-K<sup>b</sup>-t2. (B) Composite view of the footprints of a TCR $\alpha\beta$  (PDB: 2CKB) and the preTCR on the same K<sup>b</sup> (gray surface and green ribbon). The  $\beta$ -chain footprints of TCR $\alpha\beta$  and preTCR are delineated by magenta and blue dashed lines, respectively. All CDR loops are displayed. The VSV8 is in red ribbon representation with its exposed residues V4 and Q6 shown. (C) Simplified illustration of pMHC binding of preTCR versus TCR $\alpha\beta$ . An atomistic model comparison is provided in fig. S6. Only CDR3 is labeled. APC, antigen-presenting cell.

The topological fitting skews N15 $\beta$  binding toward the peptide C-terminal segment in the MHC groove (Fig. 3B), suggesting that TCR $\alpha\beta$  canonical docking polarity onto pMHC (23, 24) is preset at the  $\beta$ -selection stage.

The C-terminal half of the bound peptide is the most structurally featured segment of pMHC-I ligands, as exemplified by overlaying four K<sup>b</sup> bound peptides on the VSV8-K<sup>b</sup>-t2 structure (Fig. 3C). When loaded in an MHC-I molecule, a peptide's two termini are fixed in the groove by mainchain hydrogen bonds to conserved MHC residues (26). Beginning at the p4 residue, the peptides bulge out and diverge in backbone conformations (Fig. 3C). Topological fit enabled preTCRs to recognize this featured C-terminal backbone display, complementing the limited number of exposed peptide side chains to shape the  $\alpha\beta$ TCR repertoire as described below. A featured peptide conformation applied to MHC-II (fig. S7 and table S6) suggested analogous preTCR recognition. By contrast, certain nonclassical MHCs lack a regular peptide-binding groove (fig. S7).

The N15 $\beta$ -VSV8-K<sup>b</sup>-t2 interface had two distinct areas (Fig. 3, A and D): (i) a large hydrophobic patch on the N15 $\beta$  C''C'-face like the "palm" of a hand to contact the K<sup>b</sup>-t2  $\alpha$ 2-helix and (ii) N15 $\beta$  CC' and FG (CDR3 $\beta$ ) loops like the "thumb" and "fingers," respectively. The thumb residue E42 on the N15 $\beta$  CC' loop formed a specific electrostatic interaction with K<sup>b</sup>-t2 residues R157 and K131 as a binding register. Finger residues W97, E100, and Q101 on the CDR3 $\beta$  loop made extensive interactions with K<sup>b</sup>-t2 at the  $\alpha$ 2 apex to facilitate CDR3 $\beta$  loop sampling of the VSV8 C-terminal segment. These two contact areas are likely a general feature for the preTCR-pMHC interaction.

The N15 $\beta$ -VSV8-K<sup>b</sup>-t2 interaction was somewhat degenerate (Fig. 3A and tables S3 and S5). Hydrophobic interactions in the palm area were promiscuous. Although N15 $\beta$ -VSV8-K<sup>b</sup>-t2 potentially had seven maximal interfacial hydrogen bonds, only a few were conserved (Fig. 3A). On average, there should be  $9 \pm 5$  hydrogen bonds in a PPI to afford sufficient specificity (25), whereas the number in N15 $\beta$ -VSV8-K<sup>b</sup>-t2 is rather low, implying plasticity in the fit. W97 on the CDR3 $\beta$  loop tip had its large side chain distributing on either side of VSV8 (Fig. 3E and fig. S5), indicative of conformational variability. Transience may enable the CDR3 $\beta$  loop to sample myriad self-peptides. To investigate sampling directly, the N15 $\beta$  subunit was examined alone or with VSV8-K<sup>b</sup>-t in solution by NMR relaxation dispersion (Rex). The N15 $\beta$  W97 side-chain atom (W97N $\epsilon$ ) showed a Rex effect only upon addition of VSV8-K<sup>b</sup>-t (Fig. 3F and fig. S8), indicative of dynamic changes in the microsecond to millisecond time scale and consistent with ligand-dependent chemical exchange.

To examine the functional consequences of the observed preTCR interaction with pMHC, we seeded wild-type hematopoietic stem cells onto stroma expressing or lacking surface MHC (16) and followed thymocyte development (Fig. 4A). At DN3, both preTCR-independent (Notch-related) and preTCR-dependent cellular expansion occurs, whereas at DN4, signaling

is dominated by the preTCR (27). Proliferation at the DN3 stage was observed at d9 independently of MHC expression, whereas progression to the DPsm stage only occurred robustly on the MHC<sup>+</sup> stroma (Fig. 4B and fig. S9). By d13, progression to the DPsm stage was maintained on the MHC<sup>+</sup> but strongly diminished on MHC<sup>-</sup> stroma. DN4 cell numbers

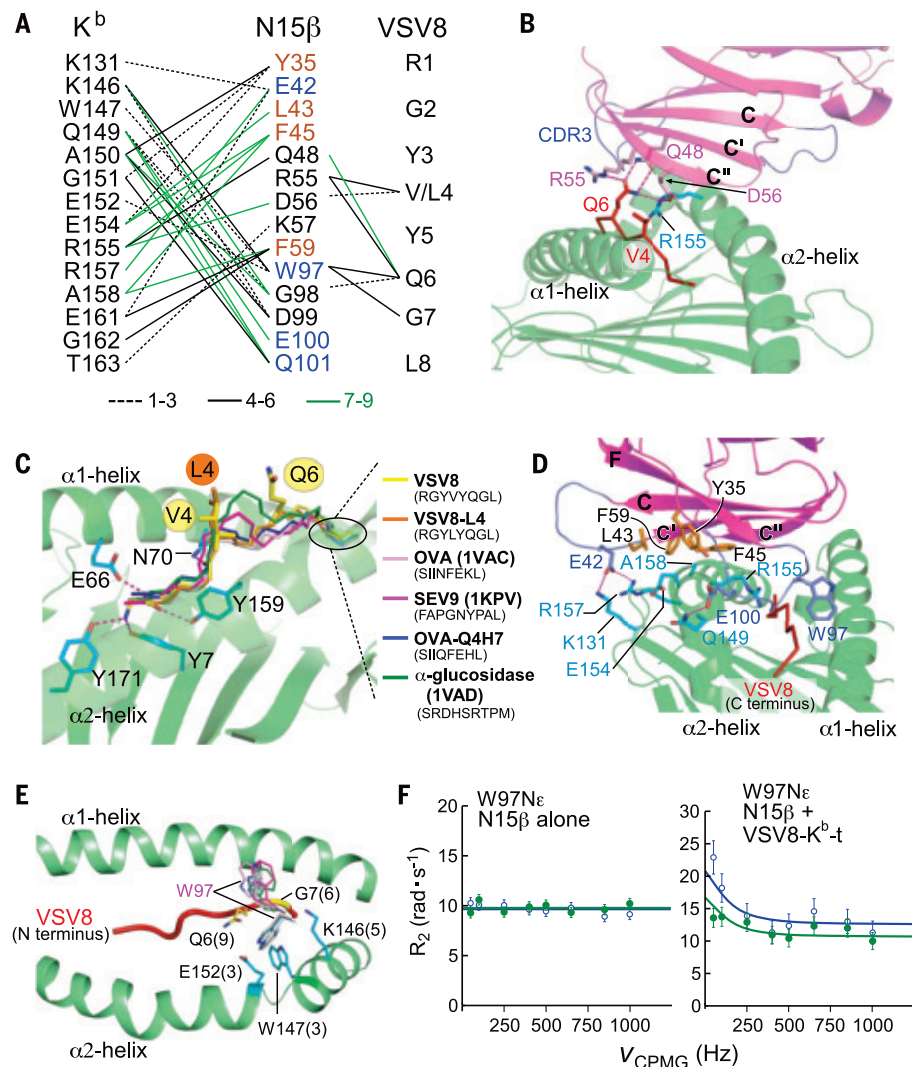


**Fig. 3. The interactions of N15 $\beta$  with VSV8-K<sup>b</sup>-t2.** (A) Interaction network of N15 $\beta$  with K<sup>b</sup>-t2 and VSV8 (4-Å cutoff). Black dashed lines, black solid lines, and green lines denote those interactions observed in 1 to 3, 4 to 6, or 7 to 9 complexes in three crystals, respectively. N15 $\beta$  residues in orange and blue are located in two distinct K<sup>b</sup>-t2-contacting regions, respectively [see (D)]. (B) N15 $\beta$  binding to the VSV8 peptide. Only the C-terminal part of VSV8, particularly V4 and Q6, are involved in the N15 $\beta$  contact. Dashed lines represent hydrogen bonds. (C) Two K<sup>b</sup>-binding octapeptides (OVA and OVA variant Q4H7) and nonapeptides (SEV9 and  $\alpha$ -glucosidase) are superimposed on VSV8-K<sup>b</sup>-t2. The backbone of N-terminal p1-p3 peptide residues is held in the binding-groove by hydrogen bonds to conserved MHC residues, whereas their protruding C-terminal residues diverge in backbone conformation. (D) Two distinct VSV8-K<sup>b</sup>-t2-binding areas on N15 $\beta$  are the "palm" in orange and the "thumb and fingers" in blue. Their interacting residues on K<sup>b</sup>-t2 are colored in cyan. (E) Conformational variability of W97 on the N15 $\beta$  CDR3 $\beta$  loop. Numbers in parentheses represent the frequency of each contact among the nine complexes. Note that the W97 side chain can position on either side of the VSV8 peptide. (F) <sup>15</sup>N relaxation dispersion profiles of W97 showing changes consistent with chemical exchange on ligand binding with addition of VSV8-K<sup>b</sup>-t. Blue circles and green points represent measured transverse relaxation ( $R_2$ ) at 700 and 600 MHz, respectively, at a given Carr-Purcell-Meiboom-Gill pulse frequency ( $V_{CPMG}$ ).

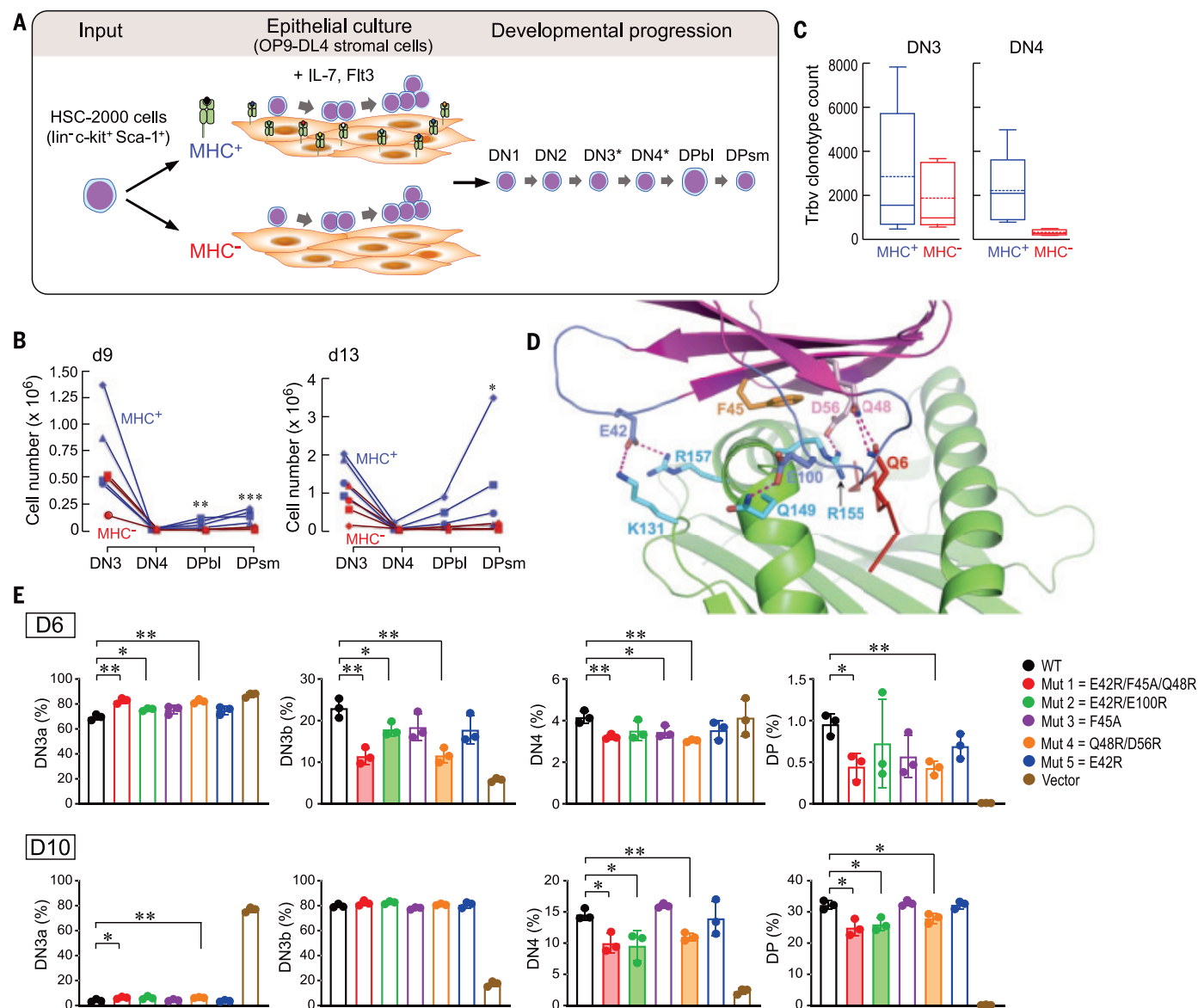


**Fig. 4. Impact of preTCR-pMHC interactions on  $\beta$ -chain repertoire expansion.**

(A) Schematic for thymocyte development. B6 hematopoietic stem cells (HSCs) (light blue and magenta) were cultured on OP9-DL4 cells (light brown) expressing or lacking MHC. For simplicity, the numerically minor immature single-positive thymocytes before DP blast (DPbl) are omitted, with subpopulations expressing preTCRs starting at DN3 and persisting through DN4 denoted by asterisks.

(B) Thymocyte cell number per stage [DN3 to DPsmall (DPsm)] at d9 and d13 after HSC seeding (2000 cells) on MHC<sup>+</sup> or MHC<sup>-</sup> OP9-DL4 stromal cells. Each symbol represents an independent experiment ( $n = 4$ ). \* $P < 0.05$ ; \*\* $P < 0.02$ ; \*\*\* $P < 0.01$ , two-tailed Student's  $t$  test. (C) PreTCR  $\beta$ -chain unique clonotype representation

in  $10^4$  DN3 and DN4 cells after 9 days of growth on MHC<sup>+</sup> or MHC<sup>-</sup> stromal cells. For each condition, the box bounds the 25th and 75th percentile with the internal 50th percentile (solid line) and mean (dotted line). Whiskers with bars define upper and lower values for each condition ( $n = 5$ ). For DN4,  $P < 0.05$  for the comparison of MHC<sup>+</sup> and MHC<sup>-</sup> conditions. (D) Key interface contacts in the N15 $\beta$ -VSV8-K<sup>b</sup>-t2 structure used for mutagenesis studies in (E). (E) Top row highlights the DN3a-DN3b transition and the bottom row shows later DN4 and DP changes ( $n = 3$ ). \* $P < 0.05$ ; \*\* $P < 0.01$ , two-tailed Student's  $t$  test. DN3a, DN3b, and DN4 percentages were derived by gating on the CD4<sup>+</sup>CD8<sup>+</sup>CD44<sup>+</sup> population (fig. S12). Shading indicates interface mutants that significantly inhibited thymocyte developmental progression.

were low across all experiments because of their short-lived but essential transitional nature (28).

Because the preTCR is expressed on a substantial fraction of DN3 and DN4 thymocytes, we investigated whether the presence or absence of pMHC recognition by the preTCR affected functional preTCR $\beta$  clonotype representation (Fig. 4C). The DN3 subset expansion

was essentially independent of pMHC presence on stroma with similar clonotype representations. By contrast, at the DN4 stage, when cells also expressed functional  $\beta$  chains without TCR $\alpha$  chains,  $\beta$ -chain clonotype diversity was 10-fold higher in the presence of MHC (Fig. 4C). Clonotype expansion on the MHC<sup>+</sup> stroma was caused by the inclusion of many distinct single-copy  $\beta$  chains absent from the

MHC<sup>-</sup> stromal cultures (table S7). DN3 and DN4 thymocyte  $\beta$  chains harvested from both types of stroma showed comparable CDR3 length and hydrophobicity (fig. S10).

Finally, we studied stromal cells selectively expressing VSV8-K<sup>b</sup> (16) and stem cells from B6 *Rag2*<sup>-/-</sup> mice (lacking endogenous TCR  $\alpha$  and  $\beta$  chains) as retroviral transduction recipients. Either wild-type N15 $\beta$  (wtN15 $\beta$ ) or



one of five N15 $\beta$  chains mutated at interface residues in the N15 $\beta$ -VSV8-K<sup>b</sup>-t2 structure (Fig. 4D) were transduced, purified by fluorescence-activated cell sorting, and cultured (figs. S11 to S13). All mutant constructs expressed surface preTCRs at levels comparable to wild-type (fig. S14). On day 6, capturing the DN3a to DN3b transition, or day 10, highlighting DN4 and DP development, mutants 1, 2, and 4 significantly blocked developmental progression (Fig. 4E and fig. S15), confirming the crystallographically defined interaction site.

Like the  $\alpha\beta$ TCR, the preTCR is a mechanosensor in which bioforces load and enhance receptor–ligand bond lifetimes through the  $\beta$  subunit (16, 29). Linked preTCR structural transitions exhibit greater reversibility compared with those of TCR $\alpha\beta$ , reflecting unpaired V $\beta$  domain compliance. Facile PreTCR signaling (30) fosters  $\beta$ -chain repertoire formation, and T-lineage repertoire logic is programmed through alterations in pMHC-binding receptor structures. PreTCRs exploit a topological fit that only permits CDR3 $\beta$  to interact with pMHC, supporting self-pMHC reactivity and reduced ligand specificity to favor  $\beta$ -clonotype inclusiveness. Subsequently, beginning in DP thymocytes, when TCR $\alpha$  replaces pT $\alpha$ , the same C' C' CFG  $\beta$ -sheet face of the V $\beta$  domain combines with that of the V $\alpha$  domain to form the V $\alpha$ -V $\beta$  module in the  $\alpha\beta$ TCR, which prevents horizontal pMHC binding. Instead, a vertical geometry is mandated to foster greater specificity among pMHC interface interactions, testing all six CDRs through positive and negative selection. Laxity of pMHC binding permitted at the  $\beta$ -selection stage is eliminated, thereby augmenting self-versus-nonself discrimination. Successful passage through this gauntlet allows a diverse set of matured T-lineage cells to move into the periphery to discern and confront in their vertical  $\alpha\beta$ TCR mode abnormal cells altered by pathogens or cancerous transformations.

## REFERENCES AND NOTES

1. K. Shortman, M. Egerton, G. J. Spangrude, R. Scollay, *Semin. Immunol.* **2**, 3–12 (1990).
2. U. Koch et al., *J. Exp. Med.* **205**, 2515–2523 (2008).
3. H. R. Rodewald, M. Ogawa, C. Haller, C. Waskow, J. P. DiSanto, *Immunity* **6**, 265–272 (1997).
4. T. Kreslavsky et al., *Immunity* **37**, 840–853 (2012).
5. H. von Boehmer, *Cancer Immunol. Res.* **2**, 592–597 (2014).
6. C. Saint-Ruf et al., *Science* **266**, 1208–1212 (1994).
7. B. H. Koller, P. Marrack, J. W. Kappler, O. Smithies, *Science* **248**, 1227–1230 (1990).
8. M. J. Grusby et al., *Proc. Natl. Acad. Sci. U.S.A.* **90**, 3913–3917 (1993).
9. H. J. Fehling, A. Krotkova, C. Saint-Ruf, H. von Boehmer, *Nature* **375**, 795–798 (1995).
10. B. A. Irving, F. W. Ait, N. Killeen, *Science* **280**, 905–908 (1998).
11. S. S. Pang et al., *Nature* **467**, 844–848 (2010).
12. S. Yamasaki et al., *Nat. Immunol.* **7**, 67–75 (2006).
13. P. Smelty et al., *Proc. Natl. Acad. Sci. U.S.A.* **107**, 19991–19996 (2010).
14. B. Zhou et al., *Front. Immunol.* **2**, 5 (2011).
15. A. M. Michie et al., *Int. Immunol.* **19**, 1421–1430 (2007).
16. D. K. Das et al., *J. Biol. Chem.* **291**, 25292–25305 (2016).
17. R. J. Mallis, H. Arthanari, M. J. Lang, E. L. Reinherz, G. Wagner, *J. Biol. Chem.* **293**, 754–766 (2018).
18. R. J. Mallis et al., *Proc. Natl. Acad. Sci. U.S.A.* **112**, 8373–8378 (2015).
19. R. J. Mallis et al., *J. Biomol. NMR* **73**, 319–332 (2019).
20. X. Yang, R. A. Mariuzza, *Proc. Natl. Acad. Sci. U.S.A.* **112**, 8166–8167 (2015).
21. C. López-Rodríguez, J. Aramburu, R. Berge-Bolaños, *Cell. Mol. Life Sci.* **72**, 2305–2321 (2015).
22. L. Klein, B. Kyewski, P. M. Allen, K. A. Hogquist, *Nat. Rev. Immunol.* **14**, 377–391 (2014).
23. M. G. Rudolph, R. L. Stanfield, I. A. Wilson, *Annu. Rev. Immunol.* **24**, 419–466 (2006).
24. J. H. Wang, E. L. Reinherz, *Immunol. Rev.* **250**, 102–119 (2012).
25. L. Lo Conte, C. Chothia, J. Janin, *J. Mol. Biol.* **285**, 2177–2198 (1999).
26. C. Zhang, A. Anderson, C. DeLisi, *J. Mol. Biol.* **281**, 929–947 (1998).
27. H. Hosokawa, E. V. Rothenberg, *Cold Spring Harb. Perspect. Biol.* **10**, a028621 (2018).
28. F. Vasseur, A. Le Campion, C. Pénit, *Eur. J. Immunol.* **31**, 3038–3047 (2001).
29. D. K. Das et al., *Proc. Natl. Acad. Sci. U.S.A.* **112**, 1517–1522 (2015).
30. Y. Feng, E. L. Reinherz, M. J. Lang, *Trends Immunol.* **39**, 596–609 (2018).
31. M. K. Teng et al., *Curr. Biol.* **8**, 409–414 (1998).

## ACKNOWLEDGMENTS

We thank E. Dodson for helpful discussions on crystallography. **Funding:** This work was supported by NIH grants P01AI143565, AI136960, AI136301, GM047467, AI0037581, and EB002026; a Rosctocz Foundation Scholarship; NIH grant 5T32HL066987; and a Claudia Adams Barr award. The use of SBC 19-ID at Argonne National Laboratory was supported by DOE contract no. DE-AC02-

06CH11357. **Author contributions:** E.L.R. and J.H.W. conceived, organized, and supervised the project. E.L.R., J.H.W., and X.L. prepared the manuscript with input from all authors. R.M. and R.J.M. designed, cloned, refolded, and purified protein samples. X.L. produced crystals. X.L., K.T., and J.H.W. collected and processed diffraction data and determined and refined the structure models. X.L. deposited the structures. R.J.M., A.D., G.W., and H.A. performed NMR experiments. J.S.D.-C. performed thymic repertoire analysis. A.A. and P.W.T. performed cell and FACS experiments and animal breeding. J.H.W., X.L., K.T., and E.L.R. analyzed x-ray crystal structures. R.J.M., A.D., G.W., and H.A. analyzed NMR data. J.S.D.-C., A.A., P.W.T., and E.L.R. analyzed functionally experimental data. **Competing interests:** G.W. is a cofounder and has equity in the following companies: Enanta Pharmaceuticals, PIC therapeutics, Cellmig Biolabs, Skinap Therapeutics, Virtual Discovery, and Olaris Therapeutics. None of these companies is related to the topic of this manuscript. The remaining authors declare no competing interests. **Data and materials availability:** All structural data have been deposited in the Protein Data Bank (<https://www.rcsb.org>) with PDB codes: 6WL2, 6WL3, 6WL4, 7J12. All other data associated with this study are in the main text or supplementary materials.

## SUPPLEMENTARY MATERIALS

science.sciencemag.org/content/371/6525/181/suppl/DC1  
Materials and Methods  
Figs. S1 to S16  
Tables S1 to S8  
References (32–52)  
MDAR Reproducibility Checklist

30 July 2020; accepted 3 December 2020  
10.1126/science.abe0918

## ECOTOXICOLOGY

# A ubiquitous tire rubber-derived chemical induces acute mortality in coho salmon

Zhenyu Tian<sup>1,2</sup>, Haoqi Zhao<sup>3</sup>, Katherine T. Peter<sup>1,2</sup>, Melissa Gonzalez<sup>1,2</sup>, Jill Wetzel<sup>4</sup>, Christopher Wu<sup>1,2</sup>, Ximin Hu<sup>3</sup>, Jasmine Prat<sup>4</sup>, Emma Mudrock<sup>4</sup>, Rachel Hettinger<sup>1,2</sup>, Allan E. Cortina<sup>1,2</sup>, Rajshree Ghosh Biswas<sup>5</sup>, Flávio Vinicius Crizóstomo Kock<sup>6</sup>, Ronald Soong<sup>5</sup>, Amy Jenne<sup>5</sup>, Bowen Du<sup>6</sup>, Fan Hou<sup>3</sup>, Huan He<sup>3</sup>, Rachel Lundeen<sup>1,2</sup>, Alicia Gilbreath<sup>7</sup>, Rebecca Sutton<sup>7</sup>, Nathaniel L. Scholz<sup>8</sup>, Jay W. Davis<sup>9</sup>, Michael C. Dodd<sup>3</sup>, Andre Simpson<sup>5</sup>, Jenifer K. McIntyre<sup>4</sup>, Edward P. Kolodziej<sup>1,2,3\*</sup>

In U.S. Pacific Northwest coho salmon (*Oncorhynchus kisutch*), stormwater exposure annually causes unexplained acute mortality when adult salmon migrate to urban creeks to reproduce. By investigating this phenomenon, we identified a highly toxic quinone transformation product of *N*-(1,3-dimethylbutyl)-*N'*-phenyl-p-phenylenediamine (6PPD), a globally ubiquitous tire rubber antioxidant. Retrospective analysis of representative roadway runoff and stormwater-affected creeks of the U.S. West Coast indicated widespread occurrence of 6PPD-quinone (<0.3 to 19 micrograms per liter) at toxic concentrations (median lethal concentration of 0.8 ± 0.16 micrograms per liter). These results reveal unanticipated risks of 6PPD antioxidants to an aquatic species and imply toxicological relevance for dissipated tire rubber residues.

**H**umans discharge tens of thousands of chemicals and related transformation products to water (1), most of which remain unidentified and lack rigorous toxicity information (2). Efforts to identify and mitigate high-risk chemical toxicants are typically reactionary, occur long after their use becomes habitual (3), and are frequently stymied by mixture complexity. Societal management of inadvertent, yet widespread, chemical pollution is therefore costly, challenging, and often ineffective.

The pervasive biological degradation of contaminated waters near urban areas (“urban stream syndrome”) (4) is exemplified by an acute mortality phenomenon that has affected Pacific Northwest coho salmon (*Oncorhynchus kisutch*) for decades (5–9). “Urban runoff mortality syndrome” (URMS) occurs annually among adult coho salmon returning to spawn in freshwaters where concurrent stormwater exposure causes rapid mortality. In the most urbanized watersheds with extensive impervious surfaces, 40 to 90% of returning salmon

may die before spawning (9). This mortality threatens salmonid species conservation across ~40% of the Puget Sound land area despite costly societal investments in physical habitat restoration that may have inadvertently created ecological traps through episodic toxic water pollution (9). Although URMS has been linked to degraded water quality, urbanization, and high traffic intensity (9), one or more causal toxicants have remained unidentified. Spurred by these compelling observations and mindful of the many other insidious sublethal storm-water impacts, we have worked to characterize URMS water quality (10, 11).

Previously, we reported that URMS-associated waters had similar chemical compositions relative to roadway runoff and tire tread wear particle (TWP) leachates, providing an opening clue in our toxicant search (10). In this work, we applied hybrid toxicity identification evaluation and effect-directed analysis to screen TWP leachate for its potential to induce mortality (a phenotypic anchor) in juvenile coho salmon as an experimental proxy for adult coho (6). Using structural identification by means of ultrahigh-performance liquid chromatography–high-resolution tandem mass spectrometry (UPLC-HRMS/MS) and nuclear magnetic resonance (NMR), we discovered that an antioxidant-derived chemical was the primary causal toxicant. Retrospective analysis of runoff and receiving waters indicated that detected environmental concentrations of this toxicant often exceeded acute mortality thresholds for coho during URMS events in the field and across the U.S. West Coast.

Aqueous TWP leachate stock (1000 mg/liter) was generated from an equal-weight mix of tread particles ( $0.2 \pm 0.3 \text{ mm}^2$  average surface area) (fig. S1) from nine used and new tires (table S1). TWP leachate (250 mg/liter positive controls) was acutely and rapidly (~2 to 6 hours) lethal to juvenile coho (24 hours exposures, 98.5% mortality,  $n = 135$  fish from 27 exposures) (data file S1), even after heating ( $80^\circ\text{C}$ , 72 hours; 100% mortality,  $n = 10$  fish from two exposures), indicating stability during handling. Behavioral symptomology (circling, surface gaping, and equilibrium loss) (fig.

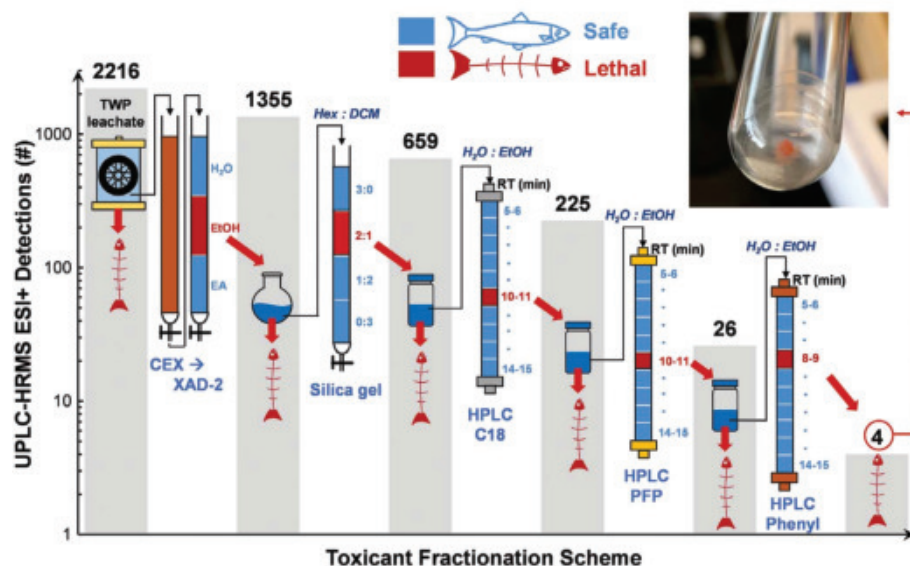


**Fig. 1. Tire rubber leachate fractionation scheme.** As a metric of mixture complexity and separation efficiency, the numbers above gray bars represent distinct chemical features detected in solid-phase extracted fish exposure water (1 liter) and subsequent fractions by means of UPLC-HRMS. Blue indicates nonlethal fractions; red indicates lethal fractions. All fractionation steps and exposures were replicated at least twice; positive and negative controls were included throughout fractionations. (Inset) Purified product (~700  $\mu\text{g}$  from 30 liter of TWP leachate) in the final lethal fraction. TWP, tire tread wear particles; CEX, cation exchange; EA, ethyl acetate; EtOH, ethanol;  $\text{H}_2\text{O}$ , water; Hex, hexane; DCM, dichloromethane; RT, retention time.

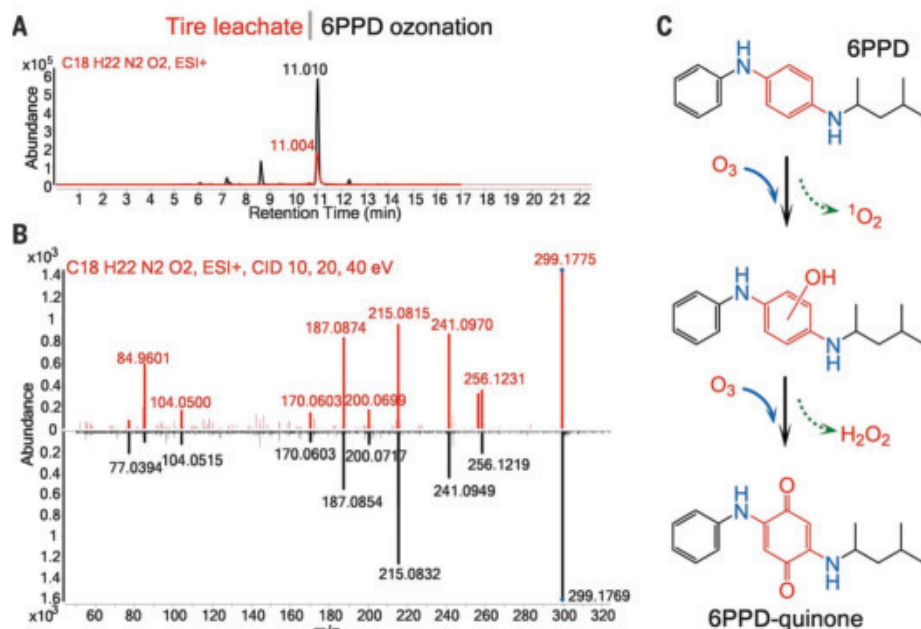


**Fig. 2. 6PPD-quinone identification and a proposed formation pathway.** (A) Extracted ion chromatograms of 6PPD-quinone from UPLC-HRMS (ESI+); red data indicate the final fraction from TWP leachate, and black data indicate the purified 6PPD ozonation mixture. (B) Observed MS/MS fragmentation (integrated from 10, 20, and 40 eV) of 6PPD-quinone in the final toxic fraction from TWP leachate (red spectra) and 6PPD ozonation (black spectra). (C) One proposed reaction pathway from 6PPD to 6PPD-quinone (alternate proposed formation pathways are provided in fig. S13). Red highlights indicate key changes in the diphenylamine structure during ozonation.

<sup>1</sup>Center for Urban Waters, Tacoma, WA 98421, USA.

<sup>2</sup>Interdisciplinary Arts and Sciences, University of Washington Tacoma, Tacoma, WA 98421, USA. <sup>3</sup>Department of Civil and Environmental Engineering, University of Washington, Seattle, WA 98195, USA. <sup>4</sup>School of the Environment, Washington State University, Pullman, WA 99317, USA. <sup>5</sup>Department of Chemistry, University of Toronto, Scarborough Campus, 1265 Military Trail, Toronto, ON M1C 1A4, Canada. <sup>6</sup>Southern California Coastal Water Research Project, Costa Mesa, CA 92626, USA. <sup>7</sup>San Francisco Estuary Institute, 4911 Central Avenue, Richmond, CA 94804, USA. <sup>8</sup>Environmental and Fisheries Sciences Division, Northwest Fisheries Science Center, National Marine Fisheries Service, National Oceanic and Atmospheric Administration, Seattle, WA 98112, USA. <sup>9</sup>U.S. Fish and Wildlife Service, Washington Fish and Wildlife Office, Lacey, WA 98503, USA.

\*Corresponding author. Email: koloj@uw.edu



S2 and movie S1) of TWP leachate exposures mirrored laboratory and field observations of symptomatic coho (5, 6). No mortality occurred in negative controls, including solvent- and process-matched method blanks subjected to identical separations (0 of 80 fish, 16 exposures) or exposure water blanks (0 of 45 fish, nine exposures).

Mixture complexity [measured here as number of UPLC-HRMS electrospray ionization (ESI+) chemical features] was a substantial barrier to causal toxicant identification because 250 mg/liter TWP leachate typically contained more than 2000 ESI+ detections. Our fractionation studies, optimized over 2-plus years through iterative exploration of toxicant chemical properties, focused on reducing these detection numbers to attain a simple, yet toxic, fraction amenable to individual compound identifications. Throughout this fractionation procedure, observed toxicity remained confined to one narrow fraction, which is consistent with a single compound or a small, structurally related family of causal toxicants. In initial studies, TWP leachate toxicity was unaffected by silica sand filtration, cation and anion exchange, and ethylenediaminetetraacetic acid (EDTA) (114  $\mu$ M) addition (12), indicating that toxicant(s) were not particle-associated, strongly ionic, or metals, respectively, and validating prior studies that eliminated candidate pollutants (13, 14) as primary causal toxicants.

Mixture complexity was reduced by using cation exchange, two polarity-based separations (XAD-2 resin and silica gel), and reverse-phase high-performance liquid chromatography (HPLC) on a semipreparative C18 column (250 by 4.2 mm ID, 5  $\mu$ m particle size). After C18-HPLC generated 10 fractions, only C18-F6 (10 to 11 min) was toxic; it contained ~225 ESI+ and ~70 ESI- features (Fig. 1). Having removed ~90% of features, we began to prioritize and identify candidate toxicants by abundance (peak area), followed by fish exposures with commercial standards at fivefold higher concentrations (mixtures at 1 to 25  $\mu$ g/liter) than those estimated in C18-F6. We identified 11 plasticizers, antioxidants, emulsifiers, and various transformation products, including some well-known environmental contaminants [such as tris(2-butoxyethyl) phosphate] and some that

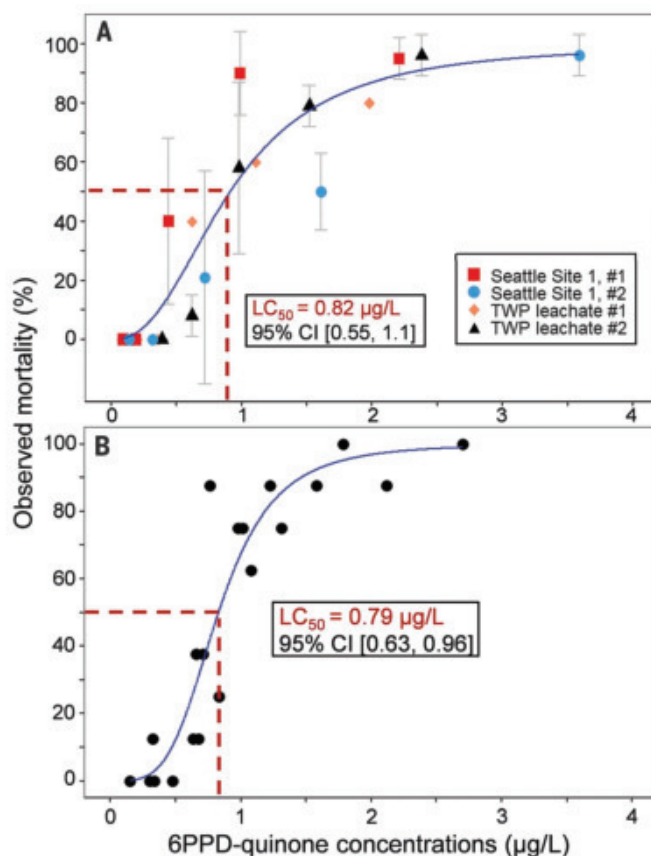


**Fig. 3. Dose-response curves.** (A) Dose-response curve for 24-hour juvenile coho exposures to roadway runoff and TWP leachate ( $n = 365$  fish). Error bars represent three replicates of eight fish (except TWP leachate 2,  $n = 5$  fish; Seattle site 1, duplicate of  $n = 10$  fish). 6PPD-quinone concentrations were from retrospective quantification. (B) Dose-response curves for 24-hour juvenile coho exposures to ozone-synthesized 6PPD-quinone (10 concentrations, two replicates,  $n = 160$  fish). Curves were fitted to a four-parameter logistic model. CI, confidence interval.

are rarely reported [such as di(propylene glycol) dibenzoate and 2-(1-phenylethyl)phenol] (table S2). We also detected several bioactive, structurally related phenolic antioxidants and their transformation products (2,6-di-*t*-butyl-4-hydroxy-4-methyl-2,5-cyclohexadienone, 3,5-di-*t*-butyl-4-hydroxybenzaldehyde, and 7,9-di-*tert*-butyl-1-oxaspiro[4,5]deca-6,9-diene-2,8-dione) (15). However, over many rounds of identification and subsequent exposure to juvenile coho, none of these identified chemical exposures reproduced URMS symptoms or induced mortality. Because these identifications used exhaustive environmental scientific literature searches (10, 16, 17), we suspected a previously unreported toxicant.

To sharpen our search, we used multidimensional semipreparative HPLC using two additional structurally distinct column phases [pentafluorophenyl (PFP) and phenyl]. Parallel fractionations (same column dimensions, mobile phase, and gradient as for C18-HPLC)

(18) of the toxic silica gel fraction generated toxic fractions of PFP-F6 (10 to 11 min; ~204 ESI+, 60 ESI- features) and phenyl-F4 (8 to 9 min; ~237 ESI+, 75 ESI- features); all other fractions were nontoxic. Across these separations (C18, PFP, phenyl), only four ESI+ and three ESI- HRMS features co-occurred in all three toxic fractions (fig. S3). Of these, one unknown compound [mass/charge ratio ( $m/z$ ) 299.1752,  $C_{18}H_{22}N_2O_2$ , RT 11.0 min on analytical UPLC-HRMS] dominated the detected peak area (10-fold higher intensity in both ESI+ and ESI-). To further resolve candidate toxicants for synthetic efforts, we converted the three-dimensional chromatography workflow from parallel to serial through sequential C18, PFP, and phenyl columns (C18-F6 to PFP-F6 to phenyl-F4; with solvent removal by means of centrifugal evaporation and toxicity confirmation between separations). The purified final fraction was chemically simple (four ESI+, three ESI- detections), highly lethal (100% mortality in 4 hours;  $n = 15$  coho, three exposures), and was again dominated by  $C_{18}H_{22}N_2O_2$ . Drying this fraction yielded a pink-magenta precipitate (Fig. 1).

Published characterizations of crumb rubber (16) and receiving waters (10, 17) did not mention  $C_{18}H_{22}N_2O_2$ . UPLC-HRMS/MS spectra indicated  $C_4H_{10}$  and  $C_6H_{12}$  alkyl losses (M-58 and M-84 fragments) (Fig. 2B), but MS<sup>3</sup> and MS<sup>4</sup> fragmentation yielded no additional structural insights (fig. S4). Additionally, in silico fragmentation (MetFrag, CSI:FingerID) of  $C_{18}H_{22}N_2O_2$  compounds in PubChem and ChemSpider (15,624 and 17,105 structures, respectively) failed to match observed fragments. Thus, to the best of our knowledge,  $C_{18}H_{22}N_2O_2$  was not described in environmental literature or databases and posed a “true unknown” identification problem (19). We then assumed a transformation product; industrial manufacturing (such as high heat or pressure, or catalysis) and diverse reactions in environmental systems generate many undocumented transformation products, most of which lack commercial standards.

Our breakthrough came by assuming that abiotic environmental transformations commonly modify active functional groups by preferentially altering the numbers of hydrogen and oxygen atoms relative to carbon and nitrogen. By searching a recent U.S. Environmental Protection Agency (EPA) crumb



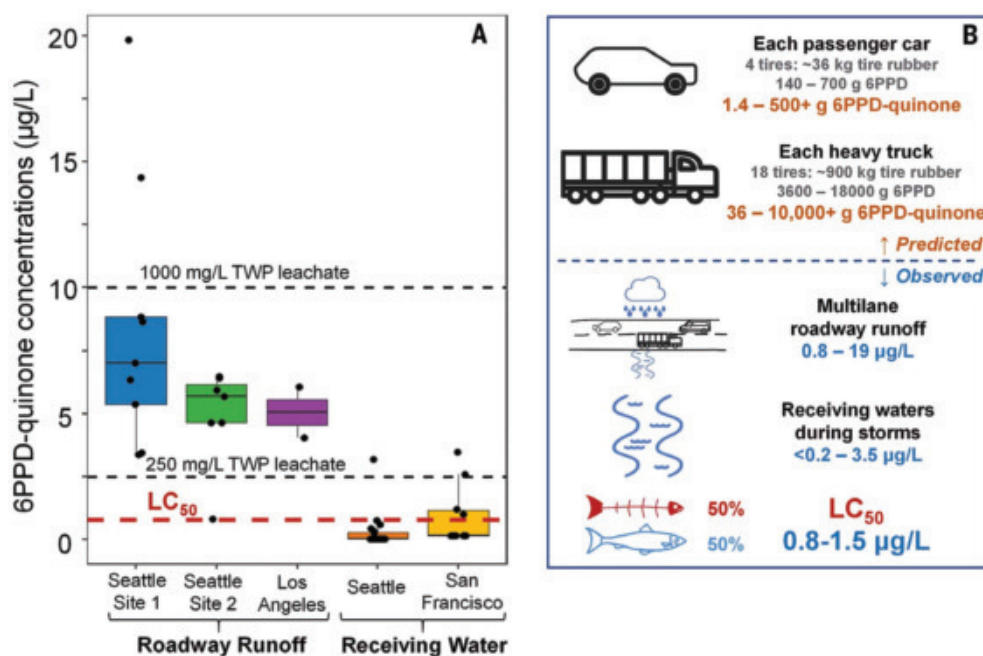


**Fig. 4. Environmental relevance of 6PPD-quinone.** (A) Using retrospective UPLC-HRMS analysis of archived sample extracts, 6PPD-quinone was quantified in roadway runoff and runoff-affected receiving waters. Each symbol corresponds to duplicate or triplicate samples, and boxes indicate first and third quartiles. For comparison, the 0.8 µg/liter LC<sub>50</sub> value for juvenile coho salmon and detected 6PPD-quinone levels in 250 and 1000 mg/liter TWP leachate are included. (B) Predicted ranges of potential 6PPD-quinone mass formation in passenger

cars (for example, four tires, ~36 kg tire rubber mass) and heavy trucks (for example, 18 tires, ~900 kg of tire rubber) (represented in orange) and measured 6PPD-quinone concentrations in affected environmental compartments (represented in blue, with experimental data italicized). Predicted ranges reflect calculations applying 0.4 to 2% 6PPD per total vehicle tire rubber mass followed by various yield scenarios (1 to 75% ultimate yields) for 6PPD reaction with ground-level ozone to form 6PPD-quinone.

rubber report (16) for related formulas ( $C_{18}H_{0-x}N_{2-4}O_{0-y}$ ), several characteristics of the  $C_{18}H_{24}N_2$  anti-ozonant “6PPD” [*N*-(1,3-dimethylbutyl)-*N'*-phenyl-*p*-phenylenediamine] matched necessary attributes. First, 6PPD is globally ubiquitous (0.4 to 2% by mass) in passenger and commercial vehicle tire formulations (20), indicating sufficient production to explain mortality observations within large and geographically distinct receiving water volumes. 6PPD was present in TWP leachate but was completely removed during fractionation through cation exchange. 6PPD crystals are purple, similar to the pink-magenta precipitate obtained after fractionation. Most compellingly, neutral losses in 6PPD gas chromatography (GC)-MS spectra matched the  $C_{18}H_{22}N_2O_2$  GC-HRMS spectra (fig. S5), and the predicted log $K_{ow}$  of 6PPD (5.6) ( $K_{ow}$ , *n*-octanol-water partition coefficient) was close to that for  $C_{18}H_{22}N_2O_2$  (5 to 5.5) (11). Last, literature detailing the industrial chemistry of 6PPD reactions with ozone [7 days, 500 parts per billion volume (ppbv)] described a  $C_{18}H_{22}N_2O_2$  product (21), leading us to hypothesize that 6PPD was the likely protoxicant (Fig. 2C).

We tested this hypothesis with gas-phase ozonation (500 ppbv  $O_3$ ) of industrial grade 6PPD (96% purity) (21). A  $C_{18}H_{22}N_2O_2$  product formed; UPLC-HRMS analysis demonstrated exact matches of retention time (11.0 min) and MS/MS spectra between this synthetic

$C_{18}H_{22}N_2O_2$  and the TWP leachate fractionation-derived  $C_{18}H_{22}N_2O_2$  (Fig. 2, A and B). When purified, the ozone-synthesized  $C_{18}H_{22}N_2O_2$  formed a reddish-purple precipitate. One-dimensional  $^1H$  NMR structural analysis confirmed identical TWP leachate-derived and ozone-synthesized  $C_{18}H_{22}N_2O_2$  structures (figs. S6 to S7). Two-dimensional NMR spectra and related simulations revealed isolated tertiary carbons and carbonyl groups (figs. S8 to S12), clearly indicating a quinone structure for  $C_{18}H_{22}N_2O_2$  rather than the dinitrone structure reported in the past 40 years of literature describing 6PPD ozonation products (21). Therefore, the  $C_{18}H_{22}N_2O_2$  candidate toxicant was unequivocally “6PPD-quinone” {2-anilino-5-[(4-methylpentan-2-yl)amino]cyclohexa-2,5-diene-1,4-dione}. Consistent with environmental 6PPD ozonation, reported 6PPD ozonation products  $C_{18}H_{22}N_2O$  (formula-matched) and 4-nitrosodiphenylamine ( $C_{12}H_{10}N_2O$ , standard-confirmed) (21) also were detected in ozonation mixtures and nontoxic TWP leachate fractions.

Exposures to ozone-synthesized and tire leachate-derived 6PPD-quinone (~20 µg/liter nominal concentrations) both induced rapid (<5 hours, with initial symptoms evident within 90 min) mortality ( $n = 15$  fish, three exposures) (fig. S2 and movie S2), which matched the 2 to 6 hours mortality observed for positive controls. Behavioral symptomol-

ogy in response to synthetic 6PPD-quinone exposures matched that from field observations, roadway runoff, bulk TWP leachate, and final toxic TWP fraction exposures, confirming the phenotypic anchor (5–9). Using synthetic 6PPD-quinone (purity ~98%), we performed controlled dosing experiments (10 concentrations,  $n = 160$  fish in two independent exposures). 6PPD-quinone was highly toxic [median lethal concentration (LC<sub>50</sub>)  $0.79 \pm 0.16$  µg/liter] to juvenile coho salmon (Fig. 3B). Estimates of LC<sub>50</sub> through controlled exposures closely matched estimates derived from bulk roadway runoff and TWP leachate exposures (LC<sub>50</sub>  $0.82 \pm 0.27$  µg/liter), indicating the primary contribution of 6PPD-quinone to observed mixture toxicity (Fig. 3A). Direct comparisons with 6PPD were performed (LC<sub>50</sub>  $250 \pm 60$  µg/liter through nominal concentrations) (fig. S14), but confident assessment of 6PPD toxicity was precluded by its poor solubility, high instability, and formation of products during exposure.

To assess environmental relevance, we used UPLC-HRMS to retrospectively quantify 6PPD-quinone in archived extracts from roadway runoff and receiving water sampling (fig. S15 and table S4) (10). In Seattle-region roadway runoff ( $n = 16$  of 16 samples), 0.8 to 19 µg/liter 6PPD-quinone was detected (Fig. 4A). During seven storm events in three Seattle-region watersheds highly affected by URMS, 6PPD-quinone

occurred at <0.3 to 3.2 µg/liter ( $n = 6$  of 7 discrete storm events;  $n = 6$  of 21 samples when including samples collected across the full hydrograph). These samples included three storms with documented URMS mortality in adult coho salmon; 6PPD-quinone was not detected in pre- and poststorm samples, but concentrations were near or above LC<sub>50</sub> values during storms. We also detected 6PPD-quinone in Los Angeles region roadway runoff ( $n = 2$  of 2 samples, 4.1 to 6.1 µg/liter) and San Francisco region creeks affected by urban runoff ( $n = 4$  of 10 samples, 1.0 to 3.5 µg/liter).

These data implicate 6PPD-quinone as the primary causal toxicant for decades of storm-water-linked coho salmon acute mortality observations. Although minor contributions from other constituents in these complex mixtures are possible, 6PPD-quinone was both necessary (consistently present in and absent from toxic and nontoxic fractions, respectively) and, when purified or synthesized as a pure chemical exposure, sufficient to produce URMS at environmental concentrations. Over the product life cycle, antioxidants [such as PPDs, TMQs (2,2,4-trimethyl-1,2-dihydroquinoline), and phenolics] are designed to diffuse to tire rubber surfaces, rapidly scavenge ground-level atmospheric ozone and other reactive oxidant species, and form protective films to prevent ozone-mediated oxidation of structurally important rubber elastomers (21, 22). Accordingly, all 6PPD added to tire rubbers is designed to react, intentionally forming 6PPD-quinone and related transformation products that are subsequently transported through the environment. This anti-ozonant application of 6PPD inadvertently, yet drastically, increases roadway runoff toxicity and environmental risk by forming the more toxic and mobile 6PPD-quinone transformation product. On the basis of the ubiquitous use and substantial mass fraction (0.4 to 2%) of 6PPD in tire rubbers and the representative detections across the U.S. West Coast (table S4), which include many detections near or above LC<sub>50</sub> values, we believe that 6PPD-quinone may be present broadly in peri-urban stormwater and roadway run-off at toxicologically relevant concentrations for sensitive species, such as coho salmon.

Globally, ~3.1 billion tires are produced annually for our more than 1.4 billion vehicles, resulting in an average 0.81 kg per capita annual emission of tire rubber particles (23). TWP are one of the most substantial microplastics sources to freshwaters (24); 2 to 45% of total tire particle loads enter receiving waters (25, 26), and freshwater sediment contains up to 5800 mg/kg TWP (23, 24, 27). Supporting recent concerns about microplastics (24, 28), 6PPD-quinone provides a compelling mechanistic link between environmental microplastic pollution and associated chemical toxicity risk. Although numerous uncertainties exist

regarding the occurrence, fate, and transport of 6PPD-quinone, these data indicate that aqueous and sediment environmental TWP residues can be toxicologically relevant and that existing TWP loading, leaching, and toxicity assessments in environmental systems are clearly incomplete (25). Tire rubber disposal also represents a major global materials problem and potential potent source of 6PPD-quinone and other tire-derived transformation products. In particular, scrap tires repurposed as crumb rubber in artificial turf fields (17) suggest both human and ecological exposures to these chemicals. Accordingly, the human health effects of such exposures merit evaluation.

Environmental discharge of 6PPD-quinone is particularly relevant for the many receiving waters proximate to busy roadways (Fig. 4B). It is unlikely that coho salmon are uniquely sensitive, and the toxicology of 6PPD transformation products in other aquatic species should be assessed. For example, used tires were more toxic to rainbow trout (75% lower 96 hours LC<sub>50</sub>) relative to new tires (29), an observation that is consistent with adverse outcomes mediated by transformation products. If management of 6PPD-quinone discharges is needed to protect coho salmon or other aquatic organisms, adaptive regulatory and treatment strategies (17, 30, 31) along with source control and “green chemistry” substitutions [identifying demonstrably nontoxic and environmentally benign replacement antioxidants (22, 32)] can be considered. More broadly, we recommend more careful toxicological assessment for transformation products of all high-production-volume commercial chemicals subject to pervasive environmental discharge.

## REFERENCES AND NOTES

1. Z. Wang, G. W. Walker, D. C. G. Muir, K. Nagatani-Yoshida, *Environ. Sci. Technol.* **54**, 2575–2584 (2020).
2. B. I. Escher, H. M. Stapleton, E. L. Schymanski, *Science* **367**, 388–392 (2020).
3. R. Altenburger *et al.*, *Environ. Sci. Eur.* **31**, 12–17 (2019).
4. C. J. Walsh *et al.*, *J. N. Am. Benthol. Soc.* **24**, 706–723 (2005).
5. N. L. Scholz *et al.*, *PLOS ONE* **6**, e28013 (2011).
6. M. I. Chow *et al.*, *Aquat. Toxicol.* **214**, 105231 (2019).
7. J. K. McIntyre *et al.*, *Environ. Pollut.* **238**, 196–203 (2018).
8. J. A. Spromberg, N. L. Scholz, *Integr. Environ. Assess. Manag.* **7**, 648–656 (2011).
9. B. E. Feist *et al.*, *Ecol. Appl.* **27**, 2382–2396 (2017).
10. K. T. Peter *et al.*, *Environ. Sci. Technol.* **52**, 10317–10327 (2018).
11. B. Du *et al.*, *Environ. Sci. Process. Impacts* **19**, 1185–1196 (2017).
12. R. M. Burgess, K. T. Ho, W. Brack, M. Lamoree, *Environ. Toxicol. Chem.* **32**, 1935–1945 (2013).
13. J. A. Spromberg *et al.*, *J. Appl. Ecol.* **53**, 398–407 (2016).
14. K. A. King, C. E. Grue, J. M. Grassley, R. J. Fisk, *Environ. Toxicol. Chem.* **32**, 920–931 (2013).
15. F. Nagai, K. Ushiyama, I. Kano, *Arch. Toxicol.* **67**, 552–557 (1993).
16. U.S. Environmental Protection Agency (EPA), “Synthetic turf field recycled tire crumb rubber research under the federal research action plan final report: Part 1—Tire crumb characterization (volumes 1 and 2),” EPA/600/R-19/051.1 (EPA, 2019).
17. S. Spahr, M. Teixidó, D. L. Sedlak, R. G. Luthy, *Environ. Sci. Water Res. Technol.* **6**, 15–44 (2020).

18. M. Muschket *et al.*, *Environ. Sci. Technol.* **52**, 288–297 (2018).
19. J. Hollender, E. L. Schymanski, H. P. Singer, P. L. Ferguson, *Environ. Sci. Technol.* **51**, 11505–11512 (2017).
20. R. O. Babbitt, *The Vanderbilt Rubber Handbook* (R. T. Vanderbilt Company, ed. 14, 2010).
21. R. P. Lattimer, E. R. Hooser, R. W. Layer, C. K. Rhee, *Rubber Chem. Technol.* **56**, 431–439 (1983).
22. N. M. Huntink, thesis, University of Twente, Enschede, The Netherlands (2003).
23. R. Sieber, D. Kawecki, B. Nowack, *Environ. Pollut.* **258**, 113573 (2020).
24. P. J. Kole, A. J. Löhr, F. G. A. J. Van Belleghem, A. M. J. Ragas, *Int. J. Environ. Res. Public Health* **14**, 1265 (2017).
25. S. Wagner *et al.*, *Water Res.* **139**, 83–100 (2018).
26. K. M. Unice *et al.*, *Sci. Total Environ.* **646**, 1639–1649 (2019).
27. K. M. Unice, M. L. Kreider, J. M. Panko, *Environ. Sci. Technol.* **47**, 8138–8147 (2013).
28. A. Kolomijica *et al.*, *Environ. Sci. Technol.* **54**, 1750–1759 (2020).
29. K. Day, K. E. Holtze, J. L. Metcalfe-Smith, C. T. Bishop, B. J. Dutka, *Chemosphere* **27**, 665–675 (1993).
30. J. K. McIntyre *et al.*, *Chemosphere* **132**, 213–219 (2015).
31. V. Dulio *et al.*, *Environ. Sci. Eur.* **30**, 5–13 (2018).
32. R. Lattimer, E. R. Hooser, H. E. Diem, R. W. Layer, C. K. Rhee, *Rubber Chem. Technol.* **53**, 1170–1190 (1980).

## ACKNOWLEDGMENTS

We thank D. Whittington; S. Edgar (University of Washington Medicine Mass Spectrometry); M. Bozlee (City of Tacoma); J. Protasio; A. Rue (Washington State Department of Ecology); M. Goehring (King County); D. E. Latch (Seattle University); J. E. Baker; C. A. James; A. D. Gipe (University of Washington Tacoma); M. Yu (Mount Sinai); S. D. Richardson (University of South Carolina); J. R. Cameron (National Oceanic and Atmospheric Administration (NOAA) NWFS); J. King (U.S. Fish and Wildlife Service); Washington State Department of Transportation; and dedicated citizen scientists from the Miller Walker Community Salmon Investigation, Puget Soundkeeper, and Thornton Creek Alliance. We gratefully thank the Puyallup Tribe and NOAA NWFS for providing juvenile coho and Agilent Technologies (T.A. and D.C.) for technical support. **Funding:** This work was supported by NSF grants 1608464 and 1803240, EPA grant 01J18101 (E.P.K.), DW-014-92437301 (N.L.S., J.K.M., and J.W.D.), Washington State Governors Funds (J.K.M. and E.P.K.), the Burges Fellowship (H.Z.), the Regional Monitoring Program for Water Quality in San Francisco Bay (A.G. and R.S.), Brazilian foundation agency FAPESP (2018/16040-5 and 2019/14770-9) (F.V.C.K.), NSERC Alliance (ALLRP 549399) and Discovery (RGPIN-2019-04165) Programs, the Canada Foundation for Innovation (CFI), the Ontario Ministry of Research and Innovation, and the Krembil Foundation (A.S.). **Disclaimer:** Findings and conclusions herein are those of the authors and do not necessarily represent the views of the sponsoring organizations. **Author contributions:** Z.T., H.Z., K.T.P., J.K.M., M.C.D., and E.P.K. designed research; Z.T., H.Z., M.G., K.T.P., C.W., R.H., and A.E.C. performed fractionation experiments; Z.T., K.T.P., R.L., and M.G. performed HRMS and data analysis; Z.T., H.Z., M.G., J.W., K.T.P., C.W., R.H., E.P.K., J.K.M., and A.E.C. conducted fish exposures; J.P., C.W., and J.W. generated TWP particles; J.W., J.P., E.M., and J.K.M. maintained the fish facility and enabled exposure studies; R.G.B., F.V.C.K., R.S., A.J., and A.S. elucidated structures by means of NMR; K.T.P., C.W., F.H., Z.T., M.G., B.D., A.G., and R.S. provided water samples; X.H., Z.T., H.Z., H.H., and M.C.D. performed ozonation experiments; N.L.S. and J.W.D. provided perspectives and context; and Z.T., H.Z., K.T.P., and E.P.K. wrote the manuscript. **Competing interests:** None declared. **Data and materials availability:** Data file S1 includes the record of the juvenile coho salmon exposure experiments. Number of tanks and coho salmon used, mortality results, and treatment information are included in the table. All other data needed to evaluate the conclusions in the paper are present in the paper or the supplementary materials.

## SUPPLEMENTARY MATERIALS

science.sciencemag.org/content/371/6525/185/suppl/DC1  
Materials and Methods  
Supplementary Text  
Figs. S1 to S15  
Tables S1 to S5  
References (33–47)  
Movies S1 and S2  
Data File S1

8 July 2020; accepted 5 November 2020  
Published online 3 December 2020  
10.1126/science.abd6951

## STRUCTURAL VIROLOGY

# A broadly protective antibody that targets the flavivirus NS1 protein

Naphak Modhiran<sup>1\*</sup>, Hao Song<sup>2,3\*</sup>, Lidong Liu<sup>4</sup>, Cheryl Bletchly<sup>5</sup>, Lou Brillault<sup>1,6</sup>, Alberto A. Amarilla<sup>1</sup>, Xiaoying Xu<sup>2</sup>, Jianxun Qi<sup>2</sup>, Yan Chai<sup>2</sup>, Stacey T. M. Cheung<sup>1</sup>, Renee Traves<sup>1</sup>, Yin Xiang Setoh<sup>1</sup>, Summa Bibby<sup>1</sup>, Connor A. P. Scott<sup>1</sup>, Morgan E. Freney<sup>1</sup>, Natalee D. Newton<sup>1</sup>, Alexander A. Khromykh<sup>1</sup>, Keith J. Chappell<sup>1</sup>, David A. Muller<sup>1</sup>, Katryn J. Stacey<sup>1</sup>, Michael J. Landsberg<sup>1</sup>, Yi Shi<sup>2†</sup>, George F. Gao<sup>2,3†</sup>, Paul R. Young<sup>1†</sup>, Daniel Watterson<sup>1†</sup>

There are no approved flaviviral therapies and the development of vaccines against flaviviruses has the potential of being undermined by antibody-dependent enhancement (ADE). The flavivirus nonstructural protein 1 (NS1) is a promising vaccine antigen with low ADE risk but has yet to be explored as a broad-spectrum therapeutic antibody target. Here, we provide the structural basis of NS1 antibody cross-reactivity through cocrystallization of the antibody 1G5.3 with NS1 proteins from dengue and Zika viruses. The 1G5.3 antibody blocks multi-flavivirus NS1-mediated cell permeability in disease-relevant cell lines, and therapeutic application of 1G5.3 reduces viremia and improves survival in dengue, Zika, and West Nile virus murine models. Finally, we demonstrate that 1G5.3 protection is independent of effector function, identifying the 1G5.3 epitope as a key site for broad-spectrum antiviral development.

Flaviviruses are a large group of positive-stranded RNA viruses and include many important human pathogens such as dengue virus (DENV), Zika virus (ZIKV), West Nile virus (WNV), Japanese encephalitis virus (JEV), and yellow fever virus (YFV) (1). Transmitted through the bite of an infected arthropod vector, these arboviruses cause a range of severe disease pathologies in humans with a broad range of symptoms including hemorrhage, neuropathology, and death (2). There are no targeted antivirals available for treatment, and vaccine use is limited to a few specific flaviviruses including YFV, JEV, and restricted use against DENV.

Until recently, the primary focus of flavivirus vaccine and immunotherapeutic development has been the virion surface envelope protein (E). However, the breadth of protection afforded by E-reactive antibodies is limited, with the current best-in-class antibodies providing protection against only a subset of the important human flaviviruses, including DENV and ZIKV, but not WNV or the JEV serogroup (3). Critically, cross-reactive but poorly neutralizing antibodies to the E protein have been shown to be responsible for

antibody-dependent enhancement (ADE) after DENV infection and vaccination (4, 5), presenting a major challenge to the development of safe and effective broad-spectrum E-based vaccines.

An alternative target for vaccine development is the flavivirus nonstructural protein 1 (NS1). NS1 is a key driver of flavivirus pathogenesis, acting through direct induction of endothelial dysfunction and proinflammatory cytokines from immune cells (6–8). NS1 is secreted from infected cells and circulates at high levels in the blood of infected patients (9), providing a tractable target for antibody-based blockade of NS1-mediated functions (10). Passive transfer of NS1 antibodies provides in vivo protection against a range of flaviviruses (11, 12). Virus-specific NS1 monoclonal antibodies (mAbs) have been shown to be protective in vivo, including the DENV mAbs 33D2 (13) and 1H7.4 (7), the ZIKV mAb AA12 (12), and the WNV mAbs 14NS1 and 16NS1 (11). Furthermore, mice vaccinated against NS1 were protected from lethal virus challenge in multiple flavivirus models, including DENV and ZIKV (14, 15). NS1-specific antibodies, unlike those targeting the proteins that make up the virion, have not been found to pose a risk of ADE.

Although these features mark NS1 as a prime target for vaccine and therapeutic development, the structural details that underpin protective antibody recognition remain largely unknown. The full-length structure of NS1 has been solved for DENV, WNV, and ZIKV (16–18), revealing three major domains (β-roll, wing, and β-ladder) (Fig. 1A). To date, only one antibody-NS1 complex structure has been resolved: that of mAb 22NS1 with the C-terminal β-ladder domain of WNV NS1 (16). However, 22NS1's cross-reactivity is limited

and it does not react with viruses outside of the JEV subgroup (11) (fig. S1). Although more broadly reactive NS1 mAbs have been identified (19), the structural basis of cross-reactivity and the potential for pan-flavivirus protection has not been ascertained.

To identify a broadly protective mAb, we screened a panel of NS1 mAbs for reactivity against the DENV and ZIKV NS1 proteins. One antibody (1G5.3), a murine mAb previously isolated from NS1-immunized mice (20), exhibited high cross-reactivity and displayed subnanomolar affinity for virus-derived NS1 (fig. S1). To understand the molecular basis of cross-reactivity, we determined the crystal structures of the antigen-binding fragment (Fab) of 1G5.3 in complex with the C-terminal fragment of NS1 (NS1c) for both DENV and ZIKV at resolutions of 2.3 and 2.8 Å, respectively. The structures show that 1G5.3 recognizes an epitope at the distal end of the β-ladder domain, farthest from the dimeric interface (Fig. 1, B and C). Key contact residues are conserved between the complexes, with a cluster of tyrosines in the 1G5.3 heavy chain contributing to extensive hydrogen bond networks and van der Waals interactions in both structures (table S1 and figs. S2 and S3).

For ZIKV, the first half of NS1c and the terminal residues beyond 339 were not resolved (Fig. 1C). In the DENV structure, the terminal region was clearly resolved and made contacts with the 1G5.3 light chain, mediated by a short α-helical loop structure in NS1c (figs. S4 and S5A). This region is not structurally conserved between different flaviviruses and has higher B factors relative to the remainder of NS1c in a number of reported structures, consistent with inherent flexibility (fig. S4, B and C). The light-chain contacts that mediate the DENV interaction in this region involve a number of framework residues. Human homolog alignment revealed several alleles of the human germline IGKV1-5 gene that include all contact residues in this region (fig. S5A). Several human homologs have been structurally resolved (21, 22) and are nearly identical to 1G5.3 within this region (fig. S5, B and C), providing a pathway for 1G5.3 humanization and indicating that there may be inherent NS1-binding capacity in human germline antibody genes that could facilitate an epitope-focused vaccine strategy, although the prevalence of these alleles in at-risk populations needs to be assessed.

Given the cross-reactivity observed for 1G5.3 between DENV and ZIKV, we examined the potential for broader recognition of NS1 by other medically important flaviviruses. NS1c constructs for a range of pathogenic flaviviruses were expressed recombinantly in a mammalian expression system (fig. S6). Indirect enzyme-linked immunosorbent assay (ELISA)

<sup>1</sup>Australian Infectious Diseases Research Centre, School of Chemistry and Molecular Biosciences, The University of Queensland, Brisbane, Australia. <sup>2</sup>CAS Key Laboratory of Pathogenic Microbiology and Immunology, Institute of Microbiology, Chinese Academy of Sciences, Beijing, China. <sup>3</sup>Research Network of Immunity and Health (RNIIH), Beijing Institutes of Life Science, Chinese Academy of Sciences, Beijing, China. <sup>4</sup>Division of Laboratory Medicine, The First Affiliated Hospital of Guangzhou Medical University, Guangzhou, China. <sup>5</sup>Microbiology, Pathology Queensland, Queensland Health, Herston, Queensland, Australia. <sup>6</sup>Centre for Microscopy and Microanalysis, The University of Queensland, Brisbane, Australia.

\*These authors contributed equally to this work.

†Corresponding author. Email: shiy@im.ac.cn (Y.S.); gaof@im.ac.cn (G.F.G.); p.young@uq.edu.au (P.R.Y.); d.watterson@uq.edu.au (D.W.)



and surface plasmon resonance binding assays showed that 1G5.3 binds NS1 from a wide range of important flavivirus pathogens with high affinity (Fig. 2A and figs. S7 and S8), including both endemic pathogens such as WNV, JEV, and YFV and viruses with emerging potential such as Rocio (ROCV), Usutu (USUV), and Ilheus (ILHV). Little to no binding was observed for tick-borne flavivirus NS1 proteins.

We next assessed complex formation of 1G5.3 Fab with NS1c derived from the flaviviruses that showed high-affinity binding by size exclusion chromatography (fig. S9) and negative-stain transmission electron microscopy. Two-dimensional (2D) class averages of 1G5.3 complexed with WNV, DENV, JEV, and USUV NS1c all revealed similar, elongated structures with clear Fab densities located at either end attached to what is presumed to be a centrally located NS1c dimer. Overall, the projections are consistent with the binding mode expected, based on the interfaces observed in the crystal structures (Fig. 2, B and C, and fig. S10). Key residues within the 1G5.3-binding site were highly conserved across all mosquito-borne flaviviruses examined in this work (Fig. 2C). G282, R299, T301, T302, S304, and G305 form a patch that interacts with the CDR-H1 and CDR-H3 loops of 1G5.3, mainly through aromatic tyrosine residues of the 1G5.3 heavy chain, further supporting the observation of a conserved binding mode. This indicates that the 1G5.3-binding mode, including angle of approach, is similar across diverse flaviviruses, and that the conserved nature of the 1G5.3-binding site underpins the broad reactivity of 1G5.3.

Superimposition of the NS1c:1G5.3 complex onto the crystal structure of the full-length, hexameric form of NS1 (Fig. 1D), which represents its biologically active, secreted form, reveals that the 1G5.3 epitope is freely accessible in this assembly. We therefore evaluated the capacity of 1G5.3 to block the activity of soluble NS1 for a range of medically important flaviviruses (Fig. 3, A to D). 1G5.3 treatment completely abrogated NS1-mediated cell barrier disruption for all NS1 species tested (DENV, ZIKV, and WNV) across a range of disease-relevant human cell lines, including microvascular and umbilical endothelial cells (HMEC-1 and HUVEC), placental trophoblasts (HRT-8/SVneo), and brain microvascular endothelial cells (HBMEC-1) (fig. S11). Dose-response analysis revealed that the *in vitro* inhibitory activity of 1G5.3 is similar for DENV and ZIKV NS1 in microvascular- and placental-derived cells, respectively, whereas relatively more 1G5.3 was required to inhibit WNV NS1 in a model of blood-brain barrier permeability (fig. S12). Given the ability of 1G5.3 to block NS1-induced cellular dysfunction, we investigated whether 1G5.3 was able to block NS1 cellular interaction.

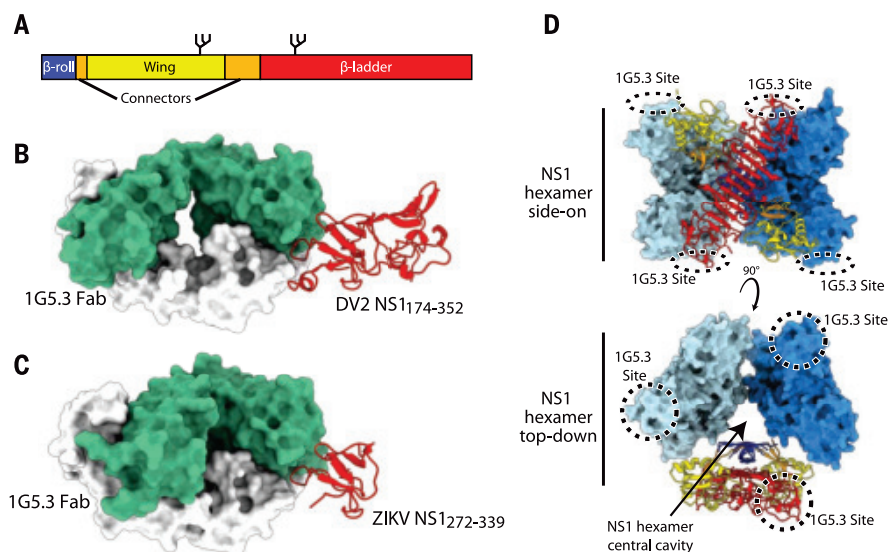


**Fig. 1. Structure of 1G5.3 in complex with NS1 from DENV-2 and ZIKV.** (A) Schematic representation of the NS1 monomer colored by domain. The N-terminal  $\beta$ -roll (residues 1 to 28) is colored blue, connector regions are colored orange (residues 29 to 37 and 151 to 179), the wing domain is colored yellow (residues 38 to 150), and the C-terminal NS1c domain is colored red (residues 180 to 352). The position of N-linked glycans is indicated with branched lines. (B) Crystal structure of DENV-2 NS1c in complex with 1G5.3 Fab. 1G5.3 Fab is shown in molecular surface representation with the heavy chain in green and the light chain in white. DENV-2 NS1c (red) is shown in ribbon representation. (C) Crystal structure of ZIKV NS1c in complex with 1G5.3 Fab. 1G5.3 is shown as in (B), with ZIKV NS1c in red. (D) 1G5.3 epitope availability on the hexameric form of NS1. For clarity, one NS1 dimer is shown in ribbon representation and colored as per (A) and the other two dimers are shown in blue and light blue surface representation. All six 1G5.3 epitopes are accessible. Four 1G5.3 sites are visible in the side-on representation shown above, with two hidden from view, as indicated. A 90° rotation of the bound hexameric form is shown below, with three 1G5.3-binding sites visible and the central cavity of the barrel-shaped NS1 hexamer indicated.

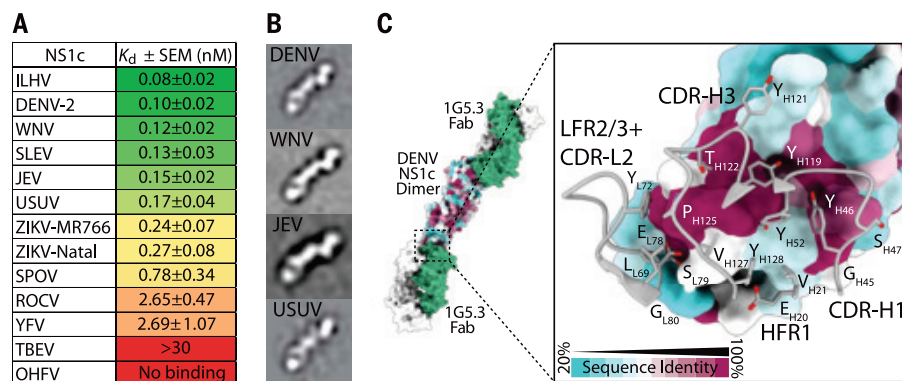


**Fig. 2. Broad reactivity of 1G5.3 is conferred by a conserved patch on flavivirus NS1.** (A) Affinity of mAb 1G5.3 for NS1c proteins derived from a range of medically important flaviviruses. Dissociation constant ( $K_d$ ) values for NS1c proteins are listed in order of affinity. (B) Representative 2D class averages produced from single-particle projection images of 1G5.3 Fab in complex with NS1c from DENV-2, WNV, JEV, and USUV imaged by negative-stain transmission electron microscopy. Clear Fab densities are observed on both ends of the NS1c dimers. (C) Molecular surface representation of the crystalized dimeric DENV-2 NS1c and 1G5.3 Fab complex shown in similar orientation to that depicted in the 2D class averages shown in (B). 1G5.3 Fab heavy and light chain are shown in green and white, respectively. NS1c surface is colored according to conservation between the viruses listed in (A) with  $K_d < 3$  nM. Inset panel shows the conserved surface patch (dark red) that spans the 1G5.3 epitope. Key binding residues that contribute to the binding interface within the CDR loops and framework regions are indicated.

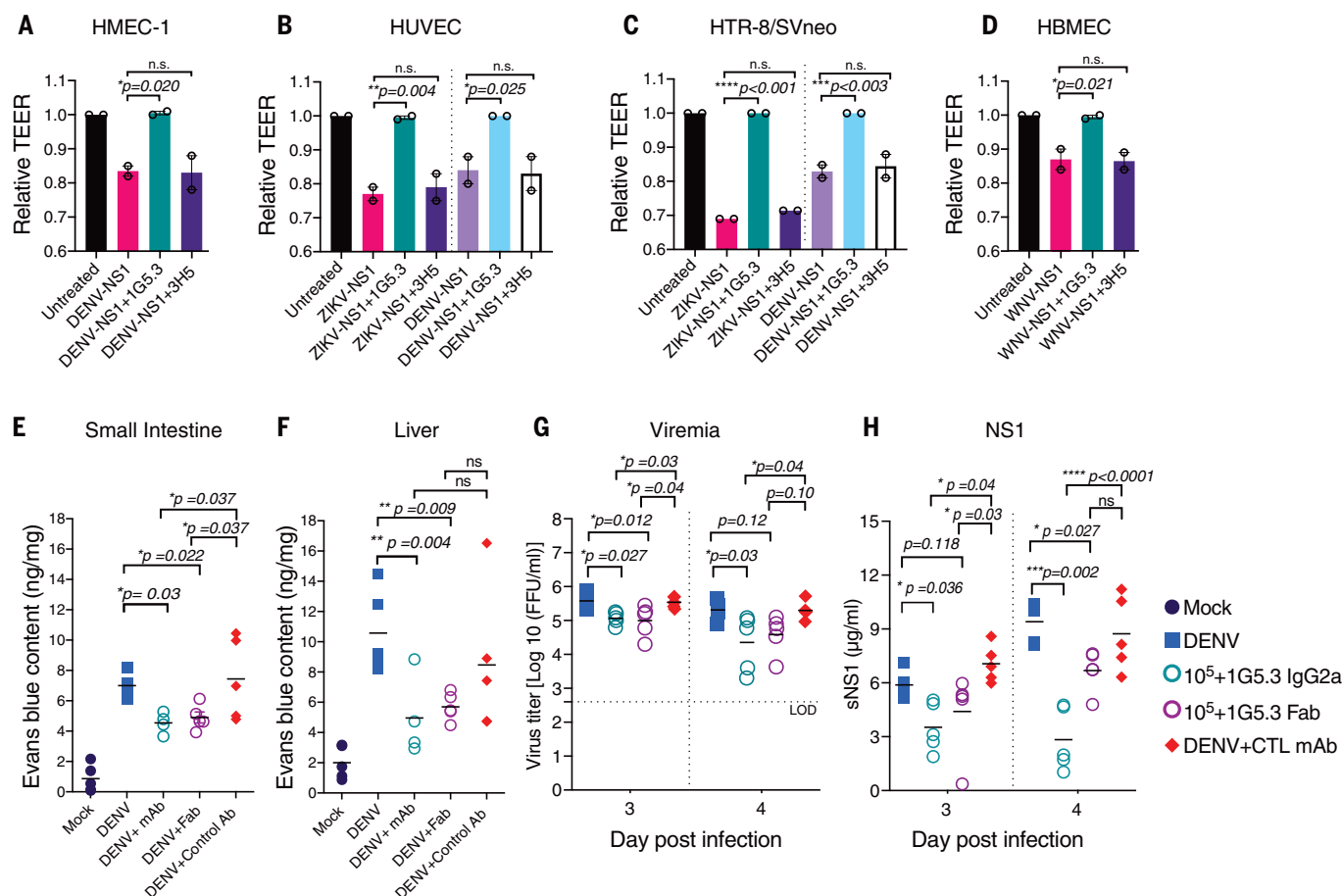


**Fig. 3. Multi-flavivirus NS1-triggered permeability is inhibited by 1G5.3 on disease-relevant cell lines, and blockade of NS1 toxicity by 1G5.3 is independent of Fc effector function in vivo.** (A to D) Induced hyperpermeability of HMEC-1 by DENV2-NS1 (A), HUVEC and HTR-8/SVNeo by DENV2-NS1 and ZIKV-NS1 (B and C), and HBMEC by WNV-NS1 and DENV2-NS1 (D) were ablated by mAb 1G5.3 but not control mAb 3H5. Data points shown as mean  $\pm$  range from two independent experiments, with two to three replicates within each replicated experiment. (E to H) In vivo inhibitory effects in DENV-induced systemic vascular leakage assay in

small intestine (E) and liver (F) were determined for mice administrated with 200  $\mu$ g of 1G5.3 mAb, 1G5.3 Fab, or control mAb 48 hours after virus exposure. Viral load (G) and circulating NS1 (H) from sera were quantified ( $n = 5$ ). Bars and dotted line denote mean values and the lower limit of quantification of immunoprecipitation assay, respectively. Statistical significances were determined using one-way analysis of variance (Sidak's test); those in (A) to (D) were compared with the NS1-treated sample and those in (E) to (H) were compared with the DENV-infected sample.  $P < 0.05$  indicates statistically significant differences.

Preincubation of NS1 with 1G5.3, but not control mAb, was observed to significantly inhibit DENV and WNV NS1 binding to HMEC-1 and HBMEC cells, respectively (fig. S13). 1G5.3 blockade of NS1-cell binding may occur through direct inhibition of receptor binding or inhibition of NS1 conformational changes that may be required to facilitate NS1 interaction with cells. In either case, 1G5.3 can inhibit the early stages of NS1-cell interaction and target the circulating NS1 population rather than inhibiting cell uptake and subsequent NS1-induced cellular activation.

Although 1G5.3 inhibits multiple flavivirus NS1-induced cellular pathologies across several relevant cell lines, previous studies have shown that some NS1 antibodies may play a role in disease pathology through different mechanisms ranging from complement activation (23) and cross-reactivity to self-antigens (24) and

damage to endothelial cell barrier function (25). NS1 antibodies have also been linked to enhanced pathology in secondary infection (13), and cross-reactivity to viral structural proteins has been reported. Although we observed no direct damage of any cellular monolayer systems with 1G5.3 treatment alone, we investigated the potential for autoreactivity and virion cross-reactivity empirically. We found that unlike some reported C-terminal NS1 mAbs (26), 1G5.3 does not cross-react with human plasminogen (fig. S14). In addition, 1G5.3 does not cross-react with purified flavivirus virions or show any activity in direct viral inhibition assays, suggesting that it is highly specific for NS1 (fig. S15). These findings are in contrast to those of Falconar, who observed some limited cross-reactivity of NS1 mAbs, including 1G5.3, to viral preparations and synthetic peptides derived from the DENV E

sequence (27). However, the use of semipurified viral preparations that still contain DENV NS1 and short synthetic peptides that can adopt non-native conformation may have confounded the earlier findings. Here, we used a chimeric recombinant system to generate purified virions to eliminate any potential DENV NS1 contamination and found no reactivity toward viral preparations for 1G5.3 (fig. S15). Furthermore, using the mAb 4G2 (28), we demonstrate that these preparations present authentic epitopes equivalent to the earlier reported cross-reactive fusion peptide sequence, suggesting that the previously reported peptide binding is not biologically relevant. Although these results are encouraging for future clinical development of 1G5.3 and similar mAbs, it will be important to closely monitor the safety profile of NS1-targeting mAbs in translational applications.

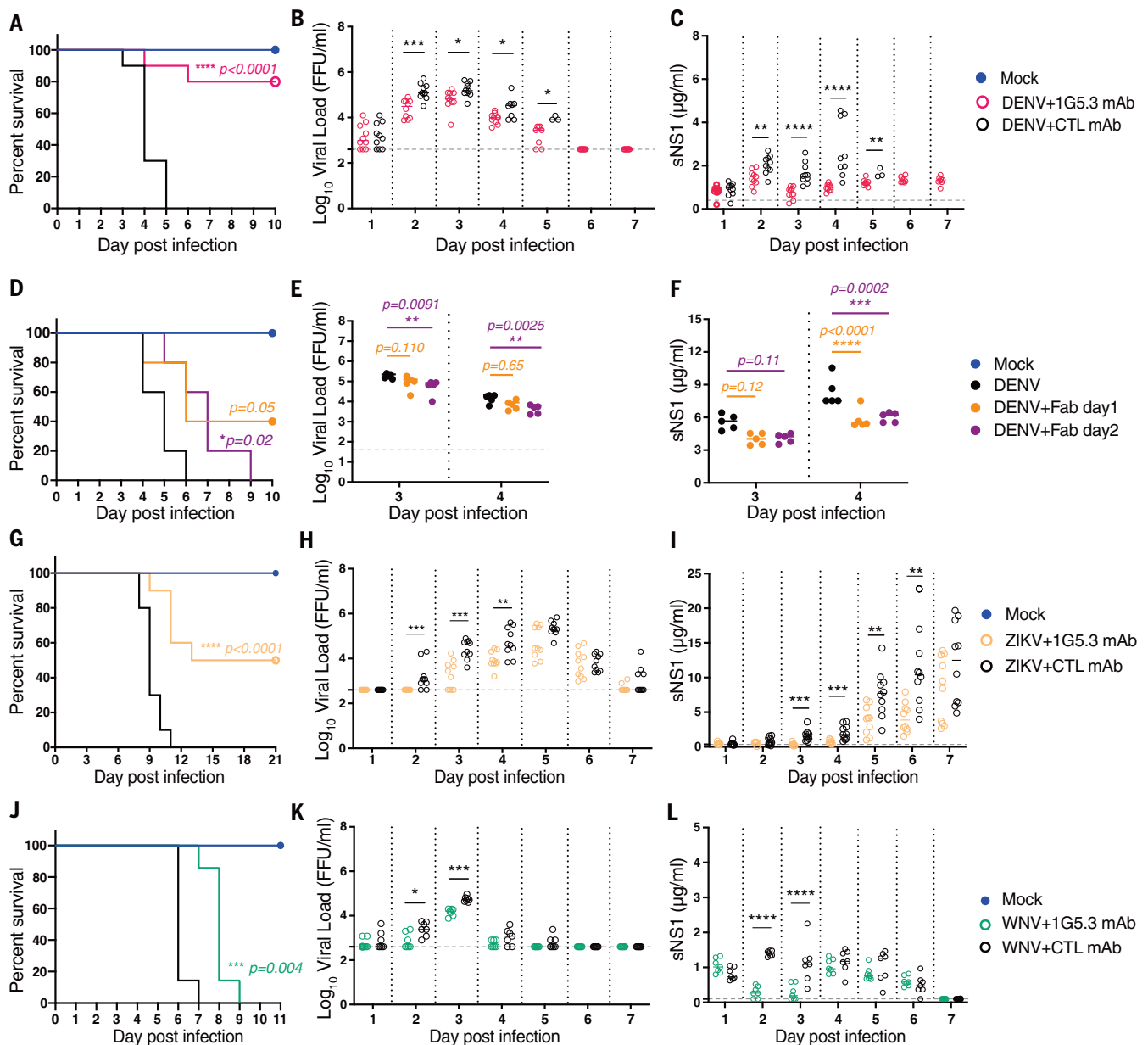


**Fig. 4. Therapeutic administration of mAb 1G5.3.** Mice were challenged with a lethal dose of a mouse-adapted strain of DENV2, ZIKV-MR766, or WNV NSW2011 on day 0 and given single 200-µg injections of 1G5.3 or control (CTL) antibody 1 day after virus exposure. **(A to F)** Challenge data from male *lfnar<sup>-/-</sup>* [(A) to (C)] or AG129 [(D) to (F)] mice infected with DENV2 at  $10^7$  or  $5 \times 10^5$  focus-forming units (FFU) per mouse, respectively, and treated with mAb or Fab as indicated. **(G to I)** Challenge data from female *lfnar<sup>-/-</sup>* mice infected with ZIKV-MR766 at 10 FFU per mouse. **(J to L)** Challenge data from female weanling CD1 mice infected with WNV NSW2011 at  $10^3$  FFU per mouse. Mice were monitored for survival [(A), (D), (G) and (J)]. Viremia [(B),

(E), (H), and (K)] and circulating NS1 [(C), (G), (I) and (L)] from sera on the indicated day were quantified by immunoplaque assay and NS1-capture ELISA. Dotted horizontal line indicates lower limit of detection. Solid bars indicate the median. Statistical significances were determined using a log-rank (Mantel-Cox) test for survival compared with CTL mAb treatment. The log<sub>10</sub>-transformed virus titers and sNS1 levels were analyzed by Mann-Whitney test.  $P < 0.05$  indicates statistically significant differences.  $n = 10$  in each group for DENV-infected mice and ZIKV-infected mice;  $n = 7$  for WNV-infected mice;  $n = 5$  for uninfected mice for the DENV and ZIKV experiments; and  $n = 3$  for the WNV experiment.

Finally, we investigated whether the ability of 1G5.3 to bind to and functionally block NS1 in vitro was reproducible in vivo. DENV-infected mice therapeutically treated with 1G5.3 at 2 days postinfection (DPI) showed significantly lower vascular leak and reduced viral and NS1 levels (Fig. 3, E to H). Thera-

peutic treatment with the 1G5.3 Fab fragment also resulted in diminished vascular leak and reduced viral load. These findings indicate that the protective effect of 1G5.3 is not dependent on Fc effector activity and that the binding of 1G5.3 alone was sufficient to inhibit the toxic effects of circulating NS1. Strong

protective effects (80% survival) were also observed in a murine lethal challenge model of DENV after therapeutic treatment with 1G5.3 at 1 DPI (Fig. 4, A to C, and fig. S16A), with 1G5.3 Fab protecting to a lesser extent (Fig. 4, D to F, and fig. S16B). These findings suggest that in addition to the direct inhibition of NS1



toxic activity by 1G5.3 binding, Fc-dependent mechanisms such as antibody-dependent cellular cytotoxicity may contribute to the protective activity of 1G5.3. However, these may also reflect the different avidity and half-life of the fragment versus the full 1G5.3 antibody. Given its broad reactivity, we also investigated the potential for 1G5.3-mediated protection in murine lethal challenge models for ZIKV and WNV and observed protective effects, albeit with a spectrum of efficacy across the viruses observed: 50% survival in ZIKV (Fig. 4, G to I, and fig. S16C) and delayed mortality in WNV (Fig. 4, J to L, and fig. S16D). In all lethal challenge models, treatment significantly reduced viral load and circulating NS1 levels. To assess the protective effects of 1G5.3 relative to previously reported mAbs, we produced a panel of NS1- and E-specific mAbs from the literature using a matched recombinant framework (figs. S15 and S17) and performed a dose-matched therapeutic comparison in the DENV and ZIKV models. Across this diverse mAb panel, only 1G5.3 was able to significantly protect from both DENV and ZIKV challenge. Moreover, the protective effects of 1G5.3 were significantly higher than published virus-specific NS1-targeting mAbs for both DENV (7) and ZIKV (12) and comparable to a leading DENV E-specific mAb, 4E11 (29) (figs. S18 and S19). In contrast to 1G5.3, the pan-reactive E mAb 4G2 provided no protection at a matched dose in either the DENV or ZIKV models, further highlighting the breadth of protection observed for 1G5.3.

The findings presented here reveal the structural basis for NS1 cross-reactivity between distinct flavivirus species spanning multiple serological groups. The breadth of reactivity of 1G5.3 can be attributed to a conserved epitope on the distal end of the NS1  $\beta$ -ladder domain. Demonstration of 1G5.3-mediated blockade of multi-flavivirus NS1 activity both in vitro and in vivo suggests that although NS1 proteins from different flavivirus species have distinct reported cell toxicity (30), the molecular mechanisms that drive these processes are conserved and can be directly targeted to develop broad-spectrum flavivirus antivirals and vaccines.

## REFERENCES AND NOTES

1. P. Simmonds et al., *J. Gen. Virol.* **98**, 2–3 (2017).
2. E. A. Gould, T. Solomon, *Lancet* **371**, 500–509 (2008).
3. G. Barba-Spaeth et al., *Nature* **536**, 48–53 (2016).
4. S. B. Halstead, *Adv. Virus Res.* **60**, 421–467 (2003).
5. S. S. Whitehead, K. Subbarao, *Cold Spring Harb. Perspect. Biol.* **10**, a028811 (2018).
6. N. Modhiran et al., *Sci. Transl. Med.* **7**, 304ra142 (2015).
7. P. R. Beatty et al., *Sci. Transl. Med.* **7**, 304ra141 (2015).
8. N. Modhiran et al., *Immunol. Cell Biol.* **95**, 491–495 (2017).
9. S. Alcon et al., *J. Clin. Microbiol.* **40**, 376–381 (2002).
10. D. Watterson, N. Modhiran, P. R. Young, *Antiviral Res.* **130**, 7–18 (2016).
11. K. M. Chung et al., *J. Virol.* **80**, 1340–1351 (2006).
12. M. J. Bailey et al., *Nat. Commun.* **9**, 4560 (2018).
13. D. Jayatilaka et al., *Nat. Commun.* **9**, 5242 (2018).
14. J. J. Schlesinger, M. W. Brandriss, E. E. Walsh, *J. Gen. Virol.* **68**, 853–857 (1987).
15. A. C. Brault et al., *Sci. Rep.* **7**, 14769 (2017).
16. M. A. Edeling, M. S. Diamond, D. H. Fremont, *Proc. Natl. Acad. Sci. U.S.A.* **111**, 4285–4290 (2014).
17. D. L. Akey et al., *Science* **343**, 881–885 (2014).
18. X. Xu et al., *EMBO J.* **35**, 2170–2178 (2016).
19. K. Stettler et al., *Science* **353**, 823–826 (2016).
20. A. K. Falconar, P. R. Young, *J. Gen. Virol.* **72**, 961–965 (1991).
21. L. E. Clark et al., *Nat. Commun.* **9**, 1884 (2018).
22. J. M. Orenge et al., *Nat. Commun.* **9**, 1421 (2018).
23. P. Avirutnan et al., *J. Infect. Dis.* **193**, 1078–1088 (2006).
24. Y. S. Lin et al., *Exp. Biol. Med.* **236**, 515–523 (2011).
25. C. F. Lin et al., *J. Med. Virol.* **69**, 82–90 (2003).
26. Y. C. Chuang et al., *J. Immunol.* **187**, 6483–6490 (2011).
27. A. K. Falconar, *Clin. Vaccine Immunol.* **15**, 549–561 (2008).
28. W. D. Crill, G. J. Chang, *J. Virol.* **78**, 13975–13986 (2004).
29. J. J. Cockburn et al., *Structure* **20**, 303–314 (2012).
30. H. Puerta-Guardo et al., *Cell Rep.* **26**, 1598–1613.e8 (2019).

## ACKNOWLEDGMENTS

We thank the staff of the BL17U beamline at the Shanghai Synchrotron Radiation Facility; R. Hall and J. Peters for providing reagents; the staff of the Australian Microscopy and Microanalysis Research Facility at the Centre for Microscopy and Microanalysis, University of Queensland, for scientific and technical assistance; and the staff of University of Queensland's Biological Resources (UQBR) for running our mouse breeding program and monitoring our mouse experiments. **Funding:** This work was supported by the Australian Government National Health and Medical Research Council (NHMRC) project numbers APP1162507 to D.W., Y.S., P.R.Y., N.M., and M.J.L. and APP1109738 to K.J.S., P.R.Y., and D.W.; the Strategic Priority Research

Program of the Chinese Academy of Sciences (XDB29010000); the National Science and Technology Major Project (2018ZX10101004, 2018ZX09711003, and 2018ZX10733403); the National Natural Science Foundation of China (NSFC) (81871658 and 81702015); and the Yanqi Lake Meeting organized by the Academic Divisions of CAS. **Author contributions:** N.M., H.S., L.L., C.B., L.B., Y.S., G.F.G., P.R.Y., and D.W. conceptualized the experiment. N.M., H.S., L.L., C.B., L.B., A.A.A., X.X., J.Q., Y.C., S.T.M.C., R.T., Y.X.S., S.B., C.A.P.S., K.J.C., D.A.M., and D.W. contributed to experiments. Y.X.S. and A.A.K. provided resources. N.M., H.S., L.L., C.B., L.B., M.J.L., Y.S., G.F.G., P.R.Y., and D.W. performed data analysis. N.M., H.S., Y.S., G.F.G., and D.W. wrote the manuscript. N.M., H.S., K.J.S., M.J.L., Y.S., G.F.G., P.R.Y., and D.W. edited the manuscript. M.J.L., Y.S., G.F.G., P.R.Y., and D.W. supervised the work. **Competing interests:** The authors declare no competing interests. **Data and materials availability:** Coordinates and structure factors have been deposited in the Protein Data Bank under accession codes 7BSC (complex structure of 1G5.3 Fab bound to DENV2 NS1c) and 7BSD (complex structure of 1G5.3 Fab bound to ZIKV NS1c). All other data are available in the main text or supplementary materials and materials described herein may be made available upon request.

## SUPPLEMENTARY MATERIALS

science.sciencemag.org/content/371/6525/190/suppl/DC1  
Materials and Methods  
Figs. S1 to S19  
Tables S1 to S4  
References (31–54)

3 April 2020; accepted 30 November 2020  
10.1126/science.abb9425

## STRUCTURAL VIROLOGY

# Structural basis for antibody inhibition of flavivirus NS1-triggered endothelial dysfunction

Scott B. Biering<sup>1\*</sup>, David L. Akey<sup>2\*</sup>, Marcus P. Wong<sup>1,3</sup>, W. Clay Brown<sup>2</sup>, Nicholas T. N. Lo<sup>1,3</sup>, Henry Puerta-Guardo<sup>1</sup>, Francielle Tramontini Gomes de Sousa<sup>1</sup>, Chunling Wang<sup>1</sup>, Jamie R. Konwerski<sup>2</sup>, Diego A. Espinosa<sup>1</sup>, Nicholas J. Bockhaus<sup>2,4</sup>, Dustin R. Glasner<sup>1</sup>, Jeffrey Li<sup>1</sup>, Sophie F. Blanc<sup>1</sup>, Evan Y. Juan<sup>1</sup>, Stephen J. Elledge<sup>5</sup>, Michael J. Mina<sup>6</sup>, P. Robert Beatty<sup>1</sup>, Janet L. Smith<sup>2,4†</sup>, Eva Harris<sup>1†</sup>

Medically important flaviviruses cause diverse disease pathologies and collectively are responsible for a major global disease burden. A contributing factor to pathogenesis is secreted flavivirus nonstructural protein 1 (NS1). Despite demonstrated protection by NS1-specific antibodies against lethal flavivirus challenge, the structural and mechanistic basis remains unknown. Here, we present three crystal structures of full-length dengue virus NS1 complexed with a flavivirus-cross-reactive, NS1-specific monoclonal antibody, 2B7, at resolutions between 2.89 and 3.96 angstroms. These structures reveal a protective mechanism by which two domains of NS1 are antagonized simultaneously. The NS1 wing domain mediates cell binding, whereas the  $\beta$ -ladder triggers downstream events, both of which are required for dengue, Zika, and West Nile virus NS1-mediated endothelial dysfunction. These observations provide a mechanistic explanation for 2B7 protection against NS1-induced pathology and demonstrate the potential of one antibody to treat infections by multiple flaviviruses.

**D**engue virus serotypes 1 to 4 (DENV1–4) are mosquito-borne flaviviruses causing 50 to 100 million dengue cases and ~500,000 hospitalizations annually, with severe forms of disease manifesting in vascular leak as a result of endothelial dysfunction (1, 2). The triggers for these pathologies are often broadly described as a “cytokine storm” resulting from uncontrolled viral rep-

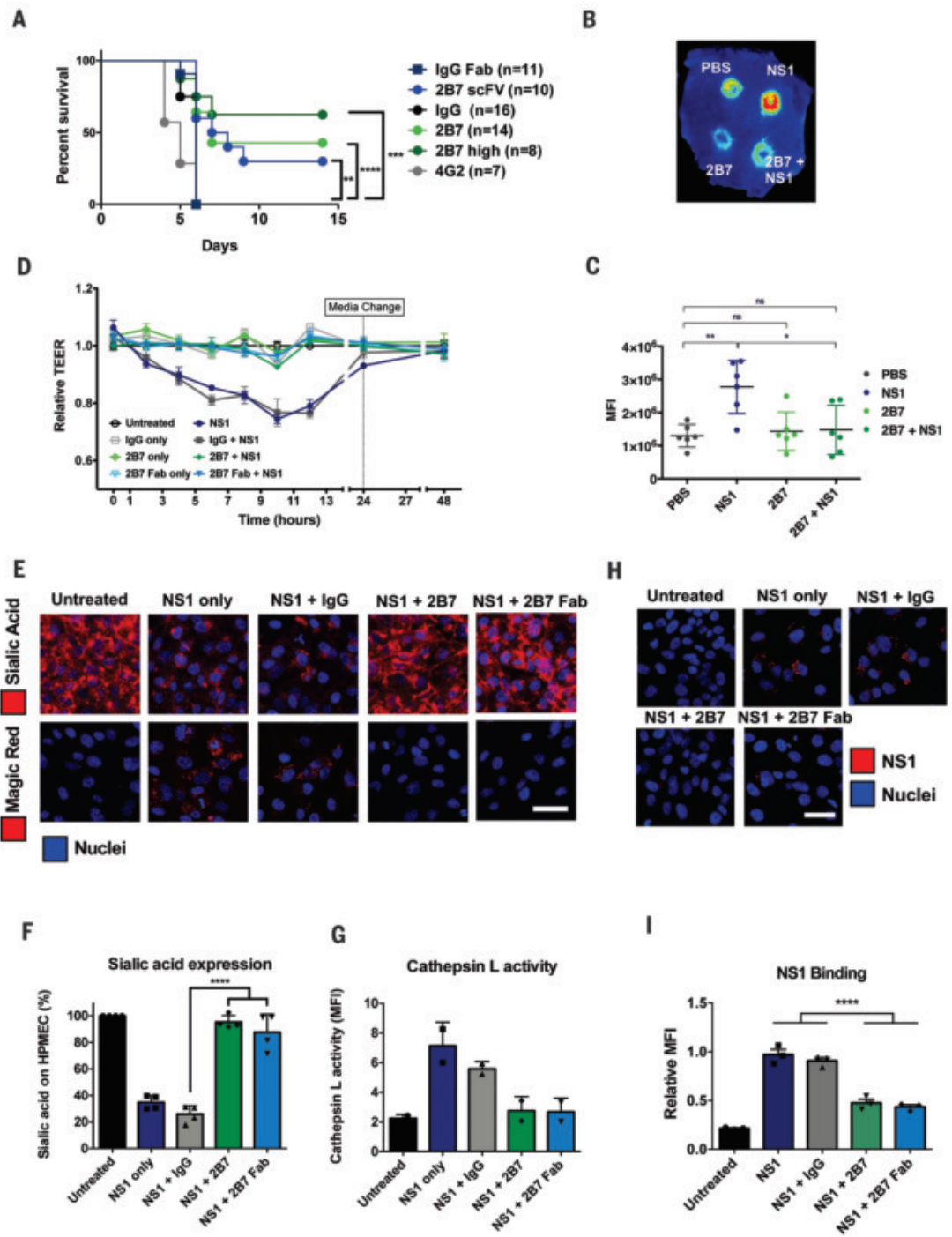
lication and activation of target immune cells, with a direct pathogenic role now characterized for the DENV nonstructural protein 1 (NS1) through interactions with endothelial and immune cells (3–5). There are currently no approved therapeutics for dengue, and the only licensed DENV vaccine, Dengvaxia, is now reserved strictly for patients with pre-existing DENV immunity owing to the risk of

# **Fig. 1. Anti-NS1 mAb 2B7 is protective against lethal dengue virus infection and NS1-mediated vascular leak and endothelial dysfunction.**

(A) Survival curve of *Ifnar*<sup>-/-</sup> mice infected with DENV2-D220. Mice were given two 150- $\mu$ g doses (300  $\mu$ g for “2B7 high”) of full-length 2B7, a 2B7 scFv, an anti-E antibody (4G2), or an isotype control antibody the day before and the day after infection. Numbers in parentheses indicate the numbers of mice in each group.

(B) Localized leak of the tracer molecule dextran-647 was measured after dorsal intradermal injection of NS1 with or without 2B7 or the indicated controls into the shaved backs of mice. One representative experiment of  $n = 6$  mice is displayed. (C) Quantification of (B) as mean fluorescence intensity (MFI). (D) TEER assay of HPMEC hyperpermeability after the addition of DENV2 NS1 with or without 2B7 or the indicated controls at the indicated time points after NS1 treatment.  $n = 3$  biological replicates. (E) Endothelial dysfunction and EGL disruption were monitored using immunofluorescence microscopy 6 hours after treatment with DENV2 NS1 with or without 2B7, 2B7 Fab, or the indicated controls. Endothelial cell dysfunction (bottom,  $n = 2$  biological replicates) was monitored

using the cathepsin L activity reporter molecule Magic Red, and EGL disruption (top,  $n = 4$  biological replicates) was monitored by staining sialic acid on the cell surface. (F and G) Quantification of (E). (H) DENV2 NS1 binding to HPMECs in the presence of 2B7, 2B7 Fab, or the indicated controls was monitored by immunofluorescence microscopy 90 min after NS1 treatment.  $n = 3$  biological replicates. (I) Quantification of (H). Scale bars, 50  $\mu$ m for all figures. n.s., not significant ( $P > 0.05$ ); \* $P < 0.05$ ; \*\* $P < 0.01$ ; \*\*\* $P < 0.001$ ; \*\*\*\* $P < 0.0001$  by one-way ANOVA analysis with multiple comparisons.



using the cathepsin L activity reporter molecule Magic Red, and EGL disruption (top,  $n = 4$  biological replicates) was monitored by staining sialic acid on the cell surface. (F and G) Quantification of (E). (H) DENV2 NS1 binding to HPMECs in the presence of 2B7, 2B7 Fab, or the indicated controls was monitored by immunofluorescence microscopy 90 min after NS1 treatment.  $n = 3$  biological replicates. (I) Quantification of (H). Scale bars, 50  $\mu$ m for all figures. n.s., not significant ( $P > 0.05$ ); \* $P < 0.05$ ; \*\* $P < 0.01$ ; \*\*\* $P < 0.001$ ; \*\*\*\* $P < 0.0001$  by one-way ANOVA analysis with multiple comparisons.

<sup>1</sup>Division of Infectious Diseases and Vaccinology, School of Public Health, University of California, Berkeley, Berkeley, CA 94720-3370, USA. <sup>2</sup>Life Sciences Institute, University of Michigan, Ann Arbor, MI 48109, USA. <sup>3</sup>Infectious Diseases and Immunity Graduate Group, School of Public Health, University of California, Berkeley, Berkeley, CA 94720-3370, USA. <sup>4</sup>Department of Biological Chemistry, University of Michigan Medical School, Ann Arbor, MI 48109, USA. <sup>5</sup>Division of Genetics, Brigham and Women's Hospital, Howard Hughes Medical Institute, Department of Genetics, and Program in Virology, Harvard Medical School, Boston, MA 02115, USA. <sup>6</sup>Center for Communicable Disease Dynamics, Department of Epidemiology, and Department of Immunology and Infectious Diseases, Harvard School of Public Health, Boston, MA 02115, USA.

\*These authors contributed equally to this work.

†Corresponding author. Email: eharris@berkeley.edu (E.H.); janetsmith@umich.edu (J.L.S.)

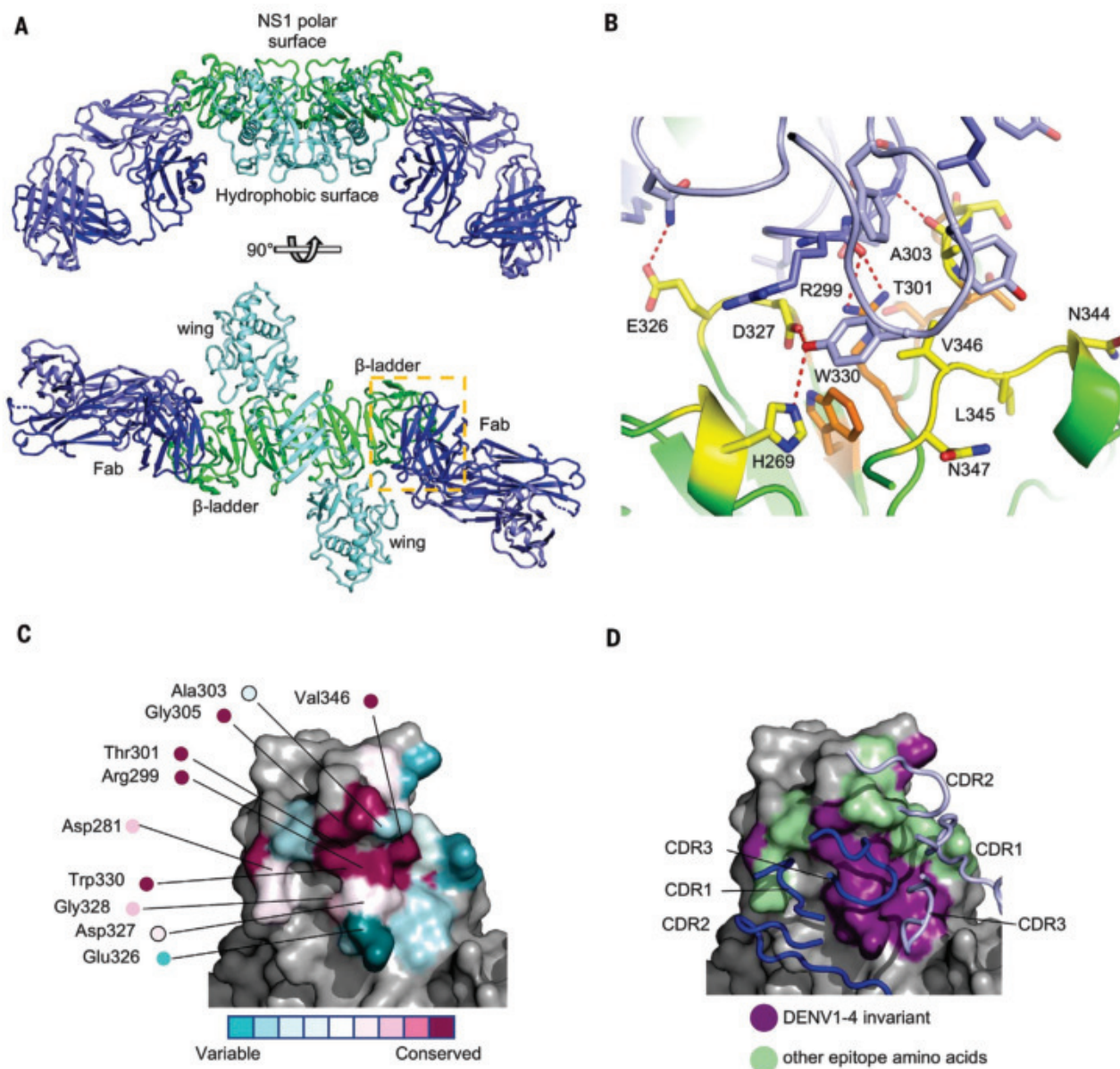


**Fig. 2. Crystal structure of the 2B7 Fab complexed with DENV NS1 reveals binding to the  $\beta$ -ladder.** (A) Perpendicular views of a 3.2-Å crystal structure of 2B7 Fab (heavy chain, dark blue; light chain, light blue) and DENV1 NS1 dimer ( $\beta$ -ladder domains, green;  $\beta$ -roll and wing domains, cyan). The combining site is boxed (yellow) in the lower image, right monomer. (B) Detail of the 2B7 scFv and the DENV2 NS1-combining site highlighting the interacting amino acids. The 2B7 backbone is shown in blue, and NS1 is shown in green with key side chains shown as sticks. Pan-flavivirus conserved side chains (orange) are at the center of the discontinuous epitope; DENV-conserved side chains (yellow) are at

the epitope periphery; and hydrogen bonds are shown as dashed lines. (C) DENV2 NS1 epitope for 2B7 scFv (colored by conservation across flaviviruses according to the key and based on the alignment in Fig. 3A), with surfaces outside the epitope in gray. Sites of mutagenesis in Fig. 3 are labeled. (D) 2B7 scFv complementarity-determining regions (CDRs, in tube rendering) for the heavy chain (dark blue) and light chain (light blue) overlaid on the DENV2 NS1 epitope surface. Surfaces of amino acids conserved among the four DENV serotypes but variable in other flaviviruses are shown in purple; other epitope residues are shown in green; view as in (C).

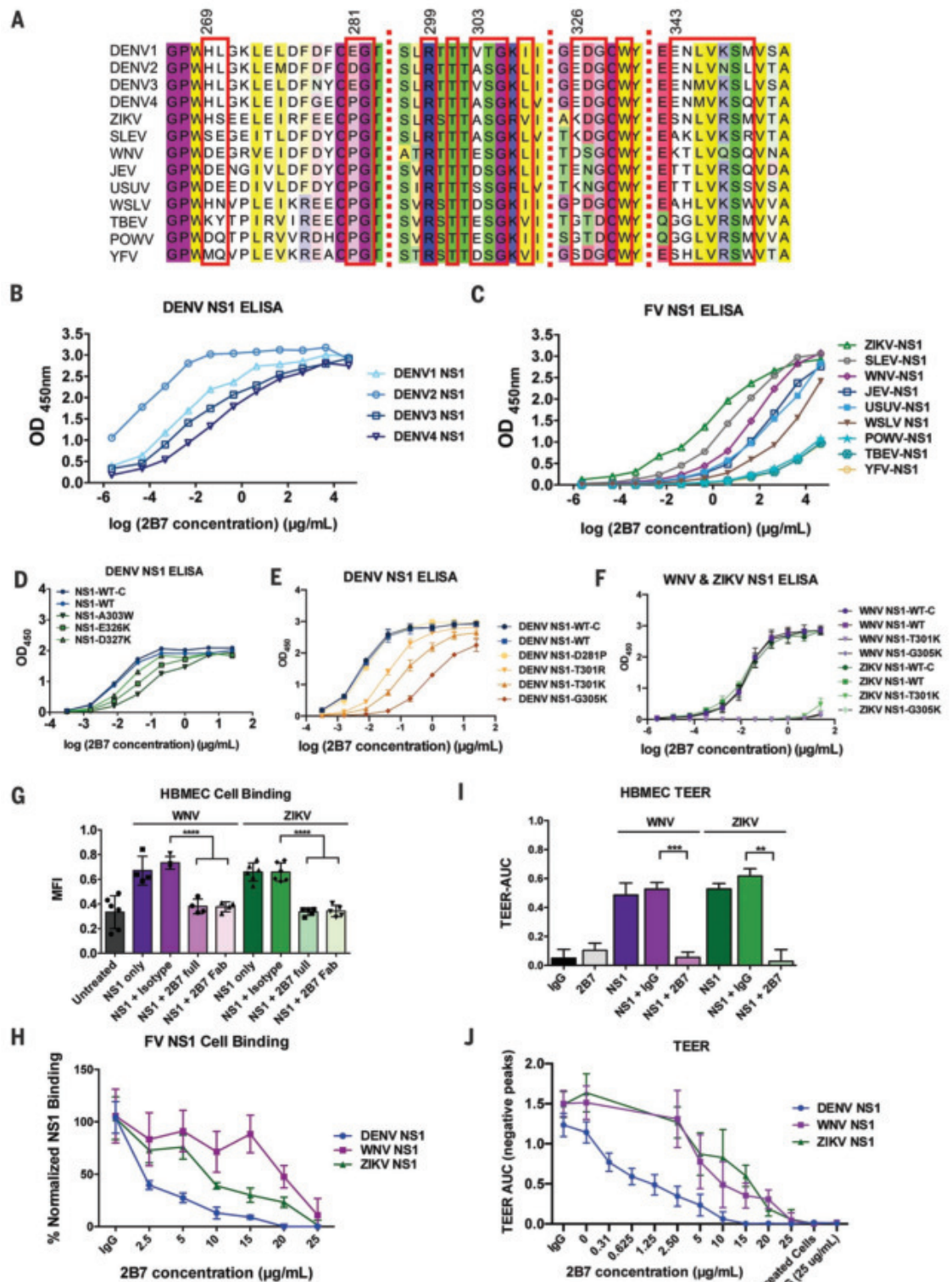
predisposing DENV-naïve patients to severe dengue disease, presumably through antibody-dependent enhancement (ADE) (6, 7). This risk has made the development of a successful vaccine targeting the DENV envelope protein (E) challenging, so targeting other DENV proteins important for pathogenesis is a critical avenue of investigation.

The multifunctional DENV NS1 protein plays a key role in viral replication as an intracellular dimer (8). NS1 is also secreted from DENV-infected cells as a barrel-shaped hexamer containing lipid cargo (9); it circulates in the blood and serves as a diagnostic antigen and biomarker of disease severity (10). Extracellular NS1 acts as a virulence factor inhibiting

complement, activating platelets and immune cells, and directly interacting with endothelial cells (11–13). This results in disruption of the endothelial glycocalyx layer (EGL) and intercellular junctional complexes, both critical for maintaining endothelial barrier integrity (13–15). NS1-mediated endothelial dysfunction is observed for multiple medically relevant



**Fig. 3. 2B7 cross-reacts with multiple flavivirus NS1 proteins.** (A) Alignment of amino acids across the discontinuous 2B7-combining site in NS1 from different flaviviruses. Residues in contact with 2B7 are boxed in red. (B) ELISAs measuring the interaction of 2B7 with NS1 from DENV1-4. Data displayed are at least  $n = 3$  biological replicates. (C) ELISAs measuring 2B7 interaction with other flavivirus NS1 proteins (at least  $n = 3$  biological replicates). (D and E) Same as (C) except for the indicated DENV2 NS1-mutagenized proteins compared with the in-house-produced (NS1-WT) or commercially purchased (NS1-WT-C) control proteins. Data displayed are  $n = 3$  biological replicates. (F) Same as (C) except for the indicated WNV or ZIKV NS1-mutagenized proteins ( $n = 3$  biological replicates). (G) WNV or ZIKV NS1 binding to HBMECs in the presence or absence of 25  $\mu\text{g}/\text{ml}$  2B7 and the indicated controls was measured by immunofluorescence microscopy 90 min after NS1 treatment. Data displayed are at least  $n = 4$  biological replicates. (H) Same as (G) but with the indicated concentrations of 2B7 (at least  $n = 3$  biological replicates). (I) Effect of WNV or ZIKV NS1 on the hyperpermeability of HBMECs was measured using TEER in the presence or absence of 25  $\mu\text{g}/\text{ml}$  2B7 or the indicated controls. AUC, negative area under the curve (fig. S8C) correlating with a drop in endothelial cell monolayer electrical resistance. Data presented are  $n = 2$  biological replicates. (J) Same as (I) but with the indicated concentration of 2B7 (at least  $n = 3$  biological replicates).  $^{**}P < 0.01$ ;  $^{***}P < 0.001$ ;  $^{****}P < 0.0001$  by one-way ANOVA analysis with multiple comparisons. FV, flavivirus. Abbreviations for the amino acid residues are as follows: A, Ala; C, Cys; D, Asp; E, Glu; F, Phe; G, Gly; H, His; I, Ile; K, Lys; L, Leu; M, Met; N, Asn; P, Pro; Q, Gln; R, Arg; S, Ser; T, Thr; V, Val; W, Trp; and Y, Tyr.



mosquito-borne flaviviruses including Zika virus (ZIKV), West Nile virus (WNV), Japanese encephalitis virus (JEV), and yellow fever virus (YFV) (16, 17). NS1 has emerged as a promising

vaccine candidate because of its prominent role in flavivirus pathogenesis. Indeed, vaccination with NS1 protects against lethal DENV or ZIKV challenge in mice (3, 18–20).

Because NS1 is conserved and triggers endothelial dysfunction through a comparable mechanism for multiple flaviviruses (16), one broadly reactive flavivirus therapeutic or

vaccine targeting NS1 would be an innovative breakthrough.

Flavivirus NS1 has three domains that may have distinct functions (21). Despite a plethora of structural data (21–25), the mechanistic basis for antibody-mediated protection against NS1-induced endothelial dysfunction and the specific functional domains of NS1 responsible for different pathogenic functions are unknown. We previously identified the anti-DENV NS1 immunoglobulin G2b (IgG2b) mouse monoclonal antibody (mAb) 2B7 as a strong inhibitor of NS1-induced endothelial hyperpermeability *in vitro* (3). Here, we show that in a DENV2 lethal challenge model, 2B7 was pro-

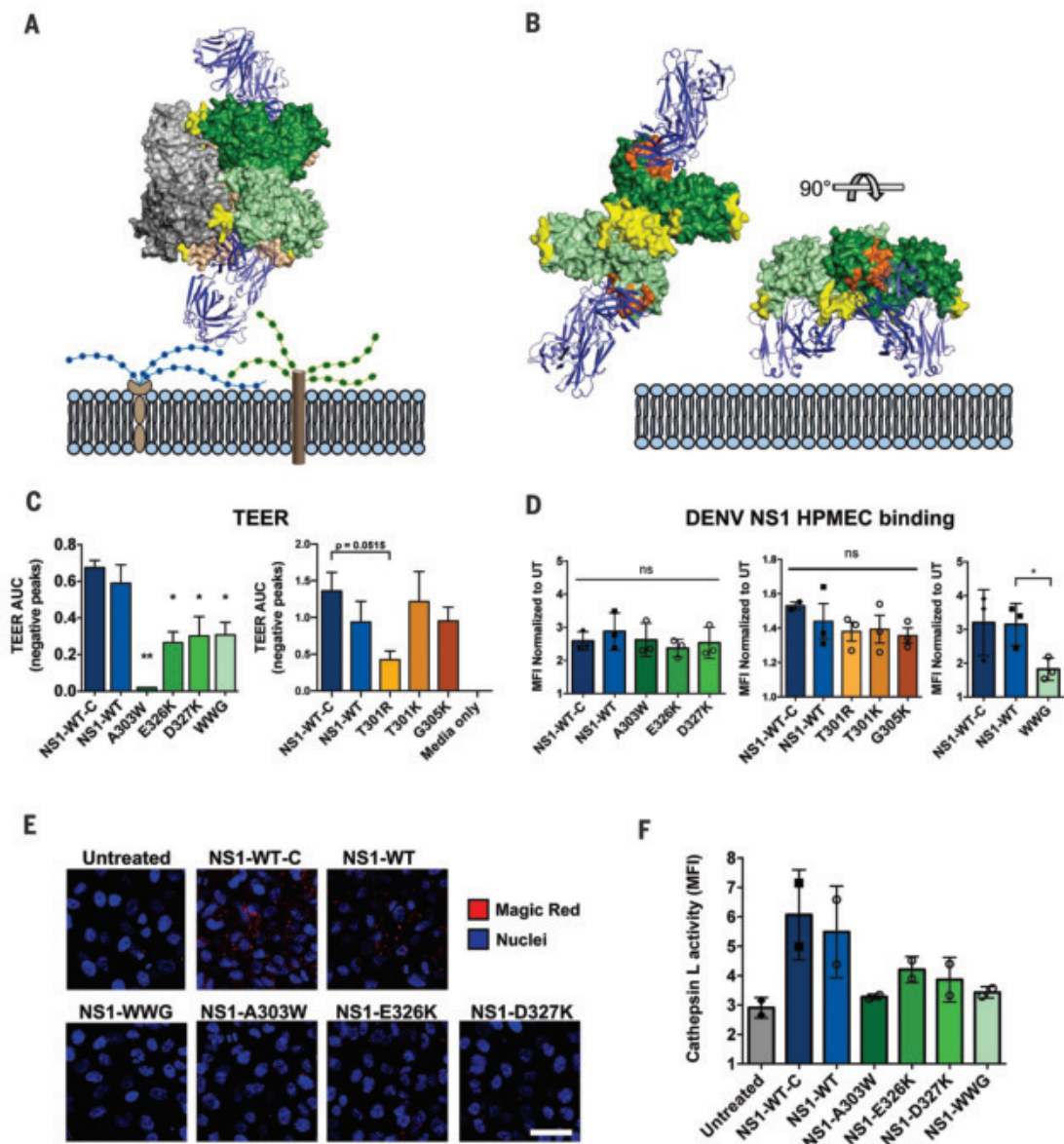
TECTIVE in mice in a dose-dependent manner compared with an IgG isotype control, as was a single-chain variable fragment (scFv) of 2B7, suggesting that protection could be achieved in a manner independent of antibody Fc effector functions (Fig. 1A and fig. S1A). By contrast, an anti-E antibody (4G2) given at the same dose was not protective and in fact led to an accelerated time to death (Fig. 1A). Further, 2B7 blocked DENV NS1-mediated vascular leak in the mouse dermis compared with an IgG isotype control (Fig. 1, B and C, and fig. S1, B and C). We next investigated the protective mechanism of 2B7 *in vitro* using human pulmonary microvascular endothelial cells

(HPMECs) and measuring electrical resistance in a transendothelial electrical resistance (TEER) assay. Both 2B7 and its antigen-binding fragment (Fab), but not an IgG isotype control, were sufficient to abrogate NS1-induced endothelial hyperpermeability (Fig. 1D). Further, 2B7 and its Fab abrogated NS1-mediated endothelial dysfunction of HPMECs as measured by cathepsin L activation and disruption of the EGL as measured by the surface concentrations of sialic acid (13, 26) (Fig. 1, E to G). We also determined that 2B7, as well as its Fab and scFv, were sufficient to block binding of NS1 to HPMECs and 293F cells (Fig. 1, H and I, and fig. S2, A to C).

**Fig. 4. Mechanistic insight into 2B7 blockade of NS1-mediated endothelial dysfunction.** (A) 2B7 Fab (blue ribbon) in complex with DENV1 NS1 hexamer above a schematic of the plasma membrane, illustrating 2B7 Fab-mediated steric hindrance of NS1 membrane interaction. The NS1 surface is colored by dimer (light and dark green at right, gray at left, and tan in the back), with hydrophobic regions shown in yellow for all three dimers. The 2B7 Fab is bound to both subunits of the green dimer and occludes cell surface interaction of the yellow wing-domain hydrophobic loop (centered on the WWG motif).

(B) Perpendicular views of the 2B7 Fab complex with DENV1 NS1 dimer illustrating Fab interference with membrane interaction of the NS1 hydrophobic face (yellow). The left image shows the dimer hydrophobic face with wing hydrophobic loops at the periphery and central hydrophobic surface of the  $\beta$ -roll domain. This face is inside the hexamer and invisible in (A) (see movie S1). The NS1 epitope for 2B7 is shown in orange.

(C) Endothelial hyperpermeability of HPMECs was monitored by TEER for the indicated DENV2 NS1 mutants compared with NS1-WT-C or NS1-WT. Data presented are  $n = 2$  biological replicates. (D) Cell binding to HPMECs of NS1 mutants or controls was monitored by immunofluorescence microscopy 90 min after NS1 treatment ( $n = 3$  biological replicates). (E) Endothelial dysfunction was monitored using immunofluorescence microscopy and the cathepsin L activity reporter molecule Magic Red 6 hours after treatment with DENV2 NS1 mutants or the indicated controls. Data presented are  $n = 2$  biological replicates. (F) Quantification of (E). n.s., not significant ( $P > 0.05$ ); \* $P < 0.05$ ; \*\* $P < 0.01$  by one-way ANOVA analysis with multiple comparisons.





Having demonstrated the protective capacity of 2B7 and its Fab against DENV NS1 in vivo and in vitro, we next investigated the structural basis of this protection. NS1 has three distinct domains: N-terminal  $\beta$ -roll, wing, and C-terminal  $\beta$ -ladder (27). An enzyme-linked immunosorbent assay (ELISA) measuring binding of 2B7 to full-length NS1, a recombinant wing domain (amino acid residues 38 to 151), or a recombinant  $\beta$ -ladder domain (residues 176 to 352) indicated that 2B7 bound strongly to both full-length NS1 and the  $\beta$ -ladder, but not the wing domain (fig. S2D). This observation was confirmed using biolayer interferometry (BLI) (fig. S2E), which also revealed NS1-binding dissociation constant ( $K_d$ ) values of  $4.8 \pm 3.1$  nM for full-length 2B7,  $8.3 \pm 6.8$  nM for the 2B7 Fab, and  $5.8 \pm 1.1$  nM for the 2B7 scFv. We then used the VirScan phage display system with 56-residue overlapping peptides tiled across the DENV2 NS1 polypeptide to identify the epitope target region and found that 2B7 interacted with two overlapping peptides from the C-terminal  $\beta$ -ladder domain (residues 260 to 316 and 288 to 344), consistent with our ELISA and BLI results (27) (fig. S3, A and B). We visualized the interaction between 2B7 and NS1 in detail by solving the crystal structures of the 2B7 Fab in complex with DENV1 NS1 (3.20-Å resolution; Fig. 2A; figs. S3B, S4A, and S5B; and table S1) and the 2B7 Fab and scFv in complex with DENV2 NS1 (scFv: 2.89-Å resolution; Fig. 2, B to D, and figs. S4B and S5A and table S1; Fab: 3.96-Å resolution, fig. S5, C and D, and table S1). Each NS1 dimer bound two copies of the scFv/Fab fragment, one to each distal tip of the  $\beta$ -ladder (Fig. 2A and figs. S4 and S5, C to E). The NS1:2B7 complex has an overall arch shape, where the antibody fragments form the sides of the arch, with the membrane-facing hydrophobic side of NS1 on the arch inner surface (Fig. 2A and fig. S4). In this configuration, the 2B7 Fab would likely prevent the hydrophobic face of NS1 from interacting with cell surfaces. The 2.89-Å electron density map was of sufficient quality to confidently build the scFv constant and variable regions as well as the side chains of the combining site of the 2B7 scFv and the DENV2 NS1 discontinuous epitope (Fig. 2, B to D, and fig. S5A). The variable loops of the 2B7 light chain make numerous contacts with NS1  $\beta$ -ladder residues, consistent with our ELISA, BLI, and phage display results (Fig. 2, B to D; figs. S3 to S5; and table S2). The binding modalities of 2B7 to NS1 were identical in our three structures (fig. S5E), and the NS1 structure was unchanged by 2B7 binding.

The amino acid residues in the 2B7 epitope can be divided into two classes: the epitope core region, composed of residues that are highly conserved across flaviviruses, and the epitope periphery, displaying varying levels of divergence among flaviviruses (Figs. 2, B

to D, and 3A). Hypothesizing that 2B7 would recognize distinct flavivirus NS1 proteins with affinities that correlated with the extent of conservation with DENV NS1, we performed ELISAs to measure the relative affinities of 2B7 for a panel of flavivirus NS1 proteins, including DENV 1-4, ZIKV, Saint Louis encephalitis virus (SLEV), WNV, JEV, tick-borne encephalitis virus (TBEV), Powassan virus (POWV), Usutu virus (USUV), Wesselsbron virus (WSLV), and YFV. 2B7 bound most tightly to NS1 from DENV1-4, followed by ZIKV, SLEV, WNV, JEV, USUV, and WSLV, with minimal binding detected for YFV, POWV, and TBEV (Fig. 3, B and C). The strength of binding correlated with the degree of conservation with DENV NS1. To determine the relative contribution of key flavivirus NS1 amino acid residues on 2B7 binding, we created single, double, triple, or quadruple substitutions of the DENV2 NS1  $\beta$ -ladder amino acids within the NS1:2B7 epitope (table S3). We initially screened NS1 mutants produced in 293T cells for candidates that were secreted and displayed diminished binding to 2B7 (fig. S6, A and B). We then selected seven DENV NS1  $\beta$ -ladder single substitutions (NS1-D281P, NS1-T301R, NS1-T301K, NS1-A303W, NS1-G305K, NS1-E326K, and NS1-D327K) for purification and 2B7-binding ELISAs. A direct ELISA revealed that with the exception of NS1-D281P, each of these mutants displayed weaker binding to 2B7 compared with NS1 wild type (NS1-WT) (Fig. 3, D and E; fig. S6A and table S3). To confirm the role of the flavivirus-conserved residues described above in 2B7 binding to multiple flavivirus NS1 proteins, we created two single mutants for both the WNV and ZIKV NS1 proteins (WNV/ZIKV NS1-T301K and NS1-G305K) (fig. S7, A to C). A direct ELISA revealed that these NS1 mutants exhibited a severe binding defect to 2B7 compared with their respective NS1-WT control proteins (Fig. 3F). To determine whether the NS1 cross-reactivity of 2B7 correlated with function, we used ZIKV and WNV NS1 proteins in NS1 cell-binding and TEER assays on human brain microvascular endothelial cells (HBMECs). 2B7, but not an IgG isotype control, blocked binding and abrogated NS1-mediated endothelial hyperpermeability in a dose-dependent manner correlating with conservation to DENV2 NS1, indicating that one cross-reactive NS1 mAb could inhibit pathogenic functions of NS1 from multiple flaviviruses (Fig. 3, G to J, and fig. S8, A to C). Because ADE of DENV infection is problematic for anti-E antibodies, we confirmed that anti-NS1 mAb 2B7 was incapable of mediating ADE of DENV, ZIKV, and the WNV strain Kunjin virus (KUNV) infection (fig. S9, A to D). Further, because anti-NS1 antibodies have been reported to modulate the clotting cascade (28) and also to bind to endothelial cells, which may directly

mediate endothelial dysfunction (29), we tested the capacity of 2B7 to alter the clotting time of human plasma and to bind to the surface of endothelial cells. These experiments determined that 2B7 does not alter human plasma clotting time and binds to the surface of endothelial cells significantly more than an isotype control only when NS1 is present, suggesting that 2B7 would likely not enhance DENV disease through these specific mechanisms (fig. S10, A to C).

Because NS1 is reported to mediate endothelial dysfunction through distinct steps including cell binding, EGL disruption, and endothelial hyperpermeability (13, 14, 16), the mode of 2B7 binding to NS1 provides an opportunity to investigate the molecular basis of NS1-mediated endothelial dysfunction. Although 2B7 binds to the  $\beta$ -ladder, its tilted orientation toward the NS1 hydrophobic surface (Figs. 2A and 4, A and B, and figs. S4 and S5) predicts that 2B7 would create indirect steric hindrance for the wing domain and interfere with a predicted interaction between the NS1 wing domain and the cell surface regardless of whether NS1 is in the dimeric or hexameric form (22, 30) (Fig. 4, A and B, and movie S1). Therefore, 2B7 is predicted to interfere with both the wing (indirect steric hindrance) and  $\beta$ -ladder (direct binding) of NS1, suggesting that both domains may be critical for NS1 pathology. To test this prediction, we generated mutant expression constructs for NS1 with substitutions predicted to hinder binding to the cell surface or to 2B7. In addition to the DENV NS1  $\beta$ -ladder mutants described above, we created a DENV NS1 triple substitution within the flavivirus-conserved  $W^{115}XXW^{118}G^{119}$  motif ( $A^{115}XXA^{118}A^{119}$ ) in an immunodominant region of the wing, which is predicted to interact with the cell surface (22, 30–32) (fig. S11 and Fig. 4, A and B). We purified six DENV NS1  $\beta$ -ladder single substitutions (NS1-T301R, NS1-T301K, NS1-A303W, NS1-G305K, NS1-E326K, and NS1-D327K) and the wing domain triple substitution (NS1-WWG>AAA, “NS1-WWG”). All proteins were expressed, secreted, oligomeric, stable, and of purity comparable to that of NS1-WT (fig. S12, A to F). Further, in contrast to the NS1  $\beta$ -ladder mutants, the wing domain mutant did not exhibit diminished binding to 2B7 compared with NS1-WT (Fig. 3, D and E, and fig. S12G). In a TEER assay on HPMECs with these mutant NS1 proteins, all NS1 mutants except the  $\beta$ -ladder mutants NS1-T301K and NS1-G305K were defective in their capacity to mediate endothelial hyperpermeability compared with NS1-WT, with NS1-A303W displaying the greatest functional defect (Fig. 4C and fig. S13A). These data indicate that several residues in the tip of the  $\beta$ -ladder and, separately, in the wing domain are critical for NS1-mediated endothelial dysfunction. To investigate



the mechanism(s) of the functional defects of these NS1 mutants, we conducted an NS1 cell-binding assay using both HPMECs and 293F cells and found that although NS1 with  $\beta$ -ladder substitutions bound to cells comparably to NS1-WT, NS1-WWG had a significant cell-binding defect (Fig. 4D and fig. S13, B and C). By contrast, when we examined steps downstream of NS1 binding, such as activation of cathepsin L, all mutants tested were defective relative to NS1-WT (Fig. 4, E and F). Taken together, these data suggest that the NS1 wing domain, specifically the WWG motif, is critical for initial attachment of NS1 to cells, whereas the tip of the  $\beta$ -ladder is critical for downstream events required for NS1-mediated endothelial dysfunction.

Overall, these findings serve as proof of concept that one cross-reactive antibody targeting flavivirus NS1 proteins can provide protection against NS1-mediated pathology from multiple flaviviruses, with no risk of ADE. Further, the structure of the 2B7 scFv or Fab in complex with NS1 revealed that 2B7 obscures the  $\beta$ -ladder through direct binding and the wing domain through indirect steric hindrance of the NS1 dimer and/or hexamer form, suggesting that one anti-NS1 mAb can simultaneously antagonize the cellular interactions of two NS1 domains. DENV NS1 mutagenesis showed the wing domain to be critical for initial binding to the endothelial cell surface and the  $\beta$ -ladder to be essential for downstream NS1-mediated events, both crucial steps for NS1-triggered pathology. Information gained from the differential binding affinities of 2B7 for multiple flavivirus NS1 proteins provides a molecular roadmap for the rational design of mAbs or other therapeutics with even broader flavivirus NS1 cross-reactivity compared with 2B7. In sum, our structural and mechanistic investigations of 2B7-mediated protection re-

veal the critical and distinct roles of the NS1 wing domain and the  $\beta$ -ladder and highlight the possibility of treating multiple flavivirus infections with one therapeutic targeting flavivirus NS1.

## REFERENCES AND NOTES

1. S. Bhatt *et al.*, *Nature* **496**, 504–507 (2013).
2. S. B. Halstead, *Lancet* **370**, 1644–1652 (2007).
3. P. R. Beatty *et al.*, *Sci. Transl. Med.* **7**, 304ra141 (2015).
4. N. Modhiran *et al.*, *Sci. Transl. Med.* **7**, 304ra142 (2015).
5. A. L. Rothman, *Nat. Rev. Immunol.* **11**, 532–543 (2011).
6. S. Sridhar *et al.*, *N. Engl. J. Med.* **379**, 327–340 (2018).
7. L. C. Katzelnick *et al.*, *Science* **358**, 929–932 (2017).
8. P. Scaturro, M. Cortese, L. Chatel-Chaix, W. Fischl, R. Bartenschlager, *PLOS Pathog.* **11**, e1005277 (2015).
9. I. Gutsche *et al.*, *Proc. Natl. Acad. Sci. U.S.A.* **108**, 8003–8008 (2011).
10. S. A. Paranavane *et al.*, *BMC Infect. Dis.* **14**, 570 (2014).
11. P. Avirutnan *et al.*, *J. Exp. Med.* **207**, 793–806 (2010).
12. C. H. Chao *et al.*, *PLOS Pathog.* **15**, e1007625 (2019).
13. H. Puerta-Guardo, D. R. Glasner, E. Harris, *PLOS Pathog.* **12**, e1005738 (2016).
14. D. R. Glasner, H. Puerta-Guardo, P. R. Beatty, E. Harris, *Annu. Rev. Virol.* **5**, 227–253 (2018).
15. S. Singh, M. G. Anupriya, A. Modak, E. Sreekumar, *J. Gen. Virol.* **99**, 1658–1670 (2018).
16. H. Puerta-Guardo *et al.*, *Cell Rep.* **26**, 1598–1613.e8 (2019).
17. H. Puerta-Guardo *et al.*, *J. Infect. Dis.* **221**, 313–324 (2020).
18. D. A. Espinosa *et al.*, *J. Immunol.* **202**, 1153–1162 (2019).
19. A. C. Brault *et al.*, *Sci. Rep.* **7**, 14769 (2017).
20. J. J. Schlesinger, M. W. Brandriss, E. E. Walsh, *J. Gen. Virol.* **68**, 853–857 (1987).
21. D. L. Akey *et al.*, *Science* **343**, 881–885 (2014).
22. X. Xu *et al.*, *EMBO J.* **35**, 2170–2178 (2016).
23. M. A. Edeling, M. S. Diamond, D. H. Fremont, *Proc. Natl. Acad. Sci. U.S.A.* **111**, 4285–4290 (2014).
24. T. Poonsiri *et al.*, *J. Virol.* **92**, e01868-17 (2018).
25. H. Song, J. Qi, J. Haywood, Y. Shi, G. F. Gao, *Nat. Struct. Mol. Biol.* **23**, 456–458 (2016).
26. D. R. Glasner *et al.*, *PLOS Pathog.* **13**, e1006673 (2017).
27. G. J. Xu *et al.*, *Science* **348**, aaa0698 (2015).
28. Y. C. Chuang, J. Lin, Y. S. Lin, S. Wang, T. M. Yeh, *J. Immunol.* **196**, 1218–1226 (2016).
29. C. F. Lin *et al.*, *J. Med. Virol.* **69**, 82–90 (2003).
30. W. C. Brown *et al.*, *Nat. Struct. Mol. Biol.* **23**, 865–867 (2016).
31. T. Hertz *et al.*, *J. Immunol.* **198**, 4025–4035 (2017).
32. Y. C. Lai *et al.*, *Sci. Rep.* **7**, 6975 (2017).

## ACKNOWLEDGMENTS

We thank A. Sandstrom (UC Berkeley) for assistance with size-exclusion chromatography; A. Sandstrom and P. S. Mitchell (UC Berkeley) for helpful discussion and critical reading of this manuscript; C. M. Warnes (UC Berkeley) for technical assistance with 2B7 antibody purification; Y. Leng (Brigham and Women's Hospital) for assistance processing 2B7 with VirScan; and M. Diamond (Washington University in St. Louis) for the pmab vector containing the WT DENV2 NS1 protein (strain 16681). Confocal imaging experiments were conducted on a Zeiss LSM 710 at the CRL Molecular Imaging Center at UC Berkeley, which is supported by the Gordon and Betty Moore Foundation. This research used the GM/CA@APS facility funded by the NIH NIGMS (AGM-12006) and the NIH NCI (ACB-12002) at the Advanced Photon Source at Argonne National Laboratory (DE-AC02-06CH11357). The Eiger 16M detector was funded by NIH (S10 OD012289). **Funding:** This work was supported by NIAID/NIH grants R01 AI24493 (E.H.), R21 AI146464 (E.H.), U19 AI109761 (E.H., Program Director I. Lipkin), and R56 AI130130 (J.L.S.). S.J.E. was supported by NIH grant 5U24AI116833-02 and Bill and Melinda Gates Foundation grant OPP1155863. M.J.M. and S.J.E. were supported by a Value of Vaccine Research Network grant. S.B.B. was partially supported as an Open Philanthropy Awardee of the Life Sciences Research Foundation.

**Author contributions:** Conceptualization: S.B.B., D.L.A., M.P.W., W.C.B., N.T.N.L., H.P.-G., C.W., P.R.B., J.L.S., E.H.; Funding acquisition: S.J.E., M.J.M., J.L.S., E.H.; Investigation: S.B.B., D.L.A., M.P.W., W.C.B., N.T.N.L., H.P.-G., F.T.G.d.S., C.W., J.R.K., D.A.E., N.J.B., D.R.G., J.L., S.F.B., E.Y.J., M.J.M.; Methodology: S.B.B., D.L.A., M.P.W., W.C.B., N.T.N.L., H.P.-G., F.T.G.d.S., C.W., J.R.K., N.J.B., P.R.B., J.L.S., E.H.; Project administration: J.L.S., E.H.; Supervision: S.J.E., M.J.M., J.L.S., E.H.; Visualization: S.B.B., D.L.A., M.P.W., W.C.B., N.T.N.L., H.P.-G., F.T.G.d.S., J.R.K., D.A.E., J.L., S.F.B., M.J.M., J.L.S., E.H.; Writing – original draft: S.B.B., D.L.A., W.C.B., J.L.S., E.H.; Writing – review & editing: S.B.B., D.L.A., M.P.W., W.C.B., N.T.N.L., H.P.-G., S.J.E., P.R.B., J.L.S., E.H.

**Competing interests:** The authors declare no competing interests.

**Data and materials availability:** The structures of DENV1 NS1-2B7 Fab, DENV2 NS1-2B7 Fab, and DENV2 NS1-2B7 scFV have been deposited in the Protein Data Bank with accession codes 6WEQ, 6WER, and 7K93, respectively. The sequences of the 2B7 mAb heavy and light chains have been submitted to GenBank with accession codes MW246826 and MW246827, respectively. Materials generated in this study are available upon request.

## SUPPLEMENTARY MATERIALS

science.sciencemag.org/content/371/6525/194/suppl/DC1  
Materials and Methods  
Figs. S1 to S13  
Tables S1 to S4  
References (33–46)  
Movie S1  
MDAR Reproducibility Checklist

3 April 2020; accepted 23 November 2020  
10.1126/science.abc0476



### Cell Thawer

Eppendorf now offers a further building block in supporting scientists with tailored solutions for the daily lab routine. Controlled, reliable cell thawing is mandatory for further downstream experiments in every cell-handling lab. Although water-bath based or

even manual thawing of cells is still commonly practiced, these methods are not as desirable due to their limited reproducibility. The Eppendorf ThermoMixer C now features an exchangeable thermoblock, the cryo-thaw SmartBlock, which provides a dedicated thawing program for reproducible, reliable thawing of cells from frozen storage conditions up to 37°C.

#### Eppendorf

For info: 800-645-3050

[www.eppendorf.com/thermomixer](http://www.eppendorf.com/thermomixer)

### Recombinant Monoclonal SARS-CoV-1/2 Antibodies

In response to the community's need for highly specific and reproducible antibodies for SARS-CoV-1/2 research, MilliporeSigma has designed ZooMAb recombinant monoclonal antibodies against various SARS CoV 1/2 targets. ZooMAb antibodies are all recombinantly produced, lyophilized, and free of animal components. Explore our offering of ZooMAb recombinant monoclonal antibodies that are suitable for COVID-19 research: Anti-SARS-CoV-1/2 NP, clone 1C7C7 ZooMAb Mouse Monoclonal Nucleoprotein; Anti-SARS-CoV-1/2 S Protein, clone 2B3E5 ZooMAb Mouse Monoclonal SARS-CoV-1/2 Spike Glycoprotein; and Anti-SARS-CoV-1/2 S Protein clone hu2B3E5 ZooMAb Chimeric Monoclonal.

#### MilliporeSigma

For info: 800-325-3010

[www.sigmaaldrich.com](http://www.sigmaaldrich.com)

### 3D Bioprinter

The BioScaffolder Prime from Analytik is an affordable, high-performance 3D bioprinter that delivers precision engineering in an advanced, customizable platform. The rapidly expanding field of 3D bioprinting for tissue engineering and regenerative medicine combines biocompatible/biodegradable polymers with living cells. This bioprinter package offers researchers the ability to create bioscaffolds for cell growth and to deposit layers of bioinks on implants or microfluidic objects. The unit can be equipped with multiple dispensing tools, including unique core/shell tools for simultaneous dispensing of different materials. Decentralized units for printing, media control, and computing save precious space in your biosafety cabinet and ensure superb heat dissipation. Silent but smart XYZ-drives deliver micrometer precision. In addition, the system comes with a Peltier heater/cooler cartridge for temperature-controlled bioprinting and a built-in UV-source UV-LED pen. Designed to fit and operate in a standard biosafety cabinet, BioScaffolder Prime enables you to undertake your 3D printing applications quickly, safely, and in a sterile environment.

#### Analytik

For info: +44-(0)-1954-232776

[www.analytik.co.uk](http://www.analytik.co.uk)

### Semiautomated Tube Picker

Ziath reports strong uptake of its Mohawk semiautomated tube picker in smaller biobanks and biorepositories, which need to select tubes from cold racks straight from the freezer but cannot afford the huge investment in robotics required to automatically pick and place tubes. The small, compact Mohawk can pick up 16 tubes simultaneously from a 96-position tube rack. By elevating sample tubes in racks using solenoids, the Mohawk enables biobank operators to quickly retrieve the correct tubes and put them in the destination racks. Additionally, because the Mohawk can seamlessly connect with Ziath rack scanners, biobank users can read a picking list, select tubes, and verify that the correct tubes are picked—making the process of finding and selecting the right tubes in your biobank more efficient and economical.

#### Ziath

For info: +44-(0)-1223-855021

[www.ziath.com](http://www.ziath.com)

### Low Temperature Flow Chemistry Module

The Cold Coil II Flow Reactor Module from Uniqsis is a flexible, entry-level solution for low temperature flow chemistry applications. Used in conjunction with an external thermoregulation circulator, the unit can maintain stable temperatures between -78°C and 150°C for extended periods of time. It is compatible with all Uniqsis coil reactors, from 2.0 mL up to 60 mL capacity. A proprietary clamping mechanism holds the coil reactor firmly in place and ensures optimal thermal contact while allowing easy interchange of coil reactors. The Cold Coil II can be easily converted into a photoreactor by coupling it with a Uniqsis PhotoSyn high-power LED light module. It is also compatible with the Uniqsis HotColumn multiple-column reactor adaptor for packed-bed applications. To ensure accurate remote measurement of the Cold Coil II reactor temperature, an optional internal temperature probe can be connected directly via RS232C.

#### Uniqsis

For info: +44-(0)-845-864-7747

[www.uniqsis.com](http://www.uniqsis.com)

### Microplate Sealing for LC/MS Applications

The RAPID EPS (Easy Piercing Seal) from BioChromato is designed for scientists looking to prevent contamination issues and autosampler-needle clogging when accessing samples stored in 96-well microplates ready for LC/MS analysis. For LC/MS users, a key criterion for an effective microplate seal is its resistance to solvents such as acetonitrile, methanol, and DMSO, which are commonly used in experiments and analysis. The RAPID EPS uses a synthetic rubber adhesive to create a high-integrity, airtight seal with microplates, and shows no contamination in the eluents. In addition, the unique construction of BioChromato's RAPID EPS does not leave particulate material when pierced, further safeguarding your samples from contamination and eliminating potentially harmful effects to your LC/MS autosampler. The RAPID EPS is proven to offer dependable microplate sealing over a working temperature range of -80°C to 80°C.

#### BioChromato

For info: +81-(0)-466-23-8382

[biochromato.com](http://biochromato.com)

Electronically submit your new product description or product literature information! Go to [www.sciencemag.org/about/new-products-section](http://www.sciencemag.org/about/new-products-section) for more information.

Newly offered instrumentation, apparatus, and laboratory materials of interest to researchers in all disciplines in academic, industrial, and governmental organizations are featured in this space. Emphasis is given to purpose, chief characteristics, and availability of products and materials. Endorsement by *Science* or AAAS of any products or materials mentioned is not implied. Additional information may be obtained from the manufacturer or supplier.



## The 2021 (37th) International Prize for Biology

### Calling for Nominations

The 2021's research field: **Biology of Human Evolution**  
Please access to: <http://www.jsps.go.jp/english/e-biol>

**Deadline: April 9, 2021**

- The International Prize for Biology was established in 1985 to commemorate the 60-year reign of Emperor Showa and his longtime devotion to biological research.
- The Prize is awarded each year to an individual who has made an outstanding contribution to the advancement of basic research in a field of biology.
- The Prize shall consist of a medal and a prize of 10 million yen.
- The award ceremony will be held in Tokyo in November or December in the presence of their Imperial Highnesses Crown Prince and Crown Princess Akishino.

### Recent Years Prize Winners



2020  
Dr. SHINOZAKI Kazuo  
(Biology of Environmental Responses)



2019  
Dr. Naomi E. Pierce  
(Biology of Insects)



2018  
Dr. Andrew H. Knoll  
(Paleontology)



JAPAN SOCIETY FOR THE PROMOTION OF SCIENCE

日本学術振興会

## Who's the top employer for 2020?

Science Careers' annual survey reveals the top companies in biotech & pharma voted on by *Science* readers.

Read the article and employer profiles at [sciencecareers.org/topemployers](http://sciencecareers.org/topemployers)



**Science 2020  
TOP EMPLOYER**



# YOU'D SMILE TOO IF YOU JUST ADVANCED YOUR CAREER.



Find your next job at [ScienceCareers.org](http://ScienceCareers.org)

There's scientific proof that when you're happy with what you do, you're better at what you do. Access career opportunities, see who's hiring and take advantage of our proprietary career-search tools. Get tailored job alerts, post your resume and manage your applications all in one place: [sciencecareers.org](http://sciencecareers.org)

## Science Careers

FROM THE JOURNAL SCIENCE AAAS





# Global Talent Recruitment Announcement

## Institute of Eco-Chongming, East China Normal University



**Institute of Eco-Chongming (IEC)**, located on the scenic Chongming Island, Shanghai, China, is a newly founded research institute of East China Normal University (ECNU). IEC strives to establish a research platform of interdisciplinary studies in ecology, environment, and Earth System Sciences. Under the concept of “opening up, collaboration, and pursuit of excellence,” IEC provides the scientific and technological support that is critical for the sustainable development of Chongming as a world-class ecological island.

### POSITIONS AVAILABLE

IEC is recruiting highly qualified individuals in the fields of ecology, environmental sciences, geoscience or other related fields for the following positions:

### 1.Professors and Associate Professors

**Requirements:** Candidates applying for this position must have obtained a PhD in addition to an outstanding international academic and research background. The research achievements should be recognized domestically as well as internationally, and have produced or intend to produce a lasting and major impact on their fields of study.

### 2.Chongming Postdoctoral Fellows

**Requirements:** Candidates must have obtained a PhD and can conduct scientific research independently.

**Research areas:** water pollution prevention and control, ecological restoration, ecological monitoring, ecological modelling and remote sensing, carbon cycle and nitrogen cycle, eco-island assessment and planning, or other fields relevant to ecology and geoscience.

### SALARIES AND BENEFITS

1.IEC shall provide an internationally competitive compensation package, including the salary, start-up research funds and housing allowance. This is contingent upon the candidate's work experience and potential achievements.

2.ECNU shall provide other benefits, such as registered permanent residence in Shanghai, social and health insurance, housing provident fund, apartments for short-term use, and children's admissions to ECNU-affiliated schools.

### APPLICATION

Candidates are to send the following documents to [mxlu@chm.ecnu.edu.cn](mailto:mxlu@chm.ecnu.edu.cn)

1.Cover letter;

2.Application Form, which can be downloaded at <http://chm.ecnu.edu.cn/iec/45/5c/c21417a279900/page.htm>;

### 3.Supporting documents

For professor/associate professor positions:

Degree certificates, diploma certificates, certificates of employment and titles, five representative published papers, completed research projects, participation in major international academic activities, appointments or memberships in professional or scientific societies, and award certificates of scientific and technological achievements at the provincial level or above;

For the position of “Chongming Postdoctoral Fellows”:

Degree certificates and diploma certificates, three representative published papers;

4.Contact details of three referees.

Contact: Maixin Lu

Tel: 8621-59611221

Website: [chm.ecnu.edu.cn](http://chm.ecnu.edu.cn)



## One-on-one Career Consultation

Professional in Job seeking, Customize your career plan

RESUME EVALUATION

CAREER CONSULTATION

JOB RECOMMENDATION

Join us and get

Assistance in your interview

Informed of latest activities

Talent policy interpretation

### OUR FEATURE »

#### Information Management

Search for thousands of job opportunities  
Direct delivery of applications

#### Workstation in 28 Cities

Close cooperation with  
School HR Dept., Colleges  
and Research Institutes

#### Thousand Jobs in

All disciplines  
Faculty & postdoc

#### Recruitment Activities

Online job fair  
“Overseas scholars visit to  
China” forums

If you are seeking job opportunities in Chinese universities or research institutes, please contact the talent service agency of AcaBridge ([consultant@acabridge.edu.cn](mailto:consultant@acabridge.edu.cn)), which provides one-on-one consultations. For more information, visit us at [www.acabridge.edu.cn](http://www.acabridge.edu.cn).



Scan to apply

**myIDP:**  
A career plan customized  
for you, by you.

For your career in science, there's only one

Science

**Features in myIDP include:**

- Exercises to help you examine your skills, interests, and values.
- A list of 20 scientific career paths with a prediction of which ones best fit your skills and interests.
- A tool for setting strategic goals for the coming year, with optional reminders to keep you on track.
- Articles and resources to guide you through the process.
- Options to save materials online and print them for further review and discussion.
- Ability to select which portion of your IDP you wish to share with advisors, mentors, or others.
- A certificate of completion for users that finish myIDP.



Visit the website and start planning today!  
[myIDP.sciencecareers.org](http://myIDP.sciencecareers.org)

**ScienceCareers** In partnership with: AAAS







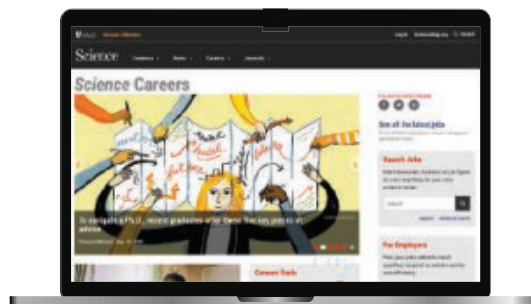
## Science Careers helps you advance your career. Learn how !

- Register for a free online account on **ScienceCareers.org**.
- Search hundreds of job postings and find your perfect job.
- Sign up to receive e-mail alerts about job postings that match your criteria.
- Upload your resume into our database and connect with employers.
- Watch one of our many webinars on different career topics such as job searching, networking, and more.
- Download our career booklets, including Career Basics, Careers Beyond the Bench, and Developing Your Skills.
- Complete an interactive, personalized career plan at "my IDP."
- Visit our Employer Profiles to learn more about prospective employers.
- Read relevant career advice articles from our library of thousands.

Visit **ScienceCareers.org**  
today — all resources are free

**ScienceCareers**

FROM THE JOURNAL SCIENCE  AAAS



SCIENCECAREERS.ORG



By Saman Razavi

# Breaking through language barriers

I was sitting in a conference room with my new labmates, eager to engage about the exciting research we were all working on. Halfway through the meeting—my first as a Ph.D. student—I tried to contribute a couple of sentences. Suddenly, the room went quiet and I got lots of funny looks. I was overcome with embarrassment as I realized what had happened. Speaking about water movement in a river basin, I meant to say “upstream” and “downstream.” But instead my brain had gone with a word-by-word translation of the terms in my first language, Farsi: “high-hand” and “low-hand.” This was just the first of many times my brain failed to summon the right English words.

When I decided to leave my home country of Iran to pursue a Ph.D. in Canada, I hadn't expected that communication would be an issue. In Farsi, I was an effective speaker. I had taken English lessons in my 20s and scored well on the English test for university admission.

But soon after my arrival in the English-speaking world, I realized how wrong I was. Expressing myself in Farsi had been effortless, but now I had to be careful and deliberate. I needed to consciously and simultaneously (1) follow the conversation and translate it to my native language, (2) reflect and generate thoughts and ideas in response, and (3) find the right English words and put them in the right order to communicate that response. I had a hard time remaining present and focused in conversations because I was constantly thinking about what I would say next. I gradually turned inward and passive, particularly when surrounded by native English speakers. And I worried about my future. After all, effective communication in English is critical to being included and recognized in many academic and professional environments.

But after another lab meeting a few months into my Ph.D. when I again failed to say exactly what I meant, a simple idea occurred to me. Why not contribute to the discussion in writing, in an email to my colleagues? That small tweak was a game changer, because writing gave me time to reflect and comfortably articulate my points in English. I made a practice of sitting at my computer and putting my Farsi thoughts into English words, taking my time to craft clear sentences with accurate vocabulary and grammar. Over time, this practice helped me simultaneously think and speak in English, as I do in my first language. I grew more comfortable with oral communication, which revived my spirits.



**“With some effort on both sides, language barriers need not be insurmountable.”**

At the same time, I learned to be open with colleagues about the language barriers I faced. I realized how essential this was when, as a third-year Ph.D. student, I joined the executive team of my department's graduate student association. I held back in our meetings because I still wasn't confident about my communication ability. Soon, however, I felt the native English speakers on the team would interpret my apparent lack of engagement as a lack of interest. So I decided to remind my peers that English is not my first language, and I asked them to speak more slowly to help me follow the discussion and participate fully.

It was a little awkward to bring it up—after all, it was already crystal clear that English was not my first language, and I was hesitant to draw

attention to something that might be seen as a weakness. And at first, the other members of the executive team seemed slightly taken aback. But the dynamic quickly improved. They seemed to become more aware of how they were speaking, and I felt more comfortable contributing to the conversation, even if it meant slowing down the discussion a little bit.

Now, 12 years after I moved to Canada, my language skills have greatly improved—but they're not perfect. In meetings where I am the only nonnative English speaker, the pace of the conversation can still sometimes present a challenge. But I have learned that I can prepare and be open with others about the difficulties I and other nonnative English speakers may experience. With some effort on both sides, language barriers need not be insurmountable. ■

Saman Razavi is an associate professor at the University of Saskatchewan School of Environment and Sustainability. He thanks Maureen Reed for comments and insights. Send your career story to [SciCareerEditor@aaaas.org](mailto:SciCareerEditor@aaaas.org).



*Science* Webinars help you keep pace with emerging scientific fields!

Stay informed about scientific breakthroughs and discoveries.

Gain insights into current research from top scientists.

Take the opportunity to ask questions during live broadcasts.

 Get alerts about upcoming free webinars.



**Sign up at: [webinar.sciencemag.org/stayinformed](https://webinar.sciencemag.org/stayinformed)**

# READY TO PUT THE SPOTLIGHT ON YOUR RESEARCH?

Submit your research:  
**[cts.ScienceMag.org](https://cts.sciencemag.org)**

ScienceImmunology



 Twitter: @SciImmunology  
 Facebook: @ScienceImmunology